UNIVERSIDADE DE LISBOA
FACULDADE DE CIÊNCIAS

Data Analysis of the Water and Scintillator Phases of SNO+: from Solar Neutrino Measurements to Double Beta Decay Sensitivity Studies

" Documento Definitivo"

Doutoramento em Física

Ana Sofia Carpinteiro Inácio

Tese orientada por:
Doutor José Carvalho Maneira
Doutora Valentina Lozza

Documento especialmente elaborado para a obtenção do grau de doutor

2022

UNIVERSIDADE DE LISBOA
FACULDADE DE CIÊNCIAS

Data Analysis of the Water and Scintillator Phases of SNO+: from Solar Neutrino Measurements to Double Beta Decay Sensitivity Studies

Doutoramento em Física

Ana Sofia Carpinteiro Inácio

Tese orientada por:
Doutor José Maneira e Doutora Valentina Lozza

Júri:
Presidente:

- Doutor José Manuel Nunes Vicente Rebordão, Investigador Coordenador e Presidente do Departamento de Física da Faculdade de Ciências da Universidade de Lisboa

Vogais:

- Doutora Jeanne Rachel Wilson Hawke, Reader do Department of Physics do King's College London, Reino Unido
- Doutor Alexandre Miguel Ferreira Lindote, Investigador Doutorado da Faculdade de Ciências e Tecnologia da Universidade de Coimbra
- Doutor José Carvalho Maneira, Investigador Auxiliar do LIP, Laboratório de Instrumentação e Física Experimental de Partículas (Orientador)
- Doutor Luís Filipe dos Santos Garcia Peralta, Professor Associado com Agregação da Faculdade de Ciências da Universidade de Lisboa.

Documento especialmente elaborado para a obtenção do grau de doutor

Doutoramento financiado pela FCT com a bolsa PD/BD/135468/2017

2022

Acknowledgements

The work presented in this thesis is the culmination not only of countless hours of work and dedication to experimental neutrino physics, but also the result of scientific collaboration with numerous researchers who have taught, supported, and guided me every step of the way.

My deepest gratitude goes towards my supervisors José Maneira and Valentina Lozza, who have been exceptional mentors and friends, going above and beyond to help me and guide my work. They gave me the tools and freedom to become an independent researcher, and plenty of constructive criticism to ensure that I would always strive to do my best at any task. I am very grateful to all the members of the LIP SNO+ group for all their support, suggestions, and interesting discussions during our lunch breaks. Their different backgrounds and life experiences pushed me to look beyond my work bubble.

I feel very fortunate to have worked for almost 7 years on the SNO+ experiment, which gave me the opportunity to work closely with many incredible collaborators scattered all around the world, and be a part of a remarkable research environment. I would like to acknowledge all the former and current members of the SNO+ Optics, Solar, Double Beta and Background groups for all their invaluable feedback, suggestions and discussions about my work. Special thanks go to Anthony Zummo (UPenn) and Max Smiley (UC Berkeley), with whom I worked closely on the target-out ROI analysis and ^{8}B solar neutrino analysis presented in this thesis, respectively. Benjamin Tam, Cindy Lin, Matt Depatie, Stephanie Walton, Charlie Mills, Rachel Richardson and Lorna Nolan: the warmth and friendship of these SNO+ members turned my long term stay at SNOLAB into an unforgettable adventure. Additional bonus points go to Lorna Nolan for being an amazing thesis writing buddy.

I would not be where I am today without the unconditional support and encouragement from my family. In fact, a part of the work in this thesis was accomplished thanks to my father, who shared with me random facts that he saw in a documentary, leading me to figure out a mistake that I was making in my calculations. Last but not least, I am deeply grateful to Diogo for his infinite patience while listening to my monologues, and for walking side-by-side with me on this crazy journey.

The work present in this thesis has been funded by Fundação para a Ciência e Tecnologia (FCT), Portugal, through the research grant PTDC/FIS-NUC/0640/2014 and through the IDPASC PhD grant PD/BD/135468/2017. I thank LIP and SNOLAB for hosting me.

Abstract

SNO+ is a leading liquid scintillator experiment for neutrino physics, with the ultimate goal of conducting a low background search for $0\nu\beta\beta$ decay using 1300 kg of ^{130}Te. The observation of this lepton-number-violating nuclear transition would provide fundamental insights regarding the neutrino mass and nature, opening doors to physics beyond the Standard Model. The success of this search relies on a complete understanding of the backgrounds contaminating the $0\nu\beta\beta$ region-of-interest, and an accurate model of the energy response of the detector. Both are addressed continuously during three different stages of the experiment's operations – water, scintillator and Te-loaded phases.

This thesis presents the analysis of data taken during the water and scintillator phases of the SNO+ experiment. Optical calibration data taken with a deployed source during the water phase allowed to measure for the first time *in situ* key optical parameters for the detector model, which will be common to all phases. The initial liquid scintillator data, taken during a 7 month transition period when the detector was half-filled with 365 tonnes of liquid scintillator on top of water, was used to characterize the intrinsic background contaminants in the scintillator. The background model was validated with a target-out double beta decay analysis, which tested for any unexpected background sources or leakage within the expected $0\nu\beta\beta$ decay region-of-interest. Moreover, these data allowed the first physics measurement using scintillator in SNO+ – a measurement of the ^{8}B solar neutrino flux, $\Phi_{^8B} = 6.534^{+26.11\%}_{-22.39\%}$ (stat.) $^{+11.38\%}_{-9.64\%}$ (syst.) $\times$ 10^6 cm^{-2} s^{-1} with an exposure of 11.2 kt day, compatible with previous measurements by other experiments.

Based on the best knowledge of the backgrounds in the detector and of its energy response, a Monte Carlo based analysis was performed in order to evaluate the expected precision for the measurement of the $2\nu\beta\beta$ decay of ^{130}Te, one of the major intrinsic background expected for the $0\nu\beta\beta$ search. Due to the large detector mass and isotope loading, SNO+ will achieve exposures competitive with other double beta decay experiments and statistical uncertainties well below 1% with a few months of data. It is expected that the future half-life measurement will be limited by systematic uncertainties due to energy scale and background correlations, which could be on the order of 5%. These will have to be accurately determined and minimized using calibrations after the tellurium is loaded.

KEYWORDS:

Double beta decay, neutrino physics, calibration, water Cherenkov detectors, liquid scintillator detectors

Resumo

SNO+ é uma experiência de física de neutrinos, localizada no SNOLAB, Canadá. A experiência reutiliza o detector construído para o Sudbury Neutrino Observatory (SNO), ativo entre 1999 e 2006, para novos estudos de física de neutrinos, tais como a detecção de neutrinos solares, geo-neutrinos, neutrinos de reatores e de supernovas, assim como estudos de física exótica como o decaimento invisível de nucleões. No entanto, o objectivo principal da experiência é a procura do decaimento beta duplo sem neutrinos ($0\nu\beta\beta$) usando 1330 kg do isótopo ^{130}Te. Uma futura observação desta transição nuclear permitiria determinar a escala e hierarquia das massas dos neutrinos, e provar que os neutrinos são a sua própria anti-partícula, o que terá consequências na explicação da assimetria entre matéria e anti-matéria observada no universo.

SNO+ recolhe dados desde 2017, inicialmente como um detector de Cherenkov cheio com 905 toneladas de água ultra-pura, e atualmente com 780 toneladas de cintilador líquido. A fase final com o telúrio irá começar em 2024. As fases iniciais da experiência permitiram caracterizar detalhadamente o detector, fornecendo informação importante necessária para as análises de física e, em particular, a procura do decaimento beta duplo. O trabalho apresentado nesta tese contribui para este objectivo de três maneiras diferentes: melhorando a caracterização das propriedades ópticas do detector com a análise de dados de calibração recolhidos durante a fase da água; desenvolvendo e validando o modelo dos fundo radioativos no cintilador líquido com a análise dos dados recolhidos durante o período de transição em que o detector estava cheio com 365 toneladas de cintilador por cima de água; e com o desenvolvimento de uma análise para a medição do tempo de vida média do decaimento beta duplo com neutrinos ($2\nu\beta\beta$) do ^{130}Te, que será um dos principais fundos para a procura do $0\nu\beta\beta$. Para além disso, foi feita uma medição do fluxo de neutrinos solares do ^{8}B, a primeira medição de física com cintilador em SNO+.

O Capítulo 4 apresenta os resultados da calibração óptica feita durante a fase da água, que foi fundamental para determinar as propriedades ópticas do detector, incluindo mudanças na resposta dos tubos fotomultiplicadores (PMTs) e respectivos concentradores desde a transição de SNO para SNO+. Alterações inovadoras na análise permitiram efetuar medições nunca antes feitas durante a experiência SNO. As regiões internas e externas ao balão de acrílico, ambas preenchidas com água ultra-pura, foram tratadas como o mesmo material, o que permitiu quebrar as correlações entre a água exterior e o acrílico, permitindo medir pela primeira vez *in situ* este último. Adicionalmente, foram utilizados dados recolhidos com a fonte de calibração no exterior do balão, perto dos PMTs, o que permitiu medir a resposta angular dos PMTs e con-

centradores a ângulos de incidência acima de 45 graus. Estas medições foram propagadas para o modelo de simulação do detector, que foi subsequentemente validado através de comparações entre dados e simulações de uma fonte de calibração de energia, emissora de partículas gama. Os resultados diminuíram o erro sistemático da escala de energia da fase da água um fator 2, de 2% para 1.02%, o que permitiu melhorar significativamente os resultados de física da fase da água. O modelo óptico calibrado do detector foi propagado para as fases seguintes da experiência, trocando a água por cintilador líquido.

A água dentro do detector começou a ser substituída por cintilador em 2018, processo este que foi finalizado em Março de 2021. A principal prioridade durante esta transição foi medir e monitorizar os níveis intrínsecos de fundos de radioatividade natural no cintilador. Estas medições foram fundamentais para determinar se o cintilador líquido tinha a pureza radioativa necessária para a adição do isótopo ^{130}Te, e para verificar que quaisquer impurezas que entraram no detector durante as operações de enchimento, como radão, decaíam. Os fundos radioativos em SNO+ são introduzidos no Capítulo 5, seguidos de discussão sobre as análises e medições feitas durante o período de transição (7 meses, de Março a Outubro de 2020) em que o detector esteve cheio com 365 toneladas de cintilador.

Apesar da configuração complexa deste período (cintilador na parte superior do balão de acrílico, e água na parte inferior), a estabilidade do detector permitiu iniciar o desenvolvimento do modelo dos fundos radioativos do cintilador. Foi desenvolvido um método para identificação dos decaimentos em coincidência dos isótopos bismuto e polónio, provenientes da cadeia do ^{238}U e ^{232}Th, com base na proximidade da distribuição temporal e espacial destes decaimentos. A identificação e consequente separação destas coincidências permitiu medir os níveis de U, Th e Rn no cintilador, e criar amostras limpas de eventos conhecidos que foram utilizados para determinar e monitorizar os níveis de emissão de luz do cintilador e, como consequência, compreender a escala dos sinais registados pelos PMTs. O modelo dos fundos do período de transição incluiu elementos que não existem na configuração final com o detector completamente cheio de cintilador: gamas de decaimentos radioativos provenientes da água por baixo do cintilador, e impurezas num tubo auxiliar para extração da água durante o enchimento. Duas análises dedicadas em regiões específicas do detector mediram as contribuições destes componentes para o modelo dos fundos radioativos.

O modelo final desenvolvido para este período foi validado com uma análise de $0\nu\beta\beta$ sem isótopo, que comparou o número de contagens da região de interesse do $0\nu\beta\beta$ com as previsões do modelo. Os resultados mostraram que ambas são consistentes, mesmo sem considerar todas as possíveis fontes de erros sistemáticos dos dados analisados (incerteza na escala de energia, na reconstrução da posição, etc). Apesar deste modelo inicial de fundos radioativos não ser inteiramente representativo do que se espera para a fase com o telúrio, esta análise permitiu validar as análises e ferramentas para as medições finais. O Capítulo 5 é complementado pelo Apêndice A, que apresenta os níveis dos fundos radioativos esperados para a fase do telúrio, incluindo as medições do período de transição, e cálculos atualizados dos fundos induzidos por ativação do telúrio por raios cósmicos.

Com o modelo completo dos fundos radioativos e com o modelo da resposta do detector calibrado, os dados recolhidos com as 365 toneladas de cintilador foram utilizados para medir

neutrinos solares do decaimento de ^{8}B. Desta análise, discutida no Capítulo 6, foram obtidos os primeiros resultados de física com cintilador líquido em SNO+, que serviram como validação das análises de neutrinos solares para as fases seguintes da experiência. Com um limite de energia de cerca de 3 MeV, foi medido um fluxo de $\Phi_{^8B} = 6.534^{+26.11\%}_{-22.39\%}$ (est.) $^{+11.38\%}_{-9.64\%}$ (sist.) $\times$ 10^6 cm^{-2} s^{-1} com uma exposição de 11.2 kt dia. Esta medição é compatível com resultados de outras experiências, incluindo as medições de neutrinos solares feitas durante a fase da água de SNO+. No entanto, a medição é limitada pela incerteza estatística, dada a baixa exposição e pequena taxa de interação dos neutrinos solares de ^{8}B no detector (cerca de 1.6 eventos por dia). O erro sistemático foi avaliado com estudos dedicados da escala de energia e da reconstrução da posição, com base em diferenças entre os dados e simulações das coincidências Bi-Po.

O último capítulo da tese apresenta uma análise baseada em Monte Carlo para determinar a precisão para a medição do tempo de vida média do decaimento $2\nu\beta\beta$ do ^{130}Te. Este decaimento é um dos fundos principais irredutíveis esperados na região de interesse do $0\nu\beta\beta$. Por essa razão, uma medição precisa da sua taxa de decaimento é fundamental para estimar a sua contribuição para a região de interesse. Os estudos apresentados no Capítulo 7 mostram que, durante um período inicial de 3 meses com 25.5 kg de isótopo (1/52 do total), SNO+ espera ser sensível ao espectro em energia do $2\nu\beta\beta$ e fazer uma primeira medição do tempo de vida média, embora com incertezas estatísticas elevadas acima de 10%. Com a quantidade total de isótopo (1330 kg), SNO+ conseguirá, em apenas alguns meses, atingir exposições competitivas com experiências como CUORE, permitindo medições do tempo de vida média com precisões estatísticas melhores que 1%. Os principais desafios para esta medição, baseado num ajuste ao espectro de energia observado, serão as correlações entre formas dos espectros dos fundos radioativos e do sinal, particularmente entre o ^{234m}Pa e o $2\nu\beta\beta$. Estas correlações ganham mais peso quando se consideram efeitos sistemáticos que alteram a resolução e escala de energia. Os estudos neste Capítulo mostram que uma incerteza de 0.6% na escala de energia, determinada em estudos dedicados no Apêndice B, resulta num erro sistemático de 6% para o tempo de vida média do ^{130}Te, se os níveis de ^{234m}Pa forem desconhecidos e este for deixado a flutuar na minimização. Este erro sistemático pode ser reduzido para 1% se os níveis de ^{234m}Pa forem determinados com uma precisão de 10%. A medição do tempo de vida média do $2\nu\beta\beta$ do ^{130}Te em SNO+ será limitado pelas incertezas sistemáticas, que terão de ser determinadas e minimizadas com fontes de calibração durante a fase do telúrio. As análises e resultados apresentados nesta tese servirão como guia às futuras análises de SNO+.

PALAVRAS-CHAVE:

Decaimento beta duplo, física de neutrinos, calibração, detector de Cherenkov, detector de cintilador líquido

Contents

List of Tables

List of Figures

List of Acronyms

SM	Standard Model of particle physics
CP	Charge-parity
CPT	Charge-parity-time reversal
PMNS	Pontecorvo-Maki-Nakagawa-Sakata
MSW	Mikheev-Smirnov-Wolfenstein
SSM	Standard solar model
CC	Charged current
NC	Neutral current
NO	Normal neutrino mass ordering
IO	Inverted neutrino mass ordering
NME	Nuclear matrix element
SEMF	Semi-empirical mass formula
PMT	Photomultiplier tube
AV	Acrylic vessel
DCR	Deck clean room
PSUP	PMT support structure
OWL	Outward looking
UPW	Ultra-pure water
LAB	Linear alkylbenzene
PPO	2,5-diphenyloxazole
DDA	N,N-Dimethyldodecylamine
PFA	Perfluoroalkoxy
QA	Quality assurance
SPE	Single photoelectron
MPE	Multi-photoelectron

FEC	Front-end card
PMTIC	PMT interface card
DB	Daughterboard
HV	High voltage
TAC	Time to analog converter
MTCA	Analogue master trigger card
QHL	Charge high gain long integration time
QHS	Charge high gain short integration time
QHX	Charge low gain and long integration time
GT	Global trigger
GTID	Global trigger ID
DAQ	Data acquisition
RAT	Reactor analysis tool, SNO+ simulation and reconstruction framework
RATDB	RAT database
OCA	Optical calibration analysis
ELLIE	Embedded LED/laser light injection system
LB	Laserball
MC	Monte Carlo
URM	Umbilical retrieval mechanism
TOF	Time-of-flight
FV	Fiducial volume
ROI	Region-of-interest
PDF	Probability density function

Chapter 1

Neutrino physics

Neutrinos are one of the most surprising and enigmatic particles that have ever been experimentally confirmed to exist. They are among the most abundant particles, and are a product of the chain reactions that fuel the Sun and other stars, as well as of the decays of heavier nuclei or particles into lighter ones. Neutrinos are one of the building blocks of the universe and are key to understand its origin and evolution. However, studying neutrinos is very difficult. They are the lightest fundamental particles by far, and do not carry electric or colour charges. They interact with matter very weakly and, therefore, their study requires very large detectors, intense neutrino sources, and an abundance of detection time.

Nevertheless, dramatic progress has been made in the field of neutrino physics over the past 60 years since their discovery. Neutrinos were observed to change from one flavour to another as they travel long distances – the phenomenon known as neutrino oscillations. This observation showed that neutrinos have very small, non-zero masses, in contradiction to their properties in the Standard Model. This created more questions than the ones it answered: What are the values of the neutrino masses? Where do the masses come from? What is the role that massive neutrinos played in the beginning of the Universe? Current and future neutrino physics experiments seek to shed light on the answers to these and other open questions in neutrino physics in the upcoming years.

The goal of this Chapter is to review the current status of neutrino physics, with particular focus on the origin and consequences of the neutrino masses. Section 1.1 provides a brief introduction of neutrinos in the Standard Model, followed by an overview of neutrino oscillations in Section 1.2. Section 1.3 discusses how neutrino masses are added to the Standard Model within the Dirac and Majorana frameworks, and gives an overview of the current experimental neutrino mass constraints. Section 1.4 concludes this Chapter by reviewing different experimental approaches to probe the nature of the neutrino.

1.1 Neutrinos in the Standard Model

The Standard Model of particle physics was developed in the mid 1970s to describe subatomic particles and their interactions. It was built from joining the electroweak theory of S. L. Glashow, A. Salam and S. Weinberg [1, 2, 3], which describes interactions via the electromag-

netic and weak forces, with quantum chromodynamics developed by H. Fritzsch, H. Leutwyler, and M. Gell-Mann [4], the theory of the strong nuclear force. Both these theories are gauge field theories, which describe the interactions between particles in terms of the exchange of intermediary messenger particles that have one unit of spin – the bosons. In addition to the bosons, the Standard Model includes two families of spin 1/2 particles (fermions) – the quarks and the leptons. All the particles that make up the Standard model are shown in Figure 1.1. For each fermion there is a corresponding antiparticle, identical in all aspects except electric charge, which is of opposite sign. The electroweak symmetry breaking mechanism developed by P. Higgs, F. Englert, T. Kibble and others [5, 6, 7] generates the masses of the weak gauge bosons and of the charged fermions, and gives rise to the appearance of a physical scalar particle in the model, the Higgs boson [8, 9].

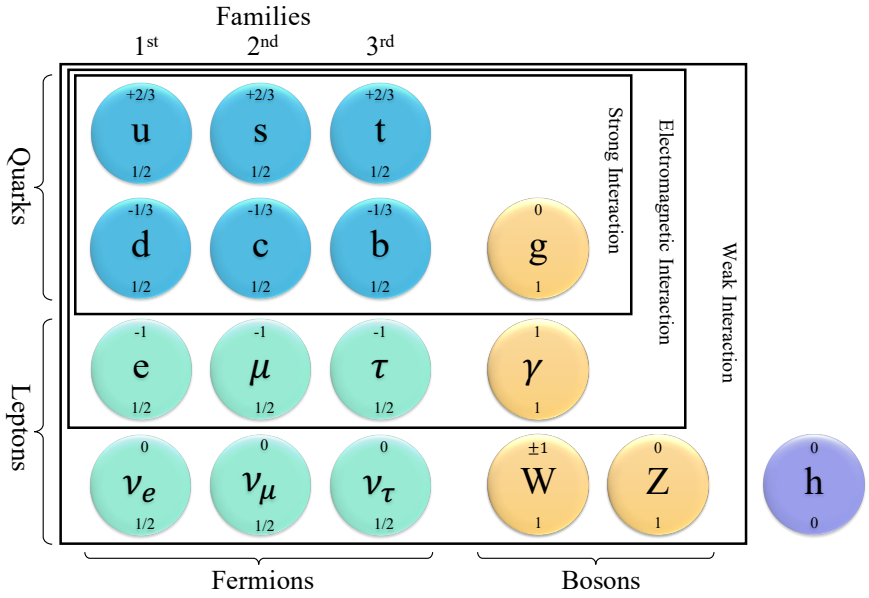

Figure 1.1: Fundamental particles in the Standard Model.

The Standard Model includes three neutrinos, each associated with one of the charged leptons e, μ and τ: the electron neutrino ν_e, the muon neutrino ν_μ, and the tau neutrino ν_τ. These are known as *neutrino flavours*, and they are directly observed through their interaction with the corresponding leptons. Neutrinos carry no electric or colour charges, thus only interact through the weak force mediated by the $W^{\pm}$ (charged current) and Z bosons (neutral current), according to the Standard Model Lagrangian:

$$\mathcal{L} = -\frac{g}{\sqrt{2}} \sum_{\alpha=e,\mu,\tau} \overline{\nu_{\alpha L}} \gamma^\mu \ell_{\alpha L} W_\mu - \frac{g}{2\cos\theta_W} \sum_{\alpha=e,\mu,\tau} \overline{\nu_{\alpha L}} \gamma^\mu \nu_{\alpha L} Z_\mu + \text{h.c.}, \tag{1.1}$$

where g is the electroweak coupling constant, θ_W is the Weinberg angle, and γ^μ are the gamma matrices. The W and Z boson fields are represented by W_μ and Z_μ, and ν_α and ℓ_α are, respectively, the neutrino and lepton fields of flavour α. The subscript L represents the left-handed chiral projections of the lepton fields, $\ell_{\alpha L} = \frac{1}{2}(1-\gamma^5)\ell_\alpha$. The strength of the weak interaction has a steep decrease with distance due to the large mass of the $W^{\pm}$ and Z bosons (m_W = 80

GeV, m_Z = 92 GeV). Consequently, the cross-section of neutrinos interacting with matter is very small, hence their extremely difficult detection.

Neutrinos were originally assumed to be massless, after work by T. Lee, C. Yang and C. Wu [10, 11], and by M. Goldhaber [12] demonstrated parity violation in weak interactions, noting that all observed neutrinos and antineutrinos are respectively, left- and right-handed. Because the Higgs mechanism requires coupling between the left and right-handed fields for each fermion, no mass term can trivially be constructed for neutrinos. The massless neutrinos were introduced in the Standard Model with the *two-component theory of neutrinos* [13, 14, 15], where the neutrino fields obey the Weyl equations:

$$i\gamma^{\mu}\partial_{\mu}\nu_{\alpha L} = 0, \tag{1.2}$$

$$i\gamma^{\mu}\partial_{\mu}\nu_{\alpha R} = 0. \tag{1.3}$$

The description of neutrinos as Weyl particles predicts maximal parity violation in weak interactions of neutrinos, as confirmed by the observations, and implies that the chirality of neutrinos coincides with helicity, the projection of the particle spin on its momentum. This minimal description of neutrinos in the Standard Model was shattered by the observation of neutrino oscillations, which are going to be described in the following Section.

1.2 Neutrino oscillations

In the 1960s, R. Davis began an experiment deep in the Homestake mine with the goal of measuring the neutrinos emitted by the fusion reaction in the Sun, through the inverse beta decay reaction proposed by B. Pontecorvo in 1946 [16]:

$$^{37}\mathrm{Cl} + \nu_e \rightarrow {}^{37}\mathrm{Ar} + e^{-}. \tag{1.4}$$

The rate of observed solar neutrinos interactions was three times smaller than the predictions by the Standard Solar Model (SSM) [17], which became known as the *Solar Neutrino Problem*. Over the next two decades, the SSM theoretical calculations were refined and the predictions became more precise. In parallel, the sensitivity of the Homestake experiment was increased, and several tests were performed to evaluate the detection efficiency, for which no significant error was found [18, 19]. Complementary experiments, such as the ^{71}Ga experiments SAGE [20] and GALLEX[21], and the water Cherenkov detector Kamiokande-II [22] attempted to solve the solar neutrino problem. Due to the use of different targets, these experiments had different thresholds for the neutrino energies, and showed different discrepancies from the predictions, as shown in Figure 1.2. These energy threshold dependent discrepancies could not be explained by modifications of the Standard Solar Model. Additionally, in 1988, the Kamiokande-II experiment measured atmospheric neutrinos [23] emitted in the decay of pions and muons from cosmic ray interactions. The number of observed muon neutrinos was about 40% smaller than the predictions.

One hypothesis to explain the differences postulated that the neutrino flavours had non-zero

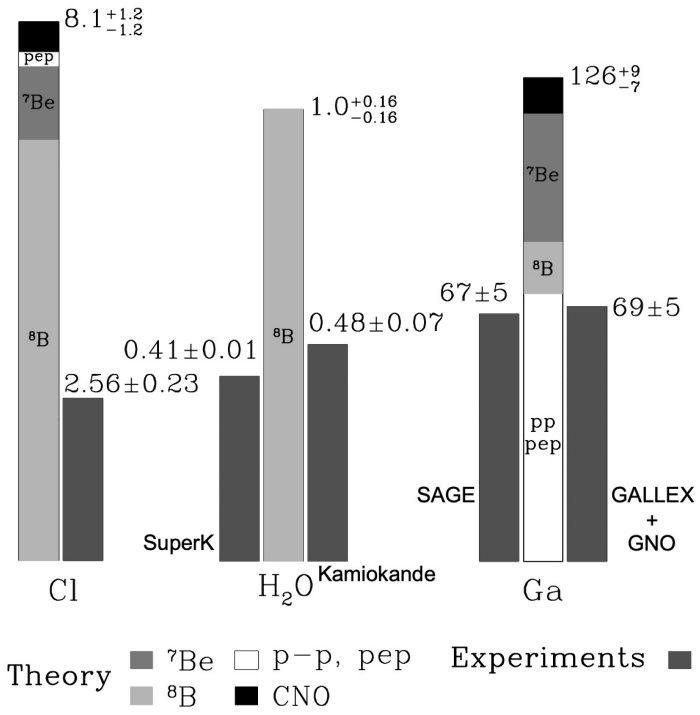

Figure 1.2: Comparison of the predictions of the standard solar model plus the SM of electroweak interactions with the measured rates in solar neutrino experiments. Values for Cl and Ga are expressed in SNU (solar neutrino unit), whereas the values for H_2O represent the ratio between the measured experimental fluxes and the theory predictions. Adapted from [24].

and slightly different masses, and that they could oscillate from one flavour to another during their path to Earth. This theory was confirmed by the Super-Kamiokande experiment in 1998 [25] and by the SNO experiment in 2002 [26], solving the atmospheric neutrino anomaly and the solar neutrino problem, respectively. The discovery of neutrino oscillations proved that neutrinos have mass and, thus, provided the first observation of physics beyond the Standard Model.

1.2.1 Vacuum oscillations

In 1957, B. Pontecorvo developed the theory of oscillations between neutrinos and antineutrinos [27], in analogy with K^0–$\overline{K}^0$ oscillations. Later in 1962, Z. Maki, N. Nakagawa and S. Sakata applied this idea to the oscillation of neutrino flavours [28]. Neutrino flavour oscillations arise due to the inequality of basis states: the neutrino weak eigenstates do not coincide with the mass eigenstates:

$$|\nu_\alpha\rangle = \sum_{i=1}^{3} U^*_{\alpha i}|\nu_i\rangle, \quad \alpha = e, \mu, \tau. \tag{1.5}$$

The weak eigenstates $|\nu_\alpha\rangle$ are labelled by the corresponding lepton family ($\alpha = e, \mu, \tau$), while the mass eigenstates are labelled $|\nu_i\rangle$ where $i = 1, 2, 3$. The mass eigenstates are the stationary states of the free-particle Hamiltonian which satisfy Schrödinger's equation, while the flavour eigenstates participate in the electroweak interactions. The coefficients $U_{\alpha i}$ are elements of

a unitary matrix U known as the Pontecorvo-Maki-Nakagawa-Sakata (PMNS) mixing matrix, which can be parametrised by three mixing angles, θ_{12}, θ_{23}, θ_{13} and a charge-parity (CP) phase δ_{CP}:

$$U = \begin{pmatrix} c_{12}c_{13} & s_{12}c_{13} & c_{13}e^{-i\delta_{CP}} \\ -s_{12}c_{23} - c_{12}s_{23}s_{13}e^{i\delta_{CP}} & c_{12}c_{23} - s_{12}s_{23}s_{13}e^{i\delta_{CP}} & s_{23}c_{13} \\ s_{12}s_{23} - c_{12}c_{23}s_{13}e^{i\delta_{CP}} & -c_{12}s_{23} - s_{12}c_{23}s_{13}e^{i\delta_{CP}} & c_{23}c_{13} \end{pmatrix}, \tag{1.6}$$

with $c_{ij} = \cos\theta_{ij}$ and $s_{ij} = \sin\theta_{ij}$. If the value of δ_{CP} is different from zero, it breaks the symmetry of the interactions involving the mixing matrix and would cause neutrino oscillations to behave differently from antineutrino oscillations. The evolution of a neutrino state ν_α in vacuum can be derived by solving the Schrödinger equation using a plane wave solution:

$$|\nu_\alpha\rangle(\vec{x}, t) = \sum_i U^*_{\alpha i} e^{-i(E_i t - \vec{p}_i \vec{x})} |\nu_i\rangle = \sum_i U^*_{\alpha i} e^{-i(E_i t - p_i L)} |\nu_i\rangle, \tag{1.7}$$

where E_i and $\vec{p}_i = p_i \hat{k}$ are the energy and momentum of the corresponding mass eigenstate, $\vec{x} = L\hat{k}$, and $\hat{k}$ is the unit vector in the direction of the neutrino momentum. The probability of observing a neutrino that was created as ν_α in the weak eigenstate ν_β after a distance of propagation L is:

$$P(\nu_\alpha \to \nu_\beta) = |\langle \nu_\beta | \nu_\alpha \rangle(\vec{x}, t)|^2 = \sum_i \sum_j U^*_{\alpha i} U_{\beta i} U_{\alpha j} U^*_{\beta j} e^{-i((E_i - E_j)t - (p_i - p_j)L)}. \tag{1.8}$$

The oscillatory term can be re-written as:

$$(E_i - E_j)t - (p_i - p_j)L = (E_i - E_j)\left(t - \frac{E_i + E_j}{p_i + p_j} L\right) + \left(\frac{m_i^2 - m_j^2}{p_i + p_j}\right) L. \tag{1.9}$$

The first term can be shown to be small by noting that the distance travelled by the neutrino is related to the time elapsed by:

$$L \sim \bar{v}t \equiv \frac{p_i + p_j}{E_i + E_j} t, \tag{1.10}$$

where $\bar{v}$ is an average wave packet velocity. Using this approximation and $E = \bar{p}$,

$$P(\nu_\alpha \to \nu_\beta) = \sum_i \sum_j U^*_{\alpha i} U_{\beta i} U_{\alpha j} U^*_{\beta j} \exp\left(-i \frac{\Delta m^2_{ij} L}{2E}\right). \tag{1.11}$$

Equation 1.11 shows that the probability of flavour transition varies with the distance travelled L and the neutrino energy E, and is weighted by the mass squared differences Δm^2:

$$\Delta m^2_{21} = m^2_2 - m^2_1; \quad \Delta m^2_{31} = m^2_3 - m^2_1; \quad \Delta m^2_{32} = m^2_3 - m^2_2. \tag{1.12}$$

Only two of these mass differences are independent, because Δm^2_{31} can be expressed as $\Delta m^2_{31} =$

$\Delta m^2_{32} + \Delta m^2_{21}$. Additionally, flavour transition is only possible if at least one of the masses m_i is different from zero. Thus, the observation of neutrino oscillations implies massive neutrinos.

1.2.2 Matter oscillations

When neutrinos propagate through matter, additional interactions can complicate the vacuum oscillation scenario described above. In 1978 L. Wolfenstein discovered that while travelling through matter, neutrinos are affected by a potential due to coherent forward elastic scattering with the electrons and nucleons in the medium, causing a modification of the vacuum evolution equation [29]. S. Mikheev and Y. Smirnov [30, 31, 32] further developed this theory, demonstrating the existence of resonant flavour transitions when neutrinos travel through a medium of varying density. This mechanism became known as the Mikheev-Smirnov-Wolfenstein (MSW) effect.

All three neutrino flavours experience the coherent forward elastic scattering interactions with the matter through which they pass. ν_μ and ν_τ can interact with the constituent electrons and nucleons by neutral current (NC) processes only, whereas ν_e can also interact with electrons via the charged current (CC) process. The contribution of these interactions can be interpreted as effective potential energy terms V_{NC} and V_{CC} [33]:

$$V_{NC} = -\frac{1}{2}\sqrt{2}G_F N_n, \tag{1.13}$$

$$V_{CC} = \sqrt{2}G_F N_e, \tag{1.14}$$

where G_F is the Fermi constant and N_n and N_e are the number densities of neutrons and electrons in the medium, respectively. For the neutral current interaction, the contributions from protons and electrons to the potential cancel each other – due to electrical neutrality in astrophysical environments –, hence only neutrons play a role. Thus, the total potential induced by matter on a neutrino of flavour α is:

$$V_\alpha = V_{CC}\delta_{\alpha e} + V_{NC} = \sqrt{2}G_F\left(N_e\delta_{\alpha e} - \frac{1}{2}N_n\right), \tag{1.15}$$

with $\delta_{\alpha e} = 1$ if $\alpha = e$, or $\delta_{\alpha e} = 0$ otherwise.

In order to consider the enhancement caused by matter, the flavour basis Hamiltonian has to be re-written in order to accommodate both the vacuum and matter components:

$$H = H_V + H_M \text{ , with } H_M|\nu_\alpha\rangle = V_\alpha.|\nu_\alpha\rangle \tag{1.16}$$

In the Schrödinger picture, a neutrino state with initial flavour α obeys the evolution equation

$$i\frac{d}{dt}|\nu_\alpha(t)\rangle = H|\nu_\alpha(t)\rangle \text{ , with } |\nu_\alpha(0)\rangle = |\nu_\alpha\rangle. \tag{1.17}$$

Developing this equation and performing the approximation for ultra-relativistic neutrinos, and performing a transformation t→x, one can obtain the following evolution equation for the

flavour transition $\psi_{\alpha\beta}(t) = \langle\nu_\beta|\nu_\alpha(t)\rangle$ in space coordinates:

$$i\frac{d}{dx}\psi_{\alpha\beta}(x) = \left(p + \frac{m_1^2}{2E} + V_{NC}\right)\psi_{\alpha\beta}(x) + \sum_\eta\left(\sum_i U_{\beta i}\frac{\Delta m_{i1}^2}{2E}U_{\eta i}^* + \delta_{\beta e}\delta_{\eta e}V_{CC}\right)\psi_{\alpha\eta}(x). \tag{1.18}$$

The first term is irrelevant for the flavour transitions, since it generates a phase common to all flavours. It can be eliminated by the phase shift:

$$\psi_{\alpha\beta}(x) \to \psi_{\alpha\beta}(x)e^{-i(p_\nu + m_1^2/2E)x - i\int_o^x V_{NC}(x')dx'}, \tag{1.19}$$

which does not have any effect on the probability of $\nu_\alpha \to \nu_\beta$ transitions. Therefore, the relevant evolution for the flavour transition amplitudes is:

$$i\frac{d}{dx}\psi_{\alpha\beta}(x) = \sum_\eta\left(\sum_i U_{\beta i}\frac{\Delta m_{i1}^2}{2E}U_{\eta i}^* + \delta_{\beta e}\delta_{\eta e}V_{CC}\right)\psi_{\alpha\eta}(x), \tag{1.20}$$

which shows that neutrino oscillations in matter, as neutrino oscillations in vacuum, depend on the differences of the squared neutrino masses, not on the absolute value of neutrino masses. Writing it in matrix form,

$$i\frac{d}{dx}\Psi_\alpha = H_F\Psi_\alpha, \tag{1.21}$$

the structure of a Schrödinger equation is recovered, with the effective Hamiltonian matrix H_F in the flavour basis given by:

$$H_F = \frac{1}{2E}(UM^2U^\dagger + A). \tag{1.22}$$

In the case of three-neutrino mixing:

$$\Psi_\alpha = \begin{bmatrix}\psi_{\alpha e}\\ \psi_{\alpha\mu}\\ \psi_{\alpha\tau}\end{bmatrix}, \qquad M^2 = \begin{bmatrix}0 & 0 & 0\\ 0 & \Delta m_{21}^2 & 0\\ 0 & 0 & \Delta m_{31}^2\end{bmatrix}, \qquad A = \begin{bmatrix}A_{CC} & 0 & 0\\ 0 & 0 & 0\\ 0 & 0 & 0\end{bmatrix}, \tag{1.23}$$

where $A_{CC} = 2EV_{CC} = 2E\sqrt{2}G_F N_e(x)$. This potential is usually very small (due to the dimension of G_F), unless the electron density grows to very large values as a function of the travelled distance x, as in the case of the Sun. Reducing to the two flavour neutrino case is sufficient to highlight the main matter oscillations' characteristics. In this case, Equation 1.21 can be re-written as:

$$i\frac{d}{dx}\begin{bmatrix}\psi_{ee}\\ \psi_{e\mu}\end{bmatrix} = \frac{1}{4E}\begin{bmatrix}A_{CC} - \Delta m^2\cos 2\theta & \Delta m^2\sin 2\theta\\ \Delta m^2\sin 2\theta & -A_{CC} + \Delta m^2\cos 2\theta\end{bmatrix}\begin{bmatrix}\psi_{ee}\\ \psi_{e\mu}\end{bmatrix}. \tag{1.24}$$

The Hamiltonian matrix can be diagonalized such that it takes the form:

$$H_M = \frac{1}{4E}\begin{bmatrix}-\Delta m_{eff}^2 & 0\\ 0 & \Delta m_{eff}^2\end{bmatrix}, \tag{1.25}$$

where Δm^2_{eff} is the effective mass difference due to matter effects. With this transformation the unitary mixing matrix is:

$$U_M = \begin{bmatrix} \cos\theta_{eff} & \sin\theta_{eff} \\ -\sin\theta_{eff} & \cos\theta_{eff} \end{bmatrix}, \tag{1.26}$$

with

$$\Delta m^2_{eff} = \sqrt{(\Delta m^2 \cos 2\theta - A_{CC})^2 + (\Delta m^2 \sin 2\theta)^2}, \tag{1.27}$$

$$\sin 2\theta_{eff} = \frac{\sin(2\theta)}{\sqrt{(A_{CC}/\Delta m^2 - \cos 2\theta)^2 + \sin^2 2\theta}}. \tag{1.28}$$

When considering a matter potential of $A^R_{CC} = \Delta m^2 \cos(2\theta)$, there is a resonance which causes the mixing angle to be maximal. This resonance corresponds to the electron number density:

$$N_e = \frac{\Delta m^2 \cos(2\theta)}{2\sqrt{2} E G_F}. \tag{1.29}$$

At the resonance, the effective mixing angle θ_{eff} is equal to $\pi/4$, i.e. the mixing is maximal, leading to the possibility of total transitions between the two flavours. Since, in normal matter, A_{CC} is positive, the resonance can only occur if the vacuum mixing angle θ is smaller than $\pi/4$, otherwise $\cos(2\theta) < 0$ leading to an unphysical negative electron number density. It is important to note that because the potential flips signs for antineutrinos, the mixing in matter is different for neutrinos and antineutrinos. This effect is different from CP violation, but if it is not accounted for, it can mimic CP violation.

Another important consequence of matter oscillations is that they provide sensitivity to the sign of Δm^2, unlike vacuum oscillations. If $\Delta m^2 \to -\Delta m^2$ in Equation 1.28, the term $(A_{CC}/\Delta m^2 - \cos 2\theta)$ in the denominator will have a different value and the effective mixing angle will be different. Additionally, experiments which have a large baseline and in which neutrinos travel through a significant amount of matter have the largest sensitivity to the sign of Δm^2.

If the matter density is constant, the transition probability can be rewritten using the effective mixing parameters as:

$$P_{\nu_e \to \nu_\mu}(x) = \sin^2(2\theta_{eff}) \sin^2\left(\frac{\Delta m^2_{eff} x}{4E}\right), \tag{1.30}$$

which has the same structure as the two-neutrino transition probability in vacuum, with the mixing angle and the squared-mass difference replaced by their effective values in matter.

For a medium with a variable electron density, such as the Sun, the value of N_e is effectively changing with time as the neutrino propagates through the medium. The value of the matter mixing angle is therefore also time-dependent:

$$\frac{d\theta_{eff}}{dx} = \frac{1}{2} \frac{\sin 2\theta_{eff}}{\Delta m^2_{eff}} \frac{dA_{CC}}{dx}. \tag{1.31}$$

The treatment of matter oscillations in three active flavours is hard to achieve as it requires solving Equation 1.20 which can lead to interplays of effects from the different Δm^2 terms. Usually a numerical solution is achieved by performing a numerical integration of the time evolution equation over the Solar radius. Alternatively, it is possible to employ a series of approximations for different oscillation scenarios, deriving analytical solutions to describe the survival probability, such as the adiabatic approximation for the transport of the neutrino states [30].

1.2.3 Status of the oscillation parameters

Over the past 20 years, neutrino oscillations have been experimentally studied using several neutrino sources and different detection techniques. In the three-neutrino oscillation scenario, the probability for a neutrino to oscillate between flavours is described by two mass parameters, Δm^2_{21} and $|\Delta m^2_{31}|$, three mixing angles, θ_{12}, θ_{13} and θ_{23}, and the CP-violating phase δ_{CP}. These parameters have been measured with different degrees of accuracy in solar and atmospheric neutrino experiments, in long and short-baseline reactor experiments, and in long-baseline accelerator experiments. Table 1.1 shows the most up-to-date values of the oscillation parameters, coming from global fit analyses to the results from various experiments.

Table 1.1: Results of the global three-neutrino oscillation analyses from the Neutrino Global Fit [34] (second column) and from NuFIT 5.1 [35, 36] (second column). When integrating the results from solar neutrino experiments, the Neutrino Global fit uses low metallicity solar models (preferred by the astrophysics field), while NuFit uses high-metallicity models, hence the difference between the values for $\sin^2\theta_{12}$.

Parameter	Neutrino Global Fit [34]	NuFit 5.1 (2021) [35, 36]
$\sin^2\theta_{12}$	0.318 ± 0.016	$0.304^{+0.013}_{-0.012}$
$\sin^2\theta_{13}$ (IO)	$0.02225^{+0.00064}_{-0.00070}$	$0.02238^{+0.00064}_{-0.00062}$
$\sin^2\theta_{13}$ (NO)	$0.02200^{+0.00069}_{-0.00062}$	$0.02220^{+0.00068}_{-0.00062}$
$\sin^2\theta_{23}$ (IO)	$0.578^{+0.010}_{-0.017}$	$0.578^{+0.017}_{-0.021}$
$\sin^2\theta_{23}$ (NO)	0.574 ± 0.014	$0.573^{+0.018}_{-0.023}$
Δm^2_{21}	$7.50^{+0.22}_{-0.20} \times 10^{-5}$ eV^2	$7.42^{+0.21}_{-0.20} \times 10^{-5}$ eV^2
$\lvert\Delta m^2_{31}\rvert$ (IO)	$2.45^{+0.02}_{-0.03} \times 10^{-3}$ eV^2	$2.498^{+0.028}_{-0.029} \times 10^{-3}$ eV^2
$\lvert\Delta m^2_{31}\rvert$ (NO)	$2.55^{+0.02}_{-0.03} \times 10^{-3}$ eV^2	$(2.515 \pm 0.028) \times 10^{-3}$ eV^2
δ_{CP}/π (IO)	$1.58^{+0.15}_{-0.16}$	$1.59^{+0.15}_{-0.18}$
δ_{CP}/π (NO)	$1.08^{+0.13}_{-0.12}$	$1.08^{+0.29}_{-0.14}$

The parameters θ_{12} and Δm^2_{21} have been measured using the ν_e disappearance of solar neutrinos observed by the Homestake [17], GALLEX/GNO [37], SAGE [38], Super-Kamiokande [39], SNO [40], and Borexino [41] experiments. The solar neutrino experiments, through the observation of the MSW effect, have constrained the sign of Δm^2_{21} to be positive. Additionally, KamLAND [42] measurements of the survival probability of $\overline{\nu}_e$ from nuclear reactors also constrain these parameters, specially Δm^2_{21}.

The parameters θ_{23} and $|\Delta m^2_{32}|$ are measured by long-baseline accelerator experiments such as MINOS/MINOS+ [43], T2K [44], and NOνA [45], as well as by the atmospheric neutrino experiments Super-Kamiokande [46] and IceCube [47]. These parameters are measured via the ν_μ disappearance channel. The sign of $|\Delta m^2_{32}|$ is not yet known, which is known as the *Neutrino*

Mass Ordering Problem. If m_2 is lighter than m_3, the ordering is said to be "normal", but if it is heavier the ordering is called "inverted" (Figure 1.3).

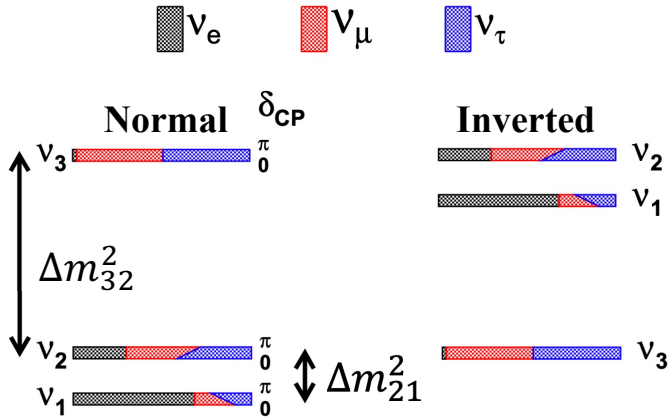

Figure 1.3: The two possibilities for the neutrino mass ordering: normal, where $m_3 > m_2$, and inverted, where $m_3 < m_2$. Modified figure from [48].

The parameter θ_{13} has been measured by the reactor neutrino experiments Daya Bay [49], Double Chooz [50], and RENO [51], as well as by the accelerator-based T2K [52] experiment.

The value of δ_{CP}. which is still unknown, can be probed by studying the neutrino oscillation channels $\nu_\mu \rightarrow \nu_e$ and $\bar{\nu}_\mu \rightarrow \bar{\nu}_e$ in long baseline neutrino experiments. Currently, the best constraints are given by T2K [44] and NOνA [45]. There is, however, some tension between the T2K and NOνA results in the normal ordering picture, since the T2K best fit δ_{CP} is in a region disfavoured by Noνa [45]. A definite measurement of δ_{CP} is the primary purpose of the current and future accelerator-based long-baseline neutrino oscillation experiments, including DUNE [53] and Hyper-Kamiokande [54].

1.3 Neutrino masses

The experimental observation of neutrino oscillations opened up fundamental questions about neutrinos, their mass scale and how to introduce neutrino masses in the Standard Model. In principle, neutrinos could behave like the other Dirac fermions, and their masses could be generated from the coupling to the Higgs field. The problem with this approach is that it does not explain why the neutrino masses would be so much smaller than the masses of the other fermions. Additionally, it would require the existence of non-interacting (*sterile*) right-handed neutrino fields, which have not been observed to date.

However, the fact that neutrinos do not carry either colour or electric charge could imply that they are fundamentally different from the other fermions. Neutrinos could be Majorana fermions, i.e. their own antiparticle. In the case of Majorana neutrinos, new physics beyond the Standard Model is required to explain their mass. One of the most appealing models is the Seesaw mechanism, which postulates the existence of the small neutrino masses by the introduction of heavy Majorana neutrinos, which would have masses of the order of the scale of grand unification ($\sim 10^{16}$ GeV).

1.3.1 Dirac neutrino masses

In simple extensions of the Standard Model, a Dirac neutrino mass can be generated with the same Higgs mechanism that gives masses to quarks and charged leptons if one introduces the right-handed components $\nu_{\alpha R}$ of the neutrino fields ($\alpha = e, \mu, \tau$) [33]. These fields are called *sterile* because they do not couple to any of the gauge bosons; their only interaction is gravitational. If sterile neutrinos mix with the active flavours, their existence could be inferred from the oscillation properties of the active flavours. Besides, they are singlets, invariant under the SM symmetries, making them fundamentally different from the fields of other elementary fermions.

In the natural extension with three right-handed neutrino fields, the diagonalized Higgs-lepton Yukawa Lagrangian is:

$$-\mathcal{L}_{\text{Higgs-lepton}} = \left(\frac{v+H}{\sqrt{2}}\right)\left[\sum_{\alpha=e,\mu,\tau} y_\alpha^\ell \overline{\ell_{\alpha L}}\ell_{\alpha R} + \sum_{i=1}^{3} y_i^\nu \overline{\nu_{iL}}\nu_{iR}\right] + \text{h.c.}\,, \tag{1.32}$$

where H is the Higgs field and v is the Higgs vacuum expectation value (VEV) ($\sim$246 GeV). ℓ_α are the Dirac charged lepton fields, ν_i are the Dirac neutrino massive fields, and y_α^ℓ and y_i^ν are, respectively, charged lepton and neutrino Yukawa couplings.

The neutrino masses are given by

$$m_{Di} = \frac{y_i^\nu v}{\sqrt{2}} \quad (i = 1, 2, 3). \tag{1.33}$$

The neutrino masses obtained with this mechanism are proportional to the Higgs vacuum expectation value, as the masses of charged leptons and quarks. However, it is known that the masses of neutrinos are much smaller than those of the charged leptons and quarks. To account for the tiny neutrino masses $\mathcal{O}(0.1)$ eV, the Yukawa couplings have to be $\mathcal{O}(10^{-12})$ GeV, more than ten orders of magnitude smaller than the Yukawa couplings of the heavier quarks and τ lepton. The small size required for the coupling constant leaves theorists sceptical about using the Higgs mechanism to explain the neutrino masses.

1.3.2 Majorana neutrino masses

In 1937, E. Majorana [55] found a way to construct a mass term for the neutrinos using only the left-handed chiral state. He proposed that neutral massive fermions could be described by simpler Weyl spinors carrying only two independent components instead of the four-component Dirac model, under the condition:

$$\psi = \psi^C \quad \text{with} \quad \psi^C = C\overline{\psi}^T,\ C = i\gamma^2\gamma^0\,, \tag{1.34}$$

where ψ^C is the charge conjugated field and C is the charge conjugation operator, which converts particles into antiparticles. In this description, the left-handed and right-handed compo-

nents are not independent:

$$\psi_R = \psi_L^C = C\overline{\psi_L}^T. \tag{1.35}$$

This condition only holds for neutral particles, meaning that neutrinos are the only elementary fermions that could be Majorana particles. Due to this relation, the Majorana spinors have only two independent degrees of freedom (d.o.f.) instead of the 4 d.o.f. for general Dirac spinors. Moreover, a Majorana particle and antiparticle must obey the same equations of state and must then be the same particle, i.e. a Majorana particle is its own antiparticle. Consequently, lepton number is violated by Majorana neutrinos. The observation of lepton number violation would be very significant, as it would prove physics beyond the SM, but would not shatter its foundations on gauge symmetries. In fact, lepton number is not an intrinsic symmetry in the Standard Model, but it is a global accidental symmetry that comes as a consequence of the gauge invariance and the fields representation.

If neutrinos are Majorana particles, the PMNS matrix from Equation 1.6 is multiplied by an additional diagonal matrix P_M on the right hand side, with $P_M = \text{diag}(1, e^{i\alpha_1}, e^{i\alpha_2})$. These additional phases, comparatively to the Dirac case, are a consequence of the self charge-conjugation condition [56, 57]. This condition does not allow for the Majorana fields to be rephased without physical effects[1]. It is worth noting that the Majorana phases do not affect the oscillation probability, since they cancel out when the PMNS matrix is squared.

The Majorana Lagrangian for neutrinos can be written as [33]:

$$\mathcal{L}_{\text{Majorana}} = \overline{\nu_L} i\gamma^\mu \partial_\mu \nu_L - \frac{m_M}{2}\left(\overline{\nu_L^C}\nu_L + \overline{\nu_L}\nu_L^C\right). \tag{1.36}$$

The kinetic term has the same form as that of a massless neutrino in the Standard Model. The last term in Equation 1.36 is the mass term, and represents a physical effect beyond the classical Standard Model. It is important to note that the essential difference between Dirac and Majorana neutrinos is that in the case of Dirac neutrinos particle and antiparticle are distinct, whereas in the Majorana case they coincide. However, from the kinematical point of view, Dirac and Majorana masses are equivalent.

The Majorana Lagrangian mass term cannot exist in the Standard Model as it is not gauge invariant. This can be remedied by adding a right-handed chiral neutrino field ν_R singlet, and combining the Dirac and Majorana mass terms – commonly known as type-I seesaw model [58]. In the simplified framework of just one neutrino flavour, the neutrino mass Lagrangian is [56]:

$$\mathcal{L}_{mass} = -\frac{1}{2}\begin{bmatrix}\overline{\nu_L^C}, \overline{\nu_R}\end{bmatrix}\begin{bmatrix}0 & m_D \\ m_D & m_M\end{bmatrix}\begin{bmatrix}\nu_L \\ \nu_R^C\end{bmatrix} + \text{h.c.}. \tag{1.37}$$

Three scenarios occur depending on the relationship between m_D and m_M:

- $m_M \ll m_D$: the neutrino predominantly has a Dirac mass;
- $m_M \simeq m_D$: the neutrino is a mixture of both Majorana and Dirac masses;

[1] If one rotates a Majorana neutrino by a phase, this phase will appear in its mass term, which will no longer be real.

- $m_M \gg m_D$: the neutrino is predominantly Majorana.

The seesaw mechanism makes this assumption: the Dirac mass is expected to be similar in scale to the masses of the quarks and charged leptons as result from the Higgs mechanism; and the Majorana masses are generated independently, thus can be at any scale, including the extremely large scale of Grand Unification Theories. This assumption allows to rewrite the Lagrangian as:

$$\mathcal{L}_{mass} = -\frac{1}{2}\left[\overline{\nu_L^C}, \overline{\nu_R}\right]\begin{bmatrix} m_D^2/m_M & 0 \\ 0 & m_M \end{bmatrix}\begin{bmatrix} \nu_L \\ (\nu_R)^C \end{bmatrix} + \text{h.c.}. \tag{1.38}$$

The mass matrix of the type-I seesaw model describes a light neutrino ν_L with mass eigenstate $m_\nu = m_D^2/m_M$ and a heavy, right-handed, sterile neutrino ν_R with mass eigenstate m_M. Furthermore, the heavier m_M is, the lighter m_ν will be.

If the seesaw mechanism for generating the neutrino masses is true, the heavy Majorana neutrinos could explain the matter-antimatter asymmetry observed in the universe. In the theory of leptogenesis [59, 60], the heavy right-handed neutrinos may have existed in the earlier universe and, as the universe cooled, would have decayed to neutrinos and antineutrinos. Through CP violation, an asymmetry in the rates of these decays could produce an excess of leptons over anti-leptons, which would in turn cause the observed baryon asymmetry.

1.3.3 Experimental constraints for the neutrino mass

Even though the absolute neutrino mass scale is still unknown, four different approaches have been used to obtain constraints on the neutrino mass. The first approach is the measurements of neutrino oscillations, which allows to measure Δm^2_{21}, Δm^2_{31}, and Δm^2_{32}. Lower bounds are set using the oscillation data by zeroing the lightest m_i (for the NO, the lightest is m_1; for the IO, the lightest is m_3):

$$\begin{aligned}(m_1, m_2, m_3) &\geq \begin{cases} (0, \sqrt{\delta m^2}, \sqrt{|\Delta m^2| + \delta m^2/2}) & \text{(NO)} \\ (\sqrt{|\Delta m^2| - \delta m^2/2}, \sqrt{|\Delta m^2| + \delta m^2/2}, 0) & \text{(IO)} \end{cases} \\ &\geq \begin{cases} (0, 0.868, 5.028) \times 10^{-2}\ \text{eV} & \text{(NO)} \\ (5.036, 5.110, 0) \times 10^{-2}\ \text{eV} & \text{(IO)} \end{cases}\end{aligned}, \tag{1.39}$$

where $\delta m^2 = m_2^2 - m_1^2 > 0$ and $\Delta m^2 = m_3^2 - (m_2^2 + m_1^2)/2$.

A second approach to measuring the neutrino masses is to use cosmological measurements. These measurements are not sensitive to a specific neutrino flavour and thus measure the quantity $m_{\text{tot}} = m_1 + m_2 + m_3$. The neutrino masses appear in a variety of cosmological quantities, affecting anisotropies in the cosmic microwave background (CMB) and the formation of large-scale structures in the universe, among other things. Depending on the combination of the data used, experiments produce various model-dependent limits on m_{tot}. The best claimed and widely accepted is by the Planck Collaboration, $m_{\text{tot}} < 0.12$ eV [61], a combination of Planck measurements of the CMB temperature, WMAP CMB polarization data, data from various

high-resolution CMB measurements, and measurements of baryon acoustic oscillations. This measurement also relies on the accuracy of the standard ΛCDM model; that is, an expanding Universe that obeys the laws of General Relativity and is dominated by cold dark matter (CDM) and a cosmological constant (Λ). Other recent work has suggested that correlation lengths in galaxy clusters exceed that predicted by the ΛCDM model, a result that could be explained by free streaming of light neutrinos with $m_{\text{tot}} = 0.11 \pm 0.03$ eV [62].

The third approach consists on measuring with great precision the β-decay spectra near its endpoint, just below the Q-value of the decay. A non-zero neutrino mass means that the emitted electron cannot carry away the full Q-value in energy. These experiments measure an effective electron neutrino mass of:

$$m_\beta = \sqrt{\sum_i |U_{ei}|^2 m_i^2}. \tag{1.40}$$

The best β candidate for this measurement is tritium. The decay:

$$^3\text{H} \rightarrow {}^3\text{He} + e^- + \overline{\nu}_e, \tag{1.41}$$

has an endpoint energy of 18.9 keV and a half-life of 12.3 years. The tritium is chosen because it has one of the smallest Q-values of all β emitters, favourable to have sufficiently high rates close to the endpoint, and its relatively short half-life implies an acceptable number of observed events during the experiment lifetime. The tritium electronic structure is simpler than heavier nuclei, so the spectrum can be measured with small systematic uncertainties. The world-leading limit in this area comes from the KATRIN experiment looking at the tritium β decay: $m_\beta < 1.1$ eV [63].

Finally, the fourth approach is the search for neutrinoless double beta ($0\nu\beta\beta$) decay. An observation of this hypothetical process would allow to determine an effective electron neutrino Majorana mass:

$$m_{\beta\beta} = |\sum_i e^{i\alpha_i} U_{ei}^2 m_i|. \tag{1.42}$$

The $0\nu\beta\beta$ decay is going to be discussed in detail in Chapter 2.

1.4 Methods to probe the neutrino nature

Determining whether neutrinos are Dirac or Majorana particles is one of the most pressing and challenging questions in neutrino physics. The main difference between the two is the lepton number violating behaviour of the Majorana neutrinos, that comes as the consequence of neutrinos and antineutrinos being the same particle. Even if both Dirac and Majorana mass terms exist, lepton number L is not a conserved quantity [56].

However, it is important to note that all neutrinos that have been studied directly so far have been ultra-relativistic. When a neutrino is ultra-relativistic, its behaviour is almost completely insensitive to whether it is a Dirac or Majorana particle [64]. The Standard Model weak interactions are chirally left-handed. As a result, when a Majorana neutrino is created in a decay, for example $W^+ \rightarrow e^+ + \nu_e$, it will be of left-handed helicity almost 100% of the time. In contrast,

an antineutrino produced in $W^- \to e^- + \overline{\nu}_e$, will be of right-handed helicity almost 100% of the time. Because of this polarization, if the (anti)neutrino were to interact, it would always create a (positron)electron, like a Dirac neutrino would. In this case, even if there is no lepton number conservation, the helicity in ultra-relativistic neutrinos will make them behave as if there was such conservation.

In order to address the question about the neutrino nature experimentally, it is then necessary to find alternative processes that would be sensitive to the nature of neutrinos, processes in which lepton number is violated, or study the non-relativistic relic neutrinos from the early universe. Detecting relic neutrinos is extremely difficult due to their low energy ($\mathcal{O}(10^{-9}$ keV)) and very small interaction cross-sections, and thus they have yet to be observed [65]. The most discussed proposal to detect neutrinos from the cosmic neutrino background (CνB) was originally suggested by S. Weinberg [66], and consisted of looking for an excess of events beyond the tritium beta decay endpoint energy, arising from the neutrino capture process $^3\mathrm{H} + \nu_e \to {}^3\mathrm{He}^+ + e^-$. To prove that relic neutrinos are being captured, an experiment must have sufficient energy resolution to establish that some of the electrons it observes have energies very slightly beyond the endpoint of the electron energy spectrum from β decay.

Relic neutrinos were highly relativistic when they were produced, and the Standard Model interactions that produced them yielded the same number of particles with left helicity as with right helicity. In the Dirac case, only the left-handed neutrinos are active and available for the capture. However, for the Majorana case, both left and right-handed neutrinos are active, which would lead to a capture rate two times larger than that of the Dirac case [67]. Even though this difference is substantial, it is important to note that the capture rate also depends on the local density of the relic neutrinos, which is not precisely predicted. Additionally, if the lightest neutrino mass eigenstate is light enough to still be relativistic today, finite experimental energy resolution would make it impossible to distinguish the final state electron from a β from the tritium decay. Currently, KATRIN is the most advanced experiment implementing this technique and is expected to set the best constraint on CνB detection. In the future, other experiments like PTOLEMY [68] could reach sensitivity to detecting relic neutrinos.

A more exotic way of determining if neutrinos are Dirac or Majorana is by trying to measure their magnetic moments. The fact that neutrinos have a non-zero mass could imply that neutrinos have a magnetic moment, which will depend on their nature. The neutrino electromagnetic dipole moments [69] can be described by:

$$\begin{aligned} \mathcal{L} &= \mu^{\nu}_{ij}(\nu_i \sigma_{\mu\nu} \nu_j F^{\mu\nu}) + \text{h.c. (Majorana)}, \\ \mathcal{L} &= \mu^{\nu}_{ij}(\bar{\nu}_i \sigma_{\mu\nu} \nu_j F^{\mu\nu}) + \text{h.c. (Dirac)}, \end{aligned} \tag{1.43}$$

where $F^{\mu\nu}$ is the electromagnetic field strength, and μ^{ν}_{ij} is the neutrino magnetic moment. In the Standard Model, non-zero neutrino magnetic moments are generated through quantum loop effects, and are constrained to:

$$\mu^{\nu}_{ij} \leq \frac{3eG_F}{8\sqrt{2}\pi^2} m_\nu = 3 \times 10^{-20} \mu_B \left(\frac{m_\nu}{10^{-1}\ \text{eV}} \right) \text{ , with } \mu_B = e/2m_e. \tag{1.44}$$

This constraint is several orders of magnitude below the sensitivity of current experiments. The most stringent laboratory bounds on μ^{ν} are obtained by studying neutrino-electron elastic scattering of solar neutrinos and reactor antineutrinos. The current best limit has been set by the Borexino experiment [70], $\mu^{\nu}_{eff} < 2.8{\cdot}10^{-11}\ \mu_B$.

The $i = j$ elements of μ^{ν}_{ij}, or diagonal moments, couple neutrinos of the same mass, while the $i \neq j$ elements, known as transition elements, couple different mass eigenstates. For Majorana neutrinos, μ^{ν}_{ij} is constrained to be anti-symmetric by CPT invariance – the neutrino and antineutrino are required to have magnetic moments of the same magnitude. Thus, Majorana neutrinos possess only transition moments, whereas Dirac neutrinos can possess both diagonal and transition moments. This feature significantly weakens the constraints on the Majorana neutrino magnetic moments as compared to the Dirac case. Therefore, an experimental measurement of a magnetic moment larger than the Standard Model prediction could indicate that neutrinos are Majorana fermions. Further distinction between the Dirac and Majorana nature of neutrinos could come from the comparison of the effective neutrino magnetic moments μ_{ν_e}, μ_{ν_μ} and μ_{ν_τ} in future neutrino beam experiments. In [71] it is shown that, in the case of Majorana neutrinos, there are inequalities $|\mu_{\nu_\tau}|^2 \leq |\mu_{\nu_e}|^2 + |\mu_{\nu_\mu}|^2$ and cyclic permutations, which do not hold for Dirac neutrinos. Observing a violation of these inequalities would prove the Dirac nature of neutrinos, if extra light sterile neutrino modes do not exist.

Last but not least, the most promising way to probe the nature of the neutrino is to search for neutrinoless double beta decay $0\nu\beta\beta$. If this process is observed, it would show that neutrinos are Majorana particles, and allow the measurement of an effective electron neutrino Majorana mass, providing answers to the most fundamental questions in neutrino physics. This process is going to be discussed in detail in the next Chapter.

Chapter 2

Double beta decay

For some radioactive nuclei, the only option to reach stability is a second-order weak transition involving the change of the nuclear charge Z by two units, keeping the mass number A unchanged. This rare transition can happen via four different processes: double electron capture, double beta plus decays, a simultaneous electron capture and a beta plus decay, and double beta minus decay. The latter, which is the focus of this thesis, is accompanied by the emission of two electrons and two antineutrinos, and is commonly referred to as two-neutrino double beta decay ($2\nu\beta\beta$). The favourable Q-values of the $2\nu\beta\beta$ candidate nuclei and the larger phase space comparatively to the other three processes have made this process the subject of extensive experimental and theoretical work.

If the neutrino is a massive Majorana particle, the double beta decay could happen without the emission of any neutrinos, violating lepton-number conservation. This exotic process is known as neutrinoless double beta decay ($0\nu\beta\beta$), and its observation would prove the Majorana nature of neutrinos and provide information about their absolute mass scale. The experimental search for this decay is extremely challenging, with the best current half-life limits set to $> 10^{26}$ years. Furthermore, understanding the nuclear physics aspects of the decay has been a persistent challenge; particularly, the calculation of the nuclear matrix elements (NMEs) that describe the transition. Studying the $2\nu\beta\beta$ process provides vital information which can be used to test and calibrate the theoretical models used to inform the $0\nu\beta\beta$ NMEs. The detailed study of the $2\nu\beta\beta$ decay spectrum and precise measurement of its half-life is also crucial for experiments, since this process is an intrinsic background for the $0\nu\beta\beta$ searches.

This Chapter will introduce the theoretical aspects of both 2ν and 0ν modes of double beta decay in Sections 2.1 and 2.2. Section 2.3 discusses the nuclear aspects of the double beta decay, with particular focus on the nuclear matrix elements. Section 2.4 discusses the experimental requirements and presents an overview of the on-going and future experiments searching for $0\nu\beta\beta$.

2.1 $2\nu\beta\beta$ decay

Following the postulation of the neutrino by W. Pauli in 1930 [72], and the development of the β-decay theory by E. Fermi in 1934 [73, 74], M. Goeppert-Mayer proposed the existence of

the *two-neutrino double beta decay* ($2\nu\beta\beta$) [75]:

$$(A, Z) \rightarrow (A, Z + 2) + 2e^{-} + 2\bar{\nu}_e \, . \tag{2.1}$$

As a second-order weak process, schematized in terms of its Feynman diagram in Figure 2.1, $2\nu\beta\beta$ is one of the rarest known decays, with measured half-lives in the range 10^{19} – 10^{21} years. A key property of $2\nu\beta\beta$ is that it can only occur in a limited number of natural unstable isotopes with even mass number A and even atomic number Z. The stability of a nucleus is determined by its binding energy and, consequently, its mass, given by the semi-empirical mass formula (SEMF):

$$M(A, Z) = Zm_p + Nm_n - a_V A + a_S A^{2/3} + a_C \frac{Z^2}{A^{1/3}} + a_A \frac{(N - Z)^2}{A} + \delta(A, Z). \tag{2.2}$$

The first two terms simply account for the mass of all protons and neutrons in the nucleus, and the remaining terms represent the binding energy that holds the nucleus together. The pairing term $\delta(A, Z)$ captures the effect of spin coupling of the nucleons, and is zero for odd-A nuclei, negative for even-even nuclei, and positive for odd-odd nuclei.

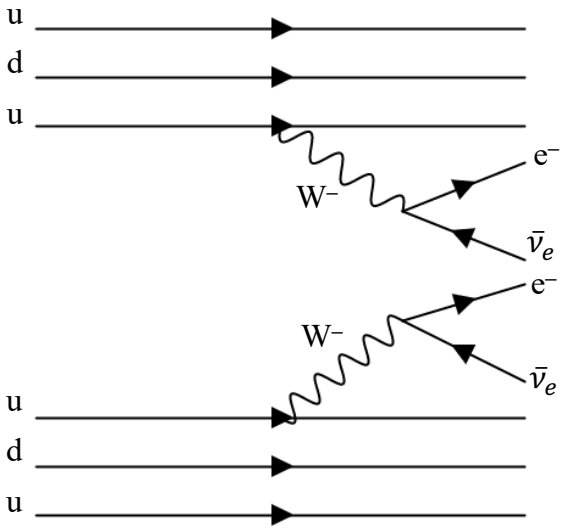

Figure 2.1: Feynman diagram for the $2\nu\beta\beta$ decay.

The SEMF gives rise to parabolic curves for a fixed A and different Z, as illustrated by Figure 2.2. For odd-A nuclei one curve exists, whereas for even-A nuclei the pairing term gives rise to a splitting which produces two curves. Nuclei transition from Z to $Z+1$ with a β^{-}-decay, and from Z to $Z - 1$ with a β^{+}-decay or electron capture (EC). However, for some even-even nuclei the transition to the daughter nucleus is energetically forbidden, and the only way for these nuclei to achieve a more stable configuration is to undergo a double beta decay to the next available nucleus.

There are 35 naturally-occurring isotopes that undergo $2\nu\beta\beta$-decay. However, only twelve of them have been observed experimentally [76]. The measurement of $2\nu\beta\beta$ relies on the detection of the two emitted electrons. Since the antineutrinos carry away part of the decay

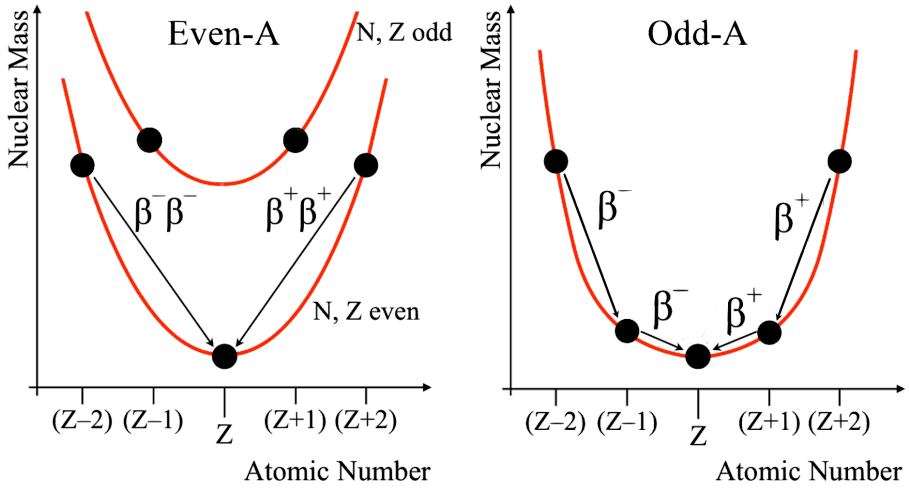

Figure 2.2: Schematic representation of the nuclear mass isobars (fixed mass number A) for isotopes with even (left) and odd (right) mass numbers.

energy, the electrons will have a continuous spectrum with an endpoint at $Q_{\beta\beta}$, defined as the total energy released in the decay:

$$Q_{\beta\beta} = M(A, Z) - M(A, Z + 2) - 2m_e. \tag{2.3}$$

This equation ignores the mass of the emitted neutrinos, a valid approximation for most decays given its smallness. Table 2.1 lists the isotopes which have been observed to undergo $2\nu\beta\beta$, along with their natural isotopic abundances, $Q_{\beta\beta}$ and measured half-lives.

Table 2.1: List of isotopes that have been observed experimentally to decay by $2\nu\beta\beta$ decay, along with their natural isotopic abundance, Q-value and measured half-lives.

Isotope	Isotopic Abundance (%)	$Q_{\beta\beta}$ (MeV)	$T^{2\nu}_{1/2}$ (10^{21} years)	
^{48}Ca	0.187	4.263	$(6.4^{+0.7+1.2}_{-0.6-0.9})\times10^{-2}$	[77]
^{76}Ge	7.8	2.039	(1.926 ± 0.094)	[78]
^{78}Kr	0.36	2.848	$(19^{+13}_{-7}\pm3)$	[79]
^{82}Se	9.2	2.998	$(8.6^{+0.2}_{-0.1})\times10^{-2}$	[80]
^{96}Zr	2.8	3.348	$(2.35\pm0.14\pm0.16)\times10^{-2}$	[81]
^{100}Mo	9.6	3.035	$(7.12^{+0.18}_{-0.14}\pm0.10)\times10^{-3}$	[82]
^{116}Cd	7.6	2.813	$(2.63^{+0.11}_{-0.12})\times10^{-2}$	[83]
^{128}Te	31.74	0.868	$(2.3\pm0.3)\times10^{3}$	[84]
^{130}Te	34.08	2.527	$(0.771^{+0.008+0.012}_{-0.006-0.015})$	[85]
^{136}Xe	8.9	2.459	$(2.23\pm0.03\pm0.07)$	[86]
^{150}Nd	5.6	3.371	$(9.34\pm0.22^{+0.62}_{-0.60})$	[87]
^{238}U	99.2745	1.144	(2.0 ± 0.6)	[88]

The half-life of the $2\nu\beta\beta$ decay can be factorized as

$$\frac{1}{T^{2\nu}_{1/2}} = G^{2\nu}(Q_{\beta\beta}, Z)|M^{2\nu}|^2, \tag{2.4}$$

where $G^{2\nu}$ is the phase space of the leptons emitted in the decay, and $M^{2\nu}$ is the nuclear matrix element (NME) responsible for the transition probability between the initial and final nuclear states. The NMEs are not easily calculable since they require an accurate nuclear model of the dozens of nucleons of each isotope. More details about the NMEs will be given in Section 2.3.

The phase-space factor is obtained by integration over all possible energies and angles of the electrons and antineutrinos emitted in the decay [89]:

$$G^{2\nu} \propto \int_{m_e}^{Q_{\beta\beta}+m_e} F(Z, E_{e1}) p_{e1} E_{e1} dE_{e1} \times \int_{m_e}^{Q_{\beta\beta}+2m_e-E_{e1}} F(Z, E_{e2}) p_{e2} E_{e2} dE_{e2} \times \int_{0}^{Q_{\beta\beta}+2m_e-E_{e1}-E_{e2}} E_{\nu 1} E_{\nu 2} dE_{\nu 1}, \tag{2.5}$$

where $F(E, Z)$ is the Fermi function that describes the Coulomb effect on the outgoing electrons, and E and p are the energy and momentum of the emitted fermions. A complete overview of the phase space factor for various isotopes, from precise numerical calculations, can be found in [90].

2.2 $0\nu\beta\beta$ decay

In 1939, W. H. Furry applied Majorana's fields to Goeppert-Mayer's double beta disintegration [91], showing that if neutrinos were Majorana particles, double beta decay should be possible without the emission of two antineutrinos:

$$(A, Z) \rightarrow (A, Z+2) + 2e^{-}. \tag{2.6}$$

This is know as *neutrinoless double beta decay* ($0\nu\beta\beta$), and has never been observed to date. While $2\nu\beta\beta$ is allowed in the Standard Model, $0\nu\beta\beta$ is not, since it violates lepton number conservation by two units. Lepton number conservation is required by the renormalizability of the classical SM Lagrangian [92]. Accommodating the $0\nu\beta\beta$ decay would therefore require changes to the Standard Model.

The standard mechanism mediating $0\nu\beta\beta$ decay is the exchange of a light Majorana neutrino within the nucleus, as illustrated in Figure 2.3. The parent nucleus emits a virtual W boson, creating an electron and an antineutrino. Due to the left-handed chiral character of the SM charged-current interaction, the emitted antineutrino will be in a state that is dominantly of right-handed helicity, with a negative helicity component strongly suppressed by a factor of m_ν/E_ν. In order for it to be absorbed, creating the second electron, the antineutrino has to be a Majorana particle, so that $\bar{\nu} = \nu$. Furthermore, only the small left-handed helicity component can be absorbed by the SM left-handed charged current without suppression, which is only possible if neutrinos have a non-zero mass. A variety of other mechanisms for $0\nu\beta\beta$ have been proposed: for example, right handed currents, exchange of heavy Majorana neutrinos, or exchange of supersymmetric particles. However, regardless of the mechanism, the observation of $0\nu\beta\beta$ implies a Majorana mass term for the neutrino [93].

Without the emission of the neutrinos in the $0\nu\beta\beta$, the electrons will be responsible for car-

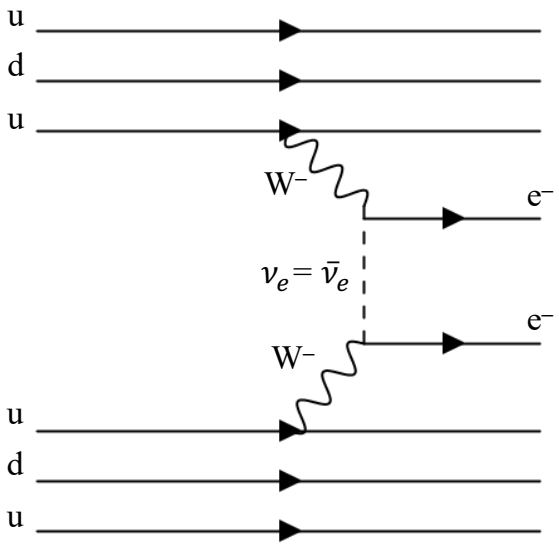

Figure 2.3: Feynman diagram for the $0\nu\beta\beta$ decay.

rying the totality of the decay energy. Therefore, the search for this process relies on searching for a small peak at $Q_{\beta\beta}$, as illustrated in Figure 2.4. The $0\nu\beta\beta$ decay rate is commonly written as:

$$\frac{1}{T^{0\nu}_{1/2}} = G^{0\nu}(Q_{\beta\beta}, Z)|M^{0\nu}|^2 \left(\frac{m_{\beta\beta}}{m_e}\right)^2. \tag{2.7}$$

This expression is similar in form to that for $2\nu\beta\beta$ (Equation 2.4), containing the phase space factor $G^{0\nu}$ and nuclear matrix element $M^{0\nu}$. However, it contains an additional component, which is the effective electron neutrino Majorana mass $m_{\beta\beta}$:

$$m_{\beta\beta} = |\sum_i e^{i\alpha_i} U^2_{ei} m_i|. \tag{2.8}$$

The $0\nu\beta\beta$ is therefore sensitive to not only the values of the neutrino mass eigenstates, but also to the elements of the PMNS mixing matrix connected to ν_e. The sum over the elements of the PMNS matrix comes from the fact that the electron (anti)neutrino is a superposition of mass eigenstates and, hence, the probability of a W boson in the $0\nu\beta\beta$ to interact with a mass state ν_i is proportional to U^2_{ei}. The masses m_i in Equation 2.8 arise from the required helicity flip, which is less likely to happen for smaller masses. It is due to this helicity suppression that the half-life of $0\nu\beta\beta$ is expected to be even longer than the $2\nu\beta\beta$, which makes the detection of this process very difficult.

Using the knowledge on the mixing angles and squared-mass differences from oscillation experiments, it is possible to plot the value of $m_{\beta\beta}$ as a function of the lightest neutrino mass (m_1 for normal ordering, m_3 for inverted ordering), as shown in Figure 2.5. The width of the allowed bands are due to the uncertainties on the PMNS matrix parameters, mainly the unknown Majorana phases α_i. For the inverted ordering, $m_{\beta\beta}$ is bounded to be larger than 10^{-2} eV. For the normal ordering, the large phase space for the Majorana phases could lead to cancellations between the terms of Equation 2.8, pushing the value of $m_{\beta\beta}$ to zero when m_1 is in the interval

$(2\text{–}8)\times10^{-3}$ eV. Despite this possibility, Bayesian analyses incorporating existing data to make predictions, under well-defined assumptions, of the discovery probability for true values of $m_{\beta\beta}$ suggest up to 50% discovery probabilities for the normal ordering scenario [94, 95], and a non-vanishing discovery probability even assuming the most unfavourable values for the Majorana phases [96].

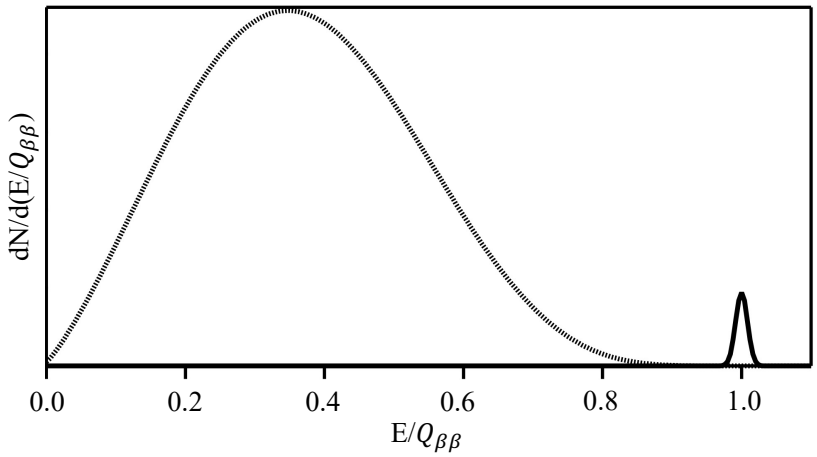

Figure 2.4: Spectra of the $2\nu\beta\beta$ and $0\nu\beta\beta$ decays (peaks not to scale).

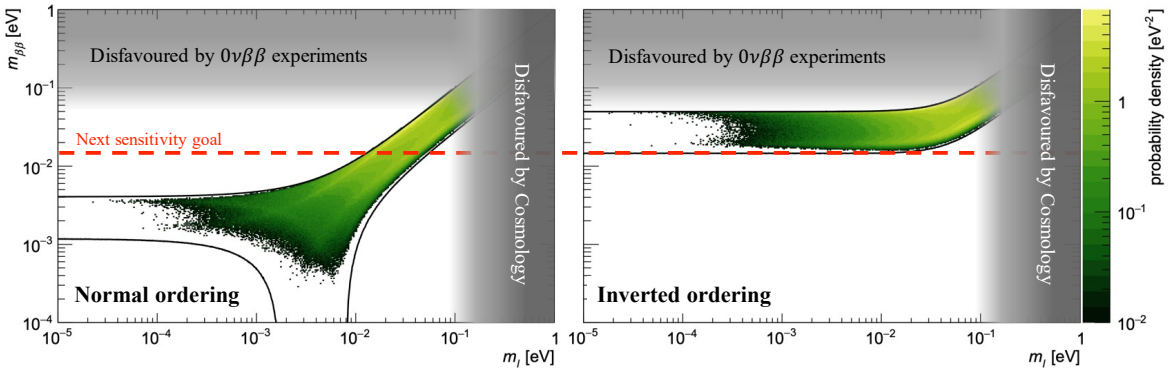

Figure 2.5: The allowed regions of the effective electron neutrino Majorana mass, $m_{\beta\beta}$ relative to the lightest neutrino mass in the normal (left) and inverted (right) orderings. The color code is a Bayesian probability distribution assuming flat priors for unknown parameters, used to illustrate the most likely parameter values under this assumption. The grey bands cover the regions that have been disfavoured by $0\nu\beta\beta$ decay experiments and by cosmology [97]. The red dashed line highlights the sensitivity goal for future experiments searching for $0\nu\beta\beta$ decay. Figure adapted from [94].

2.3 Nuclear aspects of $\beta\beta$ decay

The nuclear structure effects of double beta decay are included in the nuclear matrix elements (NMEs). The NMEs for $0\nu\beta\beta$ decay are essential to obtain predictions for the half-life of this process given the current knowledge about the neutrino masses and, once and if a positive signal is found, in order to extract the value of $m_{\beta\beta}$. The NMEs are obtained from complex

nuclear theory calculations, which require a good description of the initial and final nuclei in the $\beta\beta$ decay, using complex nuclear many-body approaches, and the evaluation of the transition operator between these states.

The nuclear matrix elements $M^{0\nu}$ and $M^{2\nu}$ connect the same nuclear states and can be written in a similar form. They generally consist of a wave function describing the final state of the daughter even-even nucleus, a wave function describing the ground state of the even-even parent nucleus, and an operator connecting those states. In the case of the $2\nu\beta\beta$, the NME can be parametrized as [98]:

$$M^{2\nu} = (g_A^{eff})^2 \left[M_{GT}^{2\nu} + \left(\frac{g_V}{g_A} \right)^2 M_F^{2\nu} \right], \tag{2.9}$$

where M_{GT} and M_F are the Gamow-Teller and Fermi matrix elements. $M_F^{2\nu}$ is suppressed because the Fermi operator does not connect states of different isospin. Since $|M_F^{2\nu}| \ll |M_{GT}^{2\nu}|$, the contribution from $M_F^{2\nu}$ is usually neglected. g_V and g_A are the vector and axial-vector weak interaction coupling constants, respectively.

g_A^{eff} is the effective value of the axial-vector coupling, quenched relative to the free-nucleon value $g_A = 1.2754 \pm 0.0023$ [76], measured in neutron decay experiments. This quenching was introduced after a systematic overestimation of the theoretical $2\nu\beta\beta$ decay rates with respect to the observed ones was found [99]. The source of the quenching factor can be nuclear medium effects, or deficiencies in the nuclear many-body approaches used for the NME calculations. The first one yields a quenching that does not depend on the mass number, and the second produces a model dependent quenching that grows with increasing mass number. Validating the NME theoretical calculations with experimental results is therefore crucial to determine the origin of the quenching.

In the case of $0\nu\beta\beta$, the NME is generally presented as [100]:

$$M^{0\nu} = (g_A^{eff})^2 \left[M_{GT}^{0\nu} - \left(\frac{g_V}{g_A} \right)^2 M_F^{0\nu} + M_T^{0\nu} \right], \tag{2.10}$$

where the additional term M_T is the tensor matrix element. The neutrino exchange operator necessary to describe $0\nu\beta\beta$ increases the contribution of the terms suppressed in the $2\nu\beta\beta$ NMEs, and requires a more complete modelling of intermediate nuclear states. As a result, the $0\nu\beta\beta$ matrix elements are very challenging to calculate. As Figure 2.6 shows, different models result in a factor of $\sim$3 difference in $M^{0\nu}$. Section 2.3.1 will describe the models and their differences.

It is important to note that the value of g_A^{eff} may or may not be the same in both the $0\nu\beta\beta$ and $2\nu\beta\beta$ transitions, depending on the causes of the same quenching [101]. Because it enters Equation 2.7 as $(g_A^{eff})^4$, its value can have a large impact on the conversion between $T_{1/2}^{0\nu}$ and $m_{\beta\beta}$. What is the correct value of g_A^{eff} is still an open issue and introduces a considerable uncertainty in the determination of $m_{\beta\beta}$ from the $0\nu\beta\beta$ rate formula of Equation 2.7 [101, 100].

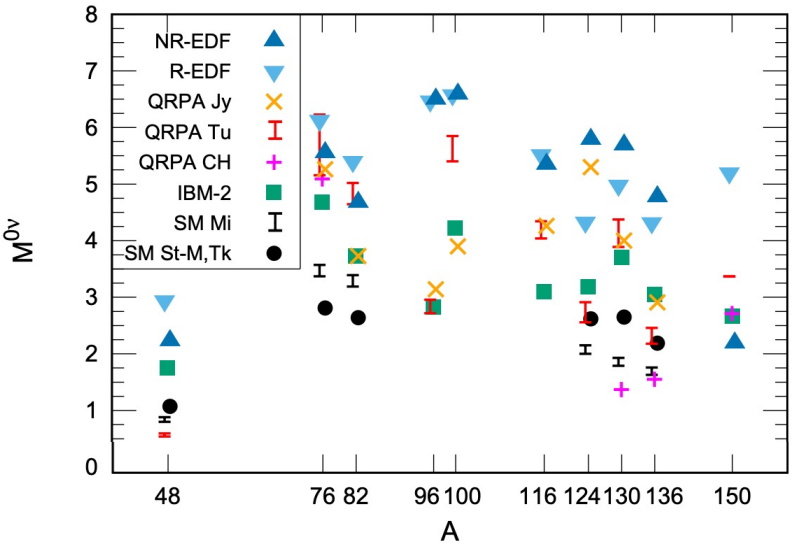

Figure 2.6: Nuclear matrix elements for $0\nu\beta\beta$ decay. Each marker type identifies the theoretical model used to calculate the nuclear matrix element. More details about the calculations are given in Section 2.3.1 for a selection of models. Figure from [101].

2.3.1 Models for NME calculations

All the methods which have been implemented for the calculation of the NMEs involve two different stages. In a first step, the interactions between nucleons and the physical mechanism behind $\beta\beta$ decay are incorporated via a many-body Hamiltonian. The second step consists in the introduction of a mean field to take into account the nuclear structure and residual interactions. It is in this second step that the models tend to differ by introducing different approximations and simplifying assumptions. The most commonly used NME models are:

- Quasi Random Phase Approximation (QRPA) [98]: it considers a high number of nuclear orbitals with restricted correlations between the nucleons. The interaction is treated using a realistic nucleon-nucleon potential adapted to the QRPA configuration space through many-body perturbation theory. The interaction strength of the proton-neutron pairing, g_{pp}, has a significant impact in the calculations. The usual procedure in the QRPA is to fix the value of g_{pp} so that the measured rate of $2\nu\beta\beta$ decay is correctly reproduced. Then the same value is used to predict the rate of $0\nu\beta\beta$ decay. The reason for the sensitivity to the proton-neutron pairing strength has been the subject of many investigations over the years and led to the development of variants of the QRPA, such as the "renormalized QRPA" (RQRPA).

- Interacting Shell Model (ISM) [102]: the ISM is based on the idea that most of the nucleons do not contribute to the interaction, except the ones close to the Fermi sea. This model considers all the possible correlations between the valence nucleons, proton-proton, neutron-neutron and proton-neutron, such that both proton and neutron numbers are conserved. This model works well for light nuclei, but problems start arising for heavier or deformed nuclei, where orbitals far from the Fermi level play a non-negligible

role.

- Energy Density Functional (EDF) [103]: this method is based on the minimization of an energy functional with respect to local density functions, such as nucleon number density, spin density, current density, etc. The Hamiltonian is minimized, with constraints, over these quantities to obtain the energy density functional, which can be used to compute exact nuclear properties. The functional parameters are adjusted to match ground-state properties of a set of nuclei, and then used with no change for any nucleus. EDF provides a good description of the ground state properties and spectroscopy of medium-mass and heavy nuclei. NMEs from EDF calculations are typically larger than those obtained with other models because proton-neutron pairing correlations are not explicitly taken into account by EDF calculations [104].

- Interacting Boson Model (IBM) [105]: in this model, protons and neutrons pair up and act as a single particle with boson properties. Two versions of the model exist depending if protons and neutrons are treated in the same way (IBM-1) or separately (IBM-2). Due to the pairing, only the even-even nuclei are taken into account by the IBM model, which is not a problem since only even-even nuclei can undergo $\beta\beta$ decay.

2.4 Experimental searches for $0\nu\beta\beta$ decay

All the experiments searching for $0\nu\beta\beta$ have some characteristics in common. This rare decay is possible for a limited number of isotopes and, if it exists, has an extremely long half-life. Therefore, all experiments aim to have as many atoms as possible of the isotope that undergoes $2\nu\beta\beta$. This is accomplished by having a large experimental mass and the possibility of isotopic enrichment. Additionally, choosing an isotope with a high natural abundance helps maximize the isotope mass while minimizing the enrichment costs. The chosen isotope should also have a high Q-value. Since the phase-space factor scales with the Q-value, a higher $Q_{\beta\beta}$ lowers the half-life of $0\nu\beta\beta$, improving the chances of its detection. Furthermore, with a higher $Q_{\beta\beta}$, the search region will be above most of the natural radioactivity backgrounds, which are particularly problematic below 2 MeV. As a result of these criteria, the experimental efforts focus mostly on isotopes with $Q_{\beta\beta}$ larger than 2 MeV, highlighted in Figure 2.7.

Another common goal amongst $0\nu\beta\beta$ experiments is the reduction of possible sources of background. Cosmic ray induced backgrounds are suppressed by placing the experiments in underground facilities. Environmental radioactivity is controlled and minimized by using extremely radio-pure construction materials for the experiment, and by shielding the active medium, for example using water. Furthermore, intrinsic background levels are minimized by using high-purity $\beta\beta$ active materials, with further periodic purification allowed in the case of liquid-based experiments. Veto systems and particle discrimination techniques also play a crucial role in minimizing the backgrounds at the analysis level.

There are however sources of background that cannot be avoided, such as the intrinsic contamination of $2\nu\beta\beta$ events caused by the same isotope used for the $0\nu\beta\beta$ decay searches. The

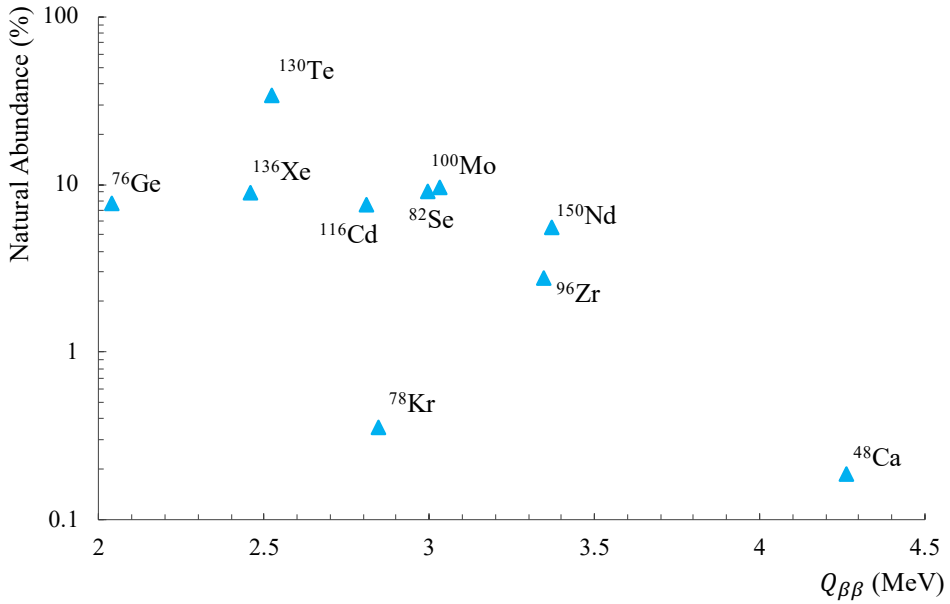

Figure 2.7: Candidate isotopes for $0\nu\beta\beta$ searches with Q-value larger than 2 MeV, as a function of their natural abundances.

best strategy is having an energy resolution high enough to clearly discriminate the two signals. However, not all the detection techniques allow such high energy resolution: in this latter case the only way to isolate the possible $0\nu\beta\beta$ signal is by statistical subtraction of the background which implies the use of Monte Carlo simulations and requires a deep understanding of the background model of the experiment. Another intrinsic source of backgrounds for $0\nu\beta\beta$ experiments comes from solar neutrinos.

So far, no evidence for the existence of the $0\nu\beta\beta$ has been found. Hence, experimental results can only provide limits on the $0\nu\beta\beta$ half-life of some isotopes and, implicitly, on the value of $m_{\beta\beta}$. The sensitivity of an experiment, $S^{0\nu}$, is defined as the half-life corresponding to the minimum number of signal events observable above background at a given confidence level n_σ. The corresponding background level B is defined as the number of expected background events in the region-of-interest (ROI) per mass, energy and time. $S^{0\nu}$ can be parametrized as [100]:

$$S^{0\nu} = \frac{\ln 2}{n_\sigma} \frac{x \cdot a \cdot N_A \cdot \epsilon}{M} \sqrt{\frac{m t_{exp}}{B \Delta E}}, \tag{2.11}$$

where x is the number of nuclei of the element containing the $\beta\beta$ isotope per molecule, a is the isotopic abundance of the $\beta\beta$ nuclide, N_A is the Avogadro constant, M is the molar mass of the compound, ϵ is the detection efficiency, m is the total mass of the compound containing the $\beta\beta$ isotope, and ΔE is the width of the ROI. In order to increase the sensitivity, experiments have to maximize the detection efficiency ϵ, the available number of $\beta\beta$ isotopes and the measuring time t_{exp}, while at the same time keeping the background level B in the ROI as low as possible[1] and achieving a sufficiently good energy resolution at around $Q_{\beta\beta}$. Various scientific collaborations take different experimental approaches to achieve the best sensitivity. The current best limits

[1]For some experiments, the background level can have a contribution from backgrounds that scale with the isotope mass ($B \cdot m$) and backgrounds from constant sources (C), like those coming from detector components or

on $T^{0\nu}_{1/2}$ for several isotopes are listed in Table 2.2. Below follows a summary of the current and planned $0\nu\beta\beta$ experiments.

Table 2.2: List of the current best $0\nu\beta\beta$ half-life limits and corresponding experiment, total isotope mass and exposure.

Isotope	$T^{0\nu}_{1/2}$ (years)	Experiment	Isotope Mass (kg)	Exposure (kg year)	
^{48}Ca	$>5.8\times10^{22}$	CaF_2(Eu) scintillators	0.1748	13.6	[108]
^{76}Ge	$>1.8\times10^{26}$	GERDA	25.6 (Phase I), 44.2 (Phase II)	127.2	[109]
^{82}Se	$>3.5\times10^{24}$	CUPID-0	4.65	5.29	[110]
^{100}Mo	$>1.5\times10^{24}$	CUPID-Mo	2.258	2.16	[111]
^{116}Cd	$>2.2\times10^{23}$	Aurora	1.162	4.7	[83]
^{130}Te	$>2.2\times10^{25}$	CUORE	206	288.8	[112]
^{136}Xe	$>2.3\times10^{26}$	KamLAND-Zen	344	970	[113]

2.4.1 Current experiments

There are presently several large scale experiments trying to measure $0\nu\beta\beta$ decay in different isotopes using a variety of detector technologies.

Even though it stopped acquiring data at the end of 2019, the GERmanium Detector Array (GERDA) experiment [114] will be briefly introduced due to its outstanding results and contributions to the $0\nu\beta\beta$ field. It was located at the Laboratori Nazionali del Gran Sasso (LNGS) in L'Aquila, Italy. It consisted of 86%-enriched ^{76}Ge high purity germanium detectors, immersed in a liquid-argon cryostat which was used for shielding and cooling. Furthermore, liquid argon scintillates and, hence, it was used to actively veto backgrounds that deposit energy inside this shield. The GERDA collaboration also employed a digital analysis of the detector signal pulses to discriminate between single-site energy deposition, such as the one expected from the $0\nu\beta\beta$ electrons, and more distributed deposition from background events involving γs. The combination of high radiopurity of the detector material, good shielding, active background rejection through liquid argon and pulse shape discrimination resulted in an exceptionally low background count in the ROI. GERDA has the current best limit on the ^{76}Ge half-life, $T^{0\nu}_{1/2} > 1.8 \times 10^{26}$ years (90% C.L.), with an exposure of 127.2 kg year [109].

A similar experiment is the Majorana Demonstrator [115], operating 29.7 kg of 88%-enriched ^{76}Ge and 14.4 kg of natural p-type point-contact detectors at the Sanford Underground Research Facility in Lead, SD, USA. The collaboration has reported a lower limit of $T^{0\nu}_{1/2} > 2.7 \times 10^{25}$ years (90% C.L.), with an exposure of 26.0$\pm$0.5 kg year [116], with an unprecedented energy resolution of 2.53 keV FWHM at $Q_{\beta\beta}$.

The Cryogenic Underground Observatory for Rare Events (CUORE) experiment is located at LNGS [117]. It uses 988 cubic TeO_2 crystals with 5 cm sides and 750g each, yielding a total mass of 206 kg for the $\beta\beta$ isotope ^{130}Te. The crystals are enclosed inside a multi-layer cryostat

solar neutrinos [106, 107]. In this case, Equation 2.11 transforms into:

$$S^{0\nu} = \frac{\ln 2}{n_\sigma}\frac{x \cdot a \cdot N_A \cdot \epsilon}{M}\frac{mt_{exp}}{\sqrt{(B \cdot m + C)\Delta E t_{exp}}}\,. \tag{2.12}$$

cooled to 7 mK with helium. CUORE has demonstrated the excellent energy resolution of this technique of $\sim$0.1% at $Q_{\beta\beta}$, which is comparable to the germanium diode experiments. As it is possible to increase the isotope mass by simply adding more crystal units, the scalability is mostly limited by the size of the cryostat. The main drawback of crystal bolometers is the lack of reliable particle identification, which leads to poor background rejection. CUORE has reported a lower limit of $T^{0\nu}_{1/2} > 2.2 \times 10^{25}$ years (90% C.L.), with a TeO_2 exposure of 1038.4 kg year [112].

The search for $0\nu\beta\beta$ in ^{136}Xe is led by the EXO-200 [118] and KamLAND-Zen 800 [119] experiments. EXO-200 is a cylindrical time projection chamber filled with 200 kg of liquid xenon enriched to 80.6% in ^{136}Xe. The xenon is also surrounded by avalanche photodiodes that measure scintillation light; this combination allows for event discrimination between single-site decays and broader Compton scattering of gamma ray backgrounds. The KamLAND-Zen experiment suspends a balloon of xenon-doped liquid scintillator (745 kg of xenon with a 91% isotopic abundance of ^{136}Xe) into a 13-m-diameter outer balloon filled with pure liquid scintillator. EXO-200 has reported a half-life limit of $T^{0\nu}_{1/2} > 3.5 \times 10^{25}$ years (90% C.L.) with an exposure of 234.1 kg year [120], while KamLAND-Zen has reported $T^{0\nu}_{1/2} > 2.3 \times 10^{26}$ years (90% C.L.) with an exposure of 970 kg year [113].

A qualitatively different experiment, NEMO-3 [121], is the only major $0\nu\beta\beta$ decay experiment where the source isotope is not embedded in the detector. The best half-life limits for many $0\nu\beta\beta$ decay candidate isotopes not addressed by dedicated experiments have come from the NEMO-3 detector, due to its ability to study any isotope that can be added to a thin source film. These source films are placed inside a gas tracking chamber that is surrounded by calorimeters, which allows for both electron tracking and energy reconstruction and thus extremely low backgrounds. The experiment is, however, limited by the relatively poor energy resolution of the calorimeters ($\sim$10%) and the low source masses that can be used. NEMO-3 has used the isotopes ^{48}Ca [77], ^{82}Se [122], ^{96}Zr [81], ^{116}Cd [123], ^{130}Te [124], ^{150}Nd [87], and ^{100}Mo [125], to measure the $2\nu\beta\beta$ and search for $0\nu\beta\beta$ decay.

2.4.2 Future experiments

The aim of the next generation of experiments is to reach the sensitivity required to start to investigate (or, possibly, cover completely) the inverted mass ordering band (Figure 2.5). This means reaching a sensitivity of about 10^{-2} eV for $m_{\beta\beta}$, an improvement of about an order of magnitude with respect to the current best results. The complete investigation of the inverted ordering band would lead to two possible results: either $0\nu\beta\beta$ decay is observed, proving that neutrinos are Majorana particles, but the mass ordering would remain unknown; or the decay is not observed, which would indicate that the ordering is normal, if neutrinos are Majorana particles. However, if other experiments (such as oscillation experiments) demonstrate that the neutrino mass ordering is inverted and $0\nu\beta\beta$ is not observed, it would indicate that neutrinos are Dirac particles.

Some of the planned projects are upgrades of the experiments discussed in Section 2.4.1. The EXO-200 experiment will be succeeded by nEXO [126], a tonne-scale single-phase liquid-

xenon time projection chamber, containing 5000 kg of xenon enriched to 90% in ^{136}Xe. The projected half-life sensitivity for the experiment is approximately 10^{28} years, three orders of magnitude higher than the current EXO-200 results. Two other collaborations, NEXT [127] and PandaX-III [128], are planning experiments with high-pressure xenon gas TPCs.

Similarly, the NEMO collaboration is scaling up to produce SuperNEMO [129], a modular detector aimed at improving energy resolution and signal efficiency. CUPID (CUORE Upgrade with Particle IDentification) [130] is an upgrade of the CUORE experiment, which will use Li_2MoO_4 scintillating crystals enriched in ^{100}Mo. CUPID aims to improve background rejection through active particle discrimination, particularly the rejection of the dominant α backgrounds in CUORE.

The Large Enriched Germanium Experiment for Neutrinoless double beta Decay (LEGEND) collaboration was recently formed to pursue a tonne-scale ^{76}Ge-based experiment [131]. The project will combine the strengths of the two operating experiments – the shielding and scintillating veto for background suppression from GERDA, and ultra-pure materials and components from the Majorana Demonstrator – to attempt a $T^{0\nu}_{1/2}$ discovery sensitivity of $\sim 10^{28}$ years in a phased program. In the first phase, LEGEND-200, the GERDA experimental infrastructure at LNGS will be modified and repurposed to accommodate up to about 200 kg of ^{76}Ge-enriched detectors. The $0\nu\beta\beta$ decay discovery potential for LEGEND-200 is expected to be $\sim 10^{27}$ years, with a background level 5 times lower than GERDA. To reach the ultimate discovery potential, the second phase LEGEND-1000 will use 1000 kg of detectors.

Finally, the SNO+ experiment will use tellurium-loaded liquid scintillator to search for the $0\nu\beta\beta$ decay of ^{130}Te and is currently in commissioning without tellurium. It will take advantage of the hardware used in the SNO experiment, which was filled with heavy water to detect solar neutrinos. With the upgrade of CUORE to CUPID, and its change of isotope (^{130}Te to ^{100}Mo), SNO+ will be the only experiment in the upcoming years searching for $0\nu\beta\beta$ decay using ^{130}Te. Able to deploy tonne-scale amounts of isotope, it expects to achieve the best half-life limit for ^{130}Te. SNO+ is the subject of this thesis, and will be discussed in detail in Chapter 3.

Chapter 3

The SNO+ experiment

SNO+ is a kilo-tonne scale liquid scintillator experiment located at SNOLAB, Canada [132, 133]. The deep underground location (2070 m, 6010 m.w.e.), the detector technology, and the low background levels make SNO+ an impressively versatile experiment able to explore several topics of neutrino and exotic physics. The experiment has and will operate in three phases distinguished by the target material within the main detector volume. After acquiring data as a pure-water Cherenkov detector between May 2017 and June 2019, the experiment currently uses 780 tonnes of liquid scintillator as its target material. For its next operating phase, the scintillator will be loaded with 3.9 tonnes of natural tellurium (0.5% by weight) to perform a search for the $0\nu\beta\beta$ decay of the isotope ^{130}Te, but the collaboration is actively pursuing the possibility of higher loading, from 1.5% to 3%.

This Chapter describes the functioning of the SNO+ experiment. Section 3.1 gives an overview of the physics goals of the experiment. The detector and its components are thoroughly described in Sections 3.2–3.6. Section 3.7 discusses the modelling and reconstruction of physics events in SNO+, and Section 3.8 provides an overview of the calibration efforts to constrain the unknowns in the detector model. Finally, Section 3.9 summarizes the physics results of the water and scintillator phases, while Section 3.10 discusses the prospects for the ^{130}Te $0\nu\beta\beta$ search during the SNO+ Te-loaded phase.

3.1 Physics goals

The primary goal of the SNO+ experiment is to perform a competitive search for $0\nu\beta\beta$ decay using ^{130}Te. The strength of the SNO+ approach relies on the large liquid scintillator volume and unique tellurium loading technique, allowing the use of a high isotope mass, and the potential to economically scale it in future upgrades.

By loading 3.9 tonnes of natural tellurium into the liquid scintillator (0.5% loading by weight), the initial SNO+ search will make use of more than 1.3 tonnes of ^{130}Te. ^{130}Te undergoes $2\nu\beta\beta$ with a half-life of:

$$T^{2\nu}_{1/2} = \left(7.71^{+0.08}_{-0.06}(\text{stat.})^{+0.12}_{-0.15}(\text{syst.})\right) \times 10^{20} \text{ years [85]} \tag{3.1}$$

and has an end point energy of:

$$Q_{\beta\beta} = 2527.518 \pm 0.013 \text{ keV [134]} \tag{3.2}$$

^{130}Te has multiple advantages over other isotopes, including its high natural abundance (34.1%) and relative low cost (1000 USD per kg of ^{130}Te). This enables the deployment of generous isotope masses without the need for enrichment. The favourable phase space and nuclear matrix elements result in better prospects of observing the $0\nu\beta\beta$ decay. ^{130}Te also has one of the longest $2\nu\beta\beta$ decay half-lives of all the $0\nu\beta\beta$ candidates, hence the rate of irreducible background events due to $2\nu\beta\beta$ decays in the $0\nu\beta\beta$ region-of-interest will be lower, which is particularly important when dealing with the relatively poor energy resolution of a typical liquid scintillator detector. In SNO+, the expected energy resolution is $\sim$3 % around the ^{130}Te Q-value.

The Q-value of ^{130}Te is below both the highest natural radioactivity γ line (2.6 MeV), from ^{208}Tl, and above the β decay Q-value of ^{214}Bi (3.270 MeV), which result from radon daughters. This requires a careful control of the radio-purity of the detector materials, in particular of the liquid scintillator. However, an advantage of the liquid scintillator approach is that it can be purified to a high degree, even during data taking, by recirculating the organic scintillator through a purification system. Similarly, the recirculation will be used to gradually mix the ^{130}Te into the scintillator. Should a $0\nu\beta\beta$ signal be observed, the scaling of the signal peak with isotope mass will be crucial in confirming the discovery.

Further background reduction in the $0\nu\beta\beta$ ROI relies on volume fiducialization and on the timing characteristics of scintillation. Given the large volume of the SNO+ target, events close to the detector components can be rejected employing volume fiducialization without greatly sacrificing the experiment's exposure. The fast rise time of scintillation light allows background discrimination and rejection by looking at time-correlated decays within the scintillator, in particular of radon daughters such as ^{214}Bi and ^{212}Bi. In addition, the scintillation timing profile depends on the ionization density of the charged particles, with signals caused by electrons being faster than those from protons or alpha particles. This property allows the discrimination among particle types. Finally, the most significant advantage of the SNO+ technique is its scalability – higher loading masses can be readily and economically achieved by increasing the Te loading at levels of several percent, while maintaining good optical properties. The SNO+ collaboration aims to pursue this course following the initial demonstration of 0.5% loading.

The described characteristics make SNO+ suitable to explore several other physics topics besides $0\nu\beta\beta$ decay. The depth of SNOLAB and the lower energy thresholds from the use of liquid scintillator lay the ground for measuring low energy solar neutrinos, like *pep*, CNO and ^{7}Be neutrinos. However, the major challenge for such a measurement is minimizing the lower energy natural radioactivity levels, which requires a dedicated scintillator purification campaign. SNO+ hopes to examine the transition region between vacuum oscillation dominated neutrinos (1.44 MeV *pep* neutrinos and the low-energy part of the ^{8}B spectrum) and matter effects dominated neutrinos (high-energy part of the ^{8}B spectrum) [132]. A measurement of the CNO neutrino flux could be used to complement those performed by Borexino [135], to help understand the distribution of elements heavier than helium in the Sun [136, 137]. Depending

on the ultimate low energy background levels, measuring the time dependences, seasonal and day-night, of the ^{7}Be flux could be useful to test different neutrino oscillations scenarios [138]. Depending on the levels of ^{14}C backgrounds and the final detector energy threshold, there also exists the potential for a precision measurement of pp neutrinos.

SNO+ will measure geoneutrinos, antineutrinos emitted by natural radioactivity in the Earth, to help understand heat production in the Earth. The radiochemical composition of the Earth can be assayed by looking at its geoneutrino emission, thereby providing constraints on the radiogenic portion of the Earth's heat flow and the radiochemical composition of the Earth's mantle and crust [139]. SNO+ expects around 90 reactor antineutrinos per year [132], 40% coming from one reactor complex in Canada at a baseline of 240 km, 20% from two other complexes at a baseline of 350 km, and the remaining 40% divided between reactors in the USA and elsewhere at longer baselines. This allows for a clean spectral shape, and provides good sensitivity to the second oscillation peak.

During all phases of the experiment, SNO+ will also serve as a supernova neutrino monitor. The SNO+ collaboration contributes to the SuperNova Early Warning System (SNEWS), an international network of experiments with the goal of providing an early warning of a galactic supernova [140]. Finally, SNO+ will also conduct searches for exotic physics such as axion-like particles and invisible nucleon decay [141].

3.2 Detector overview

The SNO+ detector is located inside a cavern at SNOLAB, a class-2000 clean room laboratory facility at Creighton Mine, an active copper and nickel mine in Sudbury, Canada. The deep underground location, with a rock overburden of 6010 m.w.e. provides an effective shield against cosmic muons. The resulting muon rate is (0.286 $\pm$ 0.009) μ/m^2/day [133]. SNO+ repurposes the original Cherenkov detector used in the SNO experiment [142], with necessary upgrades to enable the use of 780 tonnes of liquid scintillator as active material. A scheme of the detector is shown in Figure 3.1.

The inner volume of the detector consists of a spherical, UV-transparent acrylic vessel (AV), with a thickness of 55 mm and 12 m in diameter, which contains the active medium. The AV is surrounded by a 17.8 m diameter geodesic steel structure (PSUP) that holds 9362 inward-facing photomultiplier tubes (PMTs) with low-activity glass and light concentrators. 91 PMTs without light concentrators are also mounted facing outwards to detect light from muons and other sources in the region exterior to the PSUP. The volume between the AV and PMTs, as well as the rest of the cavity containing the detector, is filled with 7000 tonnes of ultra-pure water (UPW). This external water volume provides several meters of shielding for the AV from the PSUP and cavity walls, which are both sources of external radiation.

Two sets of high purity Tensylon ropes are installed to hold the AV in place. The hold-up ropes, 19 mm in diameter, are suspended from the top of the cavity and are hooked to ridges in the AV around its equator. The hold-down ropes, 38 mm in diameter, wrap around the top of the vessel and are anchored to the cavity floor. The latter set has been installed in order to compensate for AV buoyancy due to the liquid scintillator density being lower than the density

of the surrounding water. The acrylic vessel is connected to the deck level above the cavity through a cylindrical neck, used to fill the AV or deploy calibration sources. There are four additional PMTs located at the top of the neck, which are used to reject events that occur inside it.

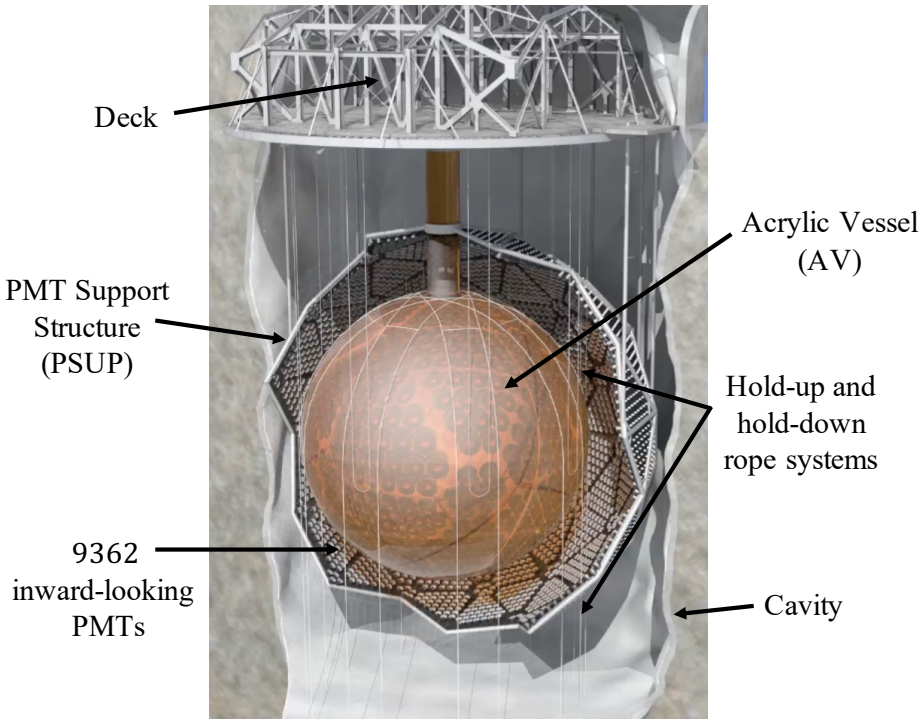

Figure 3.1: The SNO+ detector. Modified from [133].

The SNO+ detector has two inert cover gas systems. The cavity cover gas is the volume above the ultra-pure water in the cavity surrounding the AV. This volume is constantly flushed with high purity nitrogen gas at the rate of 5 litres/minute, as described in [142]. The AV cover gas is the volume above the target material inside the neck of the AV. The latter is a newly developed and completely sealed system. Both systems protect the detector from radon contamination.

3.3 Target material and operating phases

As discussed, the data taking period of SNO+ will be divided into three main phases, distinguished by the medium inside the AV. Figure 3.2 illustrates the three different phases and the intermediate partial fill period, which are going to be discussed in the following Sections.

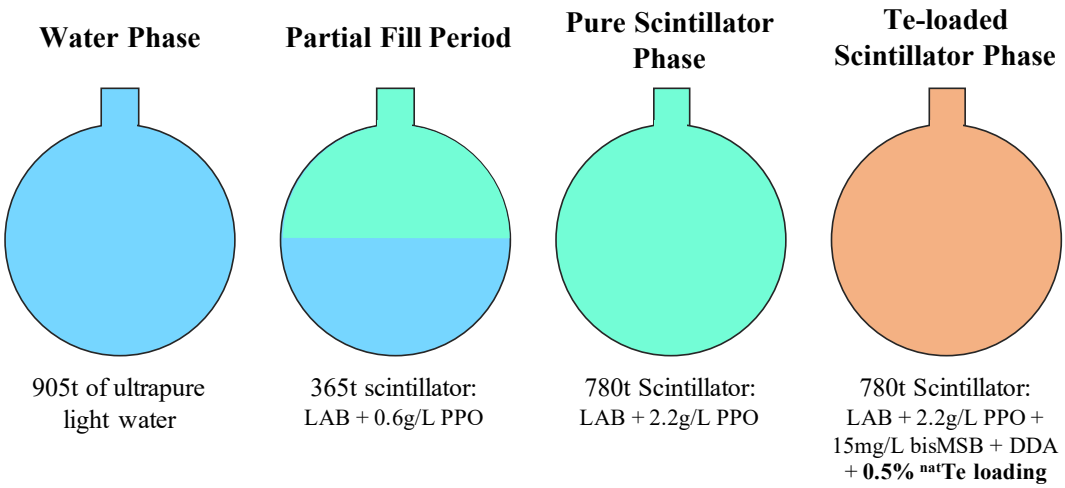

Figure 3.2: Summary of the operating phases of the SNO+ experiment.

3.3.1 Water phase

In the first operating phase, SNO+ took data as a water Cherenkov detector, filled with 905 tonnes of ultra-pure water. The detector was first ramped up in December 2016 and, after a brief commissioning period, the water phase data-taking officially started in May 2017, ending in July 2019. During this phase, SNO+ detected Cherenkov radiation emitted by relativistically charged particles arising from interactions within the detector.

When a charged particle traverses a dielectric medium of refractive index n, it polarises the molecules in the medium. After its passage, the molecules return to the unpolarised state through the emission of photons. If the velocity of the particle exceeds the speed of light in that medium, a "shock wave" of light is produced in the shape of a cone along the trajectory of the particle. The angle of the cone, θ_C, is related to the particle's velocity, v, by:

$$\cos\theta_C = \frac{1}{n(\lambda)}\frac{c}{v}, \tag{3.3}$$

provided that $v > c \cdot n(\lambda)$, with c being the speed of light in vacuum. Emission begins immediately and continues until the particle velocity drops below c/n. The above expression can be used to derive the kinetic energy threshold, E_C, for Cherenkov radiation to be produced by a charged particle of mass m:

$$E_C = m\left(\frac{1}{\sqrt{1-\frac{1}{n^2}}} - 1\right). \tag{3.4}$$

In water, this threshold is 0.26 MeV for electrons and 55 MeV for muons.

The number of emitted photons per unit track x and wavelength interval is given by the Frank-Tamm formula [76]:

$$\frac{d^2N}{dxd\lambda} = \frac{2\pi\alpha Z^2}{\lambda^2} sin^2\theta_C, \tag{3.5}$$

where x is the distance travelled by the charged particle, λ is the wavelength of the photon, Z is the charge of the particle, and α is the fine structure constant (= 1/137). For every cm of

track length, about 340 photons are produced in the wavelength range between 300 and 600 nm [33]. A key characteristic of the Cherenkov radiation is that its detection provides information not only about the particle energy, but also about its direction and original interaction point. Furthermore, the morphology of the detected radiation can be used to separate muons from electrons.

3.3.2 Scintillator phase and partial fill period

The scintillator phase of SNO+ uses 780 tonnes of liquid scintillator as target material inside the AV. The collaboration chose to use an organic liquid scintillator based on linear alkylbenzene (LAB), a long chain aromatic molecule, with 2.2 g/L of 2,5-diphenyloxazole (PPO) as the primary fluor [143], as the target material. LAB was selected for a number of reasons, including its compatibility with the acrylic, low toxicity, high flashpoint, high light yield, long attenuation length, relatively low cost, and logistical availability.

The LAB light emission peaks in the 300 nm wavelength region (UV), which overlaps with its absorption spectra. Therefore, left by itself, the LAB will re-absorb the produced light. The PPO was introduced to mitigate this effect, since it absorbs strongly in the 300-350 nm range and emits in the 350-450 nm region. The PPO is then responsible for shifting the light produced by the LAB excitation up to higher wavelengths where the chance of absorption is lower, and to the spectral range where the PMTs have higher sensitivity.

The light yield of the scintillator is about a factor of 50 higher than the light yield generated from the Cherenkov effect in water [133]. This increase in light yield results in significant improvements, including lower thresholds and a better energy resolution. Cherenkov light is still produced, but the emission of the light coincides with the de-excitation of the scintillator which produces a much higher number of photons. Thus, the Cherenkov light component gets overwhelmed by the scintillator light.

As ionising radiation passes through the liquid scintillator, it will lose energy that is going to be absorbed by the material. The energy lost in the medium from a particle passing through it is given by the Bethe-Bloch formula, and is dependent on both the particle's and medium's properties:

$$\frac{dE}{dx} = \frac{4\pi z^2 e^4}{m_e v^2} NZ \left[\ln\left(\frac{2m_e v^2}{I}\right) - \ln(1-\beta^2) - \beta^2 \right], \tag{3.6}$$

where dE/dx is the energy lost along an element dx of the particle's path, m_e and e are the electron mass and charge respectively, v, E and z are the particle's velocity ($= \beta c$), energy and charge respectively, N and Z are the medium's number density and atomic numbers (assuming the medium is isotropic and homogeneous), and I is a medium-specific constant that describes the mean excitation and ionisation potential.

The molecules of the scintillator are excited by the through-going particles, and the subsequent relaxation to the ground state is responsible for the emission of isotropic scintillation light. The excitation of the valence electrons can happen either through elastic scattering or ionisation followed by recombination into the excited state. Only spin singlet states can be created via direct excitation from elastic scattering because the ground state is also a spin singlet. With

ionisation and recombination, however, both singlet and triplet states are allowed. While the former can de-excite immediately (O(10^{-8} s)), the triplet states are metastable, which results in slower scintillation light emission. The fast component of the scintillation light emission is fluorescence, with typical decay times of nanoseconds to microseconds, and the slow component is phosphorescence, occurring on the scale of milliseconds to seconds.

It follows that a higher ratio of ionisation to direct excitation, which happens for heavier ionising particles, leads to a larger slow component of the overall emission timing profile. Heavy particles, like alphas, have a large dE/dx and therefore lose a large fraction of their energy over a short distance, creating many closely-spaced molecular ionisations and excitations. The ionisations from alpha particles can be close enough to interact with each other, and this has the effect of de-exciting some of the excited molecules non-radiatively, thus reducing the total energy that is released radiatively via luminescence - a process known as *ionisation quenching*. In SNO+, the quenching effect is responsible for an observed energy for alpha particles a factor 10 lower than their true energy.

With the addition of the PPO, the LAB molecules will transfer the excitation energy to the PPO molecules before they scintillate, either radiatively or non-radiatively. The PPO then decays, emitting light at longer wavelengths away from the LAB and PPO self-absorption ranges. The emitted light is isotropic and, therefore, is not correlated with the particle's direction. An important consequence of the scintillation process is that the different scintillation light decay times for alpha and beta particles can be used to distinguish between both types of particles. In SNO+, this feature is going to be used to reject alpha decaying backgrounds, as well as neutrons and protons.

The scintillator fill campaign started in October 2018, with the replacement of the AV neck water by liquid scintillator. In June 2019, the scintillator reached the level of the PSUP, marking the end of the water phase. Due to the COVID-19 global pandemic, the scintillator fill was paused from March to October 2020, with SNO+ taking data partially filled with 365 tonnes of liquid scintillator on top and water on the bottom of the AV – known as the partial fill period. The AV scintillator fill was concluded in March 2021, followed by a PPO top-up campaign which ended in May 2022. Since then, the SNO+ detector has been continuously taking data which will be used for the scintillator phase physics analyses. The filling process and further details about the partial fill period are discussed below.

3.3.2.1 Scintillator purification and fill

The LAB used by the SNO+ experiment was purchased from CEPSA Química Bécancour Inc. The LAB arrived to the SNOLAB surface facility on truck shipments, which were checked for quality control before storing the LAB in a stainless steel holding tank. The transport to the underground laboratory was performed by loading the LAB into stainless steel railcars. Once underground, the LAB was purified using the scintillator purification plant built by the SNO+ collaboration. The plant uses a continuous multistage distillation to remove heavy metals (Bi, K, Pb, Po, Ra and Th), and N_2 stripping to remove dissolved gases (Ar, Kr, O_2 and Rn) and volatile liquids, such as water. Larger impurities, such as dust, are removed via the use of filters,

and metallic pollutants are removed by the use of metal scavengers. The purification process is described in detail in [143].

The PPO was purchased from PerkinElmer, delivered to SNOLAB in plastic drums, and shipped directly to the underground laboratory. The PPO was mixed with purified LAB at a concentration of $\sim$120 g/L to produce a high-concentration *master solution*. The master solution was pre-purified with nitrogen vacuum purging and three cycles of solvent-solvent water extraction before it was distilled. This high concentration solution is then mixed into purified LAB during AV filling operations to reach the desired final concentration. The scintillator mixture underwent strict quality assurance (QA) testing every hour to verify that the purification performed as required.

The fill started in October 2018, when the water inside the AV neck started being replaced by pure LAB. The scintillator has lower density than the ultra-pure water, which allows it to float on top. For this reason, the scintillator was introduced at the top of the AV while the water was removed from the bottom . The two liquids are immiscible, which resulted in a clear interface between them during filling. In July 2019, the LAB started entering the AV sphere, at which point the first PPO was added. A perfluoroalkoxy (PFA) tube, with a diameter of 2.5 cm and walls with a thickness of 1.6 mm, was temporarily deployed down the middle of the AV to aid with the internal water extraction during the filling operations. The background levels and light yield of the scintillator were carefully monitored at all stages of the fill using the data acquired by the detector.

Due to the COVID-19 global pandemic, there was no access to the mine where SNOLAB is for several months in 2020. As a consequence, the scintillator filling operations were paused, leaving the AV with about 365 tonnes (355t in the spherical volume + 10t in the neck) of liquid scintillator on top of ultra-pure water. Even when access to the underground laboratory was restored, the limited number of people allowed was insufficient to resume the fill activities. Given these circumstances, SNO+ took data for 7 months in this configuration, from March 21st to October 24th 2020. During this period, the PPO concentration in the LAB was approximately 0.6 g/L, resulting in a smaller light yield for the scintillator than what is provided by the target 2 g/L of PPO. Figure 3.3 shows a photo taken during the partial fill period, where the liquid interface has been highlighted with a white line and arrow. The interface level was located 0.75 m above the AV equator.

The last few litres of ultra-pure water were removed from the AV in March 2021, and the LAB fill was concluded and the PFA tube removed. The PPO concentration inside the AV at the end of the fill was $\sim$ 0.6 g/L. A PPO top-up campaign followed, until a concentration of approximately 2.2 g/L was reached in May 2022. The scintillator is frequently recirculated through the purification plant in order to maintain the required optical clarity and radiopurity. The evolution of the light yield of scintillator with the PPO top-up campaign was closely monitored and compared to *ex situ* measurement of samples taken out of the detector. The evolution of the light yield with PPO concentration is show in Figure 3.4. The light yield of the final 2.2 g/L scintillator was determined to be 11808$\pm$630 photons/MeV.

Figure 3.3: Photo of the interior of the SNO+ detector during the partial fill period. The white line and arrow highlight the scintillator–water interface.

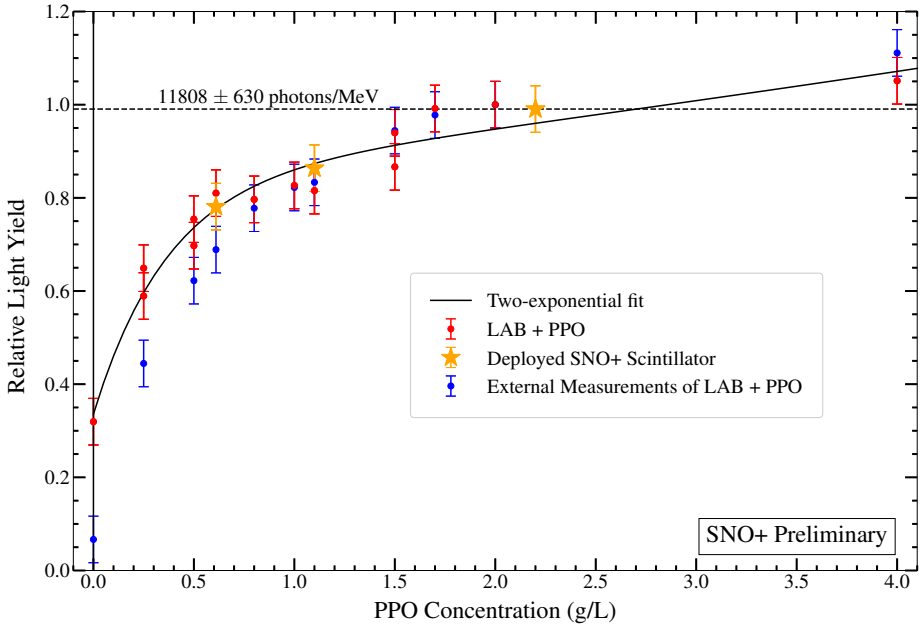

Figure 3.4: Relative light yield measurements of SNO+ scintillator (gold stars) and prepared LAB+PPO samples (red), normalised to their measurement of 2.0 g/L. Also shown in blue are externally published measurements of light yields at various PPO concentrations [144], also normalised to their measurement of 2.0 g/L.

3.3.2.2 Scintillator quality assurance

The quality of the scintillator that enters the AV is strictly controlled, both during fill operations and recirculation, by the SNO+ Quality Assurance (QA) team. Samples are taken from the purification plant and tested at the SNOLAB underground chemistry laboratory. The detector fill would only be approved after the tests showed that the samples met the strict quality standards. While filling, hourly samples were taken and tested to monitor the scintillator entering the detector, effectively checking the performance of the purification process. During a 3 month stay at SNOLAB, the author was integrated in the QA team and participated in weekly QA shifts in the underground laboratory.

The tests included monitoring the scintillator transparency and optical clarity using a UV-Vis spectrometer. An example of the UV-Vis spectra produced during this verification step is shown in Figure 3.5. The same tool was used to monitor the PPO concentration in the master solution, important for the estimates of the PPO concentration being added to the AV. Other tests included measuring the density, which was required to be around 0.86 g/cm^3 at $\sim$20 degrees, and the turbidity, which measures the concentration of suspended solids in the scintillator mixture. The latter is an important measurement to ensure a good optical quality of the scintillator and that it does not have any contaminants. For example, a turbidity value different than expected could indicate the presence of water in the scintillator sample. Less frequently, the samples were taken to a SCOUT (Scintillator Counter of Uranium and Thorium) in order to determine the intrinsic U, Th and Rn contamination in the scintillator, and to measure the light yield after irradiation of the samples with a known source.

3.3.3 Tellurium phase

In the final phase of SNO+, 3.9 tonnes of natural tellurium (0.5% by mass) will be gradually loaded into the liquid scintillator. Two underground chemical processing plants were built for the tellurium loading operations. They will process around 8 tonnes of telluric acid (TeA), $Te(OH)_6$, which have already been procured and have been stored underground for several years. When on surface, cosmic ray spallation reactions on tellurium produced long-lived isotopes which pose a threat to the $0\nu\beta\beta$ ROI, such as ^{60}Co, ^{110m}Ag, ^{88}Y, ^{124}Sb and ^{22}Na [145]. The low cosmic ray flux in SNOLAB means that the production of cosmogenics in the underground laboratory is very small. Therefore, the long storage period has given the opportunity for the cosmogenically activated isotopes to decay, without a substantial re-activation. Furthermore, the telluric acid is going to be processed in a purpose-built TeA purification plant, installed underground, to further reduce these contaminants and minimize the intrinsic levels of U and Th. The purification process consists of filtration followed by two recrystallisations (thermal and acidic) to remove both water soluble and insoluble contaminants. The procedure is described fully in [146].

After purification, the TeA will undergo a condensation reaction with 1,2-Butanediol in a synthesis plant. The products of this reaction will be water vapour, which can easily be removed, and a tellurium-butanediol (TeBD) complex, which is miscible in LAB in any required concentration. However, even though the transparency of the cocktail is still excellent, at in-

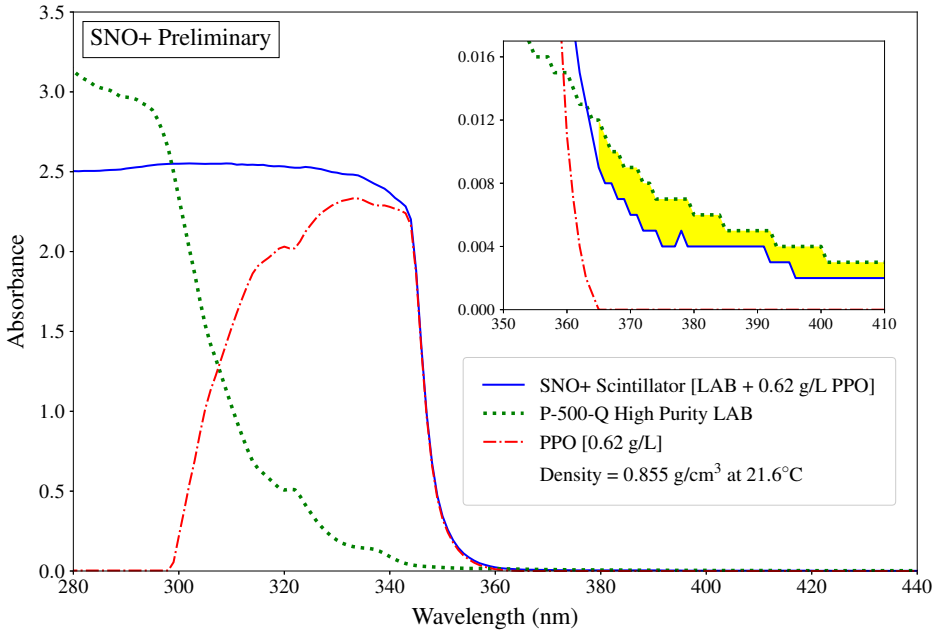

Figure 3.5: Absorption spectra measured using an Aquamate-8000 UV-Vis spectrophotometer in 1 nm increments for 1 second per measurement. The spectra were baseline subtracted with reference cell measurements. The absorbance is given as A = $\log_{10}\left(\Phi_e^i/\Phi_e^t\right)$, where Φ_e^i is the flux received and Φ_e^t is the flux transmitted. Shown in blue is the absorption spectrum of SNO+ liquid scintillator (LAB + 0.62 g/L PPO) removed from the SNO+ detector following completion of the SNO+ scintillator fill, with the reference cell filled with air. Shown in green is the absorption spectrum of the high quality P-500-Q LAB supplied from CEPSA Química Bécancour Inc. prior to purification in the underground plant, with the reference cell filled with air. Shown in red is the absorption spectrum of the same SNO+ liquid scintillator, with the reference cell filled with pure LAB, therefore inferring the absorption spectrum of 0.62 g/L PPO. As highlighted in the inset plot, the optical clarity of the SNO+ scintillator is superior to that of the sourced LAB at all wavelengths outside the absorption region of PPO.

creased Te concentrations the intrinsic light yield starts to quench. This effect will be mitigated by the addition of N,N-Dimethyldodecylamine (DDA), which also helps to stabilize the TeBD-LAB cocktail (increasing the light yield by 15% or more, depending on the Te concentration). A secondary wavelength shifter, 1,4-bis(2-methylstyryl)benzene (bisMSB) will be added to the SNO+ scintillator cocktail at a concentration below 15 mg/L. This will shift the scintillation light away from potential absorption associated with the tellurium loading method, and further increase the detected light yield.

The purification targets for the final tellurium cocktail are 10^{-15} g/g and 10^{-16} g/g of U and Th, respectively. The scintillator from the AV will be recirculated through the plant, where it will be mixed with the cocktail, and sent back to the AV. The loading is planned to start at the end of 2024. An initial batch with 1/52 of the amount of tellurium will be loaded for a three month assay run in order to evaluate the performance of the tellurium purification systems. The total concentration of 0.5% natural tellurium is expected to be reached within 36 weeks of loading operations [133], following the assay run. The loading technique is going to be described in detail in [147], and the optical properties of the final cocktail have been presented in [148].

3.4 Acrylic vessel

The acrylic vessel was inherited from the SNO experiment [142], and has been generally kept unchanged in the transition to SNO+. Figure 3.6 illustrates the AV and its components, described in this Section.

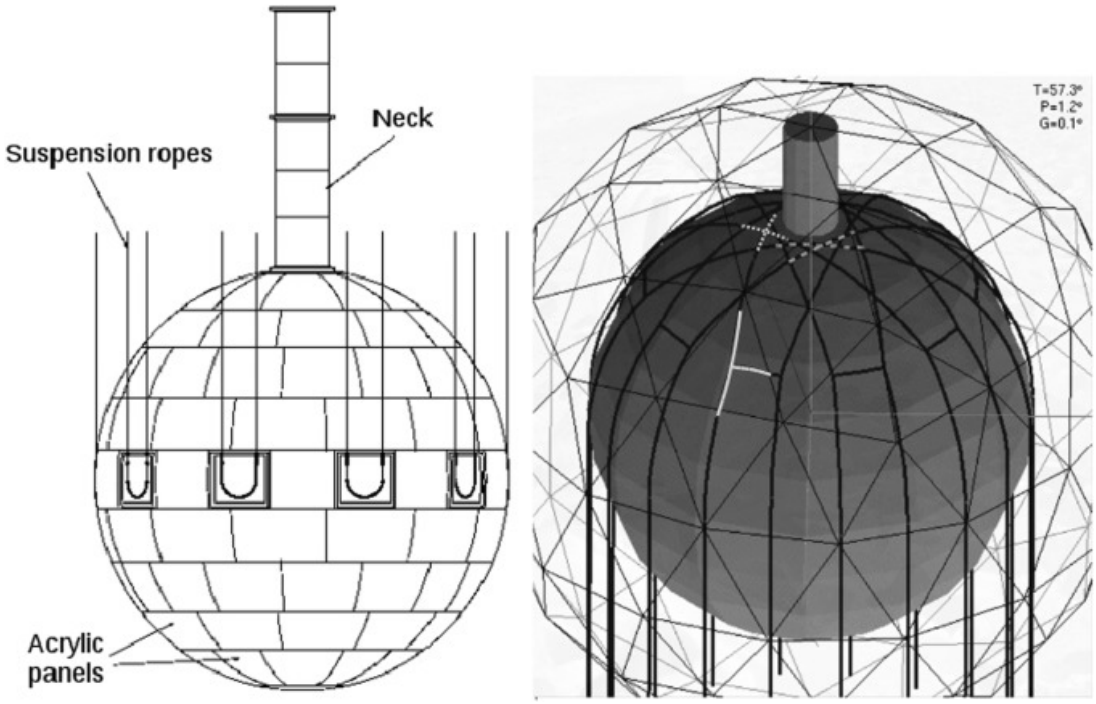

Figure 3.6: Scheme of the SNO+ acrylic vessel, including the neck and the rope systems (the hold-up ropes from SNO and the hold-down rope net installed for SNO+). Figure from [133].

The vessel is formed from 122 ultraviolet (>300 nm) transmitting acrylic panels, glued together to form a sphere maximising the volume to surface ratio. The panels are 5.5 cm thick,

with the exception of ten 11-cm thick equatorial panels containing grooves for the hold-up ropes. At the time of construction of the SNO experiment, acrylic was chosen for a number of reasons which also benefit the SNO+ program. Being a simple hydrocarbon, the acrylic could be manufactured with very low intrinsic radioactivity. Furthermore, the light transmission of the ultraviolet transmitting acrylic matches well the spectral response of the PMTs, discussed in the next Section.

The AV has a 7-m high, 1.5-m inner diameter neck made of ultraviolet absorbing acrylic. The joint between the sphere and the neck is referred as *neck boss*. The neck is connected to the deck, from where calibration sources can be introduced inside the AV. Acrylic pipes, following the curvature of the AV, are connected at different heights, including inside the neck, to allow the recirculation of the AV contents and the transition between media. The lower hemisphere of the AV includes an array of anchors used during the SNO experiment to deploy Neutral Current Detectors (NCDs).

The AV is suspended from the deck by ten rope loops that pass through the grooves inside the equatorial acrylic panels. The original hold-up ropes from SNO have been replaced with 1.85-cm diameter Tensylon ropes with lower levels of intrinsic radioactivity. A new hold-down rope net was installed in order to counteract the buoyancy of the AV filled with liquid scintillator. The hold-down rope net consists of five sub-nets, each composed of two rope pairs passing on either side of the acrylic vessel neck. Each of the 20 rope ends is anchored to the bottom of the cavity and equipped with a load cell used to monitor the force on each rope. The hold-down ropes have a diameter of 3.96 cm and are made out of high-purity Tensylon fibres, with high strength, low creep, and a low coefficient of friction. More details about the hold-down rope net and its installation during the SNO–SNO+ transition period can be found in [133]. During the transition between the water and scintillator phases, the tensions of the ropes and their lengths changed due to the scintillator buoyancy, altering the vertical position of the AV relative to the PMTs. The offset was carefully evaluated and monitored, and it is taken into account when modelling the detector and reconstructing the events (Section 3.7).

During the construction of the SNO detector, and while transitioning from SNO to SNO+, the cavity and the AV were exposed to air for several years. During this time, radon daughters from air were embedded into the AV surface. The construction phase of SNO+ included efforts to remove the embedded radon daughters by cleaning all surfaces [133]. Following the initial water fill, the cleaning efforts were completed by recirculating and repurifying the ultra-pure water deployed in the AV, thus further reducing possible contaminants. These backgrounds will be discussed in more detail in Chapter 5.

3.5 Photomultiplier tubes

SNO+ uses the Hamamatsu R1408 PMTs, with 20.3 cm in diameter, inherited from SNO. A schematic of a PMT is shown in Figure 3.7. Each PMT is individually secured within a plastic housing, and all inward-facing PMTs are surrounded by concave petal-like reflectors, formed into a Winston cone of 27 cm in diameter, referred to as concentrator. A concentrator is made of 18 pieces of thin dielectric-coated aluminium sheet, curved and placed around the

plastic housing. The optical coating consists of a layer of specular aluminium covered by a low refractive index layer of mixed titanium (TiO_2) and praeseodymium (Pr_2O_3) oxides [142]. The coating thicknesses were optimized to maximize the reflectance in water over the visible and near-UV range of wavelengths, and over a wide range of incident angles.

The concentrators redirect light onto the PMT face, increasing the effective coverage of the full PMT array to about 54%. The light collection efficiency of the PMT and concentrator assembly (or *PMT angular response*) increases with the incident angle of light in the range from 0° to 50°, but beyond this angle it rapidly drops off due to design constraints of the concentrators [149]. Over the lifetimes of SNO and SNO+, the concentrator petals have aged and dulled due to being immersed in ultra-pure water, reducing the overall reflectivity. Figure 3.8 shows one example of a set of degraded concentrators from SNO.

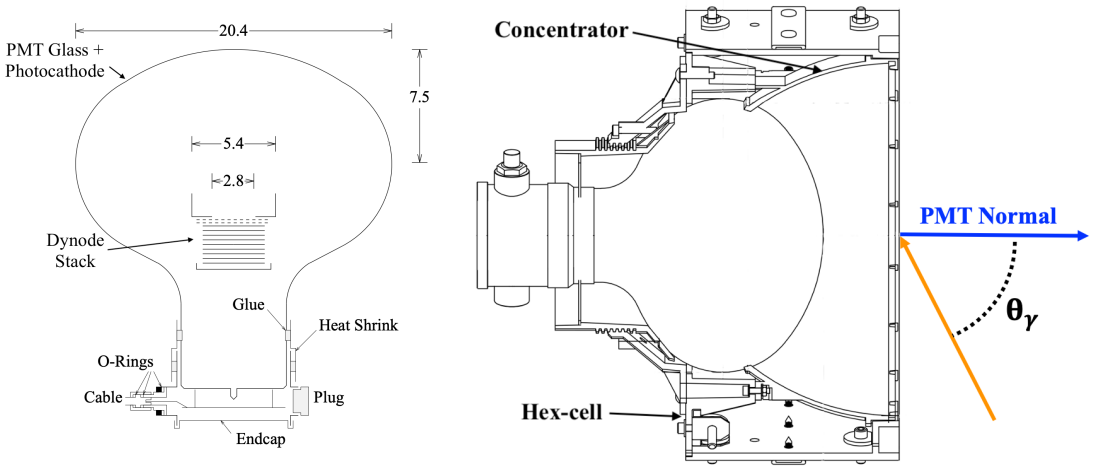

Figure 3.7: Schematics of a Hamamatsu R1408 PMT (left) and of the PMT-concentrator assembly (right). Figures modified from [142] and [150]. The incident angle θ_γ is the angle that the incident light (orange) makes with the assembly entrance, defined by a normal vector (blue).

The main structure of the PMT is a round glass containing a vacuum [142]. The inner surface of the PMT glass contains the photocathode, which is kept at ground potential. At the base of the PMT there is the anode, which is held at 1700 – 2100 V, creating a strong field inside the PMT. Photons striking the photocathode in a PMT produce photoelectrons (PEs), which are accelerated by the electric field and, subsequently, multiplied by collisions with a stack of 9 dynodes. The cascade of photoelectrons and secondary electrons generates a measurable charge signal when they are collected on the anode. Along with the charge, the timing information of the signal is also recorded by the electronics (see next Section), and these are the two observables used to reconstruct the physics events offline.

The most important characteristics of the PMTs are the noise rate, the efficiency and the transit time spread, which largely affect the energy and spatial resolutions. Even with no incident photons, the PMTs produce current at their base, known as dark current noise. In SNO+, real photoelectrons are distinguished from noise using the total charge at the base. Each PMT hit enters a discriminator which only fires if the pulse amplitude is higher than the threshold, set to around 0.25 of an average photoelectron charge. This value is determined from a single photoelectron (SPE) charge spectrum as the value where the signal is more likely to be caused

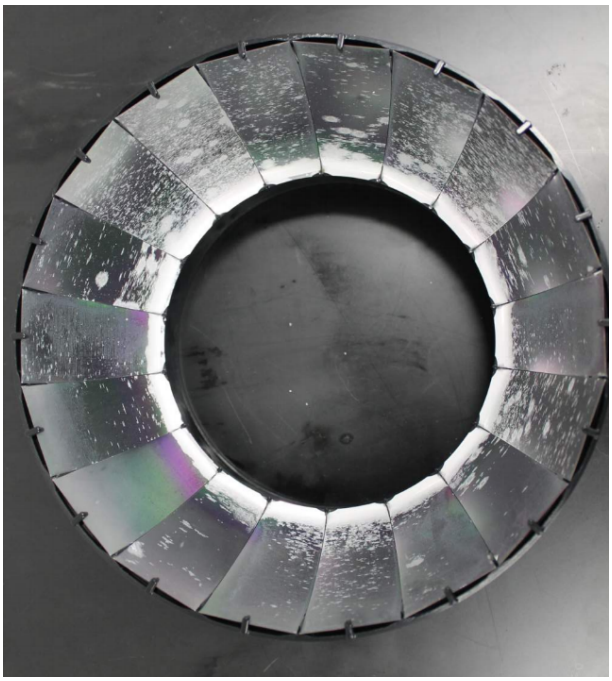

Figure 3.8: Degraded PMT concentrators [151]. The white spots are areas of degraded reflectivity.

by an incident photon rather than noise. As a result, about a quarter of genuine SPE signals are falsely identified as noise.

The PMT efficiency describes the probability of an incident photon of a given wavelength to produce a charge signal on the anode. The two contributions to the overall efficiency are the quantum and collection efficiencies. The first is the ratio of photoelectrons leaving the photocathode to incident photons, and the second is the fraction of photoelectrons magnified down the dynode stack.

Lastly, the transit time is defined as the time between a photon hitting the photocathode and the time the resulting current pulse reaches its maximum. Figure 3.9 shows a typical transit time distribution. The main prompt peak corresponds to the path described. The spread or width of this peak is largely determined by the electron optics within the PMT geometry. The sub-dominant early peak is the pre-pulsing, created by incident photons that pass through the photocathode and strike directly a dynode. The pre-pulsing signal occurs approximately 15 ns before the prompt peak, which corresponds to the transit time between the photocathode and first dynode. The two peaks later in time are formed by the late and double pulsing effects, which arise when secondary electrons escape the dynode stack towards the photocathode, creating photoelectrons.

3.6 Electronics and data acquisition system

The SNO+ trigger and readout electronics chain is responsible for recording PMT signals with nanosecond-level timing resolution and charge thresholds well below one photoelectron per channel. Much of this infrastructure was inherited from SNO, with several notable upgrades in order to deal with the higher light yield and event rates expected with liquid scintillator [133].

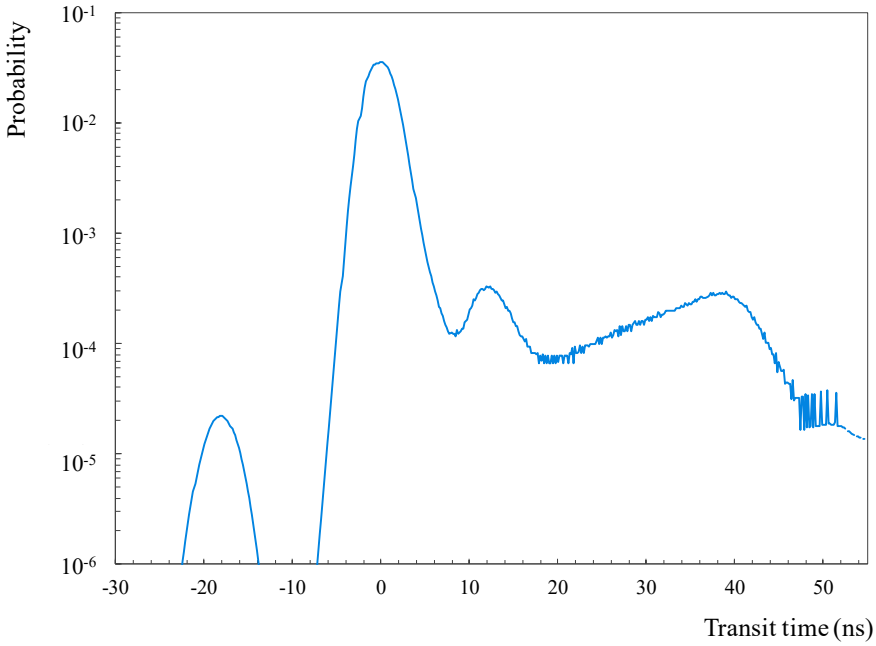

Figure 3.9: Transit time probability distribution for a R1408 PMT plotted using values saved in the SNO+ simulation software.

The electronics system consists of 19 crates each containing 16 front-end cards (FEC) and 16 PMT interface cards (PMTICs). On each FEC, four daughterboards (DBs) are attached. The DBs house custom integrated circuits for eight PMT channels that perform the important signal processing. Thus, each crate is responsible for the analogue processing and trigger generation for 512 PMT signals.

When a pulse is produced by a PMT, it travels through a waterproof coaxial cable connected to a PMTIC. The PMTICs are responsible for providing the high voltage (HV), and separate the PMT signal from the high voltage, sending it to the FEC. The FEC is responsible for signal processing and digitisation, and determines whether the signal crosses the channel discriminator threshold. A PMT is considered hit if the discriminator threshold is crossed, and the total number of PMT hits in a triggered event are referred to as the *nHit* of the event.

The FEC then calculates the time and charge recorded by the PMT – a single time value TAC (Time to Analog Converter), and three different charge values, found by integrating the pulse. The charges are given as QHL and QHS, which both use high gain with long and short integration times, respectively, and QLX, which uses a low gain and long integration time. The QHS can be considered as describing the size of the pulse that caused the PMT to trigger, while QHL takes into account the late and scattered light as well.

The triggered hit is then sent to analogue master trigger cards (MTCA), which are responsible for summing up the triggers of all PMTs within certain time windows. These signals are passed to the digital master trigger card (MTCD) which compares them to different trigger thresholds and determines if a global trigger (GT) of the detector should be issued. When a global trigger occurs, all the data from the PMTs is recorded from a period 180 ns before and 220 ns after the GT. This 400 ns period is called “event window”, as it typically contains

information about one interaction event inside the detector.

Each triggered event is identified by a global trigger ID (GTID), which is saved along with the corresponding PMT and trigger data to a custom raw *zdab* file by the data acquisition (DAQ) system. These files are indexed by runs, which are typically set to one hour for physics running. The runs themselves have important information associated with them, such as the run-number and the run-type (marking the type of running such as physics, calibration, etc.) and any common activity occurring during the run (such as recirculation, people on deck, etc.). This information is important for data quality evaluation – only runs with ideal detector conditions are used for the top-level physics analyses.

3.7 Modelling and reconstruction of events in SNO+

In order to achieve the proposed physics goals for the different phases of the experiment, SNO+ relies on a detailed model of the detector and of its response to the physics processes. The detector model is at the base of Monte Carlo simulations which are needed for predictions of efficiencies and signal expectations, as well as for constructing systematic uncertainties. Moreover, accurately relating the measured observables, the nHit and PMT hit times, to physical quantities, like energy, position and particle type, depends on the knowledge of the energy loss mechanisms in each detector medium, as well as the production, propagation and detection of the light produced as consequence, either Cherenkov or scintillation. Besides, it also depends on the characteristics of the electronics and DAQ systems.

The SNO+ Monte Carlo software package, RAT (Reactor Analysis Tool) has been designed to fully model the detector and its response to the physics events based on these parameters, most of which are determined and monitored using detailed calibrations, as will be discussed in the next Section. RAT is developed in the C++ and Python languages, and interfaces with GEANT4 [152] simulation libraries. RAT relies on a dynamic database, RATDB, containing information about the detector with adjustable parameters that can be easily tuned. RATDB contains both static tables, not expected to change as the detector runs, such as the PMT positions relative to the center of the detector, as well as tables that are uploaded every run with the detector-state information for that run. This is important both for the simulations and for the data processing. The simulations are stored in the same format as real data, using custom ROOT [153] files. In this way, simulated and real data can share the same reconstruction and analysis tools, also integrated in RAT. The reconstruction algorithms use the spatial and temporal distribution of the hit PMTs to estimate the most probable time, position, and energy of the events. Classification algorithms are used to classify events depending on some of their properties, like for example classifying an event as more α-like than β-like depending on the scintillator light timing distributions measured by the PMTs.

3.7.1 Simulation

Physics events are simulated using a series of generators. A generator decides how often a particular kind of event occurs, where it happens, and what kind of particles and energies

the event starts with. For instance, a vertex generator selects the initial particle types, number, momenta, and polarization; position generators select points within a volume for placing the initial particles, or place them at a specific position if desired; and a time generator controls the interval between events by attaching a suitable timestamp to each. Custom high-level generators that integrate all three steps have been implemented for specific physics processes and backgrounds, such as for radioactive decays, solar and reactor neutrinos, and for the simulation of calibration sources.

Once the initial event has been generated, it is passed to GEANT4, which simulates the propagation of the particles and their daughters through the detector media and components. RAT includes a detailed description of the detector components, including the position and orientation of the PMT support sphere and the PMTs, the position and thickness of the acrylic vessel including the support ropes, and the size and position of the acrylic vessel neck [154]. The processes modelled during the propagation include the production of optical photons via Cherenkov and scintillation processes, scattering, absorption, reemission from wavelength shifters, and reflection and refraction effects at the boundaries of the detector materials. The produced photons are tracked until they are lost to absorption, or until they reach a PMT.

The simulation has two distinct models for the PMTs and their surrounding concentrators (Figure 3.7): a detailed three dimensional model [154], and a simplified empirical model called the grey disc model. While the former models all the interactions of light with the PMT and concentrator geometry, the latter replaces the complex geometry with a flat disc at the front opening of the concentrator support structure. When a photon reaches the disc, instead of modelling all its interactions in the structure, the grey disc model assigns a reflection and absorption probability to the contact point, based on the incident angle and wavelength. The grey disc is the preferred PMT model in SNO+ because it speeds up the time of the simulation and its optical properties are calibrated directly from the optical calibration measurements.

If the photons are absorbed by a PMT, independently of the model used, a simulated pulse is produced with information of the PMT charge and timing. As a last step, the electronics and trigger system are simulated, determining if the simulated event would pass the global trigger. During this last step, it is possible to either use default settings for electronics and trigger thresholds, or to use the settings stored in RATDB for specific data runs. The second allows to simulate a given data-taking run, incorporating the run conditions as recorded by the detector itself. Since variations in the number of online PMTs and trigger thresholds have a non-negligible impact on the recorded data, using this *run-by-run* simulation method results in a more accurate comparison between the detector data and the simulations. Furthermore, the simulated data is stored in files that can go through the same reconstruction and analysis pipelines as the data files. The Monte Carlo files have much more information stored than the data files, such as the initial energy, direction and position of the simulated particles, either primary or secondary.

3.7.2 Reconstruction

The reconstruction algorithms are responsible for determining the energy, position and time of the events occurring inside the detector. The algorithms are adapted to each experimental phase, given that each active medium has different light production mechanisms with specific characteristics (like direction information from Cherenkov light).

Typically, the first reconstructed quantities are the initial time and position of the events, which are based on the timing information of the triggered PMTs and their positions. The true event time determines a global offset on the hit times, whereas the event position determines the shape of the hit time distribution. For example, events at the detector centre produce photons that all arrive at approximately the same time to the PMTs, but events near the AV create photons with a range of arrival times: the PMTs closest to the event are hit first and those on the far side of the detector hit last.

The position reconstruction algorithms treat photons as being created at a point at a single instant, and then calculate the arrival times using straight-path trajectories from the point source to the hit PMTs. A log likelihood is then calculated through the comparison of the measured hit times to a probability density function (PDF) determined from Monte Carlo. The algorithm finds the event position and time which maximizes the likelihood. The more photons are produced, the more PMTs can be used for reconstruction, making the accuracy of the position reconstruction energy dependent. For water phase data, this step is followed by the reconstruction of the direction of the event based on the angular distribution of the hit PMTs relative to the reconstructed initial position.

The energy reconstruction is based on the number of triggered PMTs, the nHit. This number is expected to approximately scale with the energy of an event. However, this is complicated by various detector effects. For example, photons may be attenuated, scattered, or reflected, and in scintillator may be absorbed and re-emitted. These effects not only decrease the amount of light reaching the PMTs, hence affecting the detected nHit/MeV, but also lead to position variations of the nHit for the same event energy. The reconstruction algorithms must therefore take these factors into account in order to best estimate the energy of the events.

Once the above quantities are reconstructed, event classification algorithms are applied in order to distinguish between the various event types using the differences in their timing profile, topology, or coincidence with other events. This additional information is advantageous to maximize background rejection in the different analyses of SNO+. The accuracy of the reconstruction algorithms depends on the knowledge and modelling of the detector. Hence, changes to the detector model parameters require generating new PDFs for the different fitters – this process is called *recoordination*.

3.8 Detector calibration

SNO+ has an extensive *in situ* calibration program aimed at measuring the detector model parameters, as well as evaluating the performance and systematics uncertainties of the reconstruction algorithms. The main detector parameters to be determined *in situ* are:

- the individual PMT time delays and gains. The time recorded by each PMT has an offset due to the length of the cable connecting the PMT to the DAQ systems. Additionally, smaller amplitude pulses take longer to cross the PMT discriminator thresholds than larger pulses. This *time walk effect* must also be measured and taken into account during the hit time calculation. The purpose of the gain calibration is to characterize the single photo-electron charge spectrum. This will allow a charge for that PMT to be converted into units proportional to the number of photoelectrons. Also, because of the fixed discriminator level, the gain calibration is important for estimating the effect of changing the discriminator threshold on the relative photo-tube efficiency and therefore on the energy scale of the detector.

- the PMT efficiencies, described in Section 3.5.

- the angular response of the PMTs and their concentrators, which describes the probability of a photon creating a hit depending on its incidence angle when entering the PMT and concentrator assembly.

- the reflectivities of the various materials in the detector, particularly of the PMT concentrators. The reflectivity of the concentrators determines the effective photocathode coverage of the detector. Furthermore, the differences in refractive indices between scintillator, acrylic and water causes reflection and refraction effects at the media boundaries. These need to be taken into account when calculating the time-of-flight of photons from their origin to the PMT.

- the scattering and absorption lengths of the medium inside the AV, the external water and the acrylic itself. These are needed to model the propagation of light inside the detector.

- the light yield of the liquid scintillator, crucial to determine the energy scale of the detector.

- the scintillator emission time constants, important for position reconstruction as well as particle identification.

Even though some of these quantities can be determined *ex situ*, the *in situ* calibrations are crucial to monitor variations over time and determine the set of parameters that best describe the detector at a given moment. For example, the PMT angular response and the concentrator reflectivity was measured before installation [155], but their immersion in ultra-pure water for several years in SNO and SNO+ led to degradation of the PMT response. For this reason, *in situ* calibrations are needed to determine the most up-to-date PMT response parameters. Similarly, frequent *in situ* measurements of the scintillator light yield and optical properties are needed to verify its stability over the multiple years planned for data-taking.

The detector is calibrated using optical and radioactive sources temporarily deployed inside the AV and in the external water volume between the AV and PMTs. Additionally, a calibration system of optical fibers is permanently mounted on the PSUP. The calibration sources used in SNO+, as well as the deployment hardware, are briefly presented below.

3.8.1 Radioactive sources

Deployed radioactive sources are used to introduce known particles, with known energies, into the detector, in order to calibrate the energy scale and determine the systematic uncertainties associated with the reconstructed quantities. The radioactive sources considered for the SNO+ experiment are listed in Table 3.1, covering the energy range from 0.1 to ∼10 MeV. This energy range covers the expected energy threshold for most planned physics topics.

Table 3.1: List of radioactive sources to be deployed in the SNO+ detector, the particles and energies emitted. In the case of the AmBe source, the energies inside brackets correspond to γ de-excitations of nuclei following neutron capture.

Source	Particle	Energy (MeV)	Type	Goal
AmBe	n, γ	4.4 [2.2, 7.6, 9.0]	Tagged	Neutron capture response
^{16}N	γ	6.1	Tagged	Energy reconstruction
^{46}Sc	γ	0.9, 1.1	Tagged	Energy reconstruction
^{48}Sc	γ	1.0, 1.2, 1.3	Untagged	Energy reconstruction
^{57}Co	γ	0.122	Untagged	Energy reconstruction
^{137}Cs	γ	0.7	Untagged	Energy reconstruction

In addition to the deployed radioactive sources, internal radioactivity in the scintillator can be used to provide additional energy calibration points and, most importantly, to continuously monitor energy scale and resolution variations in time. Typical calibration references are ^{210}Po-alpha, ^{14}C-beta, delayed ^{214}Bi-Po (^{238}U chain) and ^{212}Bi-Po (^{232}Th chain) coincidences and muon followers.

3.8.1.1 The ^{16}N tagged gamma source

During the water phase, the main energy calibration source used was the ^{16}N gamma-ray source, inherited from SNO [156, 142]. This calibration source was used to determine the energy scale and the reconstruction systematics, and to validate the optical calibration measurements reported in Chapter 4. ^{16}N nuclei ($T_{1/2}$ = 7.13 s, Q-value = 10.42 MeV) are produced in a shielded pit near the detector cavity by bombarding ^{16}O, in gaseous CO_2, with 14 MeV neutrons from a Deuterium-Tritium (DT) generator. The activated gas is then transported into a decay chamber deployed in the SNO+ water volume. There, the ^{16}N beta-decays to ^{16}O* (B.R. 66.2%), which de-excites emitting a 6.1 MeV gamma. There are two other decay branches: one that produces 7.1 MeV gamma-rays in coincidence with the beta (6%), and a direct branch to the ground state (28%), resulting in a 10.4 MeV endpoint beta-particle.

The decay chamber was designed to contain the energetic beta-particles. They interact with plastic scintillator lining the walls of the chamber volume, creating optical scintillation photons that are measured by a PMT within the source, providing a tag to select ^{16}N events. The gamma-rays are able to exit the chamber and interact via Compton scattering in the detector medium to produce high energy electrons, which in turn produce Cherenkov photons that are observed and result in a broad (3–7 MeV) reconstructed spectrum.

3.8.2 Optical sources

Two optical calibration systems, shown in Figure 3.10 are used to measure *in situ* the absorption and scattering of the media, as well as the PMTs' charge, timing, angular response and efficiencies: a light diffusing sphere (laserball) and a fixed fibre based light injection system (ELLIE). These systems can trigger the detector asynchronously, making it possible to measure accurately the PMT timing delays.

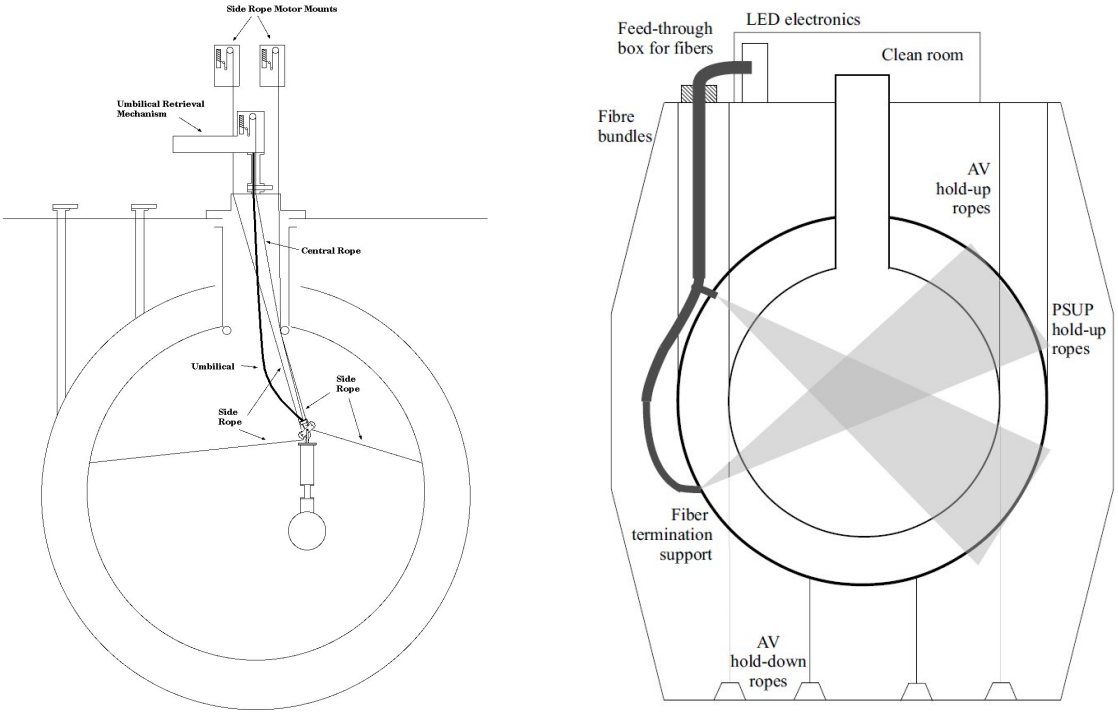

Figure 3.10: Cross sectional diagrams of the SNO+ detector. (a) shows the deployment of the laserball inside the acrylic vessel [157], and (b) shows the fibre system fixed on the PMT geodesic structure [158].

3.8.2.1 ELLIE system

The Embedded LED/Laser Light Injection system was design to allow frequent calibrations with no risk of radioactivity contamination, given the stringent radiopurity requirements during the scintillator and Te-loaded phases [133]. This calibration system consists of optical fibres permanently installed at several positions in the PSUP, hence allowing detector calibrations without compromising the scintillator volume. The fibres inject LED or laser light across the detector at different angles, providing coverage of light to all the PMTs.

ELLIE consists of three subsystems: the Timing system (TELLIE) for PMT hit-time and gain calibration, the Attenuation Module (AMELLIE) for monitoring relative changes in attenuation lengths of materials in the detector, and the Scattering Module (SMELLIE) for measuring the optical scattering cross sections of these materials as functions of scattering angle and photon wavelength.

ELLIE calibration campaigns do not require any instrumentation to be moved into the detector, hence minimizing detector downtime. In addition, this easy operation allows ELLIE to

take data frequently, crucial to monitor the stability of the measured variables over time.

3.8.2.2 Laserball

The laserball is a light diffusing sphere which is used to measure the attenuations of the detector media and the angular response of the PMTs and concentrators. The water phase optical calibration used a laserball inherited from SNO [157], and the analysis of its data is at the core of Chapter 4. For the scintillator phase, a new laserball has been built to ensure scintillator compatibility, using materials with low background emanation rates [133].

The laserball consists of an $\sim$11 cm diameter spherical quartz flask filled with small air-filled glass beads (50 μm in diameter) suspended in silicone gel. The beads diffuse light injected into the flask through a fiber guide. The light comes from a nitrogen pumped dye laser system, located in the deck clean room (DCR) above the detector. In addition to the primary wavelength of the laser (337.1 nm), during the water phase five selected dyes provided additional wavelength ranges centered at 365 (PBD), 385 (BBQ), 420 (BIS-MSB), 450 (Coumarin-450) and 500 nm (Coumarin-500). Figure 3.11 shows the stimulated emission spectra of each of the dyes, measured directly from the calibration laser system with an Ocean Optics USB 2000+ UV-VIS Spectrometer. For the scintillator phase, a different selection of dyes may be considered, in order to accommodate the scintillation light wavelength profile.

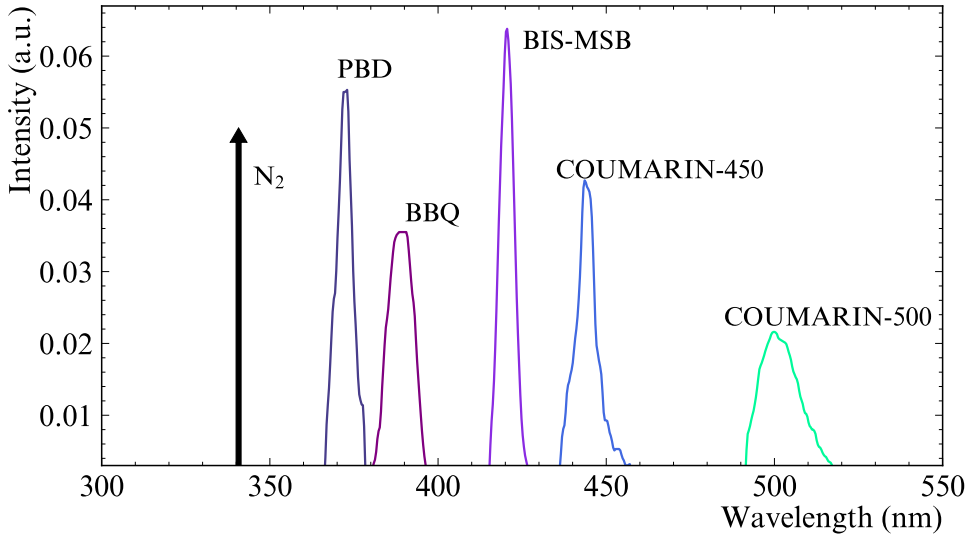

Figure 3.11: Wavelength spectra of the N_2 laser and of the dyes used during the SNO+ water phase.

A photodiode close to the laser produces a timing signal that triggers the data acquisition system. The laser beam intensity is controlled by the use of two successive sets of neutral density filters mounted in rotating supports. The light then passes through about 30 m of optical fiber to the laserball. Although the laserball was designed to be an isotropic light source, the mounting hardware on top of the flask partially shadows the light going upwards, reducing the intensity of the light traveling in this direction by about 50%. This anisotropy is expected to be reduced with the design of the new scintillator phase laserball. As will be discussed in Section 4.1, the overall anisotropy of the laserball is important to consider when interpreting laserball data, and it is part of the information extracted from the optical calibration analysis.

When deployed internally, the laserball is attached to a pair of side ropes which physically constrain it to have one of four possible azimuthal orientations (north, south, east and west). The orientations are relative to the fixed detector coordinate system, and the relations between the two coordinate systems are illustrated in Figure 3.12. When outside of the AV, the laserball orientation is not constrained and has to be determined afterwards, as will be discussed in Section 4.1.3.

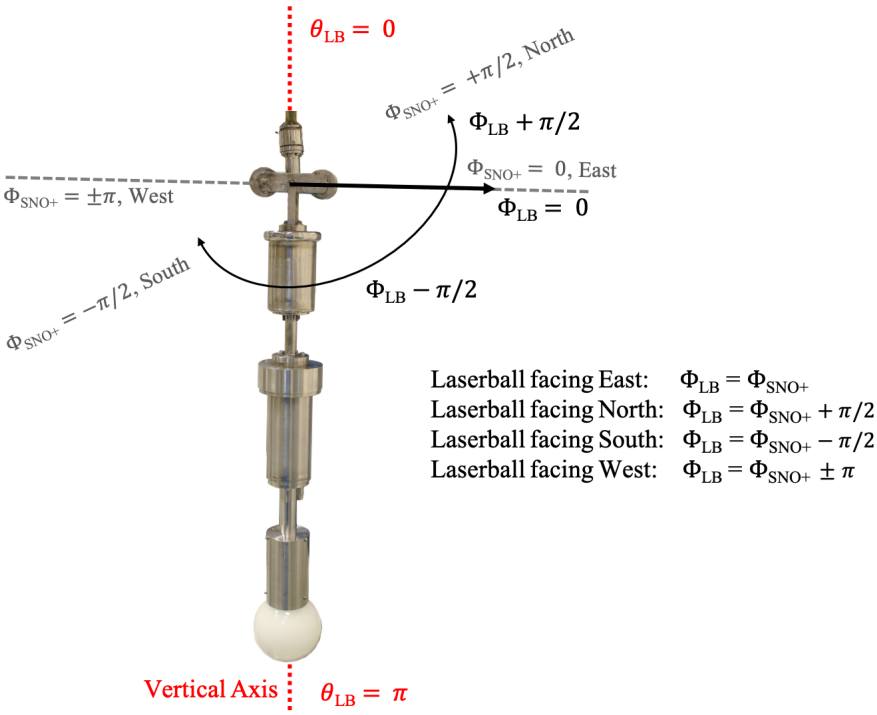

Figure 3.12: Schematic of the laserball coordinate system $(\cos\theta_{LB}, \Phi_{LB})$, defined by the direction of a reference mark in the laserball hardware, represented by the black arrow. When the laserball rotates, its coordinate system changes relative to the fixed SNO+ detector coordinate system $(\cos\theta_{SNO+}, \Phi_{SNO+})$. Since the laserball does not rotate along θ, $\cos\theta_{SNO+}$ is equivalent to $\cos\theta_{LB}$. The laserball coordinate system coincides with the detector coordinate system when Φ_{LB} points towards East.

3.8.3 Source deployment hardware

The calibration sources are deployed inside the detector using a manipulator system, illustrated in Figure 3.13, and described in detail in [133]. The sources are connected to a multi-purpose umbilical cable, containing optical fibers (for light transmission), thin coaxial gas tubing and four hook-up cables. The umbilical allows to transmit power, light pulses and other signals to the sources from instrumentation on the DCR. The source is also attached to a central rope, which supports the source weight in order to avoid a mechanical load on the umbilical.

An umbilical retrieval mechanism (URM), shown in Figure 3.14, drives the motion of the deployed sources along the central vertical axis of the detector. It is comprised of an umbilical storage system, an umbilical drive system, and a rope drive mechanism, all of which are contained within a large box and connected to the detector by a single lower opening. The water phase calibration made use of the URM inherited from the SNO experiment. However, due to

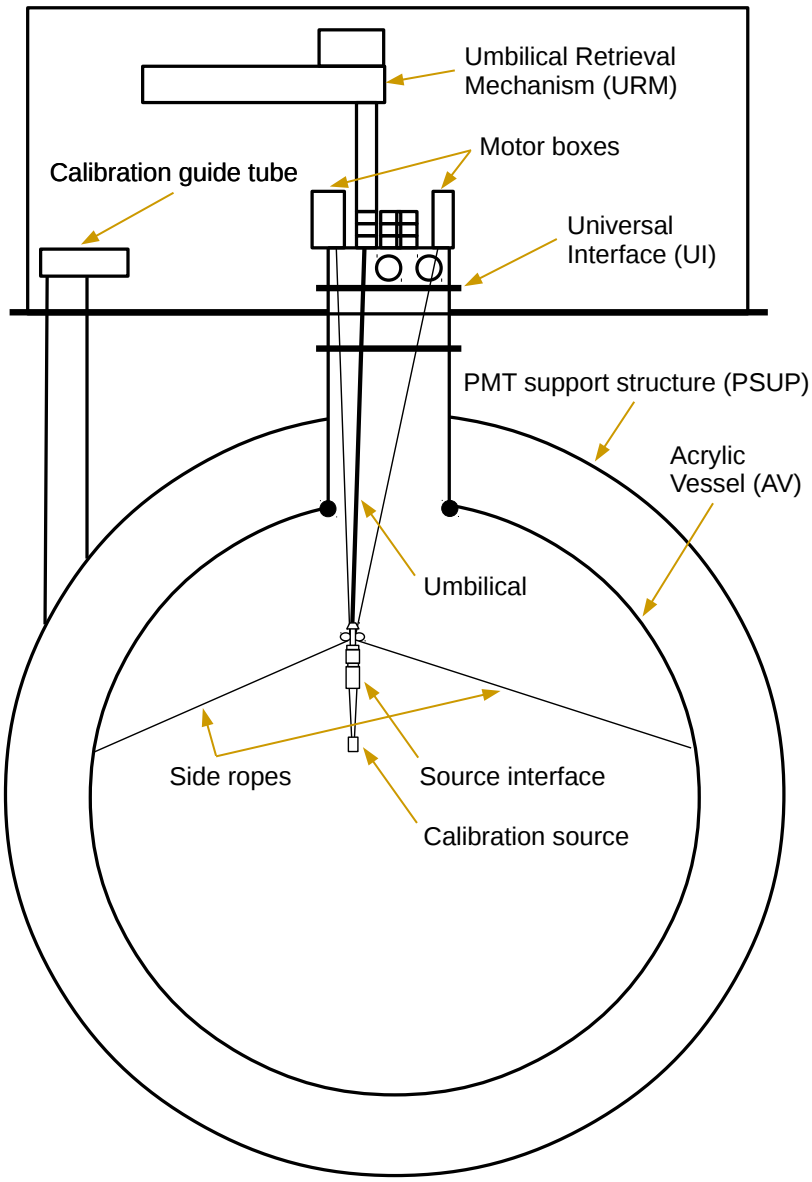

Figure 3.13: Overview of the Source Manipulator System (not to scale) showing the main components. Only one set of side ropes is shown, as the other set of ropes is in the plane orthogonal to the cross section shown here. Note that the central rope securing the source is not shown separately; it follows the same path as the umbilical. Figure from [133].

the stringent compatibility and radiopurity requirements for the scintillator phase, a new URM was designed and built by LIP at its workshop based in Coimbra. The internal parts of the URM, which are going to be in contact with the umbilical, are made of materials compatible with LAB and with a low radon emanation, and the design of the umbilical drive mechanism was updated to deal with the higher slippage of the umbilical when it is drenched in LAB. Moreover, the full structure is sealed to the exterior in order to avoid radon entering the URM and, by consequence, the detector during calibration campaigns.

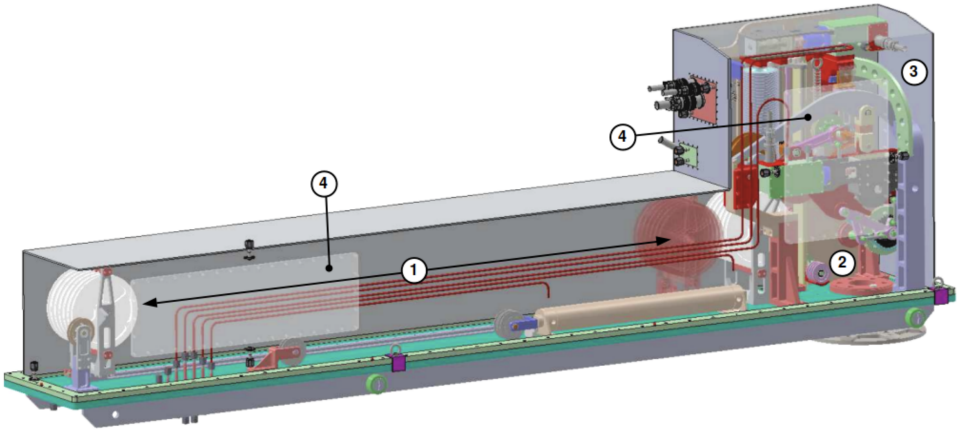

Figure 3.14: Schematic of the Umbilical Retrieval Mechanism (URM), showing (1) the umbilical storage system, (2) its drive system, (3) the rope mechanism, and (4) the acrylic viewing ports. Figure from [133].

A big fraction of a 3 month stay at SNOLAB on the scope of this PhD project was dedicated to planning and executing the transport of the scintillator URM to the underground laboratory. The URM was installed in a surface clean laboratory, where it underwent several performance tests for two years. To transport it underground, it was necessary to ensure 1) the safety of the delicate parts of the umbilical and rope drive mechanism; 2) that the URM box (and internal parts) could safely deal with the 25% pressure change between the surface and the underground level; 3) and that mine air did not get inside the system to compromise its cleanliness levels. The final transport plan included detaching the modular internal parts of the URM from the box, shipping each module inside three heat-sealed bags with enough volume to deal with the pressure change and avoid mine air contamination (Figure 3.15). The same applied to the URM box base and cover. At the time of writing, the scintillator URM is fully assembled and under final commissioning inside the DCR on top of the detector.

When the sources are deployed inside the AV, via the acrylic neck, they can be moved off-axis within two vertical perpendicular planes using a system of high-purity side-ropes. The sources can also be deployed in the region between the AV and PSUP using one of six calibration guide tubes which intersect the PSUP. In this case, the sources and umbilical are guided by the central rope alone, hence can only be moved up and down along the guide tube vertical axis. The external water region has less stringent requirements on bulk radioactivity compared to the AV. Therefore, the manipulator system can be used for deployment of sources in this volume during all phases of the experiment. This was one of the calibration strategies used to monitor the scintillator light yield during filling and during the initial part of the full scintillator phase, keeping the AV sealed and the scintillator undisturbed.

Figure 3.15: Disassembled URM in the SNOLAB surface clean room: 1) URM base plate and drive systems, 2) cover, 3) internal parts stored in triple heat-sealed bags for transport.

3.9 Physics results from the water and scintillator phases

3.9.1 Water phase results

The SNO+ water phase was dedicated to measuring the external background sources, testing the data acquisition systems and detector performance. The detector was calibrated using both optical and radioactive sources, which were deployed in many positions inside and outside the AV. The absolute energy scale and position resolution were determined using the tagged ^{16}N gamma source (Section 3.8.1), yielding a 10 cm position resolution and a 1% uncertainty for the energy scale. The laserball was used to measure water attenuation coefficients, effective attenuation coefficients for the AV, and the angular response of the PMTs, across different wavelengths. These measurements are going to be discussed thoroughly in Chapter 4. The AmBe calibration source, which emits 4.4-MeV γs for $\sim$60% of emitted neutrons, was used to determine the unprecedentedly high neutron detection efficiency of $\sim$50% [159], the highest achieved among pure water Cherenkov detectors. Furthermore, it was used to measure the neutron-proton capture cross-section, yielding $336.3^{+1.2}_{-1.5}$ mb.

Additionally, throughout the water phase there were extensive measurements of the backgrounds coming from the detector materials, the *external backgrounds*, which are going to be discussed in Chapter 5. These measurements took advantage of the simpler detector configuration (same medium inside and outside the AV) and the directionality information from Cherenkov light, which allowed to distinguish these background from the radioactivity within the internal water.

The water phase produced two main physics datasets with 115 and 190 live days, the first collected between May and December 2017, and the second from October 2018 to July 2019. The main differences between the two are the radon levels within the AV. During the first part of this phase, corresponding to the first dataset, the background levels inside the AV were at the level of O(10^{-14}) gU/gH_2O. Between the two datasets, a new cover gas system was installed on top of the AV neck for further background suppression. It helped decrease the radon levels in the AV water to O(10^{-15}) gU/gH_2O. Thus, the second dataset has much lower backgrounds than the first.

The main physics analyses carried out during the water phase were the search for invisible nucleon decay, and a measurement of the ^{8}B solar neutrino flux. The invisible nucleon decay is an hypothetical beyond-the-standard-model process where a nucleon can decay into neutrinos or other particles that leave the detector without any direct energy deposition, leaving the daughter nucleus in an excited state. SNO+ searched for nucleon decay in oxygen atoms of the water, with the reactions for neutron decay:

$$\begin{aligned} {}^{16}\mathrm{O} &\rightarrow {}^{15}\mathrm{O}^{*} + \text{inv.}, \\ {}^{15}\mathrm{O}^{*} &\rightarrow {}^{15}\mathrm{O} + \gamma, \end{aligned} \tag{3.7}$$

and proton decay:

$$\begin{aligned} {}^{16}\mathrm{O} &\rightarrow {}^{15}\mathrm{N}^{*} + \text{inv.}, \\ {}^{15}\mathrm{N}^{*} &\rightarrow {}^{15}\mathrm{N} + \gamma. \end{aligned} \tag{3.8}$$

After conducting an initial search with the first water phase dataset [141], SNO+ has now analysed a total of 274.7 days of data-taking to search for five selected modes of invisible nucleon decay (n, p, nn, pp, np) [160]. The results are consistent with no observation of invisible nucleon decay for all the studied decay modes, and represent an improvement on previous limits for all but the nn decay mode. SNO+ set the world's best livetime limits of $>9.6\times10^{29}$ years for invisible proton decay and of $>9.0\times10^{29}$ years for invisible neutron decay. Additionally, the limits for dinucleon decay were set at $>6.0\times10^{28}$ years for pn and $>1.1\times10^{29}$ years for pp decay, an improvement to the limits set with the first SNO+ search [141], and to previous limits from the Borexino counting test facility [161] and radiochemical experiments [162].

With the first physics dataset, the flux of ^{8}B solar neutrinos was measured down to 5 MeV [163]. The measured flux was $2.53^{+0.31}_{-0.28}(\text{stat.})^{+0.13}_{-0.10}(\text{syst.}) \times 10^{6}$ cm^{-2}s^{-1}, consistent with measurements by other experiments [164, 165]. This analysis has been updated including the second dataset with much lower backgrounds, and with an improved detector model, including the finalized optical calibration which is going to be presented in Chapter 4. The ^{8}B solar neutrinos were measured above 5 MeV with significantly lower backgrounds, as shown in Figure 3.16 (left). Furthermore, the excellent radio-purity of the second dataset made it possible to lower the measurement's energy threshold to 3.5 MeV (Figure 3.16 (right)). At the time of writing, a publication with these results is being prepared.

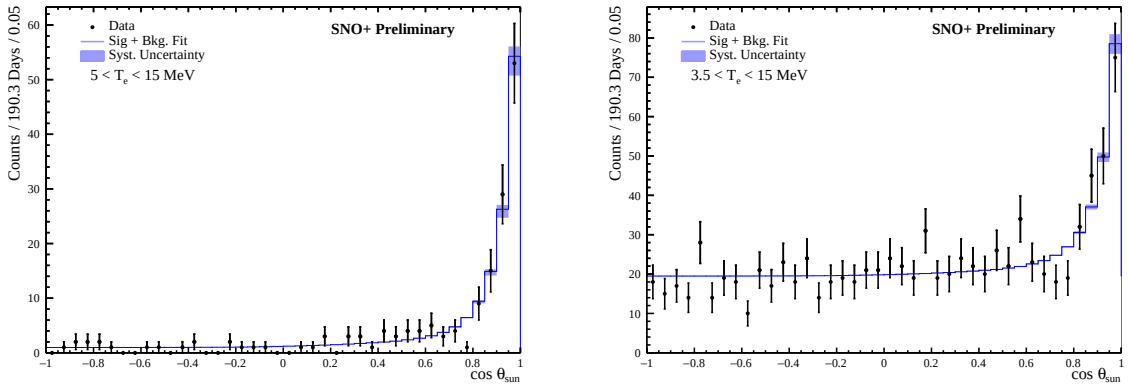

Figure 3.16: Distribution of event directions with respect to solar direction for events with energy in the range 5.0–15.0 MeV (left) and 3.5–15 MeV (right). Results of the analysis of the second dataset from the SNO+ water phase. Figures from [166]. Publication in preparation.

Lastly, the water phase data was also used to observe reactor antineutrinos. Two independent analyses were developed to suppress the dominant random coincidence background by four orders of magnitude. This background is estimated from data, along with those from (α,n) reactions and atmospheric neutrinos. Both analyses identify a small but significant number of electron antineutrino candidates, compatible with the fluxes expected from the surrounding nuclear reactors located at more than 250 km away from the experiment. These results have

been published in [167].

3.9.2 Partial fill and scintillator phase results

The partial fill period constituted an unexpected experimental phase with stable detector conditions, over which the first scintillator physics analyses were carried out, such as the ones reported in Chapters 5 and 6. The data taken during the partial fill period was used to measure the scintillator properties, such as its light yield with a PPO concentration of 0.6 g/L, as well as its variation with time after the fill was paused, while the PPO was mixing in the LAB. The preliminary measurements of the light yield, made using ^{214}Bi-^{214}Po coincidences, were crucial to start characterizing the backgrounds present in the scintillator and exploring analysis topics.

A significant effort was put into optimizing the background analyses for the half-filled detector, in order to measure accurately the rates of the different backgrounds, and their rejection techniques, such as the pulse shape discrimination algorithms. The backgrounds during the partial fill period are going to be discussed in detail in Chapter 5. The low PPO concentration provided a unique opportunity to explore Cherenkov and scintillation light separation on a event-by-event basis, in order to try to retrieve directionality information to distinguish a physics signal of interest (for example, solar neutrinos) from background. Figure 3.17 shows the first demonstration of event-by-event directional reconstruction using the low PPO concentration partial fill data, for ^{8}B solar neutrino candidate events with more than ∼5 MeV.

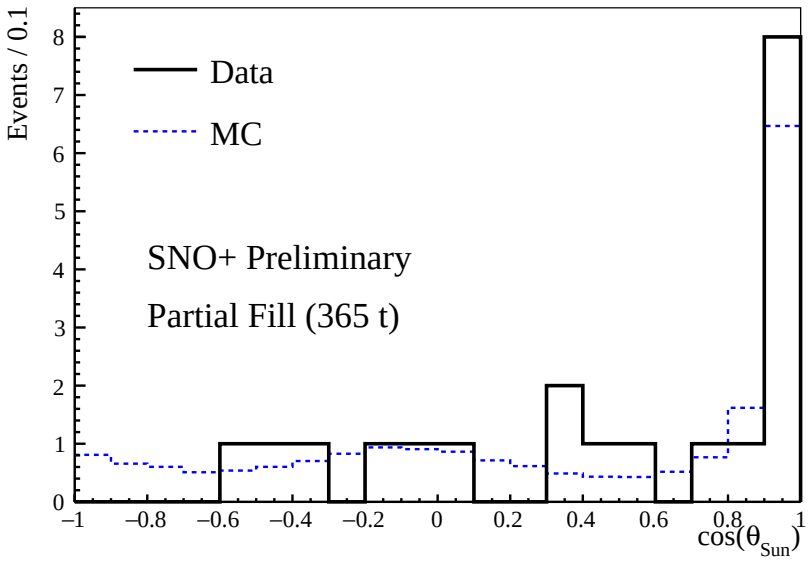

Figure 3.17: Distribution of event directions with respect to the solar direction. Results from the analysis of the partial fill data, for 20 events with a nHit larger than 1500 (∼ 5 MeV) within a spherical volume with R = 5.5 m capped at Z = 1 m to avoid the water-scintillator interface. The low 0.6 g/L PPO concentration allowed to retrieve event-by-event directionality information from the timing separation between Cherenkov and scintillation light. Figure from [168].

The event reconstruction algorithms were improved and adapted to the half-scintillator, half-water detector configuration. The main challenges for this period came from the impossibility of deploying calibration sources inside the scintillator volume, in order to keep it undisturbed.

Hence, energy and particle timing calibrations, important for an accurate Monte Carlo detector model and reconstruction algorithms, had to be performed using backgrounds, such as the ^{214}Bi-^{214}Po coincidences. After developing an as detailed as possible model for the detector during this period, a counting *target-out* $0\nu\beta\beta$ analysis was performed to validate the background and detector models and the analysis techniques. The results are presented in Chapter 5.

The background model of the scintillator continues to be evaluated and monitored using the fully-filled detector data. The primary goals are to verify the purity of the scintillator inside the detector and to check that the background levels are suitable for loading the tellurium and conducting the $0\nu\beta\beta$ decay search during the next experimental phase. Additionally, these measurements are vital for all the other current and future SNO+ analyses. Now that the scintillator fill and PPO top-up activities have been concluded, the scintillator properties, such as the light yield and the optical scattering and attenuation, will be measured both using calibration sources and tagged internal backgrounds. These measurements are required for an accurate description of the detector response in this phase.

The main analyses being carried out using the full fill scintillator data concern solar neutrinos and reactor/geo antineutrinos. Chapter 6 reports the results of a ^{8}B solar neutrino analysis using the partial fill data. At the time of writing, several other solar neutrino analyses using the full fill data are on-going. The partial fill data allowed the first detection of reactor antineutrinos in liquid scintillator at SNO+. Using 130 days of data, 45 inverse beta decay events were observed against a prediction of 44.9 (signal+background). Projections of the sensitivity to Δm^2_{21} with increased livetime for the full scintillator phase are shown in Figure 3.18. The strength of this analysis comes from the use of a time-based event classification to identify ^{13}C(α,n)^{16}O events, the primary background in this oscillation analysis. Similarly to the solar analyses, the antineutrino analyses are being continued using the new data taken with the full filled detector.

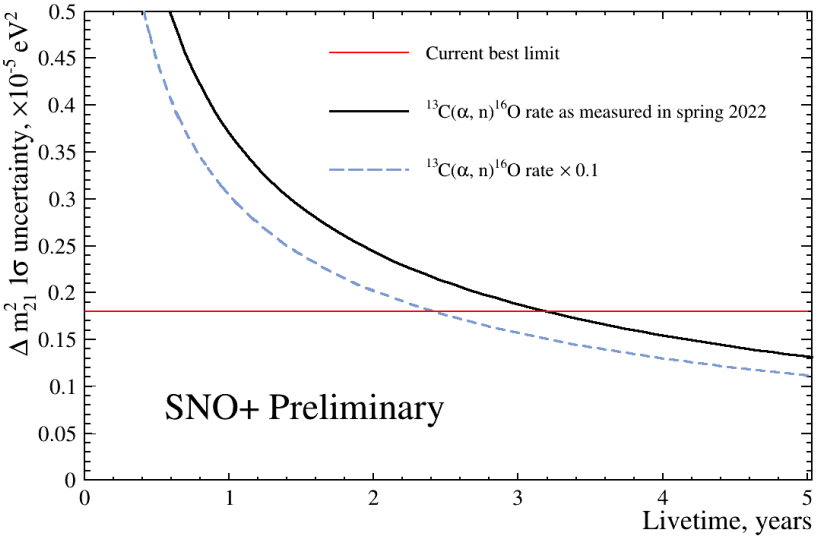

Figure 3.18: Expected sensitivity to Δm^2_{21} as a function of livetime. Figure from [169].

3.10 Prospects for the Te-loaded phase

The primary focus of the Te-loaded phase is going to be the search for $0\nu\beta\beta$ decay of ^{130}Te. Figure 3.19 shows a hypothetical $0\nu\beta\beta$ decay signal, together with the estimated background spectrum, for a five-year livetime. The $0\nu\beta\beta$ signal shown is for a $m_{\beta\beta}$ of 100 meV, using the IBM-2 model for the NME calculation. The expected sensitivity for the half-life at 90% C.L. after 5 years is 2.1×10^{26} years, corresponding to a $m_{\beta\beta}$ range of 37 to 89 meV, depending on the value of the NME.

The relatively high Q-value of the ^{130}Te means that contaminations from low energy backgrounds are reduced. However, it still coincides with several backgrounds that must be carefully characterized. Figure 3.20 shows the background contribution for a region-of-interest (ROI) between 2.42 to 2.56 MeV and a fiducial volume of 3.3 m.

The choice of using an asymmetric ROI between -0.5σ and 1.5σ around $Q_{\beta\beta}$ was made in order to reduce the contamination from the $2\nu\beta\beta$ background. The expected dominant background is ^{8}B solar neutrino elastic scattering events. Other background contributions come from naturally occurring radioactivity in the detector components: the bismuth, polonium and thallium isotopes from the ^{238}U and ^{232}Th radioactive chains, and several by-products of cosmogenic tellurium activation, such as ^{60}Co and ^{110}Ag [145]. They can be disentangled and described quantitatively by carefully analysing the shape of the measured spectrum and constructing a detailed background model, including both physics processes and instrumental effects. Events due to external backgrounds, such as 2.6 MeV gamma-rays from ^{208}Tl decays in the AV, water and PMTs, are reduced by applying a fiducial volume cut. These backgrounds are going to be discussed in more detail in Chapter 5.

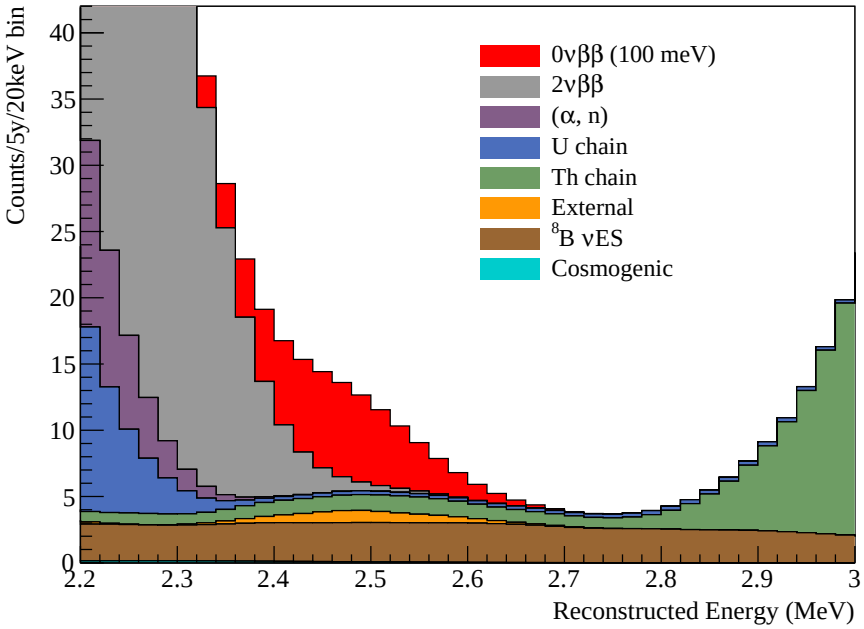

Figure 3.19: The expected reconstructed energy distribution for the backgrounds and a hypothetical $0\nu\beta\beta$ signal where $m_{\beta\beta}$ = 100 meV. The FV used is 3.3 m. An asymmetric ROI of -0.5σ to 1.5σ around the mean of the signal is chosen to avoid the $2\nu\beta\beta$ tail.

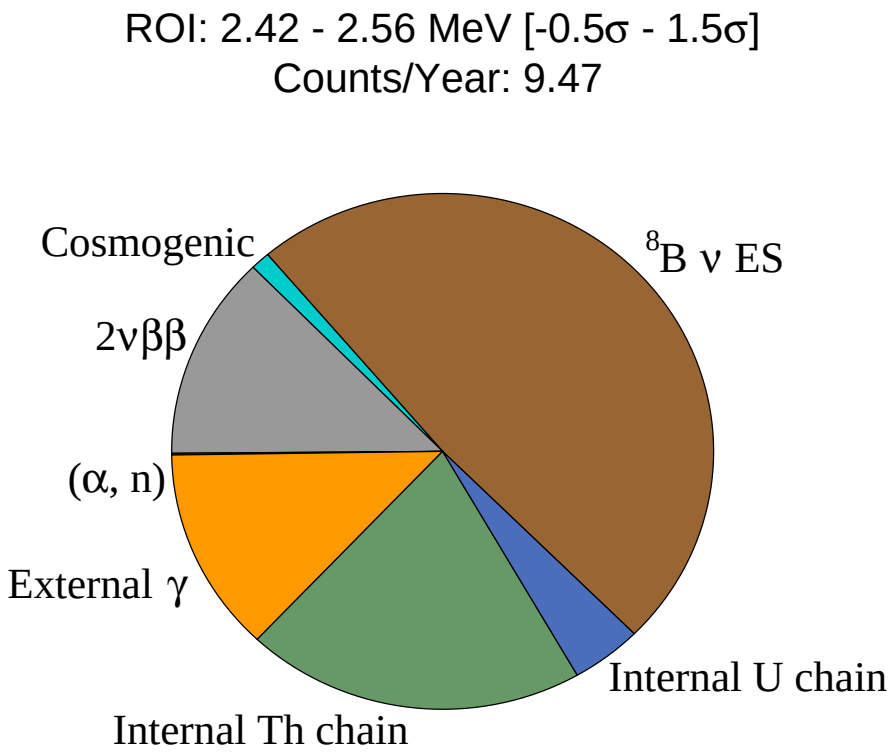

Figure 3.20: The number of background counts per year expected for the SNO+ detector in the energy ROI from 2.42 to 2.56 MeV and a FV of 3.3 m. The backgrounds are dominated by ^{8}B solar neutrino interactions. There are also significant contributions from external γ-rays, internal Thorium chain, and $2\nu\beta\beta$ leakage into the ROI.

One of the main advantages of the SNO+ technique is the possibility of moving towards higher sensitivities by increasing the tellurium loading. R&D efforts have demonstrated that the loading could be increased up to 3% by weight while maintaining a good light yield and stability. Scaling the isotope mass would allow to gain sensitivity to half-lives greater than 10^{27} years, covering the majority of the inverted neutrino mass ordering phase space.

Chapter 4

Optical calibration of SNO+ in the water phase

In all phases of the SNO+ experiment, both physics events of interest and undesired background events within the detector will create light. As it propagates, the light will be subject to optical processes such as refraction, reflection, absorption, and a variety of wavelength-dependent scattering interactions. These effects are governed by the properties of the materials in the detector: the water or scintillator inside the AV, the acrylic of the AV itself and the water outside the AV. Additionally, the sensitivity of the detector to light from different positions throughout its volume depends on the combined efficiency of the PMTs and their surrounding light concentrators as a function of wavelengths and incident angle.

Due to the aforementioned optical effects, an event near the inner surface of the AV produces a significantly different number of PMT hits than a similar event near the center of the AV. If not accounted for, this introduces a position dependence in the reconstructed energies of the events. An *in situ* measurement of the optical properties of the SNO+ detector is therefore essential for a realistic model describing the propagation and detection of light from all sources and to minimize the uncertainty of the absolute energy scale and the reconstructed positions.

The optical calibration during the water phase was fundamental to establish the knowledge of the optical properties of the detector and evaluating how the concentrators around the PMTs have changed since the transition from SNO to SNO+. Having water both inside and outside the AV also provided a unique opportunity to accurately measure the properties of the external water and acrylic, before the transition to using scintillator as the target medium. These optical properties were measured across a range of wavelengths using the laserball, deployed in several positions inside and outside the AV. The measurements were used to calibrate the detector simulation model, which was then validated by comparing simulations with data from the ^{16}N gamma source. The analysis and results have been published in [150].

This Chapter discusses the optical calibration of the SNO+ detector in the water phase. Section 4.1 describes the optical calibration analysis method, and Section 4.2 presents the multi-parameter optical calibration fit (OCA), the systematic uncertainties, and the analysis cross-check tools. Sections 4.3–4.4 describe the water phase calibration campaigns and report the measurements performed. Finally, Sections 4.5–4.6 describes the validation of the measure-

ments using the ^{16}N source and the impact on the SNO+ energy scale uncertainty.

4.1 Optical calibration analysis method

The optical calibration analysis of the laserball data only considers light arriving from the source to the PMTs in a narrow ± 4 ns time residual window, centered around the prompt peak, shown in Figure 4.1. The time residual, t_{res}, is the instantaneous event time which accounts for the light propagation time to the PMT (time of flight), t_{TOF}, relative to the PMT hit time, t_{PMT}, and a constant time offset, t_0:

$$t_{\text{res}} = t_{\text{PMT}} - t_0 - t_{\text{TOF}} \, . \tag{4.1}$$

Using the prompt light only allows the accurate characterization of the optical parameters without requiring detailed knowledge of the reflective properties of the PMTs, concentrators and other components in the detector, which strongly impact late light.

The PMTs register only single hits even when multiple photoelectrons (MPE) are produced in the PMT from a single laser pulse. Using simply the prompt hit count for each PMT *j* during a run *i*, N_{ij}, would then underestimate the photon intensity of the laserball. To take into account the probability of MPE hits, the number of prompt counts N_{ij} is corrected by inverting the expected Poisson distribution of the hit counts with mean ξ_{ij}:

$$\begin{aligned} \text{Prob}\,(1\text{ hit}) = \text{Prob}\,(\geq 1\text{ photoelectron}) = 1 - \text{Prob}\,(0\text{ photoelectrons}) &= \frac{N_{ij}}{N_i^{pulses}} \\ \frac{N_{ij}}{N_i^{pulses}} &= 1 - \frac{(\xi_{ij})^0 e^{-\xi_{ij}}}{0!} \\ &= 1 - e^{-\xi_{ij}} \\ \implies \frac{N_{ij}^{\text{MPE}}}{N_i^{pulses}} = \xi_{ij} &= -\ln\left(1 - \frac{N_{ij}}{N_i^{pulses}}\right) \, , \end{aligned} \tag{4.2}$$

where N_{ij}^{MPE} is proportional to the actual number of prompt photons that strike the PMT (valid for small numbers of incident photons), and N_i^{pulses} is the number of laser pulses during a laserball run *i*. The optical calibration analysis uses the occupancy O_{ij}^{data} measured by PMT *j* during a run *i*, with the laserball at a given position emitting light at a single wavelength, which is:

$$O_{ij}^{\text{data}} = \frac{N_{ij}^{\text{MPE}}}{N_i^{pulses}} \, . \tag{4.3}$$

The measured O_{ij}^{data} relates to the optical properties of the detector through a model based on geometrical optics which assumes that the detector can be characterized by averaging some of its properties. Specifically, it considers that the media are homogeneous and isotropic, and that the PMT-concentrator assembly response depends only on the incident angle of light and is the same for all PMTs. The model parameterizes the expected occupancy observed by PMT *j*

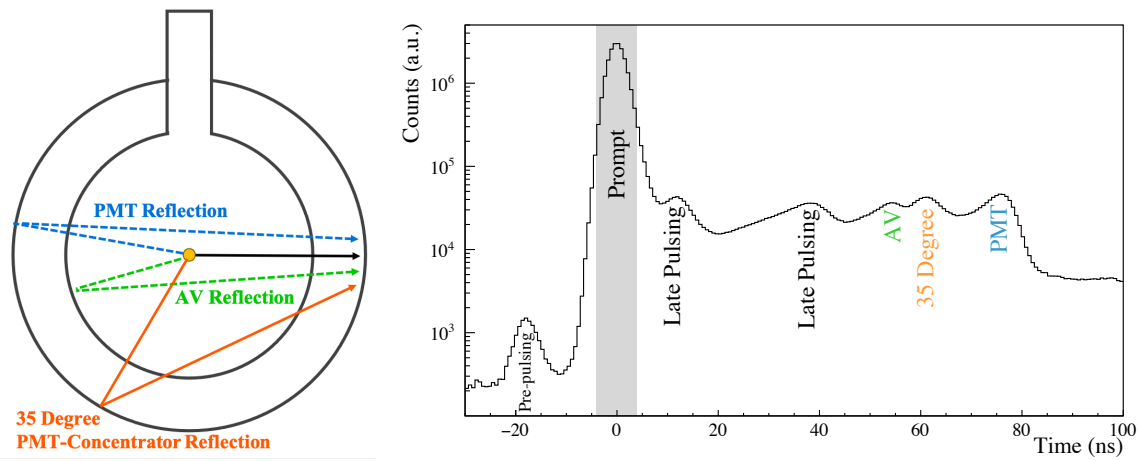

Figure 4.1: Left: Optical paths within the detector for a central laserball position. The black line represents direct light; the blue line represents light reflected by the PMT glass bulb and multiply-reflected by the PMT concentrators; the green line represents light reflected by the AV boundary; and the orange line represents light reflected off of the concentrators surrounding the PMTs. Right: PMT time distribution for a central laserball data run. The shaded region corresponds to the ±4 ns prompt time residual window used for the optical calibration analysis. This approach is used in order to avoid the late light region, which is harder to model with the same accuracy. The pre- and late-pulsing are features of the PMT time response, as identified in [170].

during a run i, O_{ij}^{model}, as follows [154]:

$$O_{ij}^{\text{model}} = N_i \Omega_{ij} R_{ij} T_{ij} L_{ij} \epsilon_j e^{-\left(d_{ij}^{\text{w}_{\text{int}}} \alpha_{\text{w}_{\text{int}}} + d_{ij}^{\text{a}} \alpha_{\text{a}} + d_{ij}^{\text{w}_{\text{ext}}} \alpha_{\text{w}_{\text{ext}}}\right)}, \tag{4.4}$$

where the terms are defined as:

- N_i — number of photons emitted by the laserball in run i, and detected within a prompt timing window at each PMT. This term is the intensity normalization for the run;
- Ω_{ij} — solid angle subtended by the PMT-concentrator assembly j from the laserball position in run i;
- R_{ij} — PMT and concentrator angular response beyond the solid angle Ω_{ij}. This factor is parameterized as a function of the photon incident angle on the face of the PMT-concentrator assembly;
- T_{ij} — Fresnel transmission coefficients for the media interfaces, calculated from the refractive indices, wavelengths and incidence angles of light at the boundaries;
- L_{ij} — the laserball light intensity distribution, parameterized as a function of the polar ($\cos\theta_{\text{LB}}$) and azimuthal (ϕ_{LB}) angles of the light ray relative to the laserball center. This parameter is included in the model to account for the small anisotropies in the laserball light emission;
- ϵ_j — relative efficiency of PMT-concentrator assembly j, combining the overall PMT efficiency and electronics threshold effects (including the quantum efficiency (QE), which refers to the wavelength-dependent probability of registering a hit);

- $d_{ij}^{\mathrm{w_{int}},\mathrm{a},\mathrm{w_{ext}}}$ — refracted light path lengths through the internal water ($d^{\mathrm{w_{int}}}$), the acrylic (d^{a}) and external water ($d^{\mathrm{w_{ext}}}$);
- $\alpha_{\mathrm{w_{int}},\mathrm{a},\mathrm{w_{ext}}}$ — attenuation coefficients for the internal water ($\alpha_{\mathrm{w_{int}}}$), the acrylic ($\alpha_{\mathrm{a}}$) and external water ($\alpha_{\mathrm{w_{ext}}}$).

The solid angles, Ω_{ij}, the Fresnel transmission coefficients, T_{ij}, and the refracted light path lengths in each medium, d_{ij}, are determined simply from the laserball and PMT positions, and the detector geometry. The remaining parameters are extracted from the laserball data through a multi-parameter fit described in Section 4.2.

By building a data set which includes many different laserball positions, it is possible to break covariances between the model parameters, such as between α_{w} and R_{ij}. However, the distances through the external water and the acrylic are correlated for laserball positions inside the AV. Therefore, for data taken only inside the AV, the covariance between α_{w} and α_{a} is difficult to break and, typically, previous *ex situ* measurements for acrylic attenuation are used as fixed inputs to the optical model and only α_{w} is fit.

When adding data from laserball positions outside the AV, it becomes easier to disentangle the correlation between the acrylic and the external water, allowing both parameters to be extracted simultaneously. External positions also probe higher incidence angles at the PMTs to characterize R_{ij} over a wider range of angles, which is useful to improve the models of the PMTs and the concentrators. However, when the laserball is very close to the PMTs and the AV boundary, there are optical paths that make it very difficult to separate light reflected off of the AV and PMTs from the direct light. For this reason, in the water phase analysis of laserball positions outside the AV, only PMTs whose light paths are fully contained in the external water volume, and within a given angular aperture from the laserball, were considered, as will be discussed in more detail in Section 4.3.1.

4.1.1 Media attenuations

The attenuation coefficients α characterize how easily light propagates along the detector media. A medium with a large attenuation coefficient attenuates a large fraction of the light passing through it, and a medium with a small attenuation coefficient is relatively transparent to light.

The attenuation coefficients include the effects of light absorption, α_{abs}, and of Rayleigh scattering, α_{RS}. Absorption happens when the full energy of a photon is transferred to the matter in the medium, whereas Rayleigh scattering corresponds to the elastic scattering of the photons by particles in the medium with sizes smaller than the light wavelength.

Rayleigh scattering affects the observed light distribution intensity and the timing of the observed photon signals. The probability of light being scattered at an angle θ with respect to the original direction is:

$$P(\theta) \sim (1 + \cos^2\theta). \tag{4.5}$$

The Rayleigh scattering is responsible for removing light from the prompt peak, i.e. typically scattered light will arrive at the PMTs at later times. However, there is a probability that light

will be scattered forward and be detected as prompt light. The forward scattered light will increase the number of counts in the prompt peak. Consequently, it increases the apparent prompt attenuation length λ_{w}, thus decreasing the attenuation coefficient $\alpha_{\mathrm{w}} = 1/\lambda_{\mathrm{w}}$. Since the forward scattered light and the unscattered direct light cannot be separated, the analysis assumes that part of the prompt light is due to forward scattering.

The forward-scattered light reduces the contribution of the Rayleigh scattering coefficient to the prompt attenuation coefficient by a factor k. The relation between the three coefficients is then:

$$\alpha_{\mathrm{w}} = \alpha_{\mathrm{abs}} + k\,\alpha_{\mathrm{RS}}\,. \tag{4.6}$$

If 100% of the scattered light is removed from the prompt peak, k should be 1. If 100% of the scattered light is forward scattered and is included in the prompt peak, then $k = 0$ and the attenuation only includes the absorption effect. This effect, which is only geometry dependent, was studied in detail during the SNO experiment and the factor *k* was determined using detailed Monte Carlo simulations of the detector, yielding a value *k* = 0.820 $\pm$ 0.003 for the medium inside the AV [149].

4.1.2 PMT angular response

The angular response of the PMTs and concentrators is the combined efficiency in collecting light at a given incident angle, θ_γ, relative to normal incidence on the front of the PMT-concentrator assembly, $\theta_\gamma = 0$. Figure 4.2 shows the PMT angular responses measured during the SNO experiment. The response increases with incidence angle almost linearly up to 30-40 degrees (depending on wavelength) and then starts rapidly decreasing. The angular responses measured in SNO were limited to incidence angles up to 45 degrees, due to only using in the analysis data with the laserball deployed inside the AV.

Figure 4.2 also shows the variation of the PMT angular response over the duration of the SNO experiment. A decrease in the response at incidence angles larger than 30 degrees has been observed, due to the degradation of the concentrator reflectivity from the immersion in ultra-pure water (discussed in Section 3.5). The rate and type of degradation of the concentrators does not seem to be the same for all PMTs, making it very difficult to create a model that would characterize it with time. Given that the PMTs have been submerged in ultra-pure water for more than 15 years since the last SNO calibration, measuring the angular response during the water phase was of utmost importance.

4.1.3 Laserball position, light distribution, and orientation

Many physical quantities in the optical model of Equation 4.4 depend directly on the accurate determination of the laserball position. Although the source deployment hardware can provide an estimate of the laserball position, its positioning algorithm is based on the tension and length of the ropes that support the source, which have large uncertainties for positions away from the center of the AV. The laserball position used in this analysis is reconstructed from the PMT data through a χ^2 minimization of the time residual in Equation 4.1, using the

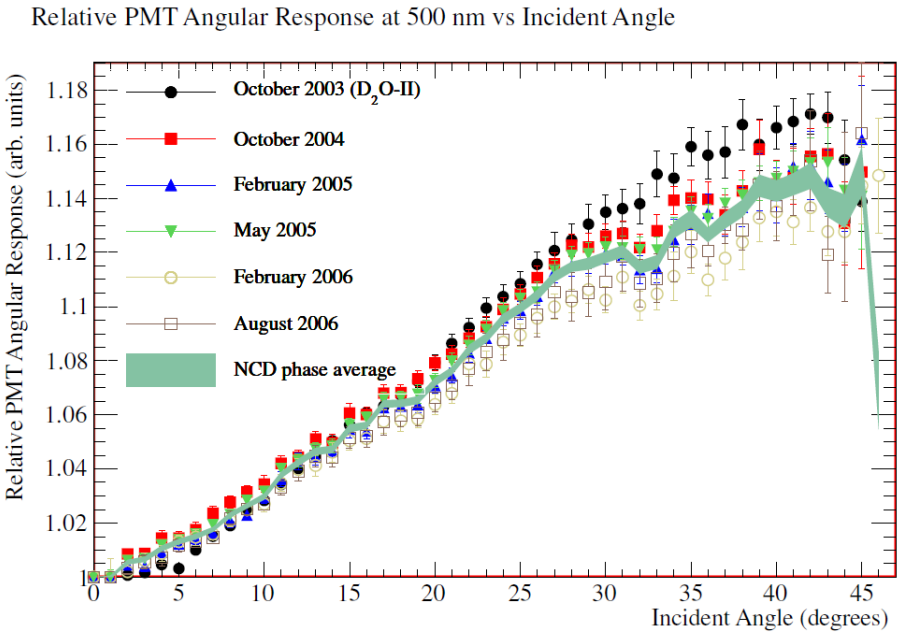

Figure 4.2: Relative PMT Angular Responses as a function of incident angle obtained during the operation of the SNO experiment. The green band represents the average of the measurements from 2004 to 2006, which were performed during the last phase of SNO when an array of ^{3}He proportional counters (NCDs) was deployed inside the AV. Figure from [171].

mean of the hit times and its uncertainty for each PMT in a given run.

The laserball is a 4π quasi-uniform light source and the anisotropies of its intensity distribution depend on the density of glass beads in the silicone gel, on the positioning of the quartz rod inside the source, and shadowing from the metal parts. Knowing those details is not needed, as those anisotropies are characterized with *in situ* laserball data taken at the center of the AV. The intensity distribution is described by twelve independent sinusoidal distributions H in the azimuthal angle ϕ_{LB}, each valid in a given range in the polar angle θ_{LB}, with different amplitudes and phases:

$$H_k(\phi_{\text{LB}}) = 1 + A_k \sin(\phi_{\text{LB}} + \delta_k), \quad k = [1, 12], \text{slices of } \theta_{\text{LB}} \, , \tag{4.7}$$

The azimuthal distributions are weighted by a single polynomial function $P(\cos\theta_{\text{LB}})$ which describes the top-down asymmetry due to shadowing by the mounting hardware on top of the laserball, which is parametrised as:

$$P(\cos\theta_{\text{LB}}) = 1 + \sum_{k=1}^{4} a_k (1 + \cos\theta_{\text{LB}})^k \, . \tag{4.8}$$

The coefficients a_k are determined by the optical calibration fit and the variation of intensity is described around a fixed normalized value, a_0 = 1. This particular choice of functions was empirically guided by prior studies in SNO [171, 172]. The total light intensity distribution of the laserball is:

$$L(\cos\theta_{\text{LB}}, \phi_{\text{LB}}) = H(\cos\theta_{\text{LB}}, \phi_{\text{LB}}) \times P(\cos\theta_{\text{LB}}) \, . \tag{4.9}$$

The parameters of the sinusoidal distribution (amplitudes and phases) are measured by ana-

lyzing the data from rotated laserball runs (relative to the fixed SNO+ coordinate system) taken at the center of the AV. For a $\cos\theta_{\text{LB}}$ slice (equivalent to $\cos\theta_{\text{SNO+}}$, since the laserball always has the same vertical orientation), the occupancy ratio of the PMTs in runs with opposite orientations (180° apart) is given by:

$$\frac{O_{1j}}{O_{2j}} = \frac{N_1\,\Omega_{1j}\,R_{1j}\,T_{1j}\,L_{1j}\,\epsilon_j\,e^{-(d_{1j}^{w_{\text{int}}}\alpha_{w_{\text{int}}}+d_{1j}^{a}\alpha_a+d_{1j}^{w_{\text{ext}}}\alpha_{w_{\text{ext}}})}}{N_2\,\Omega_{2j}\,R_{2j}\,T_{2j}\,L_{2j}\,\epsilon_j\,e^{-(d_{2j}^{w_{\text{int}}}\alpha_{w_{\text{int}}}+d_{2j}^{a}\alpha_a+d_{2j}^{w_{\text{ext}}}\alpha_{w_{\text{ext}}})}}\,. \tag{4.10}$$

All the terms, except the normalizations N and the intensity distribution L, are the same for the two runs since the source is in the same position. Hence, the ratio becomes:

$$\frac{O_{1j}}{O_{2j}} = \frac{N_1 \times P(\cos\theta_{\text{LB}}) \times H(\phi_{\text{LB}}+\Phi_1)}{N_2 \times P(\cos\theta_{\text{LB}}) \times H(\phi_{\text{LB}}+\Phi_2)}\,, \tag{4.11}$$

where Φ_1 and Φ_2 are the orientations of the laserball relative to the SNO+ coordinate system in the two runs, with $\Phi_2 = \Phi_1 + \pi$. $L(\cos\theta_{\text{LB}}, \phi_{\text{LB}})$ is expanded into the sinusoidal function H and the independent polar variation P. The latter is the same in the numerator and denominator, thus enabling sensitivity to the azimuthal sinusoidal distribution. The ratios are fitted for all the $\cos\theta_{\text{LB}}$, and the extracted sinusoidal parameters are used as the seed to the main optical calibration analysis fit.

Additionally, an independent analysis was developed to extract the laserball orientation in each external position, necessary to correctly describe its light intensity distribution, L_{ij}. For external runs, without side ropes attached, an LED was installed to determine the orientation of the laserball. From the coordinates of the region of PMTs with maximum integrated number of hits in the LED runs and the laserball position, it was possible to determine the direction of the LED relative to the detector reference axes. The LED was mounted at a known angle from the laserball reference axes, and by knowing its direction, it was then possible to determine the laserball orientation relative to the detector. The orientations obtained at the different external positions are used as input to the optical calibration analysis fit. This analysis is able to determine the orientation with a precision of $\sim$10 degrees.[1] This precision is sufficient for the optical calibration analysis fit since the laserball intensity asymmetry with ϕ_{LB} is at most 3%, and an uncertainty of 10 degrees in the source orientation would only affect the PMT occupancy by less than 0.1%. Typically, LED runs are taken before and after taking laserball data at each position. Differences between the orientations obtained from the LED runs taken before and after data taking indicate whether the laserball rotated.

4.2 Optical calibration analysis fit

The extraction of the optical parameters in Equation 4.4 from the laserball data uses a method that normalizes the occupancy at a PMT *j* for a given run *i*, O_{ij}, by the value from a run with the laserball located at the center of the detector, O_{0j} [154]. This normalization is

[1]The precision of the laserball orientation is obtained from the difference between the orientations determined using the LED runs before and after data taking at each position.

done for both the model and for the data:

$$Q_{ij}^{\text{model}} = \frac{O_{ij}^{\text{model}}}{O_{0j}^{\text{model}}} \left(\frac{\Omega_{0j} T_{0j}}{\Omega_{ij} T_{ij}} \right) = \frac{N_i R_{ij} L_{ij}}{N_0 R_{0j} L_{0j}} exp \left(- \sum_k \left(d_{ij}^k - d_{0j}^k \right) \alpha_k \right) . \tag{4.12}$$

$$Q_{ij}^{\text{data}} = \frac{O_{ij}^{\text{data}}}{O_{0j}^{\text{data}}} \left(\frac{\Omega_{0j} T_{0j}}{\Omega_{ij} T_{ij}} \right) . \tag{4.13}$$

Q_{ij} are occupancy ratios corrected by the solid angles Ω_{ij}, Ω_{0j}, and Fresnel transmission coefficients T_{ij}, T_{0j}, which are numerically calculated based on the fitted laserball position. By taking the ratio between an off-center and a central laserball run, the dependency on the PMT efficiency, ϵ_j, is removed, eliminating one parameter for each PMT (about 9000) from the model.

The distances d_{ij}^k, similarly to the Ω_{ij} and T_{ij} already corrected for, can be calculated from the fitted laserball positions. Therefore, the model occupancy ratio is entirely characterized by parameters that can be determined by the minimization of a χ^2 estimator over several iterations [154]:

$$\chi^2 = \sum_i^{\#Runs} \sum_j^{\#\text{PMTs}} \frac{(Q_{ij}^{\text{data}} - Q_{ij}^{\text{model}})^2}{\sigma_{\text{stat},ij}^2 + \sigma_{\text{PMT}}^2(\theta_{\gamma,ij})} , \tag{4.14}$$

where $\sigma_{\text{stat},ij}^2$ is the statistical uncertainty on the data occupancy ratio due to counting statistics, and $\sigma_{\text{PMT}}^2(\theta_{\gamma,ij})$ is an additional uncertainty introduced to account for variations in the PMT angular response as a function of the incidence angle of the light. The number of model parameters in the χ^2 is around 166: 3 attenuations, 90 PMT response bins[2] for R, 4 coefficients for the laserball $P(\cos\theta_{\text{LB}})$ function and 24 parameters for $H(\cos\theta_{\text{LB}}, \phi_{\text{LB}})$, and 45 run intensity normalizations N_i (average number of laserball data runs of a given wavelength in the fit). Typically, the minimization is performed with more than 100,000 data points, after applying data selection cuts (discussed in Section 4.3.1), allowing to determine the optical model parameters with a statistical uncertainty below 1%.

The minimization of the χ^2 is a non-linear least squares problem that is solved using the Levenberg-Marquardt algorithm [173, 174]. The minimization is performed over several iterations with a sequentially decreasing upper χ^2 limit. After each minimization, PMTs with a χ^2 larger than the new limit are removed from the sample (this removes between 10 and 35% of the data points from each run, depending on the source position).

The χ^2 cut removes PMTs in which some aspect of the optics is not modeled well; for instance, PMTs undergoing irregular exposure to light due to scattering or reflections which are unaccounted for by the model. To avoid a sequential minimization over the same subset of the sample, all PMTs, even those previously removed, are reconsidered in each iteration. The minimization is performed using all the laserball data for each wavelength separately. The relative PMT efficiencies ϵ_j are extracted separately in a final step from the ratio between the data and model occupancies, after all the other model parameters are characterized.

[2]Even though the model considers 90 bins for the PMT angular response, at most 60 will be free parameters in the fit. The bins for incidence angles larger than 60 degrees are typically fixed to 1 in the fit, since the laserball positions used for the analysis are not able to scan such high incidence angles.

4.2.1 Systematic uncertainties

Systematic uncertainties are estimated by repeating the optical calibration fit with shifts applied to input parameters, such as to the laserball positions, or with different fit settings, such as a different χ^2 limit. The output of these fits are used to calculate the systematic change in the nominal fit results. The overall objective is to understand how robust the optical parameters are to these systematic changes. The following systematics are considered:

- **Laserball radial 1% scale**, $|r_{\text{LB}}| \times 1.01$: The radial position of the laserball in each run is moved outward by 1%, thus reducing the average time of flight for light to reach the PMTs from the laserball. This shift accounts for uncertainties related to the group velocity of the detector materials and the timing of individual PMTs.
- **Laserball radial shift**: The radial position of the laserball is increased by a fixed distance.
- **Laserball (*x*,*y*,*z*)-coordinate discrete shift**: The coordinates of the laserball are shifted along the positive or negative *x*–, *y*– or *z*–directions.
- **Laserball wavelength shift,** $\lambda \pm \lambda_{RMS}$: The laserball wavelength is both increased and decreased by the associated RMS value of the corresponding dye wavelength distribution, shown in Figure 3.11. This small change in wavelength is designed to test the change in the refractive indices and consequently the related incident angles and the PMTs, θ_γ.
- **Squared laserball angular anisotropy**, $H^2(\cos\theta_{\text{LB}}, \phi_{\text{LB}})$: The fitted laserball angular distribution is squared in order to probe the effect of a larger anisotropy on the optical parameters.
- **Flat laserball angular anisotropy**, $H(\cos\theta_{\text{LB}}, \phi_{\text{LB}}) = 1.0$: Similar to the above, the assumption of a perfectly isotropic laserball angular distribution is enforced in order to gauge its effect on the optical parameters.
- **Final upper χ^2 limit**: The choice of the final upper χ^2 limit determines the size of the data sample over which the fit is performed. A larger upper limit is selected to check the impact on the fit parameters.
- **Laserball flask radius**, $d_{innerAV} - 50.0$ mm: The distance in the inner AV, $d_{innerAV}$, is reduced by 50.0 mm (the approximate radius of the laserball flask) to account for the fact that light will be emitted at the flask surface, no the centre.

The main systematic error comes from the laserball position uncertainties obtained by comparing the position provided by the manipulator hardware with a fitted position from the data. The main correction to the observed occupancy is the solid angle correction, which is inversely proportional to the square of the source-PMT distance (discussed in more detail in Section 4.3.1). Consequently, even small deviations in the laserball position can create big variations in the corrected occupancy, affecting primarily the attenuation coefficients.

4.2.2 Cross-check analysis of the media attenuations

The attenuations of the inner detector medium, extracted from the main analysis fit, can be validated by a simplified and independent analysis of the laserball data. This independent analysis makes use of the calibration data with the laserball placed in different internal positions along a straight line passing through the center of the detector, and only considers the occupancies of two small groups of PMTs centered around the point where the line intersects the PMT support structure. Choosing the PMTs over a straight line ensures that the incidence angle and the angular distribution do not change, to first order, from PMT to PMT (the photons travel normal to the acrylic and the PMTs), leaving the attenuation as the main parameter in the optical model. This analysis uses laserball positions along a diagonal line of the detector. Positions along the horizontal and vertical planes are not used to avoid the optical properties of the AV belly plates and of the neck, which are not accounted for by the model.

The ratio of occupancies between two opposite PMTs (one in each side of the detector), in a run *i*, can be modeled as:

$$\frac{O_{i1}}{O_{i2}} = \frac{N_i \Omega_{i1} R_{i1} T_{i1} L_{i1} \epsilon_1 e^{\left(-\sum_k d_{i1}^k \alpha_k\right)}}{N_i \Omega_{i2} R_{i2} T_{i2} L_{i2} \epsilon_{i2} e^{\left(-\sum_k d_{i2}^k \alpha_k\right)}}\,, \tag{4.15}$$

with k representing the detector media, $k = \mathrm{w_{int}}, \mathrm{a}, \mathrm{w_{ext}}$. Because the PMTs are aligned, one can assume that the distance traveled by light in the acrylic and in the external water is the same for each side ($d_{i1}^a = d_{i2}^a$ and $d_{i1}^{w_{ext}} = d_{i2}^{w_{ext}}$), yielding:

$$\frac{O_{i1}}{O_{i2}} = \frac{\Omega_{i1} R_{i1} T_{i1} L_{i1} \epsilon_1}{\Omega_{i2} R_{i2} T_{i2} L_{i2} \epsilon_2} e^{-(d_{i1}^{w_{\mathrm{int}}} - d_{i2}^{w_{\mathrm{int}}})\alpha_{w_{\mathrm{int}}}}\,. \tag{4.16}$$

The ratio of the occupancies of the two opposite PMTs will, therefore, vary exponentially with the difference between the light paths inside the AV for each PMT, with a slope equal to the attenuation coefficient of the medium inside the acrylic vessel. Because the solid angle and the Fresnel transmission coefficients can be calculated numerically, they are fixed in this analysis. The angular response and efficiency of the PMTs and the laserball light distribution, to first approximation, can be considered as constants. This leaves on the right side of Equation 4.16 a dependence on the distances $d_i^{w_{\mathrm{int}}}$ as independent variables, and the internal water attenuation as the parameter to measure.

4.3 Water phase calibration data

During the SNO+ water phase there were two main laserball data-taking campaigns: an internal laserball scan in December 2017, and internal and external scans in July 2018. The author was present during both of them, participating in the calibration shifts with other SNO+ collaborators. Some of the responsibilities during the calibration shifts included operating the source manipulator and laser, to respectively change the source position and wavelength, ensuring that the campaign plan was successfully completed, and performing live quick checks of laserball data quality. During the December 2017 campaign, data were collected in a total of 31 internal

positions (including four central positions with the laserball at different azimuthal orientations, to help understanding the anisotropies in its light output), for the six available wavelengths. This campaign had the main goal of commissioning the laser and laserball hardware, and the data were used to exercise the calibration data processing and analyses tools.

Similarly, during the July 2018 campaign data were collected at 42 internal positions, including the four central positions with different laserball orientations (Figure 4.3). Additionally, data were collected at 19 positions along a vertical axis outside the AV. Each run (internal or external) had around 8700 online, inward facing PMTs. Since the data from the central positions are used as normalization in the analysis, these runs were typically one hour long for one of the laserball orientations, and 30 minutes for the other orientations. The run length of the off-center positions was 15 minutes.

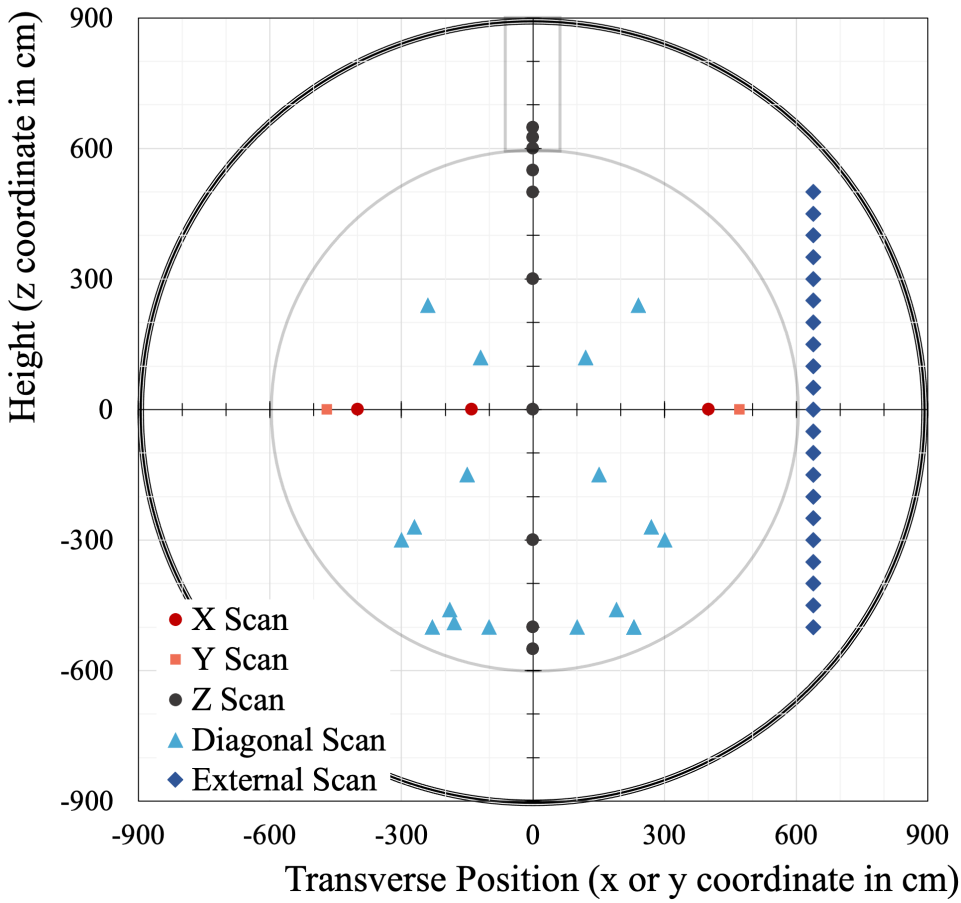

Figure 4.3: Laserball positions during the 2018 calibration campaign, projected in the transverse plane.

The laser emitted 40 light pulses per second, and the intensity was kept low using neutral density filters so that only about 5% of the PMTs register hits for each laser pulse. This ensured that the corrections applied to account for multiple photons hitting a single tube were small. The stability of the laser emission was monitored live during the calibration campaigns by looking at the integrated number of hit PMTs per second. Afterwards, the stability of the data was evaluated offline during the data quality stage of the analysis. The indicators used were the number of hit PMTs per laser pulse, as well as the width of this distribution over the course of

a laserball run. Fluctuations in the number of PMTs registering a hit per laserball pulse were smaller than 2%.

In November 2017 the ^{16}N source was deployed inside the AV, and data were collected in 80 different positions, along the detector horizontal, and vertical axis. The runs were between 20 and 30 minutes long, with an average rate of 30 to 60 tagged events per second, depending on the settings of the DT generator supply, like the CO_2 gas flow rate.

4.3.1 Laserball data selection and cuts

The occupancy of each online, inward facing PMT in each run is a candidate data point for the optical fit, giving approximately 4×10^5 data points that enter the fit for each wavelength. The analysis cut that results in the biggest fraction of PMTs excluded from the data set is the "shadowing" cut. It removes PMTs whose light paths are within a tolerance distance or intersect detector components not included in the optical model. Table 4.1 lists the detector components which cause shadowing, along the tolerance distances considered when evaluating if a PMT is shadowed by them. It also provides a breakdown of the percentage of PMTs shadowed by each detector component, for two example laserball positions. The shadowing cuts are applied sequentially and, therefore, a PMT flagged as shadowed for one component is not accounted for when evaluating the shadowing percentage for the following.

Table 4.1: List of detector components responsible for shadowing PMTs. The second column lists the maximum distance from a light path to the detector component in order to flag a PMT as shadowed. The third and fourth columns present the percentages of shadowed PMTs by each detector component, for two laserball positions.

Detector Component	Distance tolerance (cm)	Shadowed PMTs (%) $\vec{r}_{\text{LB}}$ = (0,0,0) m	Shadowed PMTs (%) $\vec{r}_{\text{LB}}$ = (5,0,0) m
AV belly plates	30	4.9	6.28
Hold-down ropes	15	21.51	20.54
Hold-up support ropes	15	7.12	5.87
AV pipes	15	3.51	2.77
AV neck boss	15	0.55	0.61
NCD anchors	15	1.35	1.06

Figure 4.4 shows a map of the PMTs shadowed by detector components for a central laserball position. The values given in the figure reflect the true total percentage of shadowed PMTs. The shadowing cut results in 39% of the fit data points being removed in the normalization run. Of the remainder, up to 28% of the data points were excluded from each internal off-axis run, depending on the position, by applying the same cut.

Figure 4.5 shows maps of the PMT occupancies for a central and an off-center laserball run, prior to any analysis cuts. For the central run, it is possible to observe directly in the data the shadowing caused by the detector components: circles of lower occupancy PMTs around the detector equator, shadowed by the rope loops inside acrylic panels mounted on the outside of the AV ("belly plates"). The shadowing effects by the hold-down rope net on the top of the AV are also clearly visible, as is the laserball hardware shadowing, resulting in lower occupancy PMTs in the top part of the detector. Such effects are harder to observe in the raw data of the

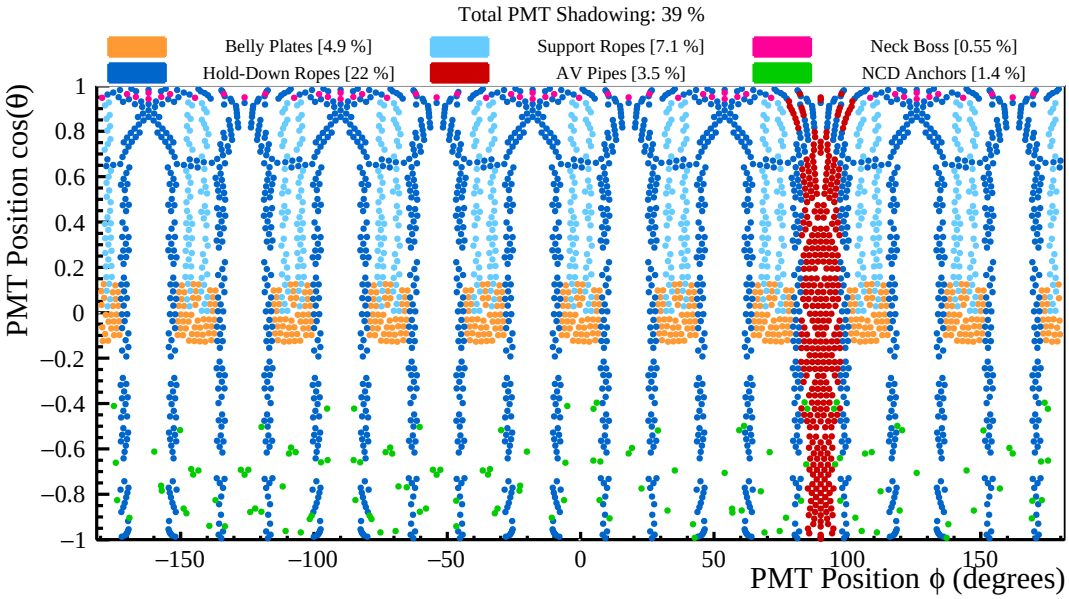

Figure 4.4: Map of PMTs shadowed by detector components for a central laserball position. The PMTs are considered shadowed if their light path, starting at the source position, comes within a tolerance distance or intersects the detector components not included in the optical model. The tolerance distance is 30 cm to the AV belly plates, and 15 cm to all the other components.

off-center run. In the latter case, the PMTs closer to the laserball will have an occupancy about 15–16% larger than the ones in the opposite side of the detector, mostly due to the solid angle effect.

The variable that affects the solid angle calculation the most is the source position. The solid angle is proportional to $1/R^2$, where R is the distance between the laserball and the PMTs. For example, a radial position scale factor of 1.01 changes the solid angle correction for a given PMT by about 2%. Since the variations of the occupancy due to the solid angle are larger than those due to the optical parameters, the laserball position needs to be determined with a high level of accuracy. Although the manipulator system provides an estimate of the laserball position, its positioning algorithm is based on the length of the ropes that move the calibration source, which depends on the rope tension and is therefore not precise enough when moving it to positions outside the vertical axis.

Comparing the position fitted from the laserball data to the manipulator position provides the systematic variation to be considered in the main analysis fit. The agreement between the fitted position and the manipulator was better than 2 cm for central positions, and $\sim$4 cm for high radii positions. A laserball position uncertainty of 4 cm was used when calculating the systematic uncertainties of the optical model parameters. This was a conservative choice, since the high radii positions given by the manipulator are less reliable than the central positions due to the varying tension of the ropes manipulator.

The introduction of the external laserball data in the optical calibration fit was a new feature and improvement of the analysis relative to SNO. Nevertheless, the only external data points considered for the analysis came from PMTs whose light paths from the source were fully contained in the external water region. This selection was made to avoid uncertainties in the

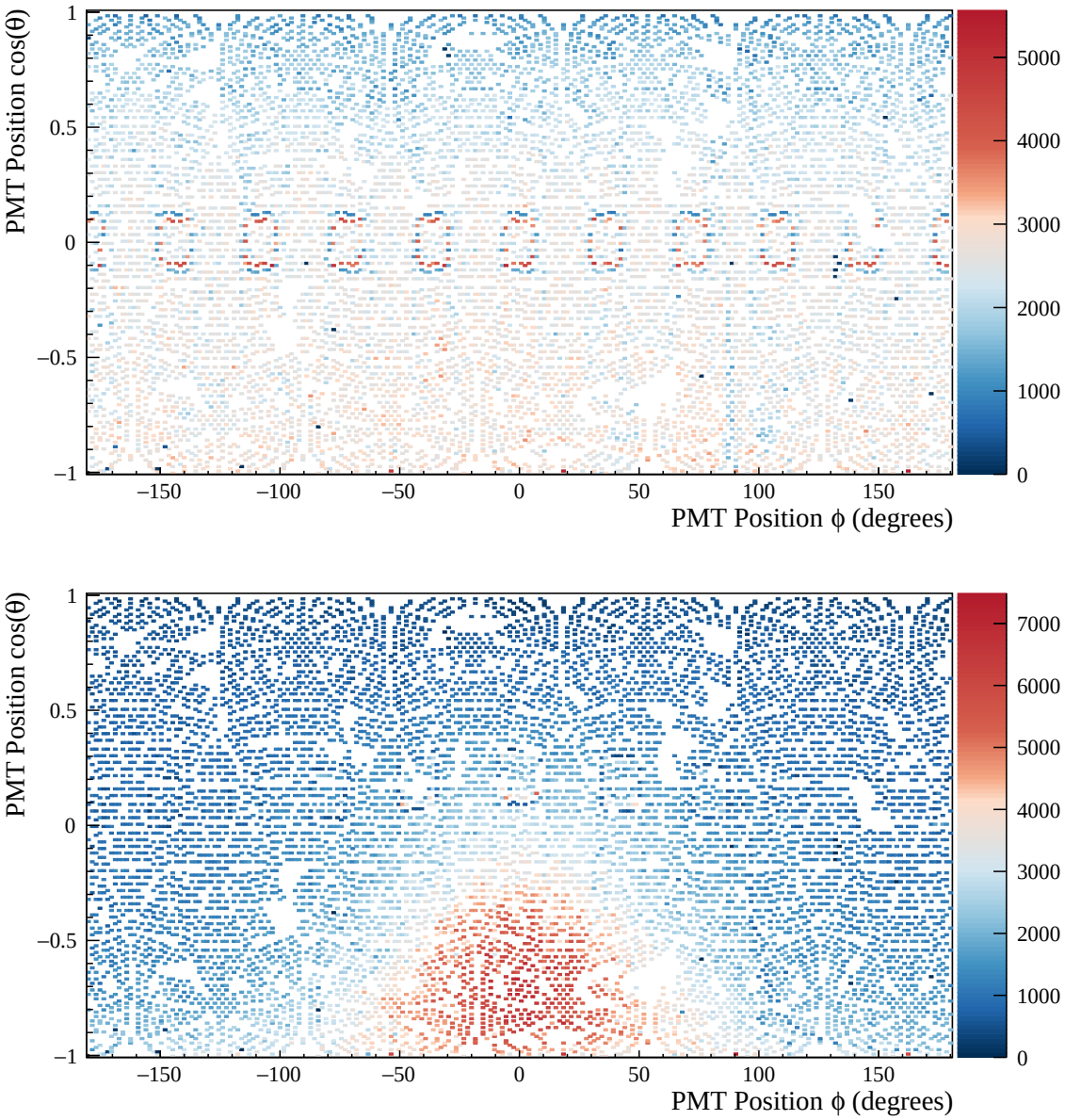

Figure 4.5: Map of PMT occupancies for central (top) and off-center (bottom) laserball runs from the 2018 calibration campaign.

solid angle calculation for PMTs that would see light crossing the full AV and intersecting the acrylic boundaries four times.

In addition, several cuts had to be implemented in order to deal with PMTs whose measured occupancy was affected by light reflected from the AV outer surface or other PMTs. These cuts were determined by comparing laserball simulations with and without reflections from the AV and from the PMTs. Figure 4.6 shows the ratio of occupancies for each PMT between the simulations with reflections on and with reflections off, as a function of cos(α), where α is the angle between the vector pointing from the detector center to the laserball position, and the vector pointing from the center of the laserball to the PMT.

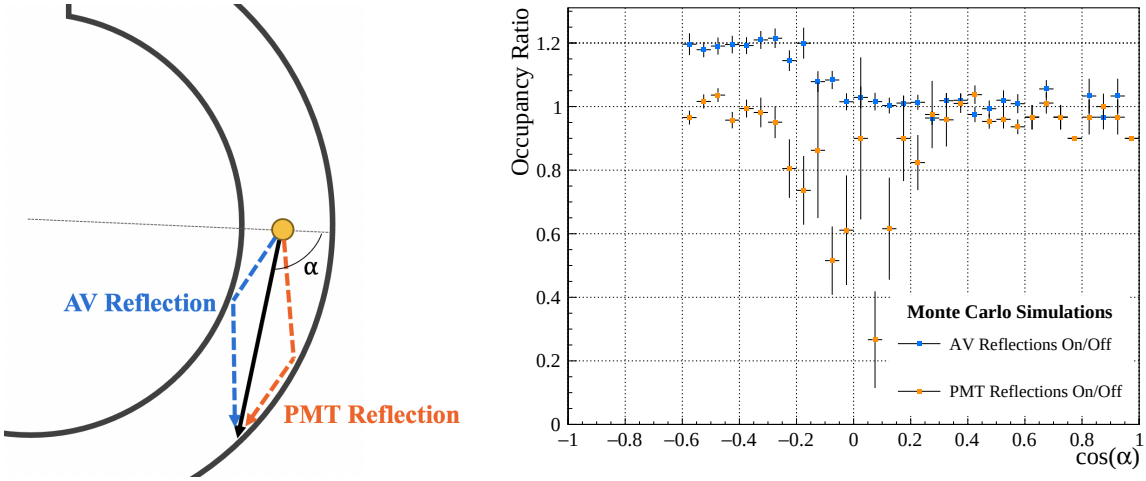

Figure 4.6: Ratio of PMT occupancies in MC simulations with AV reflections on and off (blue) and PMT reflections on and off (orange), as a function of cos(α), where α is the angle between the laserball position vector and the vector pointing from the center of the laserball to the PMT.

PMTs further away from the laserball will have a 20% overestimated occupancy due to light reflected from the AV surface that reaches the PMT in the 8 ns prompt time window. Furthermore, light entering the PMT reflector assembly at a given angle can be reflected and not detected by the PMT. Both these effects are not accounted for in the optical model (Equation 4.4), and the comparisons of simulation with data for each external position were used to determine cos(α) cuts to exclude the affected PMTs. Table 4.2 lists the cos(α) cuts applied to the external laserball data, for different vertical positions. Only PMTs with cos(α) larger than the cut values presented in the Table were selected for the analysis.

Due to the strict light path type selection and PMT cuts for the external runs, between 94% and 97% of the number of data points from each external position were excluded from the fit. Even though this results in a small sample of about 435 data points for each external position, the fit is performed using all the data available from the 61 internal and external positions, which provides enough statistics to estimate the optical parameters and mitigates any biases due to PMT sampling.

Table 4.2: Cos(α) cuts applied to PMTs in external laserball runs to reject those whose detected prompt light is contaminated by light reflected off of the AV surface. If a PMT has a cos(α) value lower than the cut value (second column), for a run with the laserball at a given external position (first column), the PMT will be rejected from the dataset.

Laserball Z coordinate (m)	cos(α) cut
$\geq$ 3.8	0
3.3 $\leq$ Z $<$ 3.8	0.05
2.3 $\leq$ Z $<$ 3.3	0.15
1.8 $\leq$ Z $<$ 2.3	0.3
1.3 $\leq$ Z $<$ 1.8	0.35
-2.3 $\leq$ Z $<$ 1.3	0.4
-2.8 $\leq$ Z $<$ -2.3	0.25
$\leq$ -2.8	0.0

4.4 Results of the optical calibration analysis

The parameters of the optical model presented in Section 4.1 were extracted from the χ^2 minimization using the internal and external laserball data. The minimization assumed the same water attenuation coefficients for the internal and external water. This decision was made after performing the fit with the attenuations separated, and verifying that the measured external water attenuation coefficients were compatible with the ones for the internal water, but with much larger uncertainties (>50%). The combined internal and external water attenuation coefficients measured in this analysis are presented on the left side of Table 4.3. Adding the external laserball data to the analysis allowed to perform the first *in situ* measurement of the effective acrylic vessel attenuation coefficients, shown on the right side of Table 4.3.

Table 4.3: Fitted water attenuation coefficients, α_w, and effective acrylic attenuation coefficients, α_a, and their corresponding statistical and systematic uncertainties.

λ (nm)	α_{w} ($\times 10^{-5}$ mm^{-1})	σ_{stat} ($\times 10^{-5}$ mm^{-1})	σ_{syst} ($\times 10^{-5}$ mm^{-1})	α_{a} ($\times 10^{-3}$ mm^{-1})	σ_{stat} ($\times 10^{-3}$ mm^{-1})	σ_{syst} ($\times 10^{-3}$ mm^{-1})
337	1.331	0.006	0.489	9.19	0.05	1.12
365	1.013	0.005	0.421	4.31	0.04	0.86
385	0.859	0.005	0.431	3.15	0.04	0.84
420	0.819	0.005	0.423	2.61	0.04	0.81
450	0.943	0.005	0.419	2.75	0.04	0.81
500	2.615	0.005	0.443	2.43	0.04	0.83

Because the Monte Carlo simulation must model both absorption and scattering, the scattering contribution is subtracted from the measured attenuation coefficient (Equation 4.6), and the resulting absorption coefficient is used as an input to the Monte Carlo.[3] Figure 4.7 shows the water absorption coefficients, which are in good agreement with literature values from [175, 176], from measurements using integrating cavities. It is important to note that the measurements from [175] at low wavelengths are affected by lower reflectivity and higher UV absorption properties of the cavity reflective material, hence overestimating the attenuation coefficients [176].

[3]The Rayleigh scattering coefficients used were determined by the fixed calibration system of optical fibers.

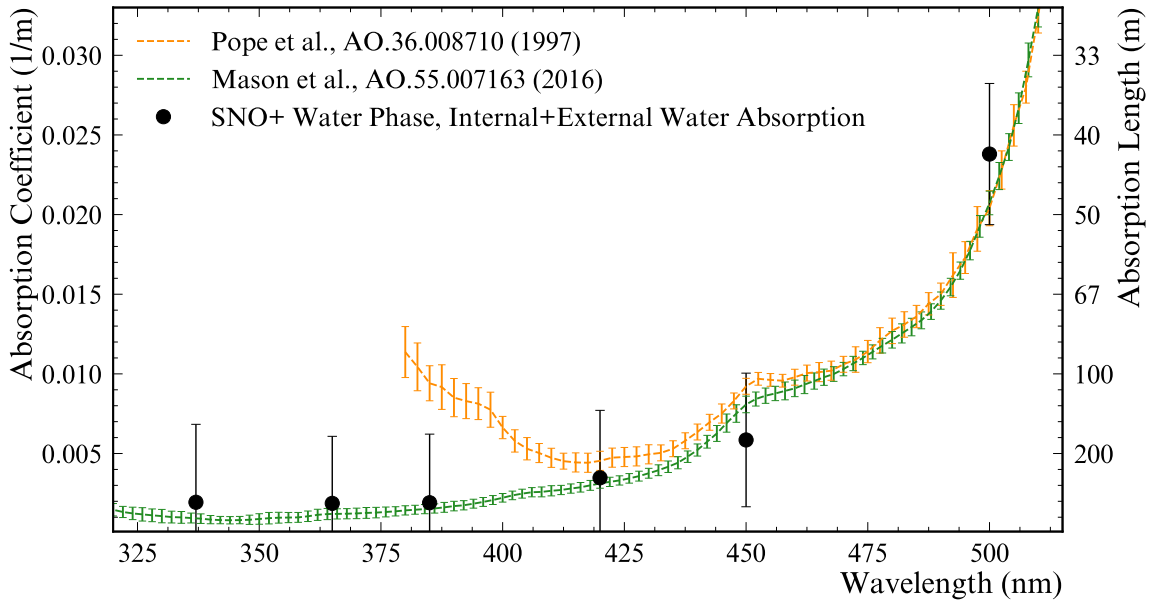

Figure 4.7: Internal and external water absorption coefficients (left axis) and lengths (right axis) as a function of wavelength. Shown are the results from the Optical Calibration Analysis for the data of the July 2018 laserball internal and external scans (black), after correcting the measured prompt attenuation for the effects of the Rayleigh scattering. The orange and green lines are water absorption values from [175] and [176], respectively.

In the case of the acrylic vessel, the fitted effective attenuation coefficients are shown in Figure 4.8. The attenuation coefficients are a factor 5 larger than *ex situ* measurements performed using acrylic samples [149]. There is not an independent way to verify if the worse attenuation is due to degradation with time of the bulk acrylic, or if it is due to surface effects. However, the acrylic attenuation measurements are modelled as effective bulk transmission, since the Monte Carlo assumes that the acrylic is uniform. Therefore, the results were directly propagated to the SNO+ Monte Carlo as absorption lengths.

In addition to the attenuation lengths, the response of the PMTs and concentrators as a function of incidence angle was also measured. The angular dependence is parameterized as a simple binned response function, with bins in steps of 1 degree ranging from normal incidence (0 degrees) to the highest angle possible, where normal incidence is defined as normal to the front plane of the PMT and concentrator assembly (Figure 3.7). The internal scan positions are only able to cover an incident angle up to 45 degrees. The addition of the external laserball data allowed to measure the response at higher angles *in situ* for the first time. Figure 4.9 shows the PMT and concentrator assembly angular response for the six laserball wavelengths, normalized by the response to light at normal incidence. The concentrators are responsible for increasing the angular response with incidence angle up to a peak at 30 – 35 degrees. However, beyond 45 degrees, light entering the PMT and concentrator assembly will be mostly reflected back out due to the design of the concentrators' shape, as is illustrated by Figure 4.10. It is important to note that there is a strong correlation between the effective acrylic attenuation coefficients and the PMT angular response parameters at high angles, between 40 and 50 degrees. The measured angular responses are directly introduced in the SNO+ Monte Carlo as the grey disc PMT model absorption probabilities.

Figure 4.11 compares the measured angular response at 420 nm with previous *ex situ* mea-

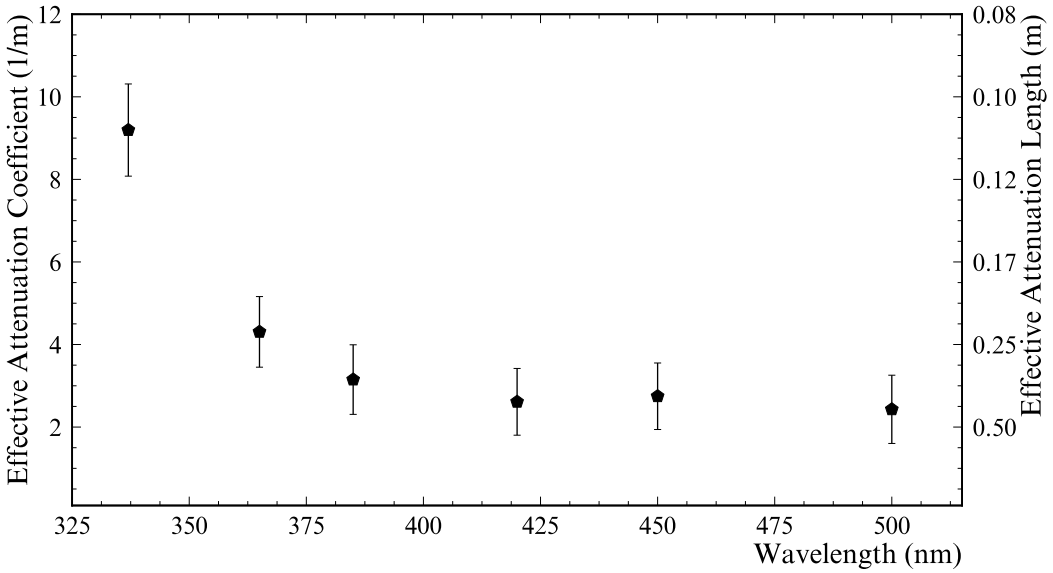

Figure 4.8: Effective acrylic vessel attenuation coefficients (left axis) and lengths (right axis) as a function of wavelength. The results come from the Optical Calibration Analysis of the data of the 2018 laserball internal and external scans. These are the first *in situ* measurements of the effective acrylic vessel attenuation.

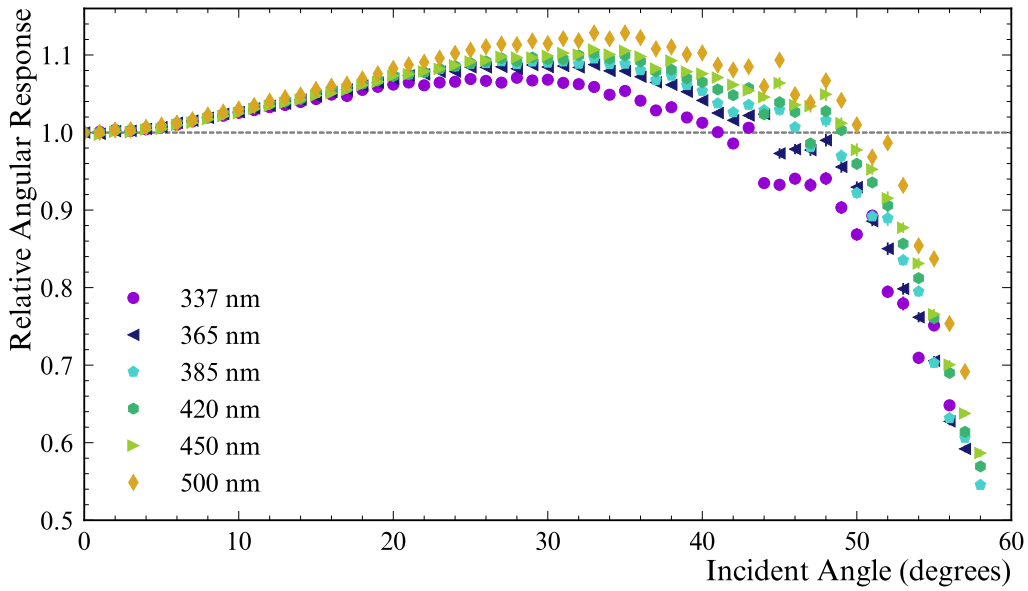

Figure 4.9: Relative PMT-concentrator assembly angular response as a function of the incidence angle, for the six laserball wavelengths used during the 2018 internal and external scans. The angular response values are normalized to the one at a normal incidence (0 degrees). The inclusion of the external scan data allowed for values above 45 degrees to be measured *in situ* for the first time. Only the statistical uncertainties are displayed.

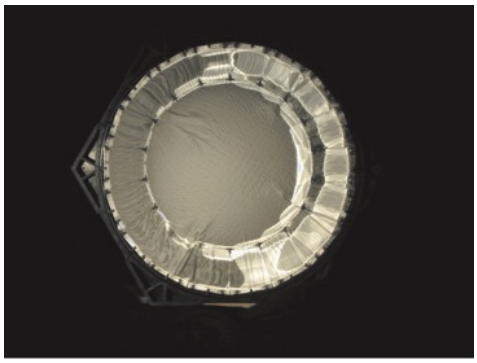

(a) 15°

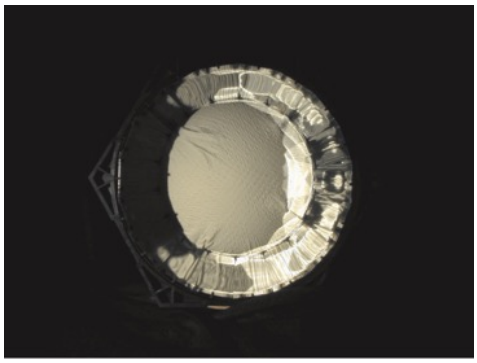

(b) 30°

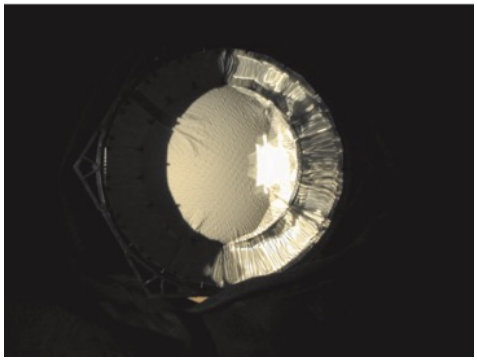

(c) 45°

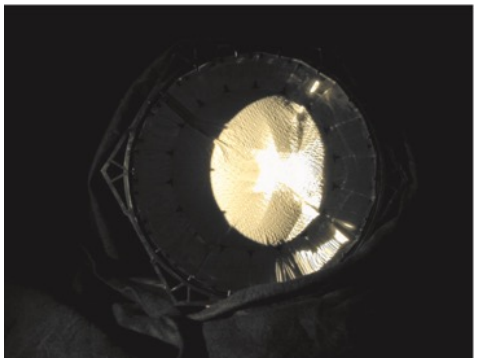

(d) 60°

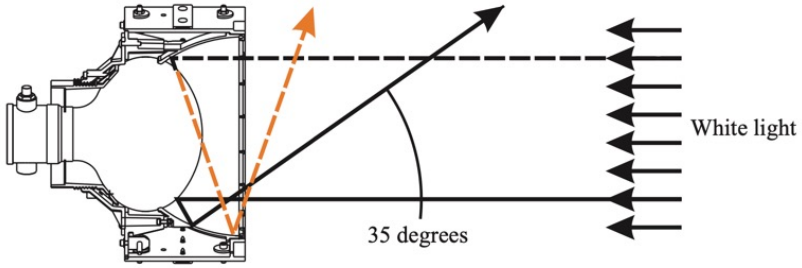

(e)

Figure 4.10: PMT and its reflector with white light illumination at several incident angles, (a) 15°, (b) 30°, (c) 45°, (d) 60°. (e) Scheme of the reflections off of the concentrator for normal incidence light. Figures from [149].

surements from SNO. It is important to notice that the angular response has been decreasing over time since the beginning of SNO, due to the degradation of the concentrator's optical surface. This degradation, which made areas of the concentrators reflect more diffusely, has been directly observed during the SNO to SNO+ transition phase from photographs taken to the PMTs and from visual inspection of PMTs+concentrators which were removed from the PSUP to accommodate the installation of the hold-down rope system. The observed degradation does not seem to follow a pattern, with some concentrators showing spot-like areas with diffuse reflections and others showing ring-like degraded areas, making it very difficult to create a model that would characterize its evolution with time.

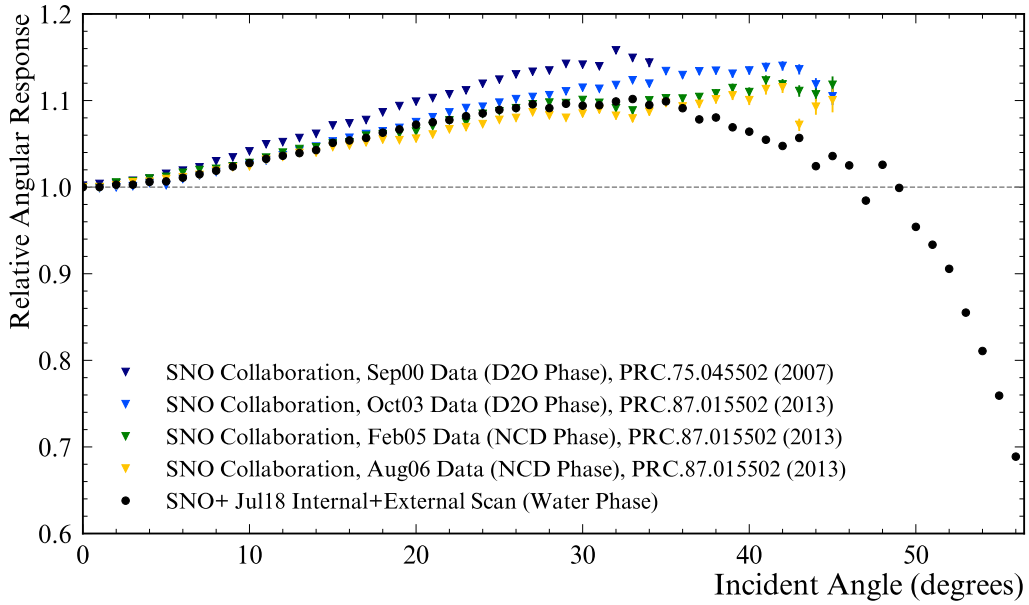

Figure 4.11: Relative PMT-concentrator angular response at 420 nm as a function of the incidence angle. In black are shown the measurements from the SNO+ water phase optical calibration analysis, compared with previous measurements from the SNO experiment. Only the statistical uncertainties are displayed.

4.4.1 Laserball parameters

Along with the main optical parameters presented above, the parameters that describe the laserball light distribution were also extracted from the fit. Figure 4.12 shows fitted polynomial function $P(\cos\theta_{\mathrm{LB}})$ for the six scanned wavelengths. It is possible to observe the top-down asymmetry of the laserball: the top part of the source emits approximately half the amount of light emitted by the bottom. Figure 4.13 shows the residual angular anisotropy $H(\cos\theta_{\mathrm{LB}}, \phi_{\mathrm{LB}})$, which can go up to 3.5% depending on the wavelength.

4.4.2 PMT efficiencies

The PMT absolute quantum efficiencies, $\bar{\epsilon_j}$, averaged over all runs, were extracted in a secondary step after the main fit. These efficiencies are a convolution between the electronics efficiencies and the overall PMT efficiencies. In order to produce tables of PMT efficiencies,

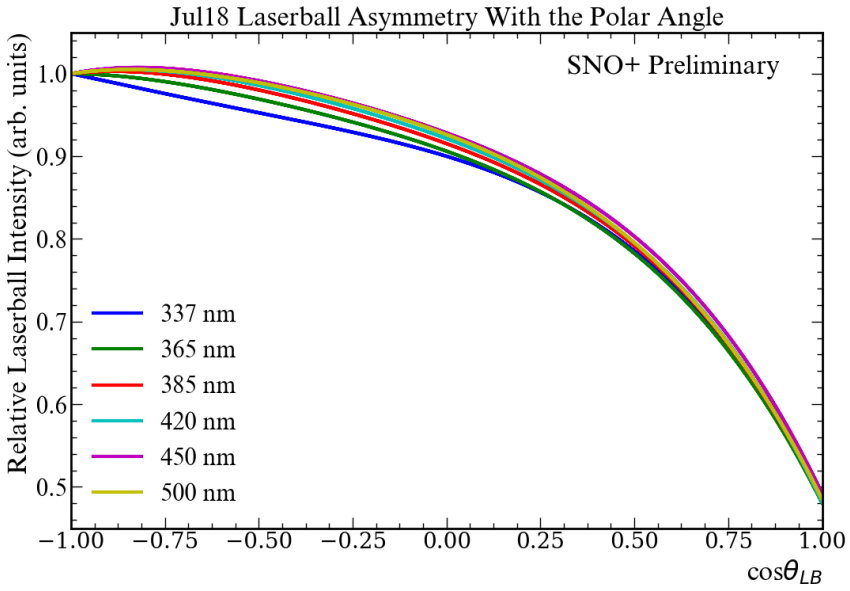

Figure 4.12: Fitted $P(\cos\theta_{\mathrm{LB}})$ functions for each of the six wavelengths scanned in the optical calibration analysis.

needed as input for the RAT simulation, the efficiencies obtained from this analysis were corrected by electronics efficiencies for each PMT provided by the SNO+ PMT Calibration group. The electronics efficiencies represent the probability of a single photo-electron to successfully fire the PMT discriminator (process described in more detail in Section 3.5). The values, one for each PMT, are given by the normalised ratio of the integral of the charge spectrum for the corresponding PMT, from threshold to the maximum, i.e. this integral divided by the integral across the full charge spectrum.

Figure 4.14 shows the distribution of the PMT efficiencies $\bar{\epsilon_j}$ obtained from this analysis. Approximately 55.4% of the 9362 SNO+ PMT efficiencies could be characterized. PMTs whose efficiency could not be calibrated were given a default value of 1.0, and are not included in Figure 4.14. The distribution is centered at 1 and has a dispersion of $\sim$11%, with a tail towards lower efficiencies. A slight spatial variation of the efficiencies was observed, with PMTs at the top of the detector having lower efficiencies than the ones in the lower hemisphere.This effect can be due to not only a variation in the PMT QE, but also due to the reflectivity of the concentrators or even some shadowing effects (given the high density of the hold-down rope net system at the top of the AV).

4.4.3 Additional tuning of the detector model

After propagating the optics measurements to the SNO+ Monte Carlo, there are two further aspects that need to be tuned: the collection efficiency scale factor, and the reflections of the PMT grey disc model that impact the late-light distributions. The collection efficiency scale factor was extracted by comparing the number of prompt hits of the ^{16}N source at the center of the detector, with Monte Carlo simulations tuned with the optical analysis measurements.

Tuning the grey disc model reflections included developing a parameterization for the re-

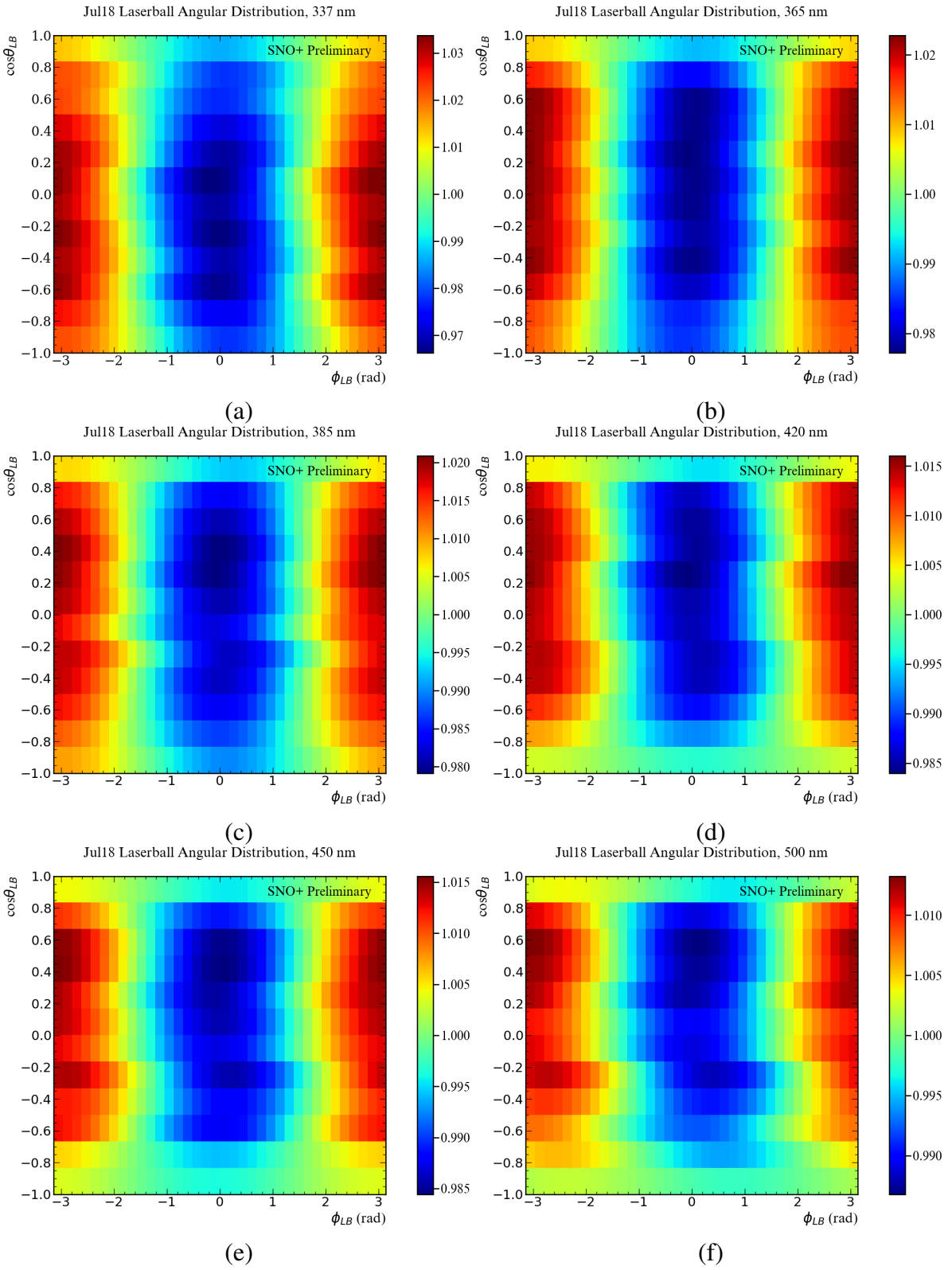

Figure 4.13: Residual laserball angular anisotropy $H(\cos\theta_{\mathrm{LB}}, \phi_{\mathrm{LB}})$ distributions at (a) 337 nm, (b) 365 nm, (c) 385 nm, (d) 420 nm, (e) 450 nm and (f) 500 nm.

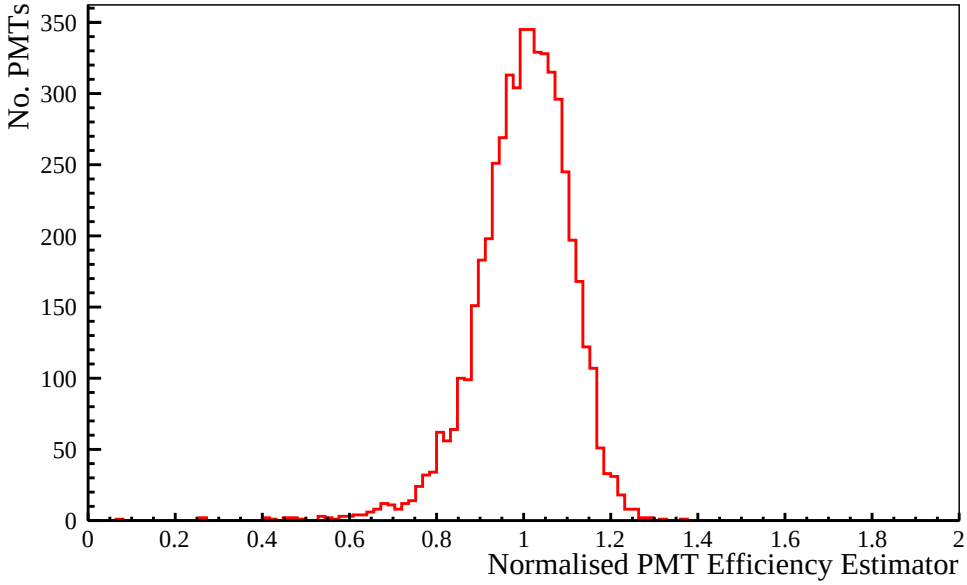

Figure 4.14: Distribution of the extracted OCA efficiencies for the internal July 2018 laserball scan. The efficiencies for each PMT were averaged across all laserball runs.

flections from the PMT-concentrator assembly. As shown in Figure 4.1, the time residual distribution for a central laserball run shows two prominent features produced by the PMTs: a specular reflection peak and an earlier peak coming from a preferred reflection mode named "35 degree PMT reflections", referring to the typical outgoing angle of photons with normal incidence.

The parameterization was done by, first, studying the outgoing angles of photons impacting the full 3D PMT model using simulations. The smear around the two reflection modes, as well as their evolution as a function of incident angle were encoded as free parameters in the parameterization model. The parameters were tuned to the data time residual distributions at longer PMT hit times, compatible with the detection of photons that suffered previous reflections on other PMTs. The time residual distributions were obtained from 420 nm laserball runs at four radial positions from the center to the edge of the AV. This study also allowed to obtain reflection probabilities as function of incident angle, which are an input to the grey disc PMT model. Despite the simplicity of the reflection parameterization for the PMT-concentrator assembly, the late light distribution in the Monte Carlo shows a good agreement with the data, as can be seen in Figure 4.15.

4.5 Validating the detector response model with the ^{16}N source

The optical properties of the SNO+ detector are responsible for variations of the energy response with radial position. This is illustrated in a simplified way by Figure 4.16, which shows how each parameter of Equation 4.4 independently affects the occupancy as a function of radial position. The curves are the sum of the calculated occupancy for all PMTs as a function of event radial position, divided by the summed occupancy for an event at the center. Comparing the total

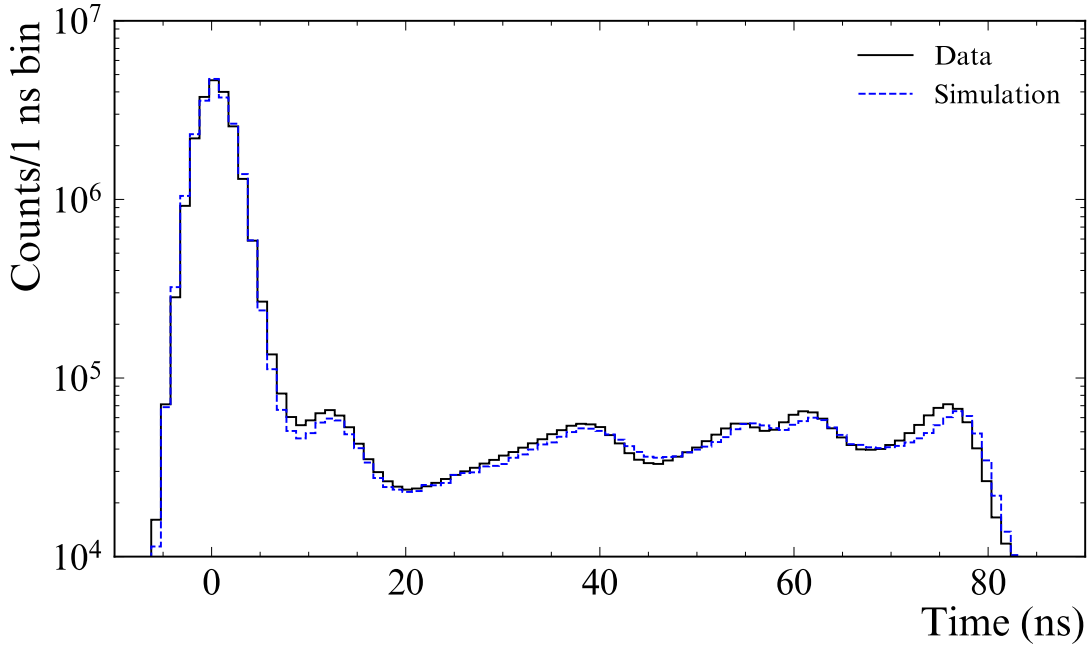

Figure 4.15: Time residual distribution for a central laserball run at 420 nm from data (black) and a simulation (blue) after tuning the SNO+ Monte Carlo with the measured optical parameters and adding the parameterization for the PMT reflection model. The peaks at ∼63 and ∼75 ns correspond to the preferred 35 degree reflection and to the specular reflection of the PMT-concentrator assembly, respectively, and were the reference for calibrating the MC PMT reflection model.

model occupancy (Equation 4.4), calculated using the optical calibration measurements at a single wavelength, with the occupancy curves calculated for each parameter gives an insight into which optical properties contribute the most for the overall detector response variations with position. Figure 4.16 shows that these are the PMT-concentrator assembly angular response and the effective acrylic attenuation. The variations of the detector response with position are one of the main contributors to the energy scale systematic uncertainty.

After tuning the SNO+ Monte Carlo with the measured optical parameters, the detector model was validated by comparing the number of prompt hits (nHits) created by ^{16}N source events in data with simulations, at different positions inside the AV. The comparison using nHit, instead of energy, avoids effects inherent to the event reconstruction. The ^{16}N data selection criteria focused on prompt PMTs with time residual between -10 and 8 ns, which is the prompt time window used for energy reconstruction in SNO+ (prompt nHit). The detector state at the time of the ^{16}N runs was also accounted for in this validation, by using only online channels, and with valid time and charge calibrations.

Figure 4.17 shows the comparison of the mean number of prompt hits in data and simulation as a function of the ^{16}N source position along two horizontal axes and the vertical axis of the detector. Overall, the variation of the mean number of prompt hits with position follows the trend depicted in Figure 4.16. As the calibration source moves away from the center, slightly more prompt light is collected relative to the central position. This increase is a direct consequence of the PMT angular response. Light produced away from the center of the detector will arrive to the PMTs with a wider range of incidence angles, in contrast to light produced at the center which mostly hit the PMTs with a normal incidence angle. The concentrators increase

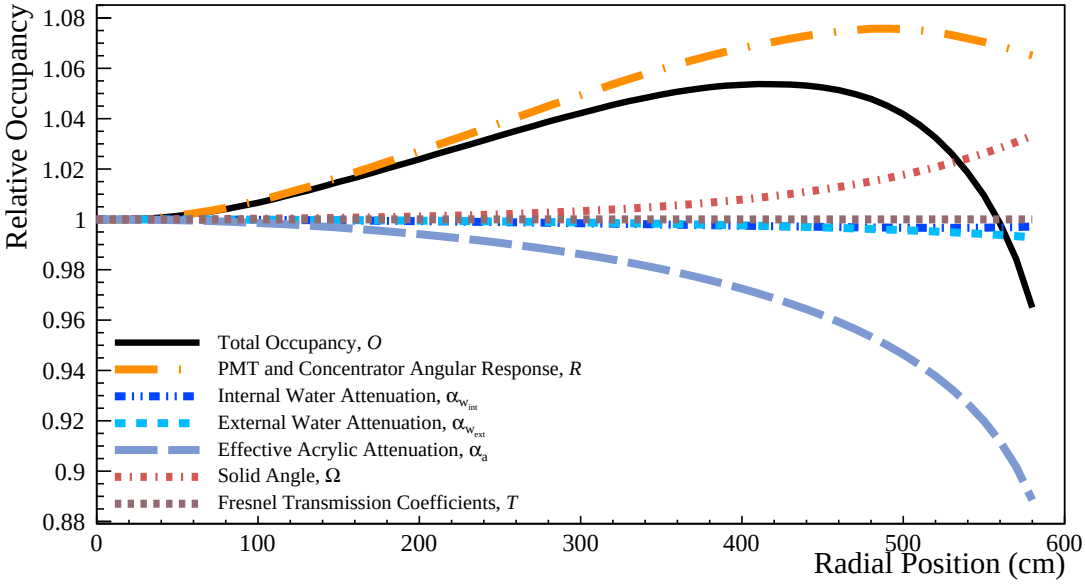

Figure 4.16: Contribution of the different optical model parameters to the integrated occupancy of all PMTs, as a function of radial position. The occupancy at each position is normalized by the occupancy at the center of the detector.

the light collection efficiency, thus increasing the number of prompt hits. On the other hand, in positions closer to the AV, the average number of hits decreases, mainly due to optical effects in the acrylic boundary. At high positions, this decrease is more accentuated due to the complex optics of the AV neck.

Figure 4.18 shows the ratio between the prompt hits in data and simulation as a function of the ^{16}N source axial position. An agreement better than 1% is found, validating the measured optical parameters. It is worth noting the good agreement in the $+z$-axis, in particular at larger axial positions where the data are affected by the optical properties of the acrylic vessel neck, which is not as UV transparent as the rest of the AV. Figure 4.19 shows the volume weighted distribution of the ratios, up to a radius of 5.5 m, from which it is possible to evaluate the contribution of the nHit position dependence to the energy scale systematic uncertainty. Adding the mean offset and the distribution width yields an uncertainty for the position dependence of the nHit of 0.6%.

4.6 Impact of the calibration on the water phase analyses

After the results of this analysis were used to calibrate the water phase detector model and reconstruction algorithms, the water phase data was reprocessed and new simulations were produced. At the time of writing, these are being used to update the water phase physics analyses: the invisible nucleon decay searches, the ^{8}B solar neutrino measurements and the measurement of reactor antineutrinos. The published results of the searches for nucleon decay in [141] reported a total energy scale uncertainty of 2.0%, dominated by the variation with position and the statistical uncertainty of the calibration data set. After the optical calibration, the total en-

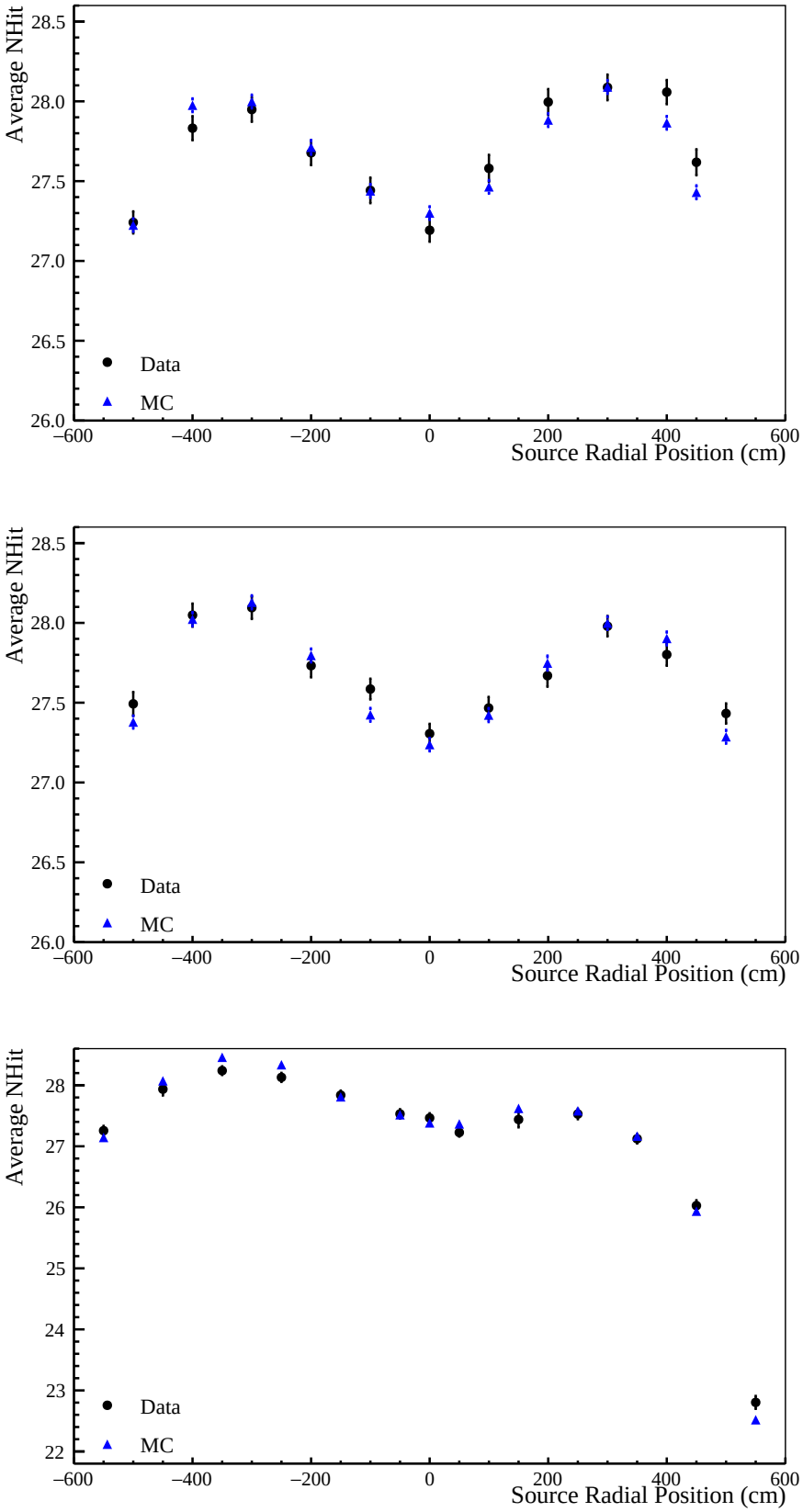

Figure 4.17: Comparison between the mean number of prompt hits of the ^{16}N source in data (black) and Monte Carlo (blue), as a function of axial position along the horizontal x axis (top), the horizontal y axis (middle) and the vertical z axis (bottom).

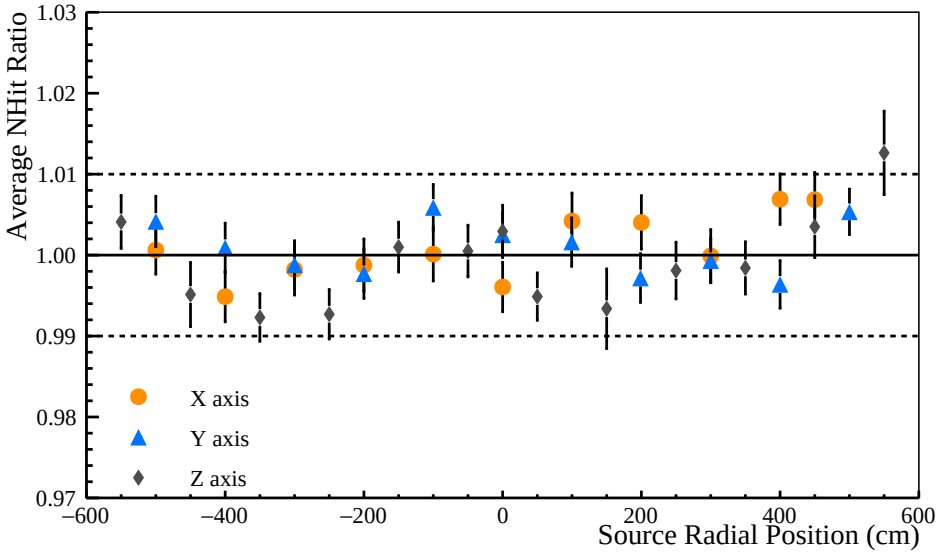

Figure 4.18: Ratio of the mean prompt number of hits of the ^{16}N source in data over Monte Carlo, as a function of axial position along the horizontal x and y axes and the vertical z axis, in orange, blue and grey, correspondingly. The horizontal dashed lines denote 1% deviations.

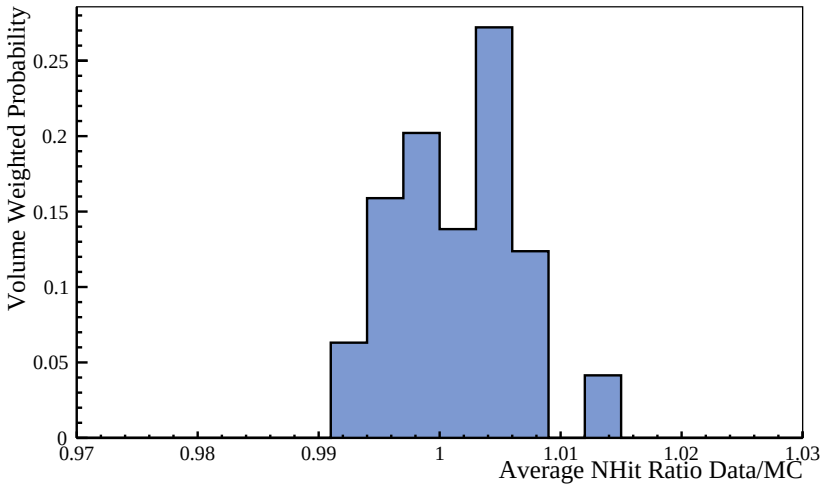

Figure 4.19: Distribution of the ^{16}N prompt nHit ratios between data and Monte Carlo weighted by volume, up to a source deployment radius of 5.5 m.

ergy scale systematic uncertainty is reduced to 1.02% [160]. In the ^{8}B solar neutrino published results [163], the reported total energy scale systematic was 3.9%. After the calibration, the uncertainty is reduced to less than 1.06%, depending on the energy threshold applied and water phase dataset used. These results show that SNO+ was able to minimize the water phase energy scale systematic to $\leq 1\%$, as was the case for the SNO detector [154, 177].

Chapter 5

The background model of the SNO+ scintillator phase

Present in all the SNO+ detector materials are trace amounts of naturally occurring radioactive isotopes, whose decays cover a wide range of the observed energy spectrum, affecting the sensitivity to the different physics topics which SNO+ aims to explore. In particular, the sensitivity to the $0\nu\beta\beta$ can be strongly limited by the background counting rate in the ROI. Even though the ^{130}Te Q-value is high enough to be away from most low-energy natural radioactivity, the limited energy resolution will result in some backgrounds spilling into the ROI. Furthermore, if a $0\nu\beta\beta$ is observed during the Te-loaded phase, a demonstration of the background model is crucial for a discovery claim.

Therefore, the accuracy of the physics analyses relies on having a complete and detailed model of the backgrounds present in the experiment. This is accomplished by identifying, locating and measuring the levels of the multiple sources of background. The background sources in SNO+ can be divided into two main categories – internal and external. Internal backgrounds are caused by impurities and interactions within the AV internal volume. External backgrounds are caused by impurities of the detector components surrounding the AV, including the acrylic itself. The external backgrounds were extensively characterized and measured during the SNO+ water phase. Since these sources are not expected to change during the lifetime of the experiment, their measurements can be propagated to the following phases.

When the AV started being filled with liquid scintillator, measuring and monitoring the backgrounds in the scintillator volume became the highest priority for SNO+. These measurements were crucial to verify that the liquid scintillator meets the radiopurity requirements prior to the ^{130}Te isotope loading, and to monitor the decay of the radon daughters that entered the detector during the fill operations. Despite the challenging detector configuration, the partial fill period, with the AV nearly half-filled with scintillator, provided the ideal stability conditions to start developing the scintillator background model. This allowed to perform a solar neutrino analysis using the data taken during this period, which is the subject of Chapter 6, and to perform a $0\nu\beta\beta$ *target-out analysis*. The target-out analysis compared the observed events in the ROI to the predictions of the background model, in order to verify that there were not any unexpected background sources present in the scintillator, and to demonstrate that the backgrounds

contributions to the $0\nu\beta\beta$ ROI were well understood. Even though the background model of the partial fill period is not entirely representative of the final Te-loaded phase, this study was crucial to validate the SNO+ analysis techniques for the $0\nu\beta\beta$ searches.

This Chapter starts by introducing the radioactive backgrounds sources in the SNO+ experiment in Section 5.1. This discussion is complemented by Appendix A, which contains the target background rates for the Te-loaded phase, as well as new calculations of the cosmogenically induced backgrounds, and background rate constraints from the analysis of the water and scintillator data. Section 5.2 presents the background model developed for the partial fill period, including the results of the Bi-Po coincidence tagging methods and sideband evaluations of the exclusive partial fill background sources which do not exist in the final scintillator background model. These included the radioactivity from the internal water below the scintillator and from hardware needed for the filling operations. Finally, Section 5.3 presents the results of the $0\nu\beta\beta$ target-out analysis.

5.1 Radioactive background sources in SNO+

5.1.1 Internal backgrounds

Internal backgrounds are defined as events generated by the decay of radioactive isotopes contaminating the scintillator cocktail. Mine air entering the AV volume through small leaks, or the deployment of calibration sources into the AV, might lead to additional internal contamination. The main internal backgrounds come from isotopes belonging to the ^{238}U and ^{232}Th chains. These naturally occurring isotopes are expected to be in secular equilibrium with the top part of the chain. However, Rn exposure can break secular equilibrium as it decays to the long lived ^{210}Pb ($T_{1/2} = 22.2$ years), whose daughters will be major backgrounds for many of the SNO+ physics analyses. An additional source of ^{210}Pb comes from radon daughters which have deposited onto the AV surface during construction and the transition years from SNO to SNO+, when the AV was drained and exposed to air. When the liquid scintillator is in contact with the AV, the ^{210}Pb and its daughters can leach into it. Other internally occurring backgrounds are ^{40}K, naturally present in the scintillator, and ^{39}Ar and ^{85}Kr, which are contaminants from exposure of the LAB to air. Each internal background source is discussed below.

5.1.1.1 ^{232}Th chain

Thorium-232 (^{232}Th) is a naturally occurring isotope with a half-life of 1.4×10^{10} years. The thorium chain, shown in Figure 5.1, is typically assumed to be in secular equilibrium, as the only noble element, ^{220}Rn, has a half-life of less than one minute. Therefore, even when ^{220}Rn occasionally ingresses the detector volume, the secular equilibrium will be reached quickly.

The isotopes contained in the thorium chain which are of most concern for the SNO+ measurements are ^{212}Bi and ^{208}Tl. ^{212}Bi has a half-life of 60.6 minutes and in 64% of the cases it β-decays to ^{212}Po with a Q-value of 2.25 MeV. Then ^{212}Po, with a half-life of 0.299 μs, α-decays with a Q-value of 8.95 MeV, which will be quenched by the scintillator resulting

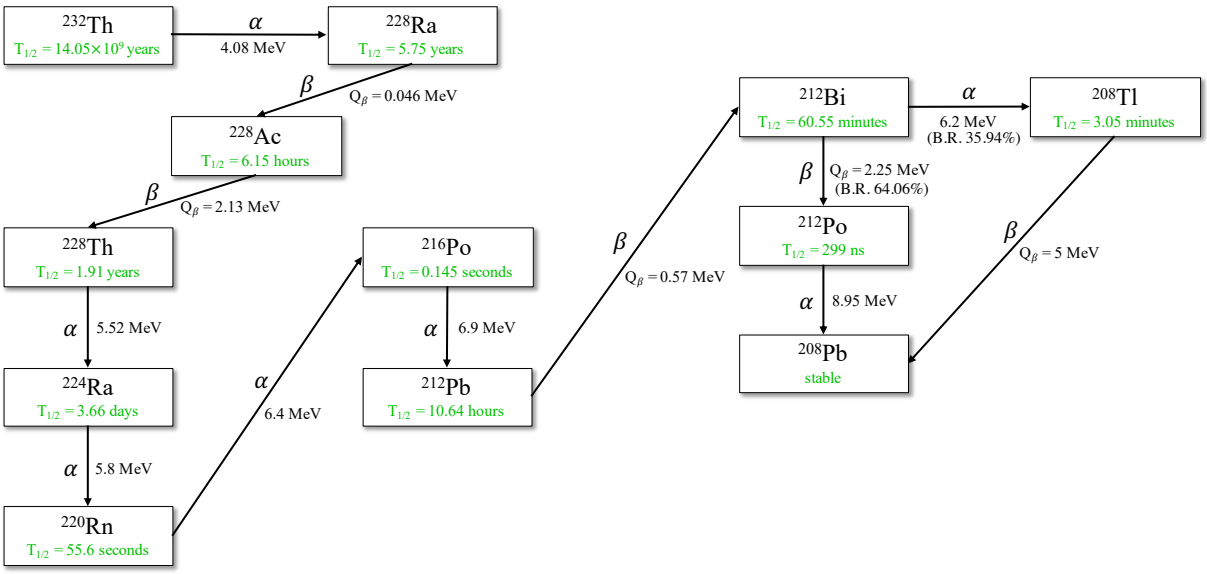

Figure 5.1: Diagram of the ^{232}Th decay chain, including the life-lives, maximum released energies, and type of decays for each isotope.

in an observed energy below 1 MeV. The β-α delayed coincidence can be used to reject this background at the analysis level, as will be discussed in Section 5.2.1. Furthermore, these coincidences are one of the methods used to estimate the ^{232}Th abundance in the scintillator (when in secular equilibrium).

In addition to the background introduced by ^{212}Bi, in SNO+ the pileup between the Bi and Po is of interest. Due to the very short half-life of the ^{212}Po, almost half of the ^{212}Bi-^{212}Po fall in the same trigger window (*in-window* events), being recorded as a single event with energy equal to the sum of the energies of the beta and quenched alpha. This pileup effect, discussed in more detail below, is problematic since it can push events into the $0\nu\beta\beta$ ROI. The ^{212}Bi-^{212}Po in-window events can be rejected from the data using the timing distribution of the PMTs.

In the remaining 36% of the times, ^{212}Bi α-decays to ^{208}Tl with a Q-value of 6.21 MeV, which will also be quenched. ^{208}Tl has a half-life of 3.1 minutes and β-decays to ^{208}Pb with a Q-value of 5.0 MeV. Given its high Q-value, the ^{208}Tl is a major background for the ^{8}B solar neutrinos analysis.

5.1.1.2 ^{238}U chain

Uranium-238 (^{238}U) is a naturally occurring isotope with a half-life of 4.47×10^9 years. Its decay chain is illustrated in Figure 5.2. The equilibrium of the uranium chain is broken if the scintillator is exposed to the surrounding mine air, which contains ^{222}Rn. The ^{222}Rn has a half-life of 3.82 days, and is followed by a cascade of short lived nuclei down to ^{210}Pb. Therefore, equilibrium of this intermediate part of the chain can be restored within a few weeks.

^{210}Pb is often encountered out of secular equilibrium because of its relatively long half-life (22.26 years) compared to the isotopes in the ^{222}Rn section of the chain. With a Q-value of 63.5 keV, ^{210}Pb itself is not a problem. However, its daughters can be significant sources of background. ^{210}Bi is a β emitter with a Q-value of 1.2 MeV, spanning the entire low-energy

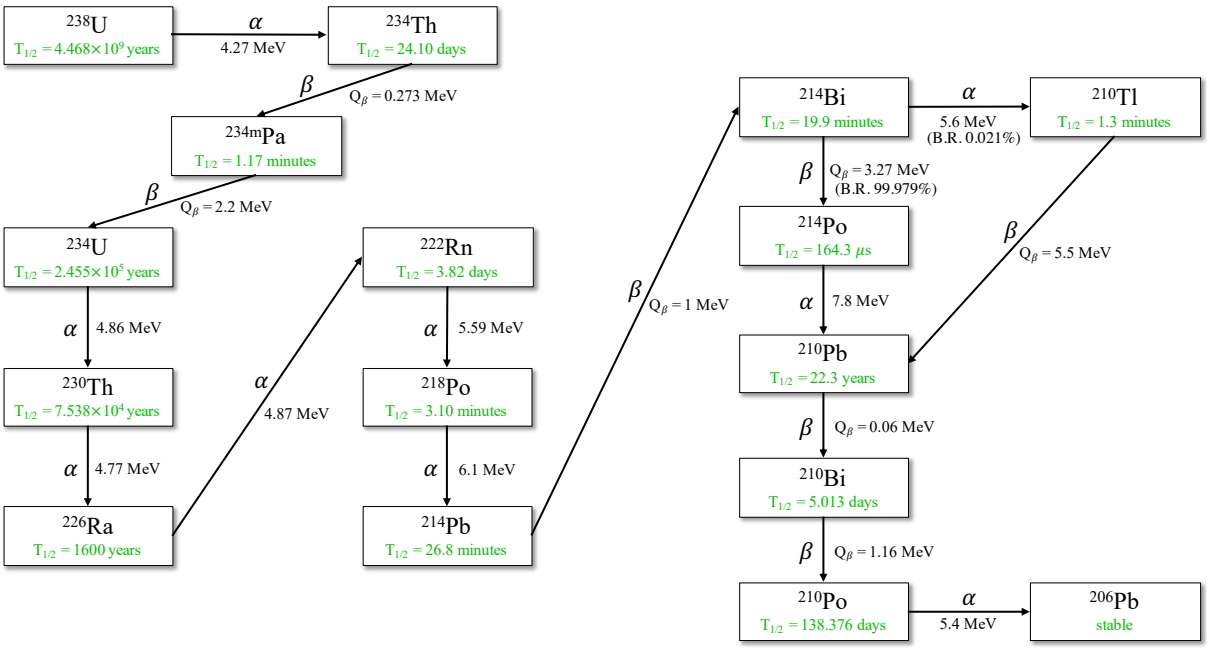

Figure 5.2: Diagram of the ^{238}U decay series, including the life-lives, maximum released energies, and type of decays for each isotope.

spectrum of solar neutrinos. ^{210}Bi decays to ^{210}Po, an α emitter with an energy of 5.3 MeV. Because α particles in liquid scintillator are quenched, the ^{210}Po peak is also present within the low-energy part of the spectrum.

Similarly to the ^{232}Th, estimating the concentration of the ^{238}U chain isotopes in the scintillator also involves utilizing a fast decay sequence, this time ^{214}Bi-^{214}Po space and time correlated events, provided that there is secular equilibrium down to the ^{214}Bi. ^{214}Bi has a half-life of 19.9 minutes and decays via two branches. In 99.979% of the cases, it β-decays to ^{214}Po, with a Q-value of 3.27 MeV. Shortly after, the ^{214}Po, with a half-life of 164.3 μs, decays emitting a 7.7 MeV α-particle. In 0.021% of occasions, ^{214}Bi α-decays to ^{210}Tl (Q-value of 5.62 MeV). ^{210}Tl has a half-life of 1.3 minutes and beta-decays to ^{210}Pb with a Q-value of 5.5 MeV.

The ^{214}Bi is a direct background to the $0\nu\beta\beta$ ROI but, similarly to the ^{212}Bi-^{212}Po, the β-α delayed coincidence is used to reject this background. The coincidence tagging method is described in detail in Section 5.2.1. Furthermore, ^{214}Bi-^{214}Po pileup can also be rejected from the data using the timing distribution of the PMTs.

5.1.1.3 Leaching backgrounds and (α,n) reactions

During the construction phase of SNO, and during the years between draining the SNO experiment in 2006 and refilling for SNO+ in 2016, the inside of the AV was exposed to mine air. This led to airborne ^{222}Rn depositing in the inner surface of the AV. Within days of the exposure, the daughters of ^{222}Rn kicked back and implanted in the surface, resulting in a layer of ^{210}Pb which, with its long half-life of 22.3 years, steadily feeds the detector with its daughters: ^{210}Po and ^{210}Bi. The majority of the signals from these backgrounds are expected to be located at the edge of the inner surface of the AV, and for that reason they usually enter the category

of AV external backgrounds (Section 5.1.2). However, over time diffusion processes can move some of them further into the scintillator, depending on the temperature. Since the quenched energy deposited in these decays is low, they are only a background for the low-energy analysis of SNO+ and do not pose a direct threat to the $0\nu\beta\beta$ ROI. However, a large rate of these backgrounds can produce pileup, and can affect the performance of the α-β coincidence tagging methods, by increasing the number of fake coincidences and, by consequence, signal sacrifice.

Additionally, the leaching backgrounds are a major source of α particles, particularly the ^{210}Po decay, which can give rise to (α,n) reactions. In these processes, the αs interact with atoms in the scintillator, producing free neutrons. In LAB, the most common reactions are

$$\alpha + {}^{13}\mathrm{C} \rightarrow {}^{16}\mathrm{O} + n, \tag{5.1}$$

$$\alpha + {}^{18}\mathrm{O} \rightarrow {}^{21}\mathrm{Ne} + n. \tag{5.2}$$

The ^{16}O and ^{21}Ne are often produced in excited states, leading to de-excitation products, most commonly γ-rays, which produce a prompt signal in the detector. This is followed by a delayed signal caused by the neutron being captured by a hydrogen nucleus with a time constant of $\sim$ 200 μs, which is also left in an excited state and de-excites with the emission of a characteristic 2.22 MeV γ. Due to the two signals, the (α,n) reactions can be rejected using coincidence tagging methods similar to the ones used for the ^{212}Bi-^{212}Po/^{214}Bi-^{214}Po. The rate of (α, n) reactions will mainly depend on the contamination of ^{210}Po in the tellurium and LAB and the leaching rates.

5.1.1.4 Internal ^{39}Ar, ^{40}K and ^{85}Kr

Other internal backgrounds that are important for SNO+, in particular for the low-energy analyses, are ^{39}Ar, ^{40}K and ^{85}Kr. ^{40}K has a half-life of 1.248×10^{9} years, and it naturally occurs in both the scintillator and the detector materials. It has two decay branches: in 89.28% of cases it β-decays to stable ^{40}Ca with a Q-value of 1.311 MeV:

$${}^{40}\mathrm{K} \rightarrow {}^{40}\mathrm{Ca} + e^{-} + \bar{\nu}_e. \tag{5.3}$$

In the other 10.72% of cases, it decays to stable ^{40}Ar via electron capture, emitting a 1.460 MeV gamma:

$$\begin{aligned} {}^{40}\mathrm{K} + e^{-} &\rightarrow {}^{40}\mathrm{Ar}^{*} + \bar{\nu}_e, \\ {}^{40}\mathrm{Ar}^{*} &\rightarrow {}^{40}\mathrm{Ar} + \gamma. \end{aligned} \tag{5.4}$$

^{39}Ar is a product of cosmogenic activation of ^{40}Ar in the atmosphere. It can enter the scintillator when it comes into contact with air or the nitrogen used in the purification process. This isotope has a half-life of 269 years and β-decays to stable ^{39}K with a Q-value of 0.585 MeV:

$${}^{39}\mathrm{Ar} \rightarrow {}^{39}\mathrm{K} + e^{-} + \bar{\nu}_e. \tag{5.5}$$

^{85}Kr is a product of nuclear fission. It is present in the atmosphere due to current nuclear fuel

reprocessing, nuclear weapons testing and accidents in nuclear plants. With a half-life of 10.739 years, ^{85}Kr β-decays to ^{85}Rb with a Q-value of 0.687 MeV (99.57% B.R.):

$$^{85}\text{Kr} \rightarrow {}^{85}\text{Rb} + e^- + \bar{\nu}_e. \tag{5.6}$$

With a small branching ratio of 0.43%, ^{85}Kr decays into the meta-stable ^{85m}Rb, emitting a β particle with maximum kinetic energy of 173 keV. The ^{85m}Rb then decays to its ground state by emitting a 514 keV γ-ray with 1.015 μs half-life.

$$\begin{aligned} ^{85}\text{Kr} &\rightarrow {}^{85m}\text{Rb} + e^- + \bar{\nu}_e, \\ ^{85m}\text{Rb} &\rightarrow {}^{85}\text{Rb} + \gamma. \end{aligned} \tag{5.7}$$

This fast β-γ sequence can be used to obtain an independent measurement of the ^{85}Kr concentration. With an average rate of 1 Bq/m^3, even extremely small air exposures during the detector filling operations would yield significant contamination. Since this isotope gets into the LAB through air, its amount can be minimised by reducing the contact time and by degassing the scintillator.

5.1.1.5 Pileup events

When two or more events are detected in the same trigger time window, they are reconstructed in SNO+ as a single event. This type of events are called *pileup* or *in-window* events. The energy of a pileup event is less or equal to the sum of the individual energies of the events which occurred simultaneously, depending on whether the events are partially or fully detected in the same trigger window. This can happen both for multiple independent decays or interactions that happen inside the detector in close temporal proximity, as well as connected processes in a decay chain such as the Bi $\rightarrow$ Po $\rightarrow$ Pb decays.

Figure 5.3 illustrates the difference between single trigger events, usually called out-of-window events when referring to the Bi-Po decays, and in-window/pileup events. The PMT hits created by the pileup events can either be fully contained within one trigger window or leak into the next trigger window (*retrigger*). The latter happens when the second event contributing to the pileup is created close to the end of the trigger window. The main feature to distinguish between pileup and single events are the hit time distributions, which will be significantly different in shape.

5.1.2 External backgrounds

External backgrounds are isotopes present in the external water, the acrylic vessel volume, the PMTs and the rope systems. Charged particles from external radioactive decays are attenuated in the external water and acrylic before reaching the scintillator volume. The same is not true for high energy gammas, such as the ones originating from ^{40}K, ^{214}Bi from the uranium chain, and ^{208}Tl from the thorium chain.

Only a small fraction of these decays result in a signal inside the scintillator volume and,

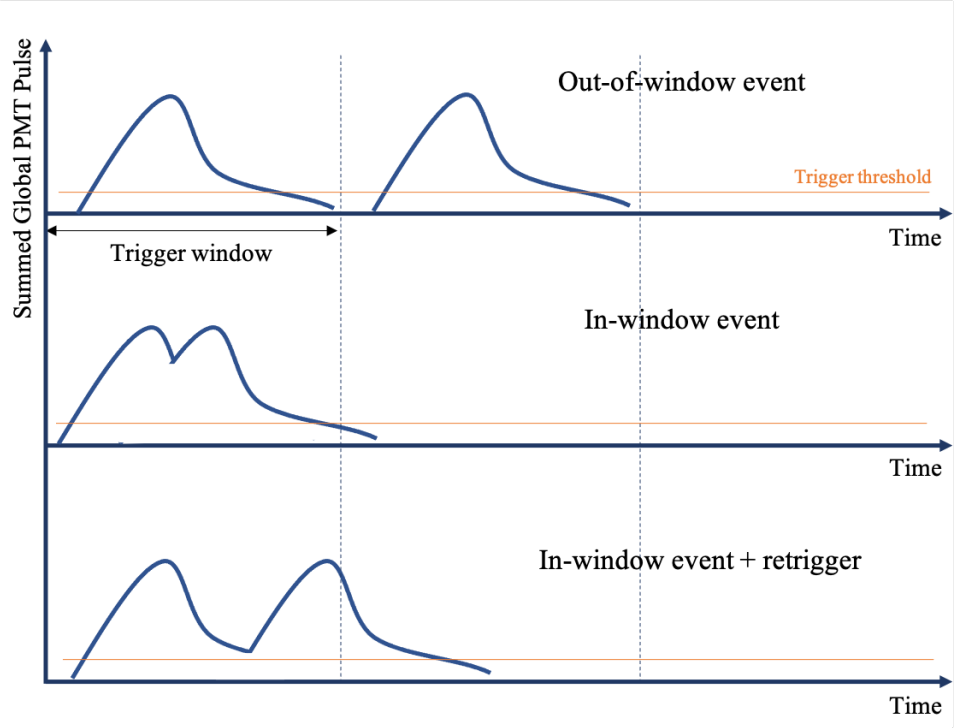

Figure 5.3: Illustration of the difference between out-of-window (top), in-window (centre) and retrigger (bottom) events.

typically, the number of events from external backgrounds decreases exponentially towards the center of the AV. The main strategy for external background mitigation is fiducialisation, where only events inside certain fiducial volumes are used in the analysis. During the water phase, two independent analyses, using dedicated sidebands shown in Figure 5.4, were performed to measure the U and Th components from the AV, hold-down ropes and water shielding. The measured rates for the external backgrounds are collected in Table A.2. These measurements, and the rates for the other external background sources, are going to be validated and further constrained during the scintillator phase.

5.1.3 Cosmogenically induced backgrounds

Interactions of cosmic neutrons, protons and muons with stable elements within the liquid scintillator cocktail produce radioactive isotopes, referred to as *cosmogenics*. The majority of those interactions occur while the scintillator components are on the surface. However, cosmogenic backgrounds can also be produced underground due to spallation by the few high-energy muons (∼3/hour) that cross the SNO+ detector. The resultant isotopes are either short-lived and quickly decay away, or are long-lived and have to be extracted from the scintillator components in the purification plant.

The main expected cosmogenic background in the scintillator is ^{7}Be ($T_{1/2}$ = 53.24 d, Q-value of 0.862 MeV), produced from activation of carbon, which can be efficiently removed by over 99% by the scintillator purification plant. An isotope which is naturally contained in the scintillator but that can also be cosmogenically induced is ^{14}C ($T_{1/2}$ = 5730 years, Q-

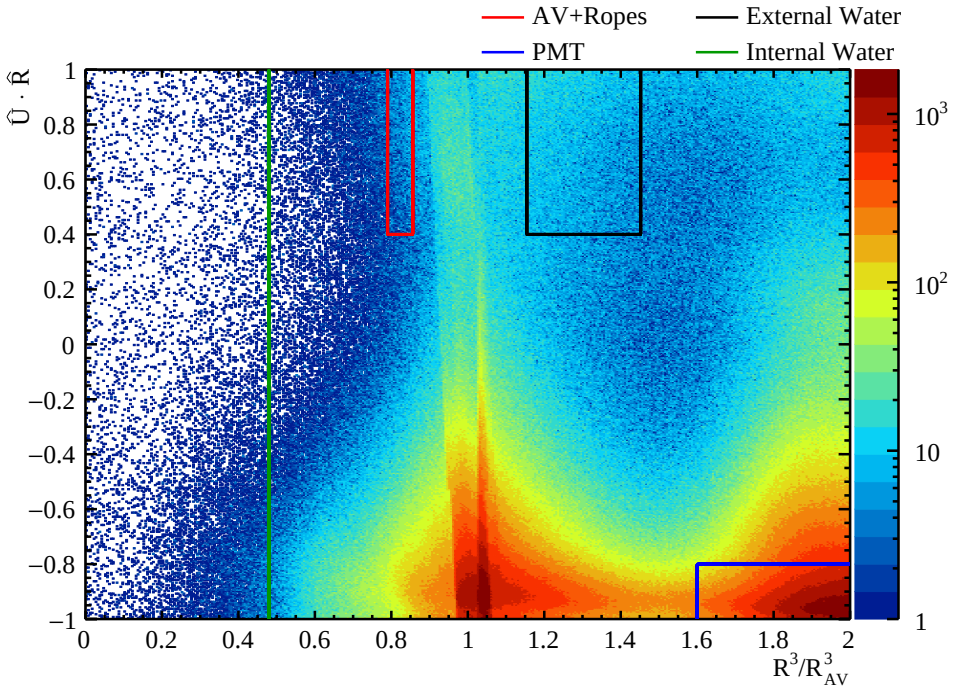

Figure 5.4: Boxes used for the analysis of the external backgrounds during the water phase. The events are distributed in $\hat{U}\cdot\hat{R}$ and R^3, where U is the reconstructed direction and R is the radial position. Figure from [178].

value of 0.156 MeV). SNO+ expects a $^{14}C/^{12}C$ ratio of 10^{-18}, similar to Borexino [179], since both experiments obtain the liquid scintillator from old petroleum fields, as petroleum is a raw product for LAB. Even though ^{14}C will not be a background for the majority of the analyses in SNO+, its high rate of a few hundred Hz can contribute to pileup backgrounds.

Muon interactions with the scintillator within the detector produce cosmogenic backgrounds such as ^{10}C ($T_{1/2}$ = 19.3 seconds, Q-value of 3.6 MeV), ^{11}Be ($T_{1/2}$ = 13.8 seconds, Q-value of 11.5 MeV) and ^{11}C ($T_{1/2}$ = 20 minutes, Q-value of 0.96 MeV). Vetoing the detector for a few minutes after each muon event rejects the majority of these backgrounds. The longer-lived ^{11}C isotopes are produced along with muons, generating prompt and delayed signals, and can therefore be rejected using coincidence tagging techniques.

An important set of cosmogenically induced backgrounds are the isotopes produced by spallation reactions on tellurium while it is on surface. These backgrounds are particularly dangerous for the $0\nu\beta\beta$ searches as they scale with tellurium loading in the same way as is expected from the signal. Furthermore, decays of some of these isotopes can appear in the $0\nu\beta\beta$ ROI. A list of these isotopes is compiled in Table 5.1.

To mitigate the production of these isotopes, and allow the majority to decay away, the telluric acid which is going to be used by SNO+ has been stored underground for several years after its production. The telluric acid arrived to the underground laboratory in three batches. The first batch (B1) arrived in January 2015 containing 0.99 tonnes of natural tellurium. In August 2016 arrived the second batch (B2) with 1.09 tonnes of natural tellurium. And finally, in June 2018 the third batch (B3) arrived with 2.2 tonnes. The batches have approximately spent 12, 13 and 14 months on surface (from production to delivery), respectively, during which time the tellurium was constantly bombarded with cosmic rays.

Table 5.1: Possible background nuclides induced by cosmogenic neutrons and protons on a natural Te target, from [145].

Isotope	Decay Mode	B.R. (%)	Q-Value (MeV)	$T_{1/2}$ (days)
^{22}Na	EC, β^+	100	2.84	950.6
^{26}Al	EC, β^+	100	4.00	2.62×10^{8}
^{42}K (direct and daughter of ^{42}Ar)	β^-	100	3.53	0.51 (1.2×10^{4})
^{44}Sc (direct and daughter of ^{44}Ti)	EC, β^+	100	3.65	0.17 (2.16×10^{4})
^{46}Sc	β^-	100	2.37	83.79
^{56}Co	EC, β^+	100	4.57	77.27
^{58}Co	EC, β^+	100	2.31	70.86
^{60}Co (direct and daughter of ^{60}Fe)	β^-	100	2.82	1925.27 (5.48×10^{8})
^{68}Ga (direct and daughter of ^{68}Ge)	EC, β^+	100	2.92	4.70×10^{-2} (271)
^{82}Rb (daughter of ^{82}Sr)	EC, β^+	100	4.40	8.75×10^{-4} (25.35)
^{84}Rb	EC, β^+ (96.2%)	96.2	2.68	32.77
^{88}Y (direct and daughter of ^{88}Zr)	EC, β^+	100	3.62	106.63 (83.4)
^{90}Y (direct and daughter of ^{90}Sr)	β^-	100	2.28	2.67 (1.05×10^{4})
^{102}Rh (direct and daughter of ^{102m}Rh)	β^- (20%), EC, β^+ (80%)	78	1.15 (20%), 2.32 (80%)	207.3
^{102m}Rh	EC (99.77%)	99.77	2.46	1366.77
^{106}Rh (direct and daughter of ^{106}Ru)	β^-	100	3.54	3.47×10^{-4} (371.8)
^{110m}Ag	β^- (98.64%)	98.64	3.01	249.79
^{110}Ag (daughter of ^{110m}Ag)	β^- (99.7%)	99.7	2.89	2.85×10^{-4}
^{124}Sb	β^-	100	2.90	60.2
^{126m}Sb (direct and daughter of ^{126}Sn)	β^- (86%)	86	3.69	0.01 (8.40×10^{7})
^{126}Sb (direct and daughter of ^{126m}Sb)	β^-	100	3.67	12.35 (0.01)

Underground, the cosmic ray flux is low, meaning that the production of cosmogenics in the laboratory is very small. Considering the arrival dates, and assuming that the Te-loaded phase starts in 2023, the cosmogenics will have 8, 6.6 and 4.5 years to cooldown, for B1, B2 and B3 respectively. Using these numbers, and following the method presented in [145], the rates of the Te cosmogenics were calculated, and are presented in Appendix A.

Even after the long cooldown times, the isotopes with half-lives on the timescale of years or that are fed by long-lived parents will still be present and contaminate the scintillator cocktail. These include ^{22}Na, ^{42}K, ^{60}Co, ^{68}Ga, ^{90}Y, ^{102m}Rh, ^{102}Rh and ^{110m}Ag, all of which will contribute to the background index in the $0\nu\beta\beta$ ROI. However, prior to deployment, these contaminants will be removed through purification of the telluric acid. The purification process is expected to reduce the rate of the cosmogenics by a factor in the range from 10^5 to 10^8, depending on the isotope. The expected rates after purification are also included in Appendix A.

5.2 Background model of the partial fill period

The unusual detector configuration during the partial fill period, schematized in Figure 5.5, presented new challenges and required a more complex model of the detector and its backgrounds than what is expected for the scintillator phase. Filled half-way through, the wide circular scintillator-water interface created optical effects difficult to model with the limited knowledge available without deploying calibration sources internally, which made reconstruction of the events near the interface very complex. Furthermore, radioactivity within the internal water became a source of backgrounds for the scintillator volume. Particles, in particular gammas from radioactive decays within the water could travel and reconstruct deep inside the

scintillator, making it difficult to remove them by fiducial volume cuts without considerably sacrificing the statistics available for the analyses. An additional source of backgrounds during this period was the PFA tube, with a diameter of 2.5 cm and 1.6 mm wall-thickness, temporarily deployed to remove the internal water during the fill (described in Section 3.4). Even though the tube went through strict cleaning procedures, natural radioactivity contained in the tube's material created signals in the scintillator volume. As will be described in Sections 5.2.2 and 5.2.3, the internal water and PFA tube backgrounds in the scintillator were verified and measured by sideband analyses.

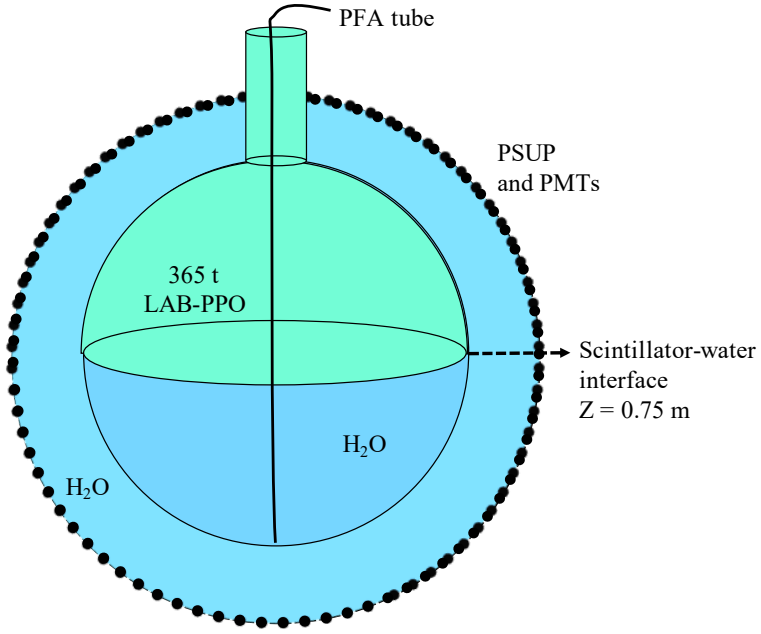

Figure 5.5: Schematic of the SNO+ detector configuration during the partial fill period, including the deployed PFA tube used for water extraction during the fill operations. The dotted arrow points the scintillator-water interface during this period, at Z = 0.75 m.

The intrinsic backgrounds of the liquid scintillator, including the U and Th concentrations, were measured and monitored during the fill using dedicated analyses which either looked at specific volume and/or energy regions, or made use of coincidence tagging methods. These measurements were a crucial first test to verify if the initial background levels of the scintillator were within the requirements for the Te-loaded phase. However, a common challenge for the majority of these analyses was ^{222}Rn, which would generally be seen ingressing the detector each time fresh LAB was added to the AV. The ^{222}Rn ingress and subsequent decay was monitored by tagging the ^{214}Bi-^{214}Po coincidences. The partial fill period provided about 7 months where the detector was stable (in terms of electronics and PPO concentration), allowing the ^{222}Rn to decay to low enough levels for the measurement of the intrinsic U and Th. These measurements yielded a concentration of $(4.7\pm1.2)\times10^{-17}$ gU/gLAB for the ^{238}U chain, and of $(5.3\pm1.5)\times10^{-17}$ gTh/gLAB for the ^{232}Th chain. The background rates measured during the partial fill period, which are relevant for the work presented in this thesis, are listed in Table 5.2. These rates are in agreement with the scintillator purity levels required for the $0\nu\beta\beta$ searches,

collected in Table A.1.

Table 5.2: Internal background rates measured during the partial fill period, within the 365 tonnes of liquid scintillator on top of ultra-pure water.

Backgrounds	Rate (Events/year)
(α,n) ^{13}C interactions in LS	4.08×10^{2}
^{238}U chain	1.44×10^{4}
^{232}Th chain	5.29×10^{3}
^{210}Bi	1.42×10^{8}
^{40}K	6.4×10^{4}

5.2.1 Bi-Po coincidence tagging in the partial fill period

Tagging the ^{214}Bi-^{214}Po and ^{212}Bi-^{212}Po coincidences allows the measurement of the U, Th and Rn levels in the scintillator, and also provides a clean sample of known events which can be used for multiple studies. Furthermore, the tagged events can be rejected from the data, allowing for a cleaner dataset for the different analyses in which they are a background.

The tagged ^{214}Bi-^{214}Po played a key role for understanding and calibrating the detector response and reconstruction algorithms during the partial fill period. They were used to measure the scintillator properties, such as the timing profile and the light yield at a PPO concentration of 0.6 g/L of LAB, and also to monitor light yield variations with position and time as the PPO was diffusing in the LAB after the fill was halted.

The coincidence tagging method starts by searching for a Bi candidate event inside a fiducial spherical cap volume, with a given radius R and height defined by a Z cut[1], as illustrated in Figure 5.6. A lower nHit cut is applied to the Bi candidate in order to reduce mistagging with ^{210}Po (peak at $\sim$120 nHits) and ^{210}Bi (endpoint at $\sim$450 nHit) events, given their large rates. The effectiveness of the tagging method comes from the ^{214}Po identification. After identifying a Bi candidate, the subsequent events are scanned to find a Po candidate. The Po decay happens in the same position as the precedent Bi decay. However, due to the position reconstruction resolution, the two decays can have different reconstructed positions. This is illustrated by Figure 5.7, showing the distribution of distances between the reconstructed positions of the Bi and Po candidates, Δr, defined as:

$$\Delta \mathrm{r} = \sqrt{(x_{\mathrm{Bi}} - x_{\mathrm{Po}})^2 + (y_{\mathrm{Bi}} - y_{\mathrm{Po}})^2 + (z_{\mathrm{Bi}} - z_{\mathrm{Po}})^2} \tag{5.8}$$

Therefore, the search of the Po is performed in a wider fiducial volume, in order to increase the probability of identifying the Po candidates reconstructed outside the Bi FV. Since the Po emits α particles at a fixed energy value, it creates a narrower and distinct peak, which is valuable to apply a strict nHit cut that reduces fake coincidences while keeping a good tagging efficiency.

[1]All the reconstructed positions (which come in the PSUP coordinate system) were corrected by the AV offset in order to translate them to the AV coordinate system. During this period, the center of the AV was 131.8 mm above the center of the PSUP.

Even though the Po α events are quenched, they create signals well above the detector energy threshold.

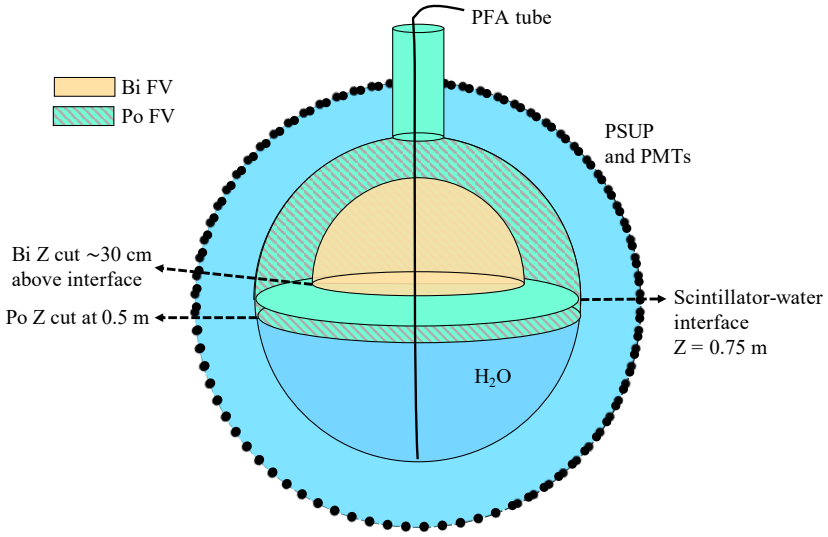

Figure 5.6: Schematic of the fiducial volumes considered for the Bi-Po coincidence tagging method during the partial fill period.

To tag a pair of events as a ^{214}Bi-^{214}Po coincidence, inter-event position (Δr) and timing (Δt) cuts are applied: the two events need to be reconstructed within 2.5 m from each other, and their time difference should be between 505 ns and 2 ms (twelve times the Po decay half-life). This tagging method, with appropriate values for the other cut parameters, can be very efficient at tagging out-of-window coincidences, not only of ^{214}Bi-^{214}Po, but also ^{212}Bi-^{212}Po (Th chain). The in-window coincidences are tagged using two strategies. In some cases, the light created by the in-window event will retrigger the detector, creating an event with low number of PMT hits. Consequently, events followed by a retrigger with nHit $>$ 40 within 505 ns are tagged[2]. It is important to note that this cut will not only tag in-window Bi-Po coincidences, but also other accidental pileup and high energy events, which create more light in the detector and thus have a higher probability of retriggering. This method, however, does not identify pure in-window events. These are only identified by looking at the event's time residuals, which will show a double peak structure. AlphaBetaLikelihood classifiers are used to reject these in-window coincidences.

The cuts, summarized in Table 5.3, were optimized using Monte Carlo simulations to maximize the tagging efficiency. This was particularly important for the target-out analysis discussed in Section 5.3. In addition to the tagging-related cuts, other general event selection cuts were applied in order to have the cleanest possible data sample. Muons crossing the detector, or events due to PMT breakdowns, create a large amount of light in the detector and, as a consequence, create events with a large nHit. These events were targeted by removing any event

[2]During the partial fill period a nHit threshold of 40 was set for the reconstruction algorithms, i.e. only 1% of the events with nHit lower than this value were reconstructed. This threshold was set due to the high rate of low energy/nHit backgrounds, whose reconstruction would considerably increase the data processing time.

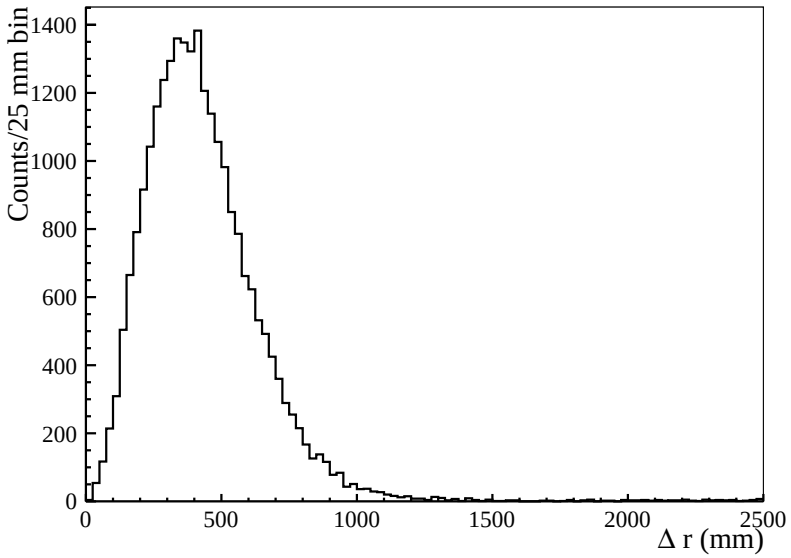

Figure 5.7: Distribution of the distance Δr between the reconstructed positions of tagged Bi and Po candidates in data.

with nHit $>$ 5000 and all the follower events in a 1 minute window. The 5000 nHit threshold was selected because no natural radioactivity or relevant physics signals are expected above this nHit value. The analysis only considered events whose position was successfully reconstructed by the partialFit fitter, and rejected events flagged by the skyShine processor, which evaluates if an event originated inside the AV neck volume. Each Bi candidate underwent data cleaning checks, where flags set by data cleaning processors are checked against an analysis mask for the partial fill in order to reject instrumental backgrounds.

The Bi-Po tagging efficiency was optimized for a fiducial volume of 84.8 m^3 (R $<$ 4 m, larger than the 3.3 m fiducial radius planned for the $0\nu\beta\beta$ analysis, and Z $>$ 1 m, about 30 cm above the water-scintillator interface level). The tagging efficiency obtained for ^{214}Bi-^{214}Po and ^{212}Bi-^{212}Po was 99.89% and 89%, respectively. The tagging efficiency for the ^{212}Bi-^{212}Po is limited by the in-window alphaBeta classifiers.

Figure 5.8 shows the nHit distribution of the Bi (red) and Po (blue) events tagged in partial scintillator fill data[3] taken from April 5$^{\text{th}}$ to October 24$^{\text{th}}$ 2020, with a total livetime of 95 days[4], in a fiducial volume of 84.8 m^3. This dataset was selected after evaluating the stability of the LAB-PPO mixing, described in more detail below. It is important to note that the tagged events include both ^{212}Bi-^{212}Po and ^{214}Bi-^{214}Po. However, due to ^{222}Rn, the tagged events are predominantly ^{214}Bi-^{214}Po coincidences.

Figure 5.9 shows the distribution of the time differences between the tagged prompt (Bi) and delayed (Po) events, Δt, whose fit with an exponential function yields a half-life measurement of (164 $\pm$ 1) μs, compatible with the expected ^{214}Po half-life of 164.3 μs. The number of accidental coincidences is about 1.4% of the total number of tagged coincidences.

[3]The analysis only includes data taken with all the detector crates online.

[4]The livetime of 95 days includes the subtraction of the time lost by the applying the muon/PMT breakdown cut.

Table 5.3: Cut variables and values for the Bi-Po tagging.

	Cut	Value
Bi candidate	Muon tagging	Reject events with nHit $>$ 5000 and followers within 1 minute window
	PartialFit valid	True
	skyShine	$>$ 1
	Data cleaning analysis mask	0x210000000242
	Radial position	$\leq$ 4.0 m
	Z coordinate	$\geq$ 1.0 m
	nHit	$\geq$ 300
	Cut	**Value**
Po candidate	In-window tagging:	
	alphaBeta212	$\leq$ 1.25
	alphaBeta214	$\leq$ 1.4
	Out-of-window tagging:	
	PartialFit valid	True
	skyShine	$>$ 1
	Radial position	$\leq$ 6.0 m
	Z coordinate	$\geq$ 0.5 m
	Retrigger tagging	Δt $\leq$ 505 ns and nHit $\leq$ 40
	Delayed candidate tagging	$\begin{cases} 505 \text{ ns} < \Delta t < 2 \text{ ms} \\ \text{nHit} \leq 150 \\ \Delta r \leq 2.5 \text{ m} \end{cases}$

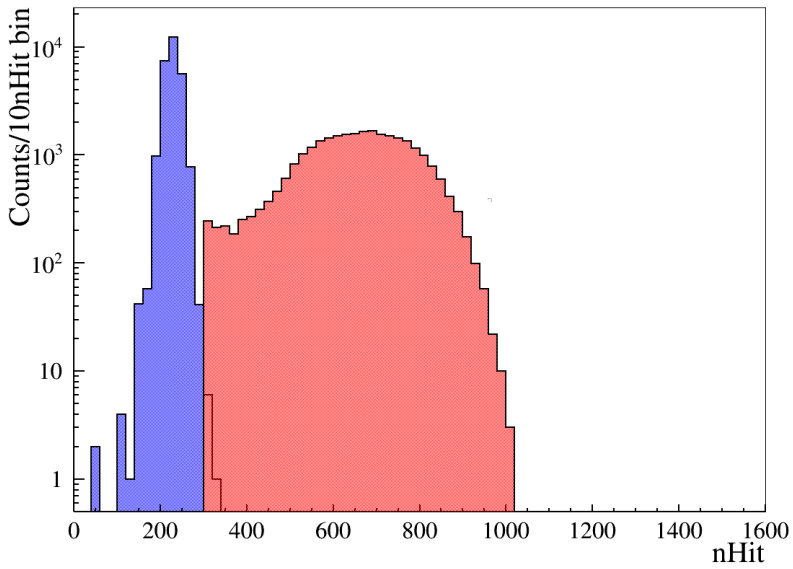

Figure 5.8: nHit distribution of the Bi (red) and Po (blue) events tagged in partial scintillator fill data taken from April 5th to October 24th 2020 (total livetime of 95 days), with a scale of approximately $\sim$320 nHit/MeV. During this period there were 365 tonnes of scintillator inside the AV+neck, and this plot was produced using data within a fiducial volume of 84.8 m^3. Even though the analysis can tag both ^{212}Bi-^{212}Po and ^{214}Bi-^{214}Po, due to ^{222}Rn, the tagged events are predominantly ^{214}Bi-^{214}Po coincidences.

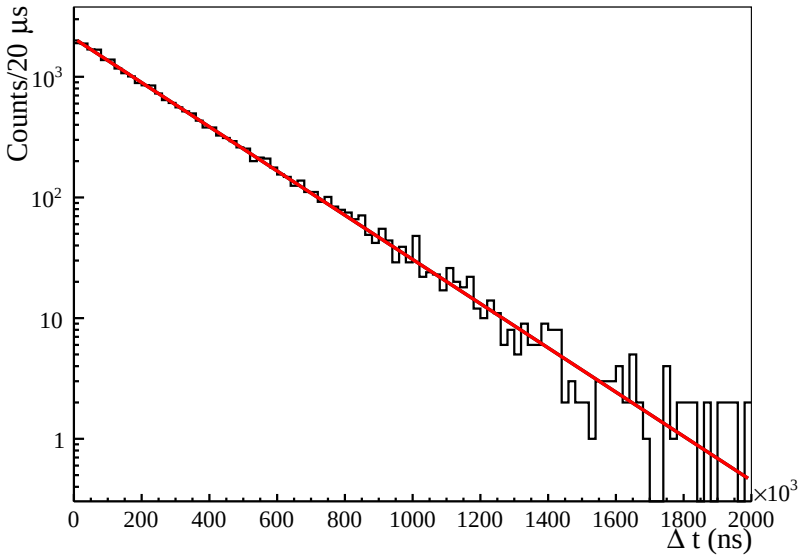

Figure 5.9: Distribution of the time differences between the tagged prompt (Bi) and delayed (Po) events, Δt. The red line represents the exponential fit to this distribution, that yields a half-life measurement of (164 $\pm$ 1) μs, compatible with the expected ^{214}Po half-life of 164.3 μs.

5.2.1.1 Light yield stability studies using tagged ^{214}Bi-^{214}Po

During the scintillator fill it was observed that the addition of LAB+PPO at different temperatures, or the addition of pure LAB, would cause a stratification between the existing scintillator and new scintillator being added to the AV. The stratification would result in inhomogeneous distributions of PPO in the scintillator, which would cause light yield variations throughout the AV volume. By consequence, this would cause distortions in the detected spectra and a worsening of the detector resolution. The stratification was usually eliminated by proceeding with the filling and with the addition of PPO.

The diffusion of PPO in the scintillator was a cause of concern at the beginning of the partial fill period, given the impossibility of adding more scintillator or using recirculation to homogenize the mixture. Furthermore, when the partial fill period started, the simulation model was not yet calibrated to reflect the scintillator properties and new detector response. For that reason, there were large discrepancies between the simulated and observed nHit of the events. Since the ^{214}Bi-^{214}Po decays were abundant during the initial weeks of the partial fill period, due to Rn ingress, and since they can be separated from other backgrounds using the tagging method described above, the tagged coincidences played a key role for monitoring the stability of the light yield throughout the scintillator volume in time. Additionally, these studies allowed to determine light yield scaling factors for the Monte Carlo, which were later used to inform and guide the direct calibration of the scintillator parameters in the detector model.

The light yield of the scintillator was monitored by comparing the observed nHit spectra of the tagged events with simulations. The discrepancy between the two was evaluated in order to determine a light yield scaling for the Monte Carlo model. Figure 5.10 shows the evolution of this light yield scaling for ^{214}Bi as a function of day, from March 20$^{\text{th}}$ to May 8$^{\text{th}}$ 2020, for three different spherical cap volumes starting at Z = 1.4 m and with R = 3, 4 and 5 m. This

Figure effectively shows how the light yield in the data varied, relative to the fixed MC light yield, as the PPO diffused in the scintillator volume. New LAB with a higher concentration of PPO enters the AV from a tube in the neck region. For that reason, in the initial days after the fill a higher light yield was observed in the top part of the AV, reflected in the higher light yield scaling for the volume up to 5 m relative to the more internal volumes. However, with time the PPO starts diffusing downwards, increasing the observed light yield in the internal regions of the scintillator. From April 12th 2020, the light yield was observed to converge to the same stable value, reflected by the agreement of the MC light yield scaling factor across the different volumes considered for the tests.

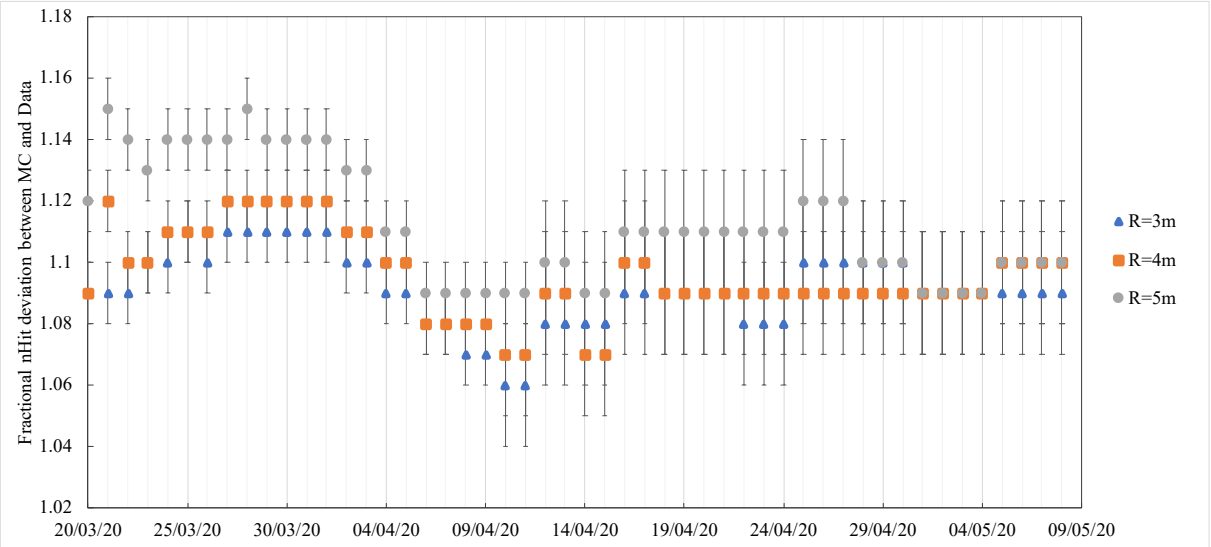

Figure 5.10: Daily variation of the tagged ^{214}Bi mean nHit, for three different spherical cap volumes with R = 3, 4 and 5 m. The fractional deviation was calculated dividing the mean nHit in MC by the mean nHit in data, obtained after fitting the spectra. The results focus on the period from March 20th to May 8th 2020, approximately six weeks following the stop of the filling operations due to the COVID global pandemic.

From this point onwards, the light yield in data was determined to be around 10-11% higher than the simulations for the ^{214}Bi spectrum. For the ^{214}Po α, the nHit in data was 5% higher than the simulations, influenced by the scintillator quenching effects. From these tests, the light yield in the detector was determined to be $\sim$320 nHit/MeV [5], compatible with later results from other background analyses and data from externally deployed sources. Another important consequence of these studies was that they allowed to determine the moment in time from which there was a uniform PPO distribution in the detector, marking the beginning of stable data-taking for the physics analyses.

5.2.1.2 Scintillator timing and light yield calibrations using the tagged ^{214}Bi-^{214}Po

A dedicated analysis, detailed in [180], used pure samples of ^{214}Bi-^{214}Po decay events to determine the scintillator emission timing profile constants, and the light yield and quenching parameters, which were used to calibrate the scintillator model. Prior to this calibration, the

[5] Variations of the light yield with energy were not considered, since these would need to be characterized more carefully with energy calibration sources.

simulations assumed scintillator optical parameters measured in benchtop experiments, which did not entirely reflect the *in situ* properties. This is visible in Figure 5.10, which shows that, after the PPO is uniformly distributed within the scintillator volume, there is a 10% difference in the nHit scale between data and MC. Even though the initial calibration with the tagged coincidences did not perfectly correct all the discrepancies between data and simulations, it provided a better data-MC agreement and improved the energy reconstruction for the partial fill period.

The tagged ^{214}Bi-^{214}Po allowed to measure the scintillator timing profiles for α and β particles separately. The simulation model was tuned such that the time residual distributions in data and simulation agreed. The timing calibration was crucial to investigate event separation via pulse shape discrimination [181], and scintillation-Cherenkov light separation in low concentration PPO [182], which was explored in the scope of the solar neutrino analyses. Similarly, the light yield and α quenching were calibrated by fitting the simulation model to data. The light yield constant was tuned such that data-simulation energy distributions agreed for ^{214}Bi decays. Following the determination of the light yield constant, any remaining discrepancy in ^{214}Po data-simulation energy distributions was corrected for by calibrating the α-quenching constant. Furthermore, discrepancies in light yield due to optical mismodelling in the region near the AV were greatly reduced by energy correction factors, also calculated using the tagged ^{214}Bi-^{214}Po. This was important to extend the fiducial volume of some physics analyses, such as the one presented in Chapter 6.

5.2.2 Validating the model of the internal water backgrounds

The levels of U and Th in the internal water were measured during the low background period of the water phase, yielding $(5.78 \pm 0.7^{+1.5}_{-1.3}) \times 10^{-15}$ gU/gH_2O and $< 4.8 \times 10^{-16}$ gTh/gH_2O (95% C.L.) respectively [160]. However, a dedicated analysis, presented in this thesis, re-measured the U concentration in the internal water using the partial fill period data, simultaneously validating the addition of the internal water radioactivity to the background model for this period. The analysis used events reconstructed near the scintillator-water interface (Z = 0.75 m), in two horizontal bands – one from 0.5 m $<$ Z $<$ 1.1 m, and the other from 0.7 m $<$ Z $<$ 1.1 m. A conservative radial cut of 4.2 m was applied to reject external backgrounds. The BiPo tagging cuts described in Section 5.2.1 are applied to reject ^{214}Bi events.

The sideband analysis performed a binned likelihood fit to 1662.8 hours of data from the end of June to the end of October 2020, including PDFs for ^{214}Bi-^{214}Po and ^{208}Tl decays in the internal water reconstructing in the scintillator, and for the internal scintillator backgrounds ^{228}Ac, ^{234}Pa, ^{40}K, ^{210}Bi and ^{212}Bi-^{212}Po. The PDFs for all these spectral components have a non-negligible contribution to the fit region, between 440 and 800 nHits. With the exception of the PDF for ^{214}Bi-^{214}Po in the internal water, all other PDFs were constrained in the fit by the measurements performed in the scintillator and water phases. The contribution of the ^{208}Tl from the internal water was expected to be almost 60 times smaller than the ^{214}Bi decays from the internal water. Since the fit did not have sensitivity to the ^{208}Tl signals, the PDF was fixed to the water phase concentration of the Th chain. Hence, the Th concentration in the internal

water was not measured with this analysis.

The results of the fit were:

$$\begin{aligned} &2.8 \times 10^{-15}\text{gU/g}H_2O \text{ in the volume with } R < 4.2 \text{ m}, 0.5 \text{ m} < Z < 1.1 \text{ m}, \\ &4.4 \times 10^{-15}\text{gU/g}H_2O \text{ in the volume with } R < 4.2 \text{ m}, 0.7 \text{ m} < Z < 1.1 \text{ m}, \end{aligned} \tag{5.9}$$

and are in agreement with the measurement from the water phase. Even though there are no error bars presented along these results, there are non-negligible uncertainties associated with the position reconstruction accuracy near the scintillator-water interface. Namely, the horizontal band from 0.5 m $<$ Z $<$ 1.1 m includes a larger fraction of events that can be misreconstructed due to the interface, yielding a lower U concentration.

5.2.3 Fitting the PFA tube backgrounds

The PFA tube deployed along the central vertical axis of the detector presented a challenge for the development of the background model of the partial fill period. Prior to its deployment, samples of the tube underwent gamma counting to determine the intrinsic radioactivity levels. The measurements yielded the upper limit of $(1.0\pm0.6)\times10^{-7}$ g^{238}U/gPFA, and $<2\times10^{-7}$ g^{232}Th/gPFA. Assuming about 6 m of tubing in the scintillator volume inside the AV, the diameter of 2.54 cm and thickness of 0.16 cm, there was $\sim$1.6 kg of tube in contact with the scintillator, yielding a ^{238}U chain rate of 182 $\pm$ 97 decays/day. The number of events observed in the data were substantially inferior to what expected based on this rate. The large uncertainty in the *ex situ* background rate, and the mismatch between expected number of events and the observations, made it critical to study and measure *in situ* the background levels of the PFA tube.

The PFA tube was added as an element of the detector geometry in RAT, and simulations of ^{214}Bi-^{214}Po decays from within the tube were produced to use as PDFs for the analyses. The choice of simulating only these isotopes of the ^{238}U chain came from the fact that the ^{214}Bi poses a threat to a wide range of detected energies, including to the $0\nu\beta\beta$ ROI studied in Section 5.3, and the higher energy βs and γs produced by its decay are not easily absorbed by the tube's material.

The study of the PFA tube backgrounds focused on the events reconstructed within a cylindrical volume of $\rho = \sqrt{x^2 + y^2}$ = 1 m around the position of the tube. The cylindrical volume is bounded by excluding events with Z $>$ 4 m (in order to avoid external backgrounds) and Z $<$ 1.3 m (in order to avoid the radioactivity of the internal water). The Bi-Po tagging cuts described in Section 5.2.1 are applied to reject ^{214}Bi decays within the scintillator.

Similarly to Section 5.2.2, this sideband analysis was performed by running a binned likelihood fit to 1662.8 hours of data, in the nHit range between 440 and 800 nHits. It included PDFs for the internal scintillator backgrounds ^{228}Ac, ^{234}Pa, ^{40}K, ^{210}Bi and ^{212}Bi-^{212}Po, and for the ^{214}Bi-^{214}Po decays within the PFA tube. All PDFs, except the last one, were constrained in the fit to their measured rates. The fit yielded a rate for the PFA tube of 0.31 decays/hour (7.44 decays/day), much lower than the upper limit of 182 $\pm$ 97 decays/day from the *ex situ* assays. This sideband measurement was validated by comparing the final background model to

the data within a larger volume and in a wider nHit range, as shown in Figure 5.11. Overall, a good agreement between the data and the background model is observed over a wide nHit range, even considering the limited statistics available. A discrepancy is observed around nHit = 600. However, that discrepancy decreases when considering the uncertainties of the different measured rates, as shown in Figure 5.12.

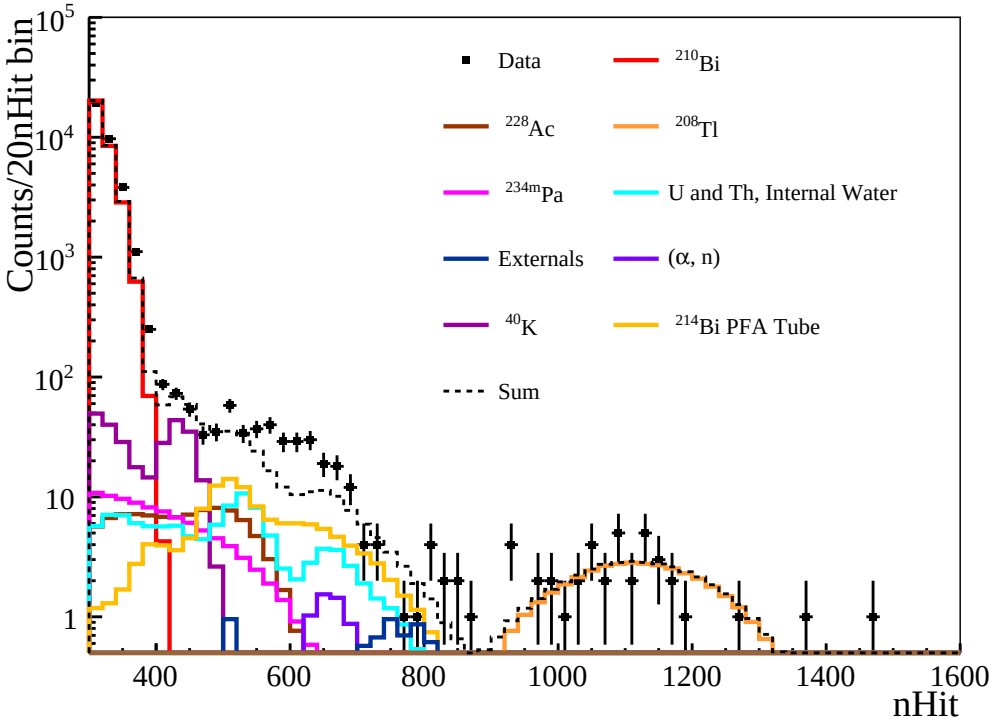

Figure 5.11: nHit distribution of the data events (black dots) in the range from 300 to 1600 nHits, for the 1662.8 hours dataset taken between June and October 2020. The colored lines show the PDFs of the different expected backgrounds, scaled by the measured rates. The PDF for the PFA tube backgrounds is highlighted in yellow.

5.3 $0\nu\beta\beta$ target-out analysis in the partial fill period

The data from the partial fill period was used to perform a $0\nu\beta\beta$ target-out analysis, comparing the observed events in the ROI to the expectations from the background measurements. This was critical to demonstrate the validity of the developed background model, and to verify that there were not any unaccounted background sources in the liquid scintillator. The target-out analysis also served to validate the model of the detector response, which allows to extrapolate the measurements of the sideband analyses to the ROI. Even though the background model and the detector response of the partial fill period are more complex than what is ultimately expected for the Te-loaded phase, this allowed to develop, exercise and improve many of the analysis approaches which are going to be used for the $0\nu\beta\beta$ searches.

This analysis was only possible after optimizing the ^{214}Bi-^{214}Po tagging and rejection from the data set (following the method described in Section 5.2.1), and understanding the light yield differences between data and the available Monte Carlo simulations. After these requirements

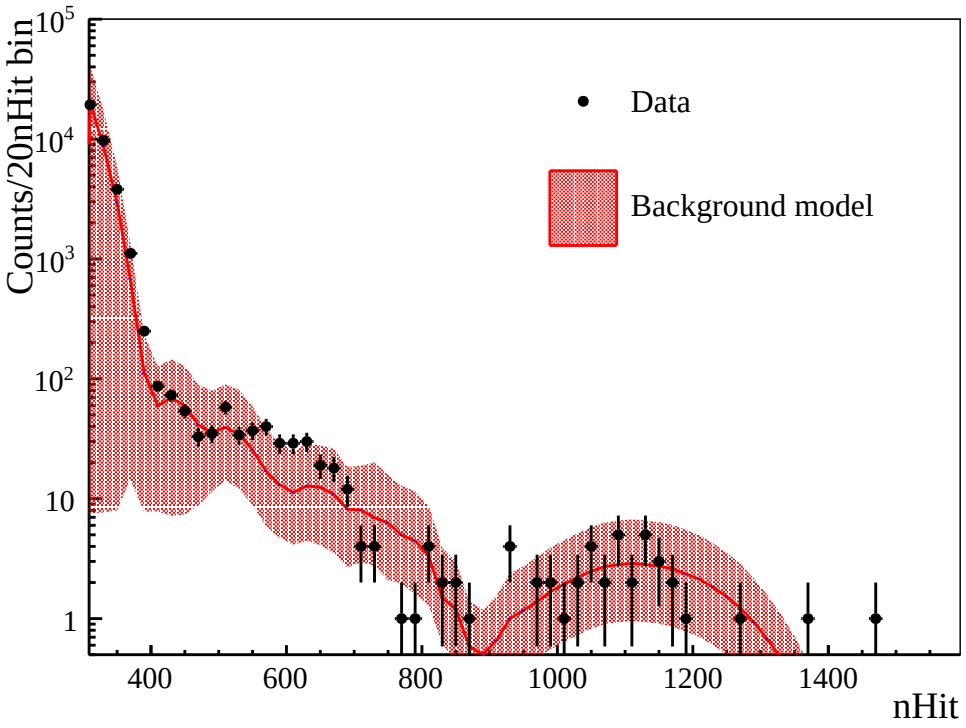

Figure 5.12: nHit distribution of the data events (black dots) in the range from 300 to 1600 nHits, for the 1662.8 hours dataset taken between June and October 2020. The red line represents the background model, where all the PDFs of the expected backgrounds, scaled by the corresponding measured rates, are summed. The red band is calculated based on the uncertainties of the measured rates.

were met, the expected contributions of each background to the ROI were calculated and compared to the observed events in a dataset of 69 days, taken from June to October 2020. Earlier data was not included due to the higher initial radon contamination. The energy ROI was determined by fitting with a Gaussian function the nHit spectrum of $0\nu\beta\beta$ simulations, yielding an ROI defined in terms of $[-0.5\sigma, +1.5\sigma]$ from 774.4 to 819.2 nHit.

Using a spherical cap fiducial volume with R $<$ 4 m and Z $>$ 1 m, 9 events were observed in the ROI. The characteristics of each of these events were evaluated (nHit, reconstructed position). Since the events reconstructed in the $0\nu\beta\beta$ ROI are expected to come mainly from the in-window ^{212}Bi-^{212}Po and from untagged ^{214}Bi, any event following them in a 2 ms time window were studied to try to identify untagged ^{214}Po candidates. Figure 5.13 shows the Z vs. $\rho^2 = x^2 + y^2$ position distribution of the data events in an expanded energy region between 700 and 900 nHits (2.2–3MeV), and for a larger volume with R $<$ 6 m. The pink stars mark the position of the ROI events (774.4 to 819.2 nHits) in the FV with R $<$ 4 m and Z $>$ 1 m.

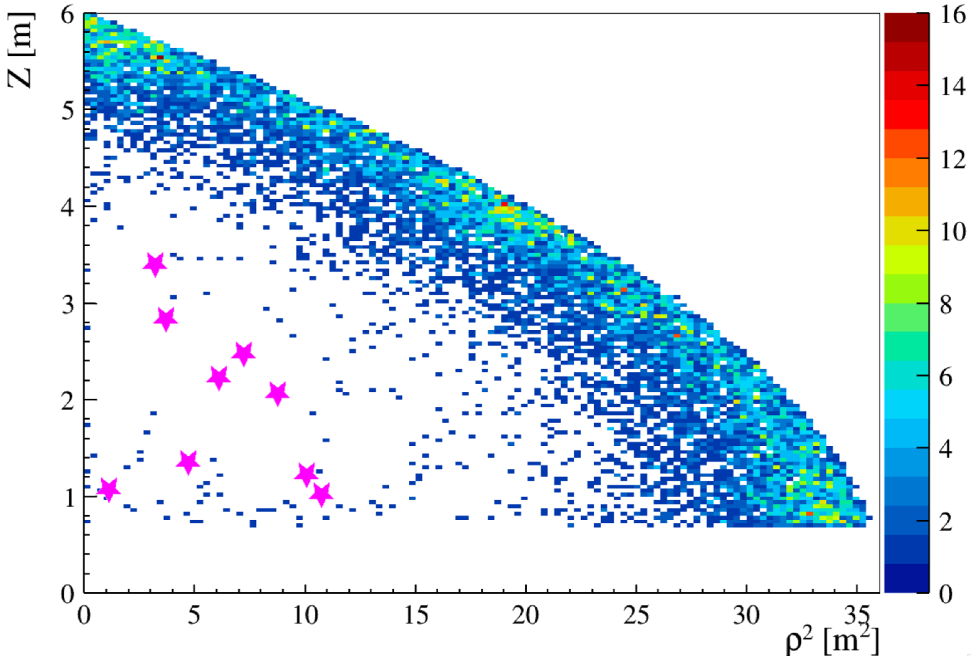

Figure 5.13: Distribution of Z vs. $\rho^2 = x^2 + y^2$ for the data events between 700 and 900 nHits (2.2–3MeV) in a fiducial volume with R $<$ 6 m and Z $>$ 0.7 m. The pink stars mark the position of the ROI events (774.4 to 819.2 nHits) in the fiducial volume of this analysis, R $<$ 4 m and Z $>$ 1 m.

In Figure 5.13, it is possible to see an excess of events along the Z axis at $\rho \sim 0$ m^2, which are believed to be coming from ^{214}Bi decays in the PFA tube; the events near the scintillator–internal water interface at Z = 0.7 m, due to internal water radioactivity; and the events due to external backgrounds at the boundaries of the volume. The first two sources of backgrounds will not exist when the detector is filled with scintillator (the tube will be removed, and there will be no water left inside the AV), and the external backgrounds can be tackled with stricter fiducial volume cuts.

Using the fiducial volume with R $<$ 4 m and Z $>$ 1 m, and applying a cylindrical cut of $\rho >$ 1.1 m to exclude the PFA tube region, there are 8 events in the $0\nu\beta\beta$ ROI. Table 5.4 lists the expected number of events in the ROI from each background in the partial scintillator fill data. The

dominant contributions are ^{212}Bi-^{212}Po decays, ^{214}Bi and ^{208}Tl γs from the internal water below the scintillator volume, and external ^{208}Tl γs from the ropes. Figure 5.14 shows the comparison between the data and the expected backgrounds, where the ROI is indicated by the shadowed region. Both Figure 5.14 and Table 5.4 show that the number of data events is consistent with the expectation, even without considering all the sources of systematic uncertainties for this dataset. Even though these numbers are not fully representative of the background contamination in the final Te-loaded phase ROI, the consistency between observation and expectation validated the preliminary SNO+ background model and analysis approaches for the full scintillator fill and for the Te-loaded phase. In fact, the analysis will be repeated during the quiet data taking period of the scintillator phase. That ultimate measurement will constitute an important determination of the count rate in the ROI, in the absence of tellurium, with all planned analysis cuts applied.

Table 5.4: Expected number of events in the ROI from each of the background sources, for a livetime of 69 days and fiducial volume with R $<$ 4 m, Z $>$ 1 m and $\rho >$ 1.1 m. The uncertainties come from the rate measurement uncertainties for each background, and do not include systematics due to light yield and position reconstruction uncertainties.

Background	Expected in the ROI	Uncertainty
Untagged ^{214}Bi in the scintillator	0.58	$\pm$0.04
^{210}Tl	0.056	$\pm$0.003
^{212}Bi-^{212}Po	1.8	$\pm$0.6
^{208}Tl	0.05	$\pm$0.02
^{214}Bi (internal water)	1.1	$^{+0.5}_{-0.3}$
^{208}Tl (internal water)	0.8	$^{+0.9}_{-0.8}$
^{208}Tl (AV)	0.7	$^{+0.4}_{-0.3}$
^{208}Tl (external water)	0.003	$^{+0.07}_{-0.003}$
^{208}Tl (ropes)	1.39	$^{+1.04}_{-0.09}$
(α, n)	0.12	$\pm$0.05
^{8}B solar ν	0.49	$\pm$0.01
Total	7.1	$^{+1.6}_{-1.1}$

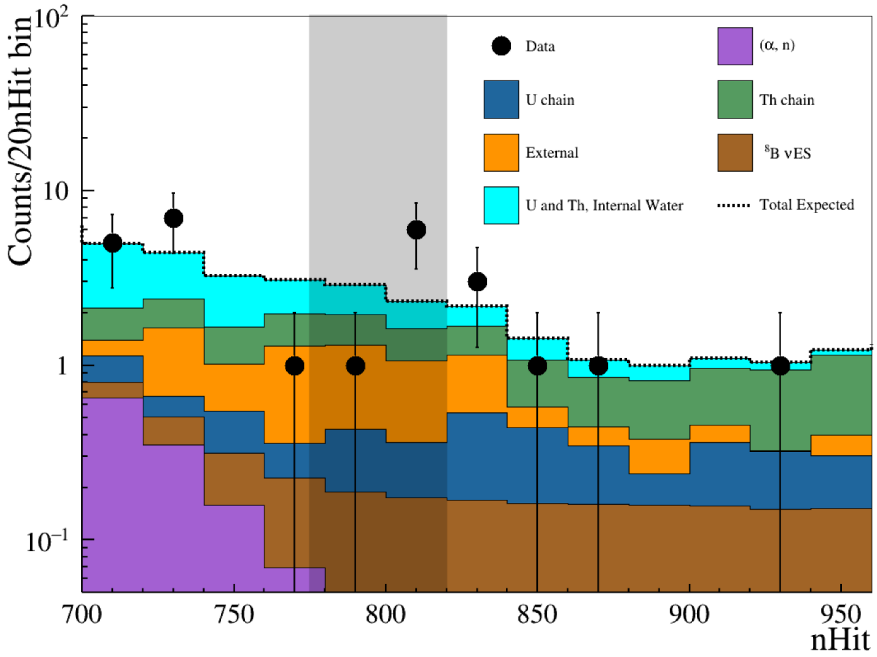

Figure 5.14: Cumulative histogram of the background model of the partial fill period compared to data measurements (black dots) for a livetime of 69 days and fiducial volume with R $<$ 4 m, Z $>$ 1 m and $\rho > 1.1$ m. The shaded region indicates the $0\nu\beta\beta$ ROI, from 774.4 to 819.2 nHits.

Chapter 6

Measurement of ^{8}B solar neutrinos in the SNO+ partial scintillator fill

The Sun is powered by nuclear reactions fusing protons into helium, releasing energy in the form of photons and neutrinos. The neutrinos produced in the core of the Sun can be detected on Earth, providing a unique direct probe of the interior of the Sun since they cross the solar medium barely interacting. For this reason, solar neutrinos have been extensively studied over the past 60 years, allowing not only to create a more complete picture of the mechanisms fuelling the Sun, but also uncovering various neutrino properties, such as neutrino oscillations and the effect of neutrino-matter interactions. Pioneering measurements of the solar neutrino fluxes were made by the chlorine and gallium radiochemical experiments [18, 20, 183, 37]. More precise measurements were then achieved by water Cherenkov detectors, like Super-Kamiokande [39] and SNO [40], and by liquid scintillator detectors like Borexino [184, 165, 135].

During the SNO+ Te-loaded phase, the scattered electrons coming from solar neutrinos interacting with the liquid scintillator via ν–e elastic scattering will be a background for the $0\nu\beta\beta$ searches. More specifically, ^{8}B solar neutrinos will be the dominant, intrinsic background source in the ROI over the Te-loaded phase. ^{8}B solar neutrinos come from the β^+ decay of ^{8}B in the *pp* chain, and have a continuous energy spectrum up to 15 MeV. Their flux is very well constrained by many experiments, including the water phase measurements of SNO+ [163], with uncertainties below 3%.

In order to demonstrate the capability of detecting ^{8}B solar neutrinos in the SNO+ liquid scintillator, a preliminary measurement of their flux was performed using the data of the partial fill period, collected between April 5$^{\text{th}}$ and October 24$^{\text{th}}$ 2020. The main advantage of such a measurement in scintillator is the much higher light yield than during the water phase, allowing lower thresholds and improved resolution. Moreover, even during the partial fill period, SNO+ has a larger target mass than Borexino, which results in an increased ^{8}B solar neutrino interaction rate within the detector. With a lower energy threshold of 1000 nHits ($\sim$3 MeV, considering the scale of 320 nHit/MeV), the partial fill period data was fitted using an unbinned likelihood fit using probability density functions (PDFs) for the signal and ^{208}Tl and ^{210}Tl decays, the major backgrounds in the region-of-interest of this analysis. Finally, preliminary systematic

uncertainties for the energy scale and position resolution were propagated to the fitted flux.

6.1 Expected ^{8}B solar neutrino interaction rate in SNO+

The solar neutrinos passing through the SNO+ detector are detected through their interactions with the liquid scintillator. They can scatter elastically with electrons, protons and neutrons, imparting energy to the target particle. The recoiling particle then ionizes the scintillator molecules around it (either directly for electrons and protons, or through scattering with protons for recoiling neutrons) producing scintillation light.

The maximum kinetic energy, T_{max}, is imparted to the recoiling particle with mass m when the neutrino with energy E_ν scatters backwards ($\theta = 0$), and can be calculated using relativistic kinematics:

$$T_{max} = \frac{2E_\nu^2}{mc^2 + 2E_\nu}. \tag{6.1}$$

Table 6.1 shows the maximum kinetic energy imparted to electrons, protons and neutrons by ^{8}B solar neutrinos. The kinetic energy of recoiling protons or neutrons is smaller than that of electrons, and given the scintillator quenching effects, these signals are not detected. The elastic scattering of neutrinos and electrons can take place through either a neutral or charged current interaction. All neutrino flavours can scatter through the neutral current interaction but, at solar neutrino energies, only electron neutrinos can scatter off electrons by exchanging a W boson.

Table 6.1: Maximum kinetic energy, T_{max}, for electrons, protons and neutrons scattered by ^{8}B solar neutrinos.

E_ν (MeV)	Particle	Mass (MeV/c^2)	T_{max} (MeV)
15.0	Electron	0.511	14.749
	Proton	938.272	0.465
	Neutron	939.565	0.464

To first order, the differential cross section for producing a recoiling electron with kinetic energy T when scattering off a neutrino with energy E_ν is [33]:

$$\frac{d\sigma}{dT} = \frac{\sigma_0}{m_e c^2}\left[g_L^2 + g_R^2\left(1 - \frac{T}{E_\nu}\right)^2 - g_L g_R \frac{T}{E_\nu}\frac{m_e c^2}{E_\nu}\right], \tag{6.2}$$

with:

$$\sigma_0 = \frac{2G_F^2 m_e^2}{\pi\hbar^4} = 8.81 \times 10^{-45}\ \text{cm}^2, \tag{6.3}$$

and:

$$\begin{aligned} g_R &= \sin^2\theta_w \sim 0.23116, \\ g_L &= \sin^2\theta_w \pm 1/2, \end{aligned} \tag{6.4}$$

where m_e is the mass of the electron, G_F is the Fermi constant, θ_w is the weak mixing angle. In g_L the plus sign corresponds to electron neutrino scattering, and the minus sign corresponds to muon or tau neutrino scattering.

J. Bahcall [185] has shown that radiative corrections to the differential scattering cross-section must be taken into account when considering a measurement of better than 5% on the solar neutrino flux. These corrections are found to be on the order of 4% for the higher energy (> 5 MeV) solar neutrinos, while for lower energies this is approximately a 2% correction. The general result for neutrino–electron scattering, taken from [185], is:

$$\frac{d\sigma}{dT} = \frac{2G_F^2 m_e}{\pi\hbar^4}\left\{g_L^2(T)\left[1+\frac{\alpha}{\pi}f_-(z)\right] + g_R^2(T)\,(1-z)^2\left[1+\frac{\alpha}{\pi}f_+(z)\right] - g_R(T)g_L(T)\frac{m_e}{E_\nu}\frac{T}{E_\nu}\left[1+\frac{\alpha}{\pi}f_{+-}(z)\right]\right\} \quad [\text{cm}^2/\text{MeV}], \tag{6.5}$$

where m_e is the electron mass, T is the kinetic energy of the recoiled electron and E_ν is the incident neutrino energy. $G_F = 1.16639 \times 10^{-5}$ GeV^{-2}, α is the fine structure constant ($\sim 1/137$), $z = T/E_\nu$, and $f_+(z)$, $f_-(z)$ and $f_{+-}(z)$ are energy dependent corrections to the cross-section.

Comparing Equation 6.2 and Equation 6.5, the form of the radiative corrections to the cross-section are immediately obvious. First, the coupling constants $g_{L,R}(T)$ have acquired an energy dependence. This is a result of virtual quark interactions resulting in quantum chromodynamics (QCD) corrections. The other obvious extension is seen in the expansion terms, of order α, which are due to electroweak loop corrections. Both calculations (with and without radiative corrections) were implemented numerically, and the differences are highlighted in Figure 6.1.

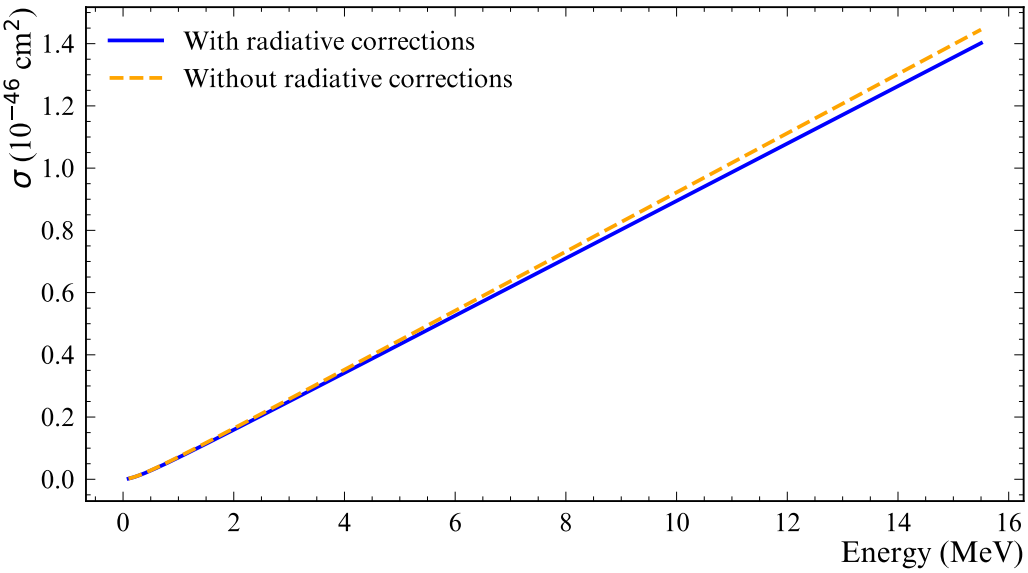

Figure 6.1: Neutrino-electron elastic scattering cross section σ, with (blue) and without (orange) radiative corrections, as a function of the incident neutrino energy, E_ν.

The expected interaction rate of ^{8}B solar neutrinos is given by:

$$R = \Phi_{^8B}\, n \int S_\nu(E)\left(P_{ee}(E)\sigma_{\nu_e}(E) + (1-P_{ee}(E))\sigma_{\nu_\mu,\nu_\tau}(E)\right)dE, \tag{6.6}$$

where $\Phi_{^8B}$ is the ^{8}B solar neutrino flux at Earth, n is the number of electron targets in the SNO+ liquid scintillator, S_ν is the normalized energy spectrum of the neutrino, P_{ee} is the electron neutrino survival probability, and σ_{ν_x} are the total interaction cross sections, calculated considering radiative corrections. The integral is performed over the ^{8}B solar neutrino energy range.

The calculation of the expected interaction rate in SNO+ uses the neutrino energy spectrum shown in Figure 6.2, from [186], which is the same used by RAT (described in Section 3.7) when producing solar neutrino simulations. The ^{8}B solar neutrino flux was obtained from [187]:

$$\Phi_{^8B} = 5.16^{+2.5\%}_{-1.7\%} \times 10^6 \text{ cm}^{-2} \text{ s}^{-1}. \tag{6.7}$$

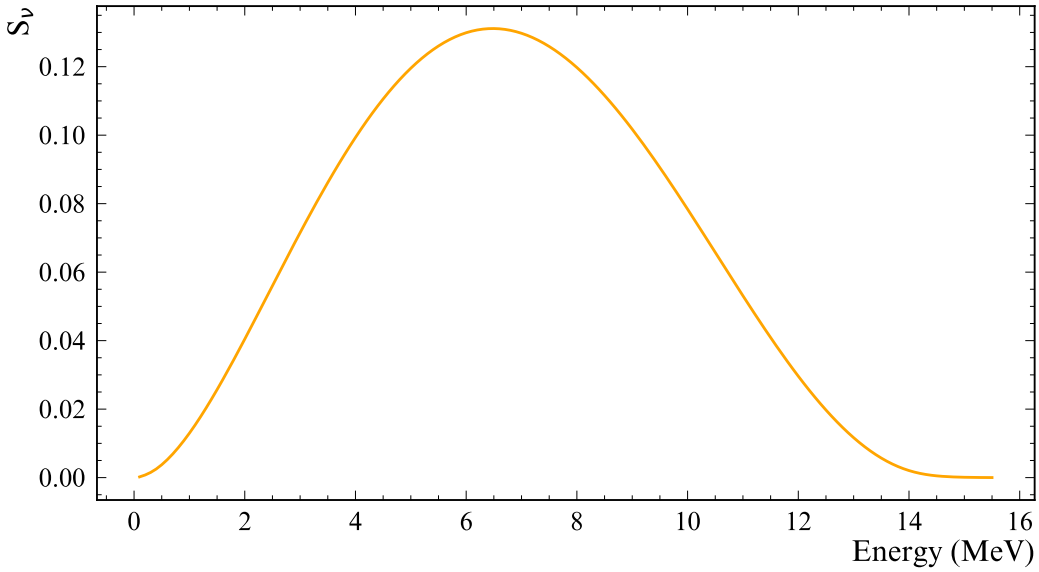

Figure 6.2: ^{8}B solar neutrino energy spectrum from [186].

The electron neutrino survival probabilities were calculated using the PSelmaa software package [40, 171], which uses a three-flavor adiabatic approximation. The calculation uses the B16 GS98 Standard Solar Model [188], and the best fit mixing parameters from [76]. Figure 6.3 shows the calculated survival probability distribution as a function of energy. This distribution was fitted with a polynomial in order to have a function to describe the P_{ee} variation with energy, necessary for the rate calculation and for other stages of this analysis.

The number of electron targets in the liquid scintillator inside the acrylic vessel is given by the expression:

$$n = \frac{(f_{LAB} n_{LAB} + f_{PPO} n_{PPO}) N_A M_{LAB}}{m}, \tag{6.8}$$

with:

- $f_{LAB} = 0.9994$ and $f_{PPO} = 0.0006$ are the fractional contributions of LAB and PPO, respectively, to the total scintillator mass during the partial fill period (concentration of 0.6 g of PPO per litre of LAB).

- n_{LAB}, n_{PPO} - number of electrons in the LAB and PPO molecules, respectively;

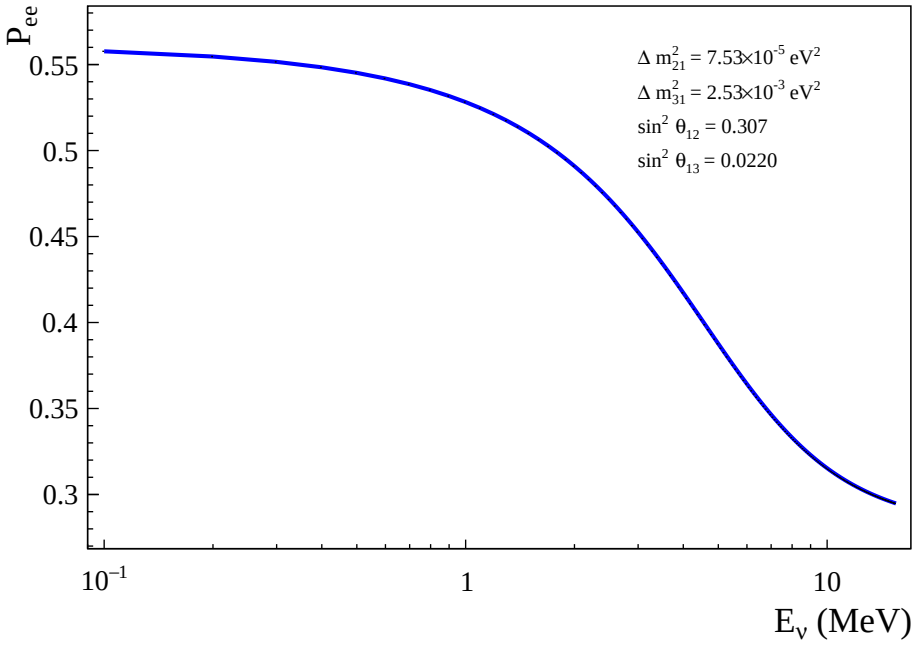

Figure 6.3: Electron neutrino survival probabilities for ^{8}B solar neutrinos, as a function of energy. The survival probabilities were calculated for the B16 GS98 Standard Solar Model [188], and using the best fit mixing parameters from [76].

- N_A - Avogadro's constant = 6.022×10^{23} mol^{-1};
- M_{LAB} - total mass of liquid scintillator inside the detector, 365 tonnes during the partial fill period;
- m - molecular weight of LAB, $m = 235$ g/mol [189].

The numbers of electrons in the LAB and PPO molecules, n_{LAB} and n_{PPO}, are calculated taking into account the different size contributions of the molecules, which are presented in Table 6.2, and the number of electrons of each atom in the molecules. The LAB molecules contribute with 131 electron targets, and the PPO with 116. This leads to a total number of electron targets during the partial fill period of:

$$n = 1.225 \times 10^{32} \text{ electrons}, \tag{6.9}$$

corresponding to about 3.356×10^{31} electrons in 100t of scintillator.

With all the parameters from Equation 6.6 determined, the ^{8}B solar neutrino interaction rate during the partial fill phase can be computed, yielding:

$$R = 0.0675 \text{ events/h}. \tag{6.10}$$

The separate contributions for ν_e and ν_μ interactions are 0.0509 events/h and 0.0166 events/h, respectively.

Table 6.2: LAB and PPO molecule content for the scintillator phase.

Chemical Equation	Content (% by mass)
LAB (99.94%)	
$C_{16}H_{26}$	20.4
$C_{17}H_{28}$	43.2
$C_{18}H_{30}$	33.4
$C_{19}H_{32}$	1.8
$C_{15}H_{24}$	1.2
0.6g/L PPO (0.06%)	
$C_{15}H_{11}NO$	

6.2 Partial fill configuration and dataset

The dataset used for this analysis comprises the data taken with all crates online from April 5th to October 24th 2020, defined as the Preliminary Partial Solar list. During runs with crates offline, part of the light from the events will not be recorded. As a consequence, the observed nHit of the events is lower than what is recorded when all crates are ON. In order to avoid having to adjust the nHit scale on a run-by-run basis, the runs with any number of offline crates were excluded. Runs from March 23rd to April 4th were excluded because the PPO was still mixing in the LAB, resulting in inhomogeneities in the scintillator volume and variation of the light yield, as described in Section 5.2.1. Monte Carlo was produced considering the detector conditions during the data-taking period [1].

6.3 Event selection

Event selection cuts, summarized in Table 6.3, were optimized to provide the cleanest possible high energy solar neutrino event sample. Muons crossing the detector, or events due to PMT breakdowns were targeted by removing any event with nHit $>$ 5000 and all the follower events in a 20 second window. The shorter deadtime, compared to what was employed in Section 5.2.1, was chosen to minimize the ^{8}B solar neutrino signal sacrifice, while rejecting the majority of the short lived, high energy cosmogenic muon induced backgrounds. The analysis only considered events whose position was successfully reconstructed by the partialFit fitter, and rejected events flagged by the skyShine processor, which evaluates if an event originated inside the AV neck volume. Furthermore, each event underwent data cleaning checks, where flags set by data cleaning processors are checked against an analysis mask for the partial fill in order to reject instrumental backgrounds.

All the reconstructed positions (which come in the PSUP coordinate system) were corrected by the AV offset in order to translate them to the AV coordinate system. During this period, the center of the AV was 13.18 cm above the center of the PSUP. In order to reject events misreconstructed in the proximity of the water–scintillator interface (where reconstruction algorithms perform poorly), only events with Z $>$ 1 m were selected. The choice of radial cut

[1] Both the data processing and accompanying Monte Carlo production used RAT-6.18.9.

for the spherical cap fiducial volume used in this analysis depends only on the accuracy of the detector response model. Several analyses, most including *in situ* backgrounds, showed that for radial cuts above 5 m the data and the Monte Carlo response model start disagreeing, due to an incomplete knowledge and modelling of the scintillator optical properties. On the other hand, having a fiducial volume as large as possible was important to get as much statistics as possible for the solar analysis. This analysis was performed for three main fiducial volumes, up to R = 4.5, 5.0 and 5.5 m.

The lower nHit threshold for the analysis was set at 1000, which is approximately 3 MeV (scale of 320 nHit/MeV). Besides ^{8}B solar neutrino signals, the analysis window will also include a considerable amount of ^{208}Tl and ^{210}Tl decays, which will be included in the fit. The number of ^{210}Tl events is constrained from the number of tagged ^{214}Bi-^{214}Po events in the data (Section 5.2.1).

Table 6.3: Cut variables and values for the ^{8}B solar neutrino analysis.

Cut	Value
Muon tagging	Reject events with nHit $>$ 5000 and followers within 20 second window
PartialFit valid	True
skyShine	> 1
Data cleaning analysis mask	0x210000000242
Radial position	$\leq$ 4.5 m, 5.0 m and 5.5 m
Z coordinate	$\geq$ 1.0 m
nHit	$\geq$ 1000

6.3.1 Livetime and number of rejected/selected events

The dataset used in this analysis has a total livetime of 2228.19 hours. However, it is necessary to take into account the livetime lost by the muon tagging cut. In this dataset, 3406 events have nHit larger than 5000. Given that all the data within 20 seconds from these events are rejected in order to avoid muon induced backgrounds, this results in a loss of 18.92 h of the total livetime. Therefore, the livetime for the analysis is 2209.27 hours (92 days). After the event selection cuts, a total of 97, 144 and 211 data events are used for the analysis, in the spherical cap fiducial volumes with R = 4.5, 5 and 5.5 m, respectively.

The same event selections cuts are applied to Monte Carlo, in order to produce PDFs for the analysis and to determine the efficiency of the selection cuts. The simulation of solar neutrinos in RAT is produced according to the un-oscillated neutrino energy spectrum. For this reason, the ^{8}B signal spectrum must be weighted afterwards by the solar neutrino survival probability P_{ee}, in order to obtain a more realistic PDF shape. Additionally, this analysis uses the oscillated rate to calculate the expected number of signal counts, and the final flux results are based on the fitted number of ^{8}B events in the detector after oscillations. As a consequence, these calculations need to use an *oscillated cut efficiency*, ϵ, which will be the number of MC events surviving the event selection cuts, weighted by the P_{ee} in the case of ν_e and weighted by (1-P_{ee}) in the case of

ν_μ, divided by the number of simulated MC events, also weighted accordingly by the survival probabilities.

The P_{ee} weights are calculated based off the curve shown in Figure 6.3 and evaluated for the initial kinetic energy of each solar neutrino in the Monte Carlo. They are subsequently applied when filling the nHit distribution histogram, and when counting the number of simulated events. Using the oscillated spectrum instead of the un-oscillated one affects the cut efficiencies by up to 4%. Table 6.4 shows the cut efficiencies for the Monte Carlo, including the survival probability weighting in the case of the solar neutrinos, which are going to be used in the following steps of this analysis.

Table 6.4: Number of simulated events before and after the event selection cuts, and corresponding cut efficiencies ϵ (number of events after cuts, divided by the number of events simulated).The solar neutrino events are weighted by P_{ee} in the case of ν_e, and by (1-P_{ee}) in the case of ν_μ. The fourth line shows the cut efficiencies for ν_e and ν_μ combined, considering their corresponding contributions of 75.46% and 24.54% to the total spectrum, respectively.

		Events after cuts		Events after cuts		Events after cuts	
	Events Simulated	R = 4.5 m	ϵ (%)	R = 5 m	ϵ (%)	R = 5.5 m	ϵ (%)
^{8}B solar ν_e	150260	22554.5	15.0	31852.4	21.2	42287.2	28.1
^{8}B solar ν_μ	145776	20628.4	14.2	29257.3	20.1	38892	26.7
^{8}B solar ν_e + ν_μ			14.8		20.9		27.8
Tl208	1151077	303854	26.4	416845	36.2	509795	44.3
Tl210	1149803	220815	19.2	307049	26.7	385535	33.5

6.4 Expected signal and background counts

The expected number of counts for the ^{8}B solar neutrinos and backgrounds, in this analysis' ROI and for the livetime of the dataset, can be determined using the expected ^{8}B solar rates from Section 6.1, and the measured background rates during the partial fill. The rate of ^{208}Tl decays, in events per hour, is calculated from the ^{232}Th concentration in the LAB, using the formula:

$$R_{^{208}Tl} = f_{b.r.}\, c_{Th}\, m_{scint} N_A \frac{\ln(2)}{A_{m,Th} T_{1/2,Th}} \frac{1}{24 \cdot 365}, \tag{6.11}$$

where:

- $f_{b.r.}$ is the branching ratio of the ^{212}Bi decay into ^{208}Tl, 36%;
- c_{Th232} is the measured ^{232}Th concentration of (5.3$\pm$1.5)$\times 10^{-17}$ gTh/gLAB;
- m_{scint} is the scintillator mass of 365$\times 10^6$ g during the partial fill period;
- N_A is the Avogadro constant;
- $A_{m,Th}$ is the atomic mass of ^{232}Th and has a value of 232 g/mol;
- $T_{1/2,Th}$ is the half-life of ^{232}Th, 1.405$\times 10^{10}$ years.

The estimate of the ^{210}Tl is calculated based on the number of tagged ^{214}Bi decays. This calculation requires knowing the efficiency of the ^{214}Bi-^{214}Po tagging method, and the branching

ratios of the decays ^{214}Bi$\rightarrow^{214}$Po (99.979%) and ^{214}Bi$\rightarrow^{210}$Tl (0.021%). Table 6.5 lists the number of tagged ^{214}Bi decays in the data, for the three FVs considered in this analysis. Even though the Bi-Po tagging method described also identifies ^{212}Bi-^{212}Po coincidences, it is assumed that all the tagged events are ^{214}Bi-^{214}Po coincidences. The expected number of ^{210}Tl events is obtained from:

$$N_{^{210}Tl} = \frac{0.00021}{0.99979} N_{tag,data} \frac{N_{tag,MC}}{N_{sim,MC}}, \tag{6.12}$$

where $N_{tag,data}$ is the number of tagged Bi-Po coincidences in data, listed in Table 6.5, $N_{tag,MC}$ is the number of tagged Monte Carlo ^{214}Bi-^{214}Po coincidences and $N_{sim,data}$ is the number of simulated ^{214}Bi decays in the same Monte Carlo. The expected number of events of each signal and background type are presented in Table 6.6.

Table 6.5: Number of tagged Bi-Po coincidences in the dataset used for the ^{8}B solar neutrino analysis, for the three considered spherical cap fiducial volumes.

Fiducial volume	Number of Bi-Po tags
Z $\geq$ 1.0 m, R $\leq$ 4.5 m	39288
Z $\geq$ 1.0 m, R $\leq$ 5.0 m	58458
Z $\geq$ 1.0 m, R $\leq$ 5.5 m	80031

Table 6.6: Expected number of signal and background counts in the dataset, within the ROI, for a livetime (t_{live}) of 2209.27 hours (92 days).

		Expected number of counts		
	Calculation	R = 4.5 m	R = 5 m	R = 5.5 m
^{8}B ν_e	0.0509 events/h $\times$ t_{live} $\times$ ϵ	16.89	23.86	31.67
^{8}B ν_μ	0.0166 events/h $\times$ t_{live} $\times$ ϵ	5.18	7.34	9.76
^{8}B ν_e + ν_μ		22.07	31.20	41.44
^{208}Tl	Equation 6.11 $\times$ t_{live} $\times$ ϵ	59.37	81.45	99.61
^{210}Tl	Equation 6.12 $\times\epsilon$	5.51	7.88	9.88

6.5 Unbinned likelihood fit overview

A one-dimensional extended unbinned likelihood fit was developed to fit the normalizations of signal and background probability distribution functions (PDFs) to the data. The likelihood function is:

$$-\ln\mathcal{L} = \ln(N_{\text{data}}!) - N_{\text{data}} \ln\left(\sum_{i=0}^{N_{\text{norm}}} N_i\right) + \sum_{i=0}^{N_{\text{norm}}} N_i - \sum_{j=0}^{N_{\text{data}}} \ln\left(\sum_{i=0}^{N_{\text{norm}}} N_i P_i(\text{nHit}_j)\right), \tag{6.13}$$

where N_{data} is the number of events in data, N_{norm} is the number of signal+background PDFs, N_i are normalizations for the PDF i, and $P_i(\text{nHit}_j)$ is the value of PDF i evaluated at the nHit of the data event j. The likelihood function is minimized using ROOT's Minuit package [190]. The fit runs first the `SIMPLEX` method for minimization in order to find good starting values for the

normalizations, followed by the MIGRAD method for the main minimization. The uncertainties of the fitted normalizations are first evaluated with the HESSE method, which calculates the Hessian matrix (second derivatives) of the likelihood function, and with the MINOS method, which calculates asymmetric errors including parameter correlations. The expected number of ^{8}B and background events in the nHit ROI and FV, shown in Table 6.6, are used as initialization of the normalization of the corresponding PDF.

6.5.1 Probability distribution functions

The nHit distributions of the MC were fitted using appropriate functions, for the three FVs with R = 4.5, 5.0 and 5.5 m, in order to obtain the PDFs to be used in the likelihood fit. In the case of the signal, the nHit distributions of the ν_e and ν_μ MC are combined in the same histogram, each scaled by the corresponding expected event rate.

The nHit distribution of the signal was fitted with a polynomial of degree 5:

$$P_{^8\mathrm{B}}(\mathrm{nHit}) = a_0 + a_1 \cdot \mathrm{nHit} + a_2 \cdot \mathrm{nHit}^2 + a_3 \cdot \mathrm{nHit}^3 + a_4 \cdot \mathrm{nHit}^4 + a_5 \cdot \mathrm{nHit}^5. \tag{6.14}$$

The nHit distributions for the ^{208}Tl and ^{210}Tl were fitted using a Gaussian function:

$$P_{\mathrm{Tl}}(\mathrm{nHit}) = p_0 \exp\left(-\frac{1}{2}\frac{(\mathrm{nHit}-\mu)^2}{\sigma^2}\right). \tag{6.15}$$

The fitted parameters of these functions are shown in Table 6.7 for each fiducial volume. Figures 6.4 (a) to (c) show the normalized PDFs obtained for the fit. The PDFs are normalized to 1 by dividing by the function integral in the fit nHit range. Outside the fit range, the values of the PDFs are 0. There are variations in the shape and nHit scale of the PDFs as the FV increases. This is caused by a worsening of the nHit resolution at high radii, given the complex optical effects caused by the presence of the AV and total internal reflection effects.

Table 6.7: Values of the parameters of the PDF functions for signal and background.

	PDF parameter	R = 4.5 m	R = 5 m	R = 5.5 m
^{8}B ν_e + ν_μ	a_0	2.87	4.45	4.70
	a_1	-2.12×10^{-3}	-3.82×10^{-3}	-1.35×10^{-3}
	a_2	2.78×10^{-6}	4.97×10^{-6}	3.15×10^{-6}
	a_3	-2.10×10^{-9}	-3.66×10^{-9}	-3.56×10^{-9}
	a_4	6.22×10^{-13}	1.09×10^{-12}	1.25×10^{-12}
	a_5	-6.23×10^{-17}	-1.11×10^{-16}	-1.39×10^{-16}
^{208}Tl	p_0	1.35×10^4	1.91×10^4	2.43×10^4
	μ	1.11×10^3	1.10×10^3	1.08×10^3
	σ	1.05×10^2	1.06×10^2	1.10×10^2
^{210}Tl	p_0	7.62×10^3	1.10×10^4	1.44×10^4
	μ	1.14×10^3	1.12×10^3	1.10×10^3
	σ	1.37×10^2	1.36×10^2	1.40×10^2

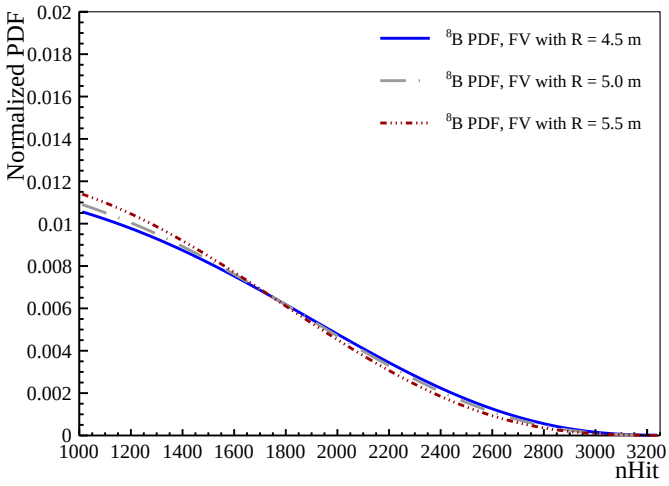

(a)

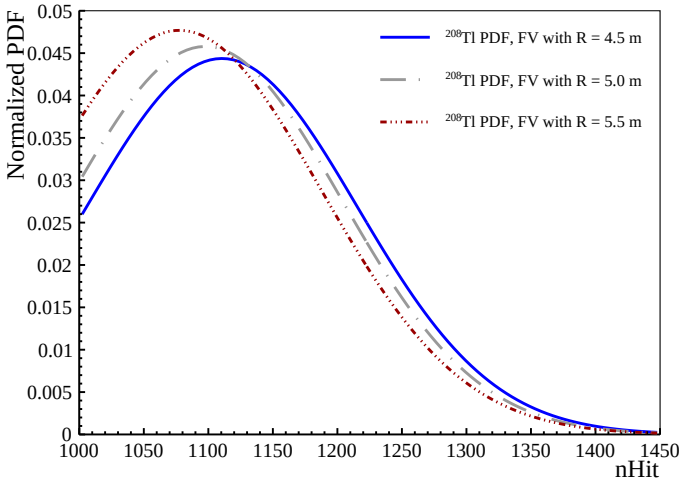

(b)

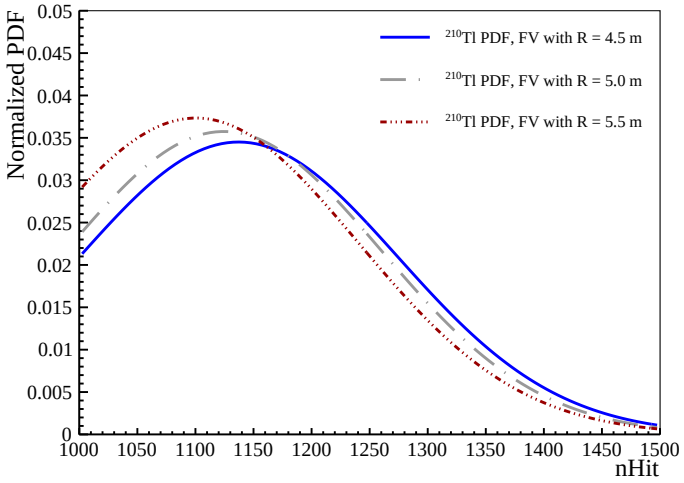

(c)

Figure 6.4: Normalized PDFs for the ^{8}B solar neutrinos (a), ^{208}Tl (b) and ^{210}Tl (c), for the three spherical cap fiducial volumes considered in this analysis, with Z $\geq$ 1 m and R $\leq$ 4.5 m (blue), 5.0 m (grey) and 5.5 m (red).

6.5.2 Fit results

The unbinned likelihood fit was run over the data as described in the previous sections. The normalization of the ^{210}Tl PDF, initialized with the values of Table 6.6, was fixed. The fitted normalizations for the ^{8}B solar neutrinos and for the ^{208}Tl are presented in Table 6.8, along the asymmetric errors from MINOS. Figures 6.5 to 6.7 show the 2-dimensional likelihood profile as a function of the ^{8}B solar neutrinos and ^{208}Tl normalizations, for the three fiducial volumes with R = 4.5, 5.0 and 5.5 m, with the minimum marked by the magenta star.

Table 6.8: Fitted normalizations for the ^{8}B solar neutrinos and for the ^{208}Tl with asymmetric errors from MINOS.

	Fitted Number of Counts		
	R = 4.5 m	R = 5 m	R = 5.5 m
^{8}B	$26.4^{+6.9}_{-5.9}$	$30.9^{+7.5}_{-6.5}$	$43.9^{+9.0}_{-8.0}$
^{208}Tl	$65.2^{+9.5}_{-8.8}$	$105.3^{+11.7}_{-11.1}$	$157.1^{+14.2}_{-13.6}$

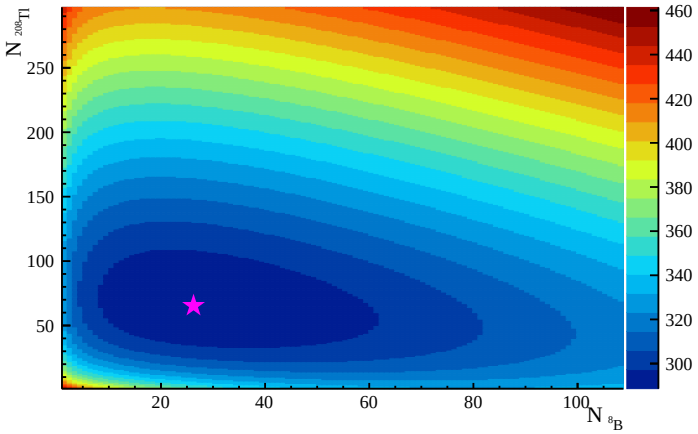

Figure 6.5: Two-dimensional likelihood profile for the FV with R = 4.5 m. The magenta star marks the minimum.

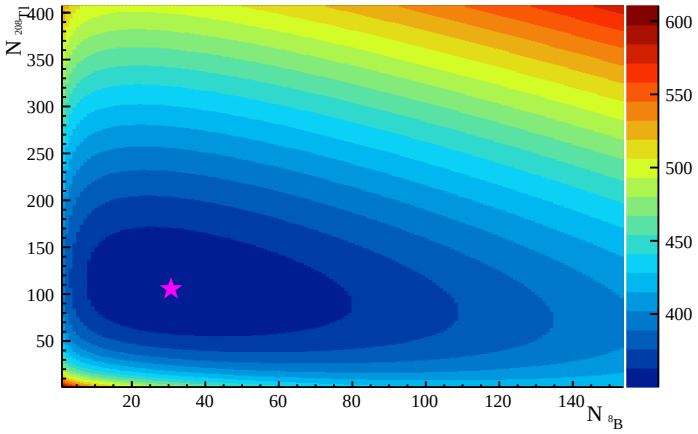

Figure 6.6: Two-dimensional likelihood profile for the FV with R = 5.0 m. The magenta star marks the minimum.

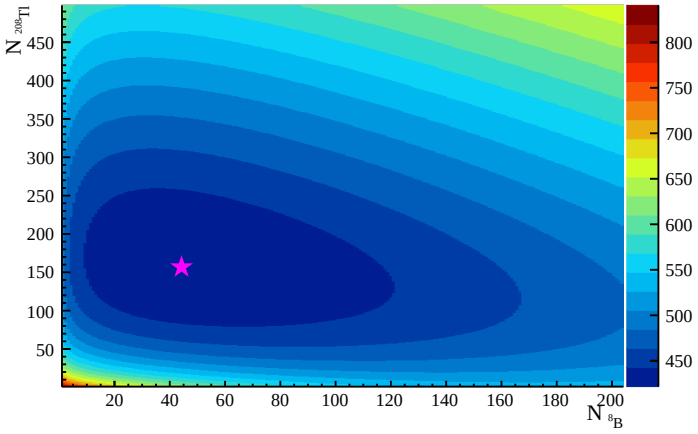

Figure 6.7: Two-dimensional likelihood profile for the FV with R = 5.5 m. The magenta star marks the minimum.

6.5.3 Bias and pull

The goodness of the likelihood fit was evaluated by looking at the bias and pull, defined as:

$$\text{Bias} = \frac{N^{\text{fit}} - N^{\text{expected}}}{N^{\text{expected}}}, \qquad \text{Pull} = \begin{cases} \frac{N^{\text{expected}} - N^{\text{fit}}}{\sigma^{\text{fit}}_{+}}, & \text{if } N^{\text{fit}} \leq N^{\text{expected}} \\ \frac{N^{\text{fit}} - N^{\text{expected}}}{\sigma^{\text{fit}}_{-}}, & \text{otherwise.} \end{cases} \tag{6.16}$$

In an unbiased fit with correct uncertainties, the pull distribution from many sample toy MC datasets is expected to follow a normal distribution centred at 0 and with standard deviation of 1. For each fake dataset, the number of expected signal and background events, N^{expected}, was drawn randomly from a Poisson distribution with mean equal to the fitted number of counts in Table 6.8. Then, the nHits for the N^{expected} fake events were randomly generated from the signal and background PDFs. The unbinned likelihood fit ran over the fake datasets and the results were used to calculate the bias and pull. The final bias and pull distributions, shown in Figures 6.8 and 6.9, are created after running the fit over 10000 fake datasets, and the resulting means and standard deviations are presented in Table 6.9.

The results show a bias smaller than 0.6% and 0.2% for the fitted ^{8}B and ^{208}Tl normalizations, respectively. The larger bias distribution width for the ^{8}B fit is caused by the small number of events, for which small fluctuations result in large biases. The standard deviation of the pull distributions, for both cases, is consistent with unity.

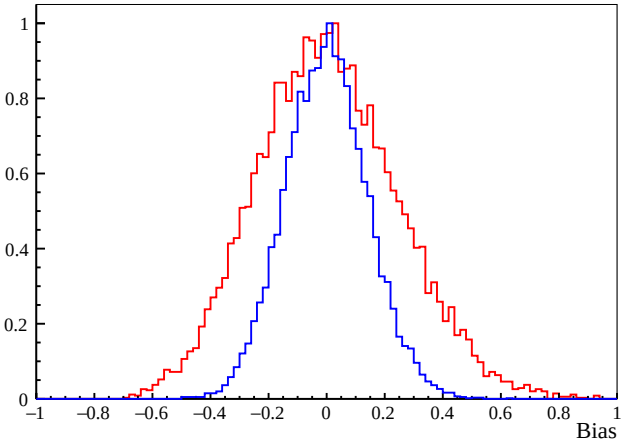

(a)

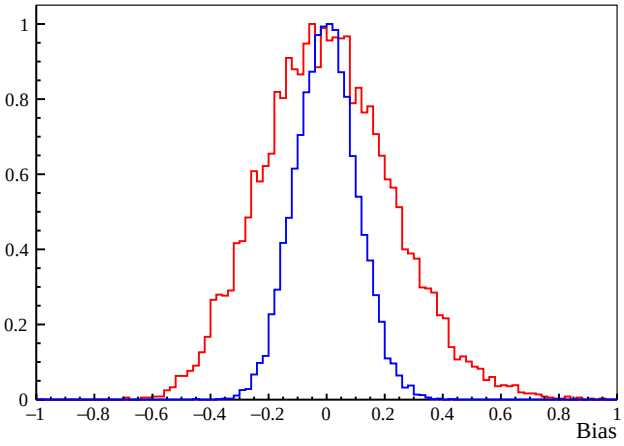

(b)

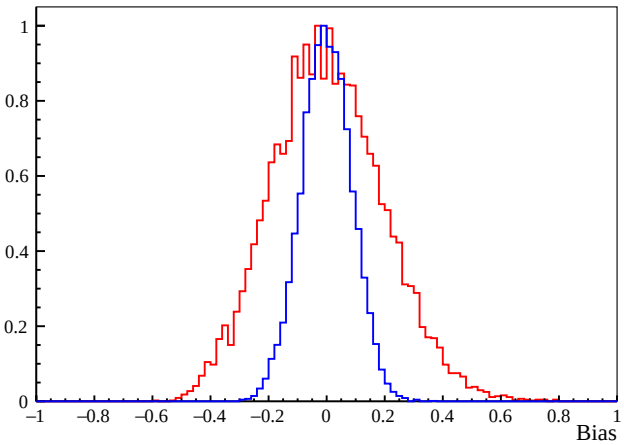

(c)

Figure 6.8: Bias distributions for the ^{8}B solar neutrino (red) and ^{208}Tl (blue) normalizations, produced by running the unbinned likelihood fit over 10000 fake datasets for the FVs with R = (a) 4.5 m, (b) 5.0 m and (c) 5.5 m.

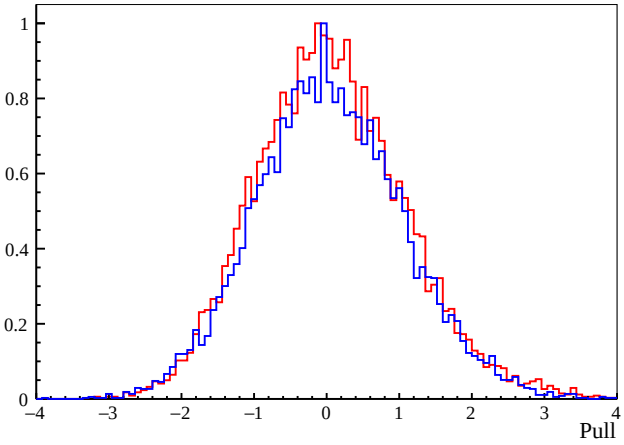

(a)

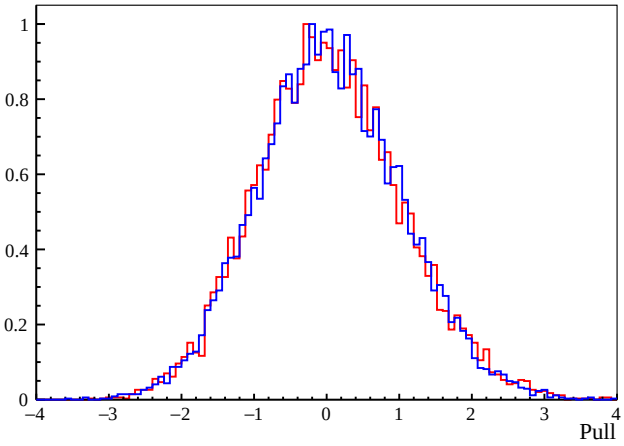

(b)

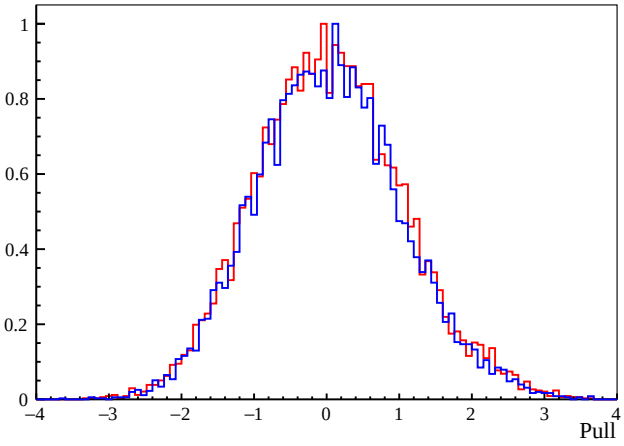

(c)

Figure 6.9: Pull distributions for the ^{8}B solar neutrino (red) and ^{208}Tl (blue) normalizations, produced by running the unbinned likelihood fit over 10000 fake datasets for the PDFs for the FVs with R = (a) 4.5 m, (b) 5.0 m and (c) 5.5 m.

Table 6.9: Means and standard deviations for the Bias and Pull of the unbinned likelihood fit, produced from 10000 fake datasets.

PDF	R Cut (m)	Mean Bias	Bias Standard Deviation
^{8}B	4.5	0.003 ± 0.047	0.24 ± 0.03
	5.0	0.006 ± 0.044	0.22 ± 0.03
	5.5	0.005 ± 0.041	0.19 ± 0.03
^{208}Tl	4.5	-0.001 ± 0.035	0.14 ± 0.03
	5.0	-0.002 ± 0.029	0.10 ± 0.02
	5.5	-0.0005 ± 0.0265	0.09 ± 0.02
PDF	R Cut (m)	Mean Pull	Pull Standard Deviation
^{8}B	4.5	0.04 ± 0.19	0.99 ± 0.14
	5.0	0.04 ± 0.19	0.98 ± 0.13
	5.5	0.04 ± 0.19	0.99 ± 0.13
^{208}Tl	4.5	0.04 ± 0.20	0.99 ± 0.14
	5.0	0.05 ± 0.19	0.98 ± 0.13
	5.5	0.03 ± 0.19	0.97 ± 0.14

6.6 Systematic uncertainties

The final step of the analysis consisted of quantifying systematic uncertainties related to the nHit scale and its variation with position, and to the position reconstruction, which affects the definition of the fiducial volume. The evaluation of systematic uncertainties is usually based on the analysis of calibration source data. During the partial fill phase, no sources were deployed in the scintillator volume. Calibrations sources were deployed in the water volume between the AV and the PMTs but, at the time of this analysis, that calibration analysis using the external source data was still being finalized. Therefore, the preliminary systematic uncertainties presented here are based on studies using the tagged ^{214}Bi.

6.6.1 nHit scale systematic

The differences between the data and MC nHit scale were evaluated by looking at the nHit spectrum of the tagged ^{214}Bi. The spectrum was fitted with a Gaussian centered on the maximum of the spectrum. The mean and width (σ) of the fitted Gaussian were compared as a function of the radial cut for the FV, shown in Figures 6.10 and 6.11. The observed differences between the data and MC, particularly when including events at high radii, are mainly due to an incomplete calibration of the light yield and scintillator optics for this dataset.

The ratios between the fitted nHit means for data and MC, and the difference of the squared widths are shown in Figures 6.12 and 6.13, respectively. Figure 6.12 shows that the absolute nHit scale of the Monte Carlo agrees with the data in the more internal fiducial volumes with R $<$ 4.5 m. However, as the radius increases, the nHit scale discrepancy between MC and the data increases up to 6%. Figure 6.13 shows that the width of the ^{214}Bi nHit spectrum is larger in data than in the MC in the FVs with radii up to 5.5 m. For larger radii, the width of the MC distribution rapidly increases, compared to the data. This is most likely due to an incomplete calibration of the optical model near the AV boundary, e.g. total internal reflection effects, and

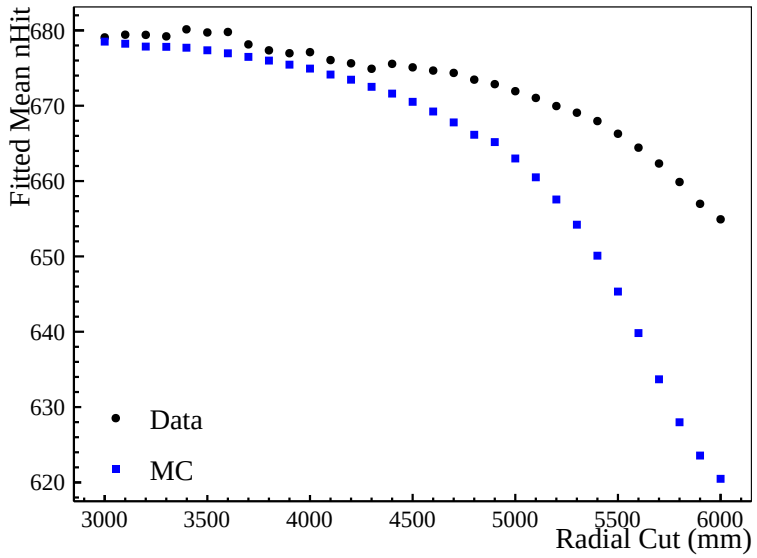

Figure 6.10: ^{214}Bi mean nHit as a function of the FV radius, for data (black circles) and MC (blue squares).

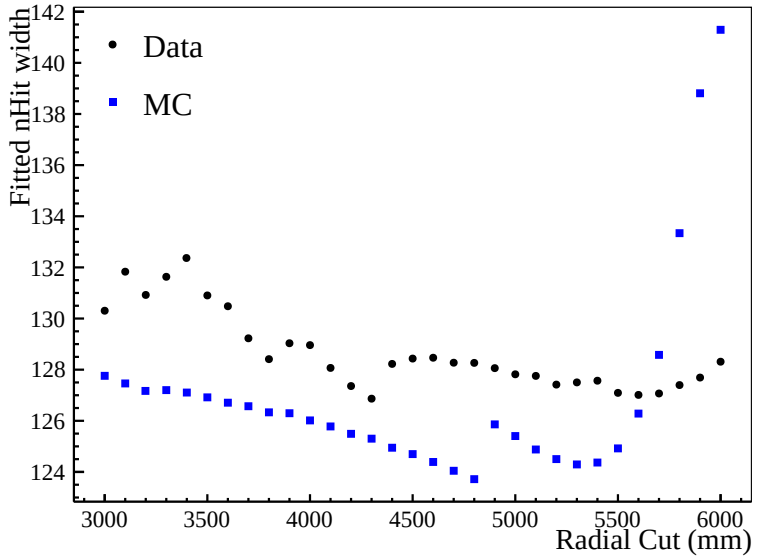

Figure 6.11: Variation of the width of the ^{214}Bi nHit distribution (fitted with a Gaussian) as a function of the FV radius, for data (black circles) and MC (blue squares). The fluctuations of the data widths at R $<$4500 are due the limited ^{214}Bi available statistics.

of the modelling of the nHit scale variations with position. The points in Figures 6.12 and 6.13 were fitted with the polynomial functions:

$$f_{\text{mean}}(R) = 0.85 + 1.3 \times 10^{-4} R - 3.8 \times 10^{-8} R^2 + 3.6 \times 10^{-12} R^3, \tag{6.17}$$

$$f_{\sigma^2}(R) = -199374 + 201.97R - 0.075R^2 + 1.2 \times 10^{-5} R^3 - 7.3 \times 10^{-10} R^4, \tag{6.18}$$

which were used to appropriately scale and smear the nHit of the MC events as a function of their radial position:

$$\begin{aligned} \text{smear} &= \sqrt{f_{\sigma^2}}, \\ \text{nHit}_{\text{new}} &= \text{Gaus}(\text{nHit} \cdot f_{\text{mean}}, \text{smear}). \end{aligned} \tag{6.19}$$

New PDFs were produced based on the new nHit distributions, and the unbinned likelihood fit was repeated. The results were compared to the nominal fit in Table 6.10, which also presents the relative systematic error.

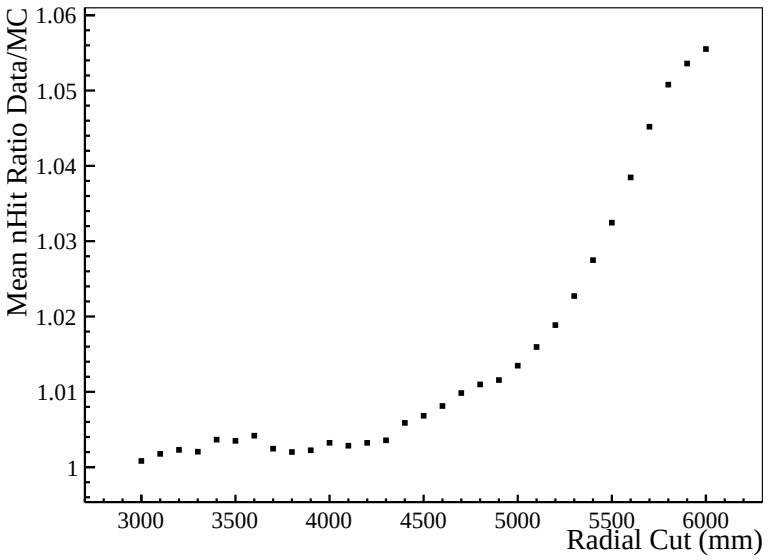

Figure 6.12: Ratio between data and MC of the mean ^{214}Bi nHit as a function of R.

Table 6.10: Fitted number of events with the nHit PDFs scaled and smeared, and the corresponding error relative to the nominal fit results.

		R = 4.5 m	R = 5.0 m	R = 5.5 m
^{8}B	Fitted Events	25.7	29.5	41.6
	Relative Error	-2.8%	-4.4%	-5.3%
^{208}Tl	Fitted Events	66.0	106.9	159.6
	Relative Error	1.2%	1.4%	1.6%

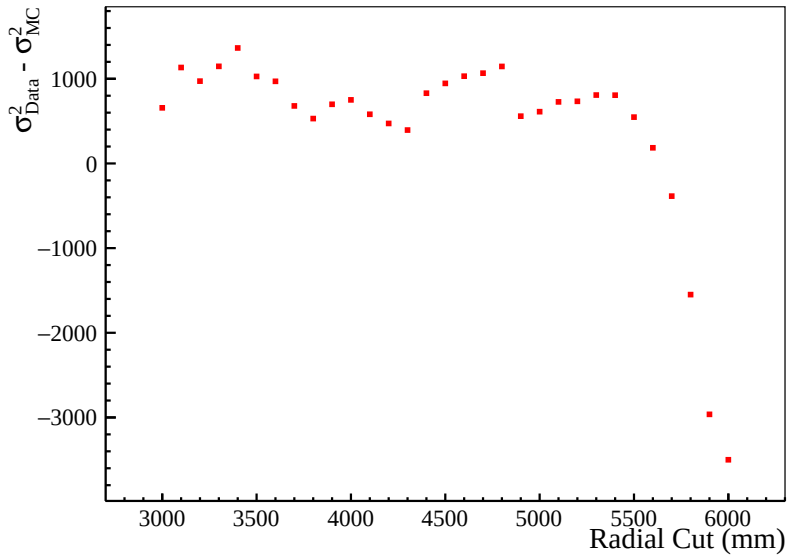

Figure 6.13: Difference of the ^{214}Bi nHit distribution σ^2 between data and MC as a function of R.

6.6.2 Position reconstruction systematic

The systematic related to the position reconstruction was evaluated by comparing the Δr distribution (the distribution of distances between the prompt and delayed event, based on the reconstructed positions) of the tagged ^{214}Bi-^{214}Po in data and MC. Tests documented in [191] found the difference between data and MC to be roughly 45 mm. The unbinned likelihood fit was then performed to the data events that fell in a larger FV with (R+45mm,Z-45mm) and in a smaller FV with (R-45mm,Z+45mm). The results are compared to the nominal fit in Table 6.11.

Table 6.11: Fitted number of events of the dataset in FVs of (R+45mm,Z-45mm) and (R-45mm,Z+45mm), and the corresponding error relative to the nominal fit results.

		R = 4.5 m	R = 5.0 m	R = 5.5 m
^{8}B	Fitted Events (R+45mm,Z-45mm)	28.82	33.25	46.48
	Fitted Events (R-45mm,Z+45mm)	23.53	28.12	41.31
	Relative Error	-10.94% +9.11%	-8.93% +7.67%	-6.02% +5.74%
^{208}Tl	Fitted Events (R+45mm,Z-45mm)	70.72	118.9	167.56
	Fitted Events (R-45mm,Z+45mm)	62.15	103.45	147.75
	Relative Error	-4.68% +8.46%	-1.80% +12.9%	-5.96% +6.64%

6.7 Final results and discussion

The fitted number of ^{208}Tl counts, $N^{fit}_{^{208}Tl}$, were converted into a ^{232}Th concentration using the equation:

$$c_{Th232} = N^{fit}_{^{208}Tl} \cdot (24 \times 365) A_{m,Th} T_{1/2,Th} \frac{1}{\ln(2) f_{b.r.}\, m_{scint} N_A} \frac{1}{\epsilon t_{live}}, \tag{6.20}$$

where the t_{live} is the livetime of 2209.27 hours, the cut efficienties ϵ come from Table 6.4, and the remaining parameters are as defined in Equation 6.11. The final ^{232}Th concentrations are:

$$c_{Th232} = \begin{cases} 5.8^{+0.8}_{-0.8}\ \text{(stat.)}\ ^{+0.3}_{-0.5}\ \text{(syst.)}\ \times 10^{-17}\ \text{gTh/g}, & \text{at R = 4.5 m} \\ 6.9^{+0.8}_{-0.7}\ \text{(stat.)}\ ^{+0.2}_{-0.9}\ \text{(syst.)}\ \times 10^{-17}\ \text{gTh/g}, & \text{at R = 5.0 m} \\ 8.4^{+0.8}_{-0.7}\ \text{(stat.)}\ ^{+0.5}_{-0.6}\ \text{(syst.)}\ \times 10^{-17}\ \text{gTh/g}, & \text{at R = 5.5 m} \end{cases} \tag{6.21}$$

The systematic uncertainties are calculated by summing in quadrature the relative errors shown in Tables 6.10 and 6.11. The results obtained for the FVs with radius of 4.5 m and 5.0 m are in agreement with the Th concentration obtained from the background analysis, within the uncertainties of both measurements. However, the fitted concentration for the FV with radius of 5.5 m is overestimated by a factor of 1.6. This increase is due to the nHit scale differences between data and MC at higher radii, which underestimate the cut efficiency and lead to an overestimation of the Th concentration.

The fitted numbers of ^{8}B solar neutrino counts were converted into ^{8}B solar neutrino fluxes using the equation:

$$\Phi_{^8B} = N^{fit}_{^8B} \frac{1}{3600 \cdot n \epsilon t_{live}} \frac{1}{\int S_\nu(E) \left(P_{ee}(E) \sigma_{\nu_e}(E) + (1 - P_{ee}(E)) \sigma_{\nu_\mu,\nu_\tau}(E) \right) dE}, \tag{6.22}$$

where n is the number of electron targets calculated in Equation 6.9, t_{live} is 2209.27 hours and the cut efficiencies come from Table 6.4. The parameters within the integral are the same as Equation 6.6.

The systematic uncertainties were calculated based on the relative errors of Tables 6.10 and 6.11, as well as the uncertainties of the neutrino oscillation parameters, which affect the neutrino survival probabilities. The latter contributes with a systematic of 1.5%. The systematic errors were summed in quadrature. It is important to note that not all the possible systematic effects were propagated to the results, e.g. the uncertainty on the scintillator mass, estimated to be on the order of 10%.

The ^{8}B solar neutrino fluxes determined by this analysis, for the different fiducial volumes, are:

$$\Phi_{^8B} = \begin{cases} 6.534^{+26.11\%}_{-22.39\%}\ \text{(stat.)}\ ^{+11.38\%}_{-9.64\%}\ \text{(syst.)}\ \times 10^{6}\ \text{cm}^{-2}\ \text{s}^{-1}, & \text{at R = 4.5 m} \\ 5.403^{+24.42\%}_{-21.16\%}\ \text{(stat.)}\ ^{+10.06\%}_{-8.95\%}\ \text{(syst.)}\ \times 10^{6}\ \text{cm}^{-2}\ \text{s}^{-1}, & \text{at R = 5.0 m} \\ 5.792^{+20.45\%}_{-18.14\%}\ \text{(stat.)}\ ^{+8.17\%}_{-7.97\%}\ \text{(syst.)}\ \times 10^{6}\ \text{cm}^{-2}\ \text{s}^{-1}, & \text{at R = 5.5 m} \end{cases} \tag{6.23}$$

The results, displayed in Figure 6.14, are in agreement with the expected solar neutrino flux and with the measurements from other experiments. The statistical uncertainties are dominant over the systematic ones, regardless of the fiducial volume considered. Figures 6.15 to 6.17 show the data against the PDFs scaled by the best fit normalizations. This analysis served as an important proof of concept for future solar neutrino analyses during the scintillator and Te-loaded phases.

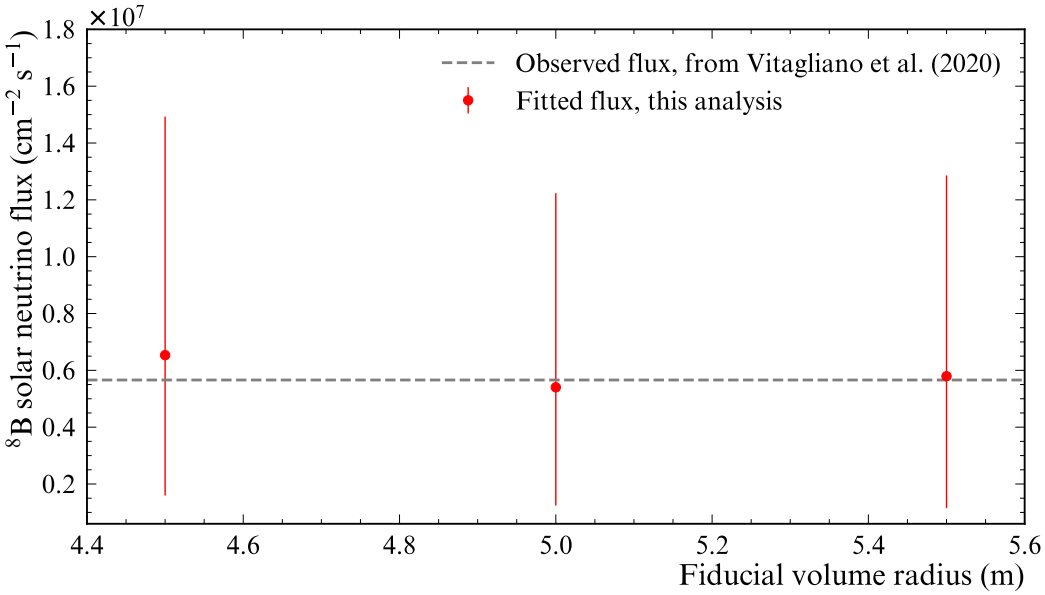

Figure 6.14: Fitted ^{8}B solar neutrino fluxes as a function of fiducial volume radius. The dashed line represents the average observed ^{8}B solar neutrino flux from multiple experiments, obtained from [187].

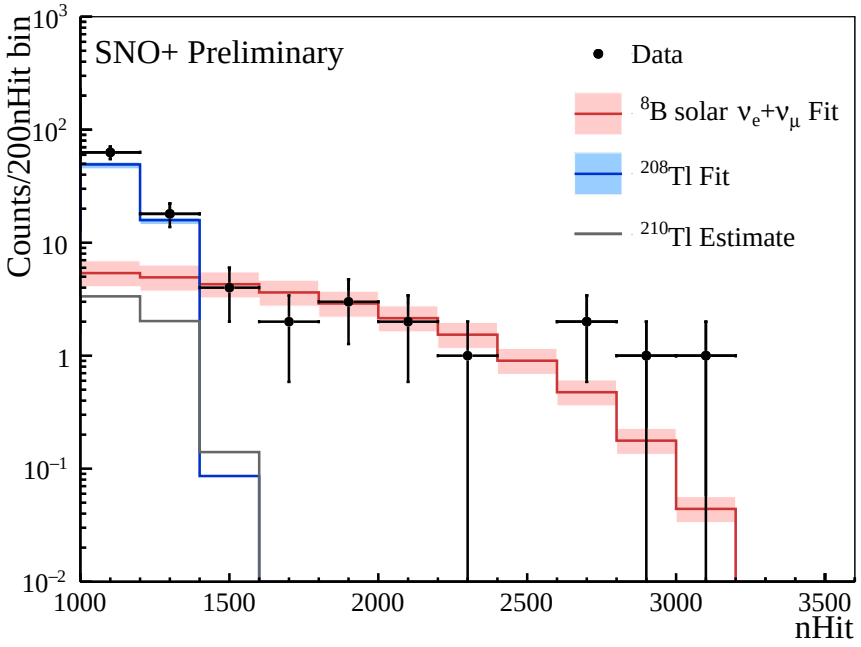

Figure 6.15: Best fit signal (red) and background models (blue and grey lines) compared with the data (black dots) for the fiducial volume with R = 4.5 m. The error bands includes the statistical and systematic uncertainties.

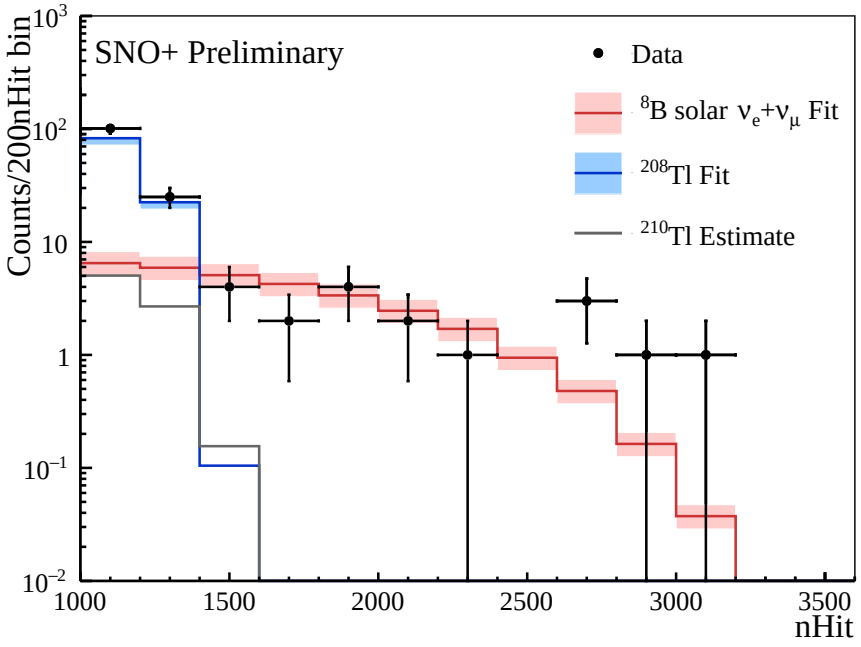

Figure 6.16: Best fit signal (red) and background models (blue and grey lines) compared with the data (black dots) for the fiducial volume with R = 5.0 m. The error bands includes the statistical and systematic uncertainties.

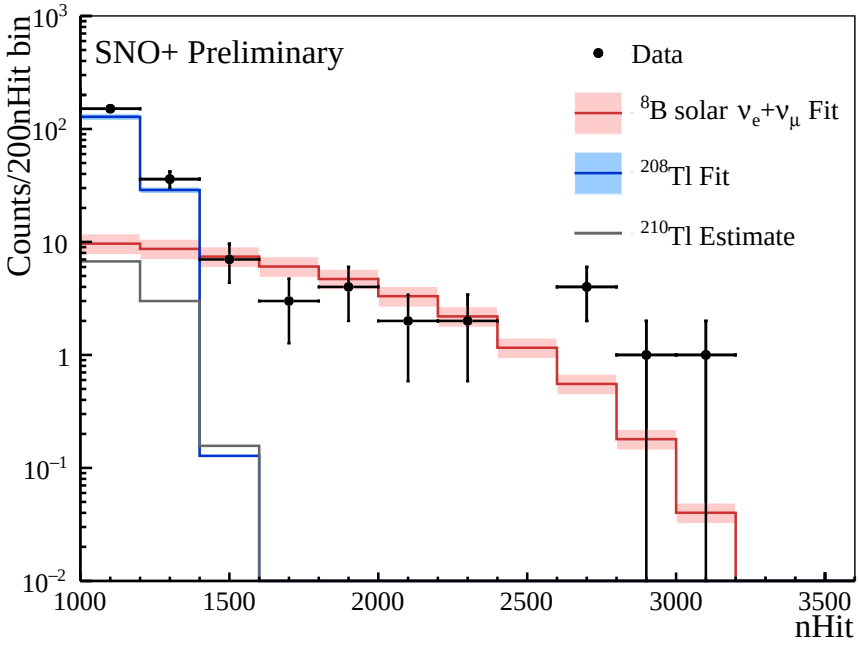

Figure 6.17: Best fit signal (red) and background models (blue and grey lines) compared with the data (black dots) for the fiducial volume with R = 5.5 m. The error bands includes the statistical and systematic uncertainties.

Chapter 7

Double beta decay sensitivity studies

This Chapter presents a sensitivity analysis for the measurement of the half-life of the ^{130}Te $2\nu\beta\beta$ decay in SNO+. The $2\nu\beta\beta$ is one of the irreducible backgrounds expected in the ROI for the $0\nu\beta\beta$ decay searches. Therefore, a precise measurement of the ^{130}Te $2\nu\beta\beta$ decay half-life is needed in order to accurately constrain the leakage of this background into the ROI.

With an expected rate of the order of 5×10^6 events per year with the 0.5% tellurium loading, the $2\nu\beta\beta$ decays are going to be clearly visible in the detected energy spectrum once the first batch of tellurium is loaded into the SNO+ detector. Specifically, it will dominate the energy spectrum above $\sim$1 MeV up to the Q-value of 2.5 MeV, an energy region populated by the β decaying isotopes of the U and Th chains which have an expected rate 1 to 2 orders of magnitude lower. The $2\nu\beta\beta$ decay rate will be extracted from a fit of the expected energy spectrum to the data. This approach is aimed at not only performing an independent measurement of the $2\nu\beta\beta$ decay half-life, but also providing a valuable constraint to the main SNO+ $0\nu\beta\beta$ decay multi-dimensional analysis. Understanding and quantifying the different backgrounds in the $2\nu\beta\beta$ region-of-interest is one of the main challenges of this measurement, along with having an accurate knowledge of the energy scale of the detector.

At the time of writing this thesis, SNO+ has not started data taking with the tellurium isotope. Therefore, the analysis framework presented in this Chapter was developed using Monte Carlo simulations based on the best available knowledge and predictions for the backgrounds and the detector response during the Te-loaded phase. Preliminary systematic uncertainties were propagated to the results, including those related to the absolute energy scale, the optical properties of the scintillator cocktail and the PMTs, and the background model constraints obtained from the water and scintillator phases' measurements. The leakage of the $2\nu\beta\beta$ decay spectrum into the ROI and its impact to the $0\nu\beta\beta$ decay sensitivity are also going to be evaluated.

Section 7.1 starts by motivating the importance of a precise measurement of the $2\nu\beta\beta$ decay half-life. Section 7.2 introduces the analysis framework developed for the studies presented in this Chapter. Section 7.3 presents the expected precision for the half-life measurement in SNO+, including studies of expected sources of systematic uncertainties, and the impact of the $2\nu\beta\beta$ decay half-life precision on the $0\nu\beta\beta$ sensitivity. Finally, Section 7.4 summarizes the prospects for the SNO+ Te-loaded phase and lists the expected challenges for the $2\nu\beta\beta$ decay half-life measurement using real data.

7.1 Motivation for a $2\nu\beta\beta$ decay half-life measurement

The $2\nu\beta\beta$ decay has been a subject of experimental research for more than 60 years. It has been detected for 11 different nuclei for transitions to the ground state (see Table 2.1) and in two cases of transitions to the 0^+ excited state of the daughter nucleus [192, 193]. A complete review of the current status and published half-lives for $2\nu\beta\beta$ decay is found in [194]. At present, the study of $2\nu\beta\beta$ decay is moving into an era of precision measurements. The accuracy of determining the half-life values and other characteristics of this process is becoming increasingly important.

From a theory perspective, a precise measurement of the $2\nu\beta\beta$ decay provides an important cross check of the nuclear matrix elements $M^{2\nu}$ calculations. Because $2\nu\beta\beta$ and $0\nu\beta\beta$ decays share initial and final nuclear states, and the transition operators are similar, a reproduction of $2\nu\beta\beta$ decay is key to reliable $0\nu\beta\beta$ NME predictions. The comparison between the measured half-lives and the models allows to tune theoretical parameters, such as the strength of the proton-neutron pairing g_{pp} of the QRPA model [195, 98]. Additionally, the comparison of exact experimental values and results of theoretical calculations of NMEs can help establishing the value of the vector coupling g_A, and help understanding its effect on the $0\nu\beta\beta$ decay [196]. If the observed g_A quenching is connected with imperfections in the description of nuclear structure and the process of double beta decay itself, adjusting the value of g_A to observations improves the description of the process.

Experimentally, the $2\nu\beta\beta$ decay is one of the major sources of background in running and planned experiments searching for $0\nu\beta\beta$. Due to the limited energy resolution in most experiments, the $2\nu\beta\beta$ spectrum tail will leak into the $0\nu\beta\beta$ ROI. Given the irreducibility of this background, it is crucial to know as best as possible what is the contribution of the $2\nu\beta\beta$ tail to the ROI, which requires an accurate knowledge of the energy response of the detector, but also requires a precise measurement of the decay rate of the $2\nu\beta\beta$.

The most precise determination of the ^{130}Te $2\nu\beta\beta$ decay half-life comes from the CUORE experiment [85]:

$$T^{2\nu}_{1/2} = 7.71^{+0.08}_{-0.06}(\text{stat.})^{+0.12}_{-0.15}(\text{syst.}) \times 10^{20} \text{ years}, \tag{7.1}$$

using a ^{130}Te exposure of 102.7 kg year. This measurement has a statistical uncertainty of 0.8%–1% and a systematic uncertainty of 1.6%–1.9%. SNO+ aims to improve on the precision of this measurement by the use of a larger isotope mass and a good control of the systematic uncertainty sources.

7.2 Analysis framework

The $2\nu\beta\beta$ decay half-life is going to be extracted from fitting probability density functions (PDFs) to data with a binned maximum likelihood fit. The PDFs describe the expected energy distributions of the $2\nu\beta\beta$ signal and backgrounds, and are generated from Monte Carlo simulations. Prior to creating the PDFs, the simulations of the signal and backgrounds go through an event selection process, where analysis cuts are applied to optimize the signal/background ratio.

Fake datasets are generated from the PDFs using the inverted cumulative distribution function method.

The parameters extracted from the fit are the normalizations of the PDFs, i.e. the number of events after cuts assigned to each background and signal. The fit is performed by minimizing the extended binned log-likelihood function:

$$-\ln \mathcal{L} = \sum_{i=1}^{N_{norm}} N_i - \sum_{j=1}^{N_{bins}} N_{data}^{j} \ln \left(\sum_{i=1}^{N_{norm}} N_i P_i^j \right), \tag{7.2}$$

where N_i are the normalizations for the PDFs, N_{norm} is the total number of normalizations (equal to the number of PDFs considered in the fit), N_{data}^{j} is the number of fake data events in bin j, P_i^j is the probability[1] of an event of type i in bin j, and N_{bins} is the total number of bins in the PDF and fake data histograms. Following the minimization, the fitted normalization for the ^{130}Te $2\nu\beta\beta$ decay is converted into a half-life value. The following Sections describe the Monte Carlo simulations used for the studies reported in this Chapter, the analysis cuts, the creation of the PDFs and fake data, the binned maximum likelihood fit, and the calculation to convert the fitted normalizations into a half-life for the $2\nu\beta\beta$ decay.

7.2.1 Monte Carlo simulations

The studies in this chapter use a Monte Carlo production simulated and reconstructed locally at LIP, using RAT 6.18.13. The production includes simulations of each of the background types presented in Tables A.1, A.2 and A.3 of Appendix A.

The detector model includes the expected optical properties of the Te-loaded scintillator cocktail, mainly based on *ex situ* bench top tests, and the measured optical parameters for the acrylic, external water, and PMTs presented in Chapter 4. Prior to running the simulations, the reconstruction algorithms for energy, position, and particle type classifiers, were coordinated (Section 3.7.2) locally at LIP.

The $2\nu\beta\beta$ decays and expected backgrounds during the Te-loaded phase were generated using the `Decay0` event generator. `Decay0` was converted from FORTRAN [197, 198] and adapted to the needs of the SNO+ experiment to generate decay-like events from natural radioactive isotopes and various double beta processes ($\beta^-\beta^-$, $\beta^+\beta^+$, ECβ^+ and ECEC) with transitions to the ground state as well as to excited levels (0^+ and 2^+) of the daughter nucleus. `Decay0` assigns the particle type, its initial energy, time and angular distributions for each decay.

Internal background decays are randomly generated in positions within the scintillator cocktail volume. External background decays are generated in the corresponding geometry component, for example in the external water, in the support ropes, in the acrylic or in the PMTs. The total number of events simulated for each internal background and for the signal was O(10^6). For the external backgrounds, about O(10^7) events were simulated in order to ensure adequate statistics for the corresponding PDFs, since the external background signals decrease exponen-

[1] Obtained by evaluating the PDF i in bin j.

tially towards the center of the AV.

7.2.2 Analysis cuts

Cuts were applied to the Monte Carlo production in order to remove events that are of no interest to the analysis, such as events that were not reconstructed correctly, and to reject backgrounds, such as the ^{214}Bi-^{214}Po coincidences. Table 7.1 gives an overview of the cuts used, and their impact on the $2\nu\beta\beta$ signal.

Table 7.1: Cut variables and values for the $2\nu\beta\beta$ analysis. The $2\nu\beta\beta$ signal sacrifice is also included, and represents the number of rejected $2\nu\beta\beta$ events by each cut, compared to the total (for each independent cut).

Cut	Value	$2\nu\beta\beta$ Sacrifice (%)
Fit valid	True	2.88
Energy	1 MeV $\leq$ E $\leq$ 3 MeV	60.04
Radial position	$\leq$ 3.3 m	82.99
In-window tagging:		
alphaBeta212	$\leq$ 6.5	
alphaBeta214	$\leq$ 12	
Out-of-window tagging:		
Delayed fit valid	True	
Delayed radial position	$\leq$ 6.0 m	0.23
Retrigger tagging	Δt $\leq$ 505 ns Delayed energy $\leq$ 1 MeV	
Delayed candidate tagging	505 ns $<$ Δt $<$ 2 ms 0.5 MeV $\leq$ E $\leq$ 1.5 MeV Δr $\leq$ 2.5 m	

First, a valid result from the reconstruction is required, meaning that both position and energy fits must have converged successfully. This leads to a $2\nu\beta\beta$ signal loss of 2.88%, which is mostly due to events generated inside the AV neck and near the AV surface, where the reconstruction is worsened by the total internal reflection effects on the AV-water interface. The energy window for this analysis goes from 1 MeV to 3 MeV. The lower energy bound was chosen in order to reject the low energy part of the spectrum, where backgrounds from ^{210}Bi and ^{210}Po dominate over the $2\nu\beta\beta$ signal. The range between 1 and 3 MeV contains about 40% of the $2\nu\beta\beta$ spectrum.

The position of the events is reconstructed in the coordinate system of the PMTs, whose centre is expected to be 17.1 cm below the centre of the AV. This offset is caused by the buoyancy of the AV filled with liquid scintillator, since the liquid scintillator has a lower density than water. The offset value used is based on measurements performed when the scintillator fill was completed in 2021. The analysis considers events in a spherical fiducial volume relative to the AV centre, of 3.3 m, equal to what has been used for the $0\nu\beta\beta$ analysis [199, 200, 201]. Therefore, the reconstructed z coordinate (along the vertical axis of the detector) is shifted by the offset before applying the radial position cut.

The chosen standard FV, with a radius of 3.3 m (R^3/R^3_{AV} = 0.17), aims to minimize the backgrounds from external γ-rays and (α,n) reactions along the AV. Figures 7.1 and 7.2 show, respectively, the $2\nu\beta\beta$ signal sacrifice as a function of the radial position cut, and the ratio signal/noise as a function of the radial position cut. Even though larger fiducial volumes lead to smaller signal sacrifices, they also lead to a larger contamination of external backgrounds in the analysis window, greatly reducing the signal/noise ratio. Figure 7.3 shows a two-dimensional map of the signal/noise distributions in energy and spherical FV limited by the radial position cut. For FVs with a radius larger than 4.0 m (R^3/R^3_{AV} = 0.30), certain areas of the energy spectrum start being dominated by external backgrounds. An example is the area around 1.4 MeV, which is dominated by the external ^{40}K decays. For this reason, FVs with radius larger than 4.0 m are not going to be considered in the studies presented in this Chapter.

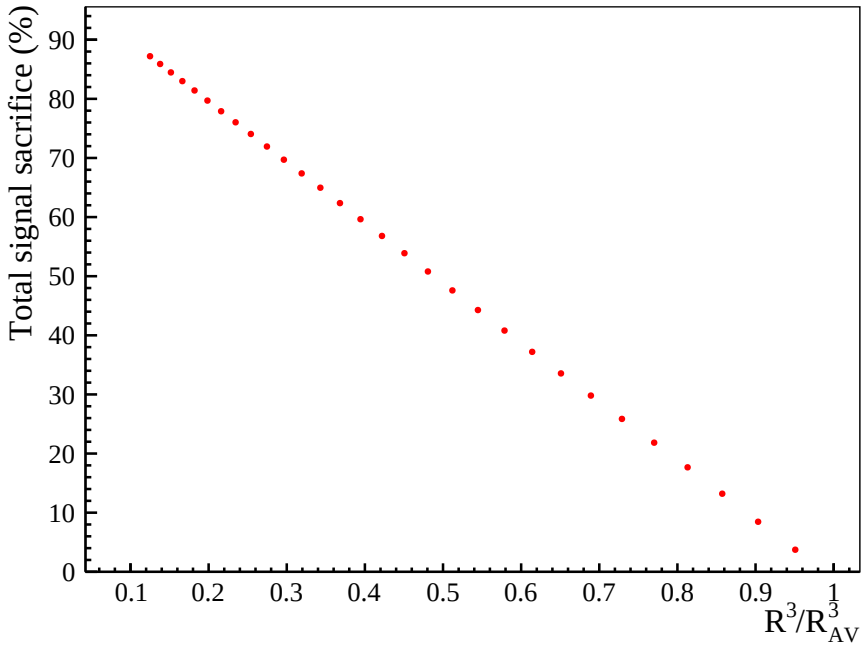

Figure 7.1: ^{130}Te $2\nu\beta\beta$ signal sacrifice as a function of fiducial volume, normalized to the volume of the acrylic vessel (R = 6 m). The sacrifice in the *y*-axis does not include the effects of the other analysis cuts.

The tagging of the Bi-Po coincidences is applied, as described in Section 5.2.1, with the cut values in Table 7.1. The values of the in-window classifiers were optimized for this analysis, in order to maximize Bi-Po rejection while minimizing $2\nu\beta\beta$ signal sacrifice. Figures 7.4 and 7.5 show the distribution of classifier values for the ^{212}Bi-^{212}Po and ^{214}Bi-^{214}Po Monte Carlo in-window events (after applying the out-of-window tagging), against the same distribution for the $2\nu\beta\beta$ Monte Carlo. The cut values were determined by identifying the classifier value that would correspond to a 0.1% $2\nu\beta\beta$ signal sacrifice, following the curves shown in Figures 7.6 and 7.7. An in-window alphaBeta212 cut of 6.5 rejects 83% of the ^{212}Bi-^{212}Po in-window coincidences, while the in-window alphaBeta214 cut of 12 rejects 47% of the ^{214}Bi-^{214}Po in-window coincidences. Even though the rejection is smaller for the latter, the ^{214}Bi-^{214}Po coincidences have a smaller probability of happening within the same trigger window given the longer ^{214}Po half-life compared to ^{212}Po. Therefore, the majority of the ^{214}Bi-^{214}Po rejection power comes

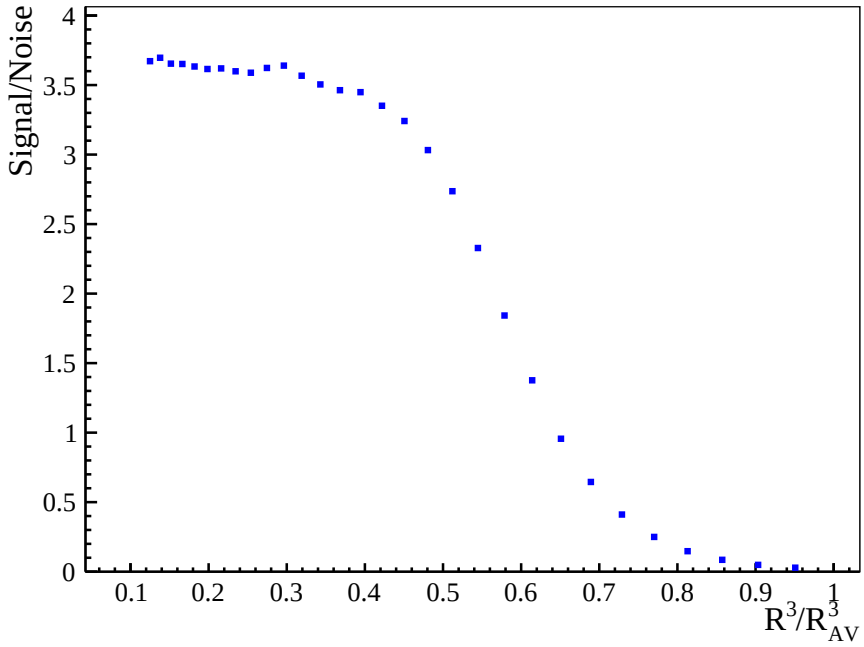

Figure 7.2: ^{130}Te $2\nu\beta\beta$ total signal/noise ratio as a function of fiducial volume, normalized to the volume of the acrylic vessel (R = 6 m). The ratio considered the total number of expected signal and background events over the analysis energy range from 1 MeV to 3 MeV.

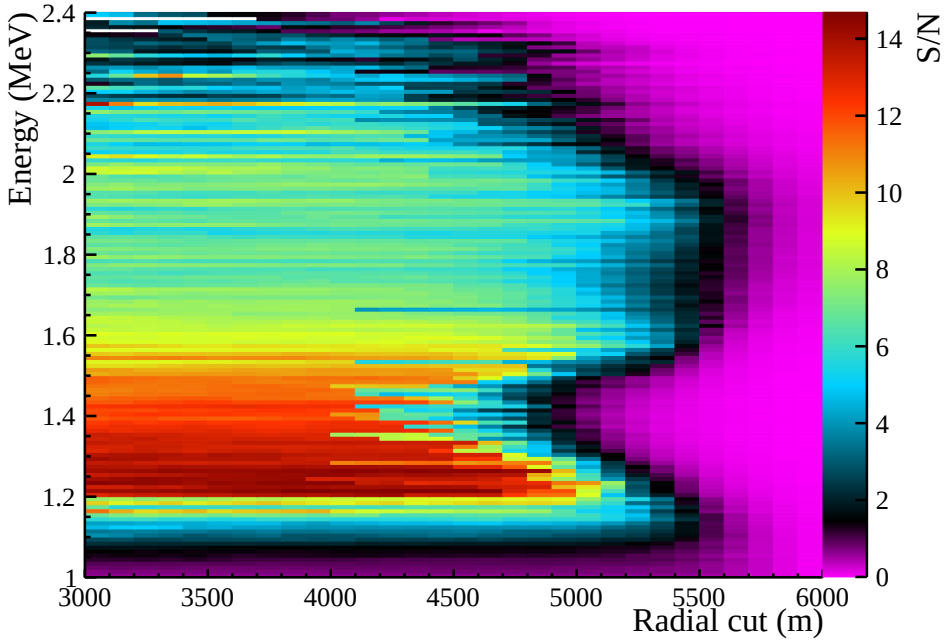

Figure 7.3: ^{130}Te $2\nu\beta\beta$ total signal/noise ratio as a function of radius R of the FV, and as a function of energy. The magenta regions represent a ratio smaller than 1, i.e. the noise dominates over the signal.

from the out-of-window tagging, whereas the ^{212}Bi-^{212}Po rejection power comes from the in-window tagging using the alphaBeta212 classifier. With the Bi-Po tagging cuts presented here, a total tagging efficiency of 99.95% is obtained for ^{214}Bi-^{214}Po, and a total tagging efficiency of 95.25% is obtained for ^{212}Bi-^{212}Po.

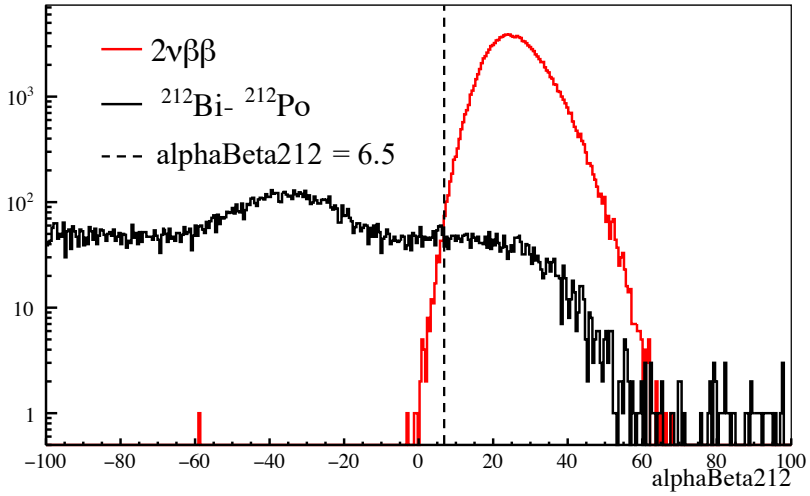

Figure 7.4: Distribution of the values of the alphaBeta212 classifier for ^{212}Bi-^{212}Po (black) and $2\nu\beta\beta$ (red) simulated events, after rejecting the majority of out-of-window coincidences using the tagging method described in the text.

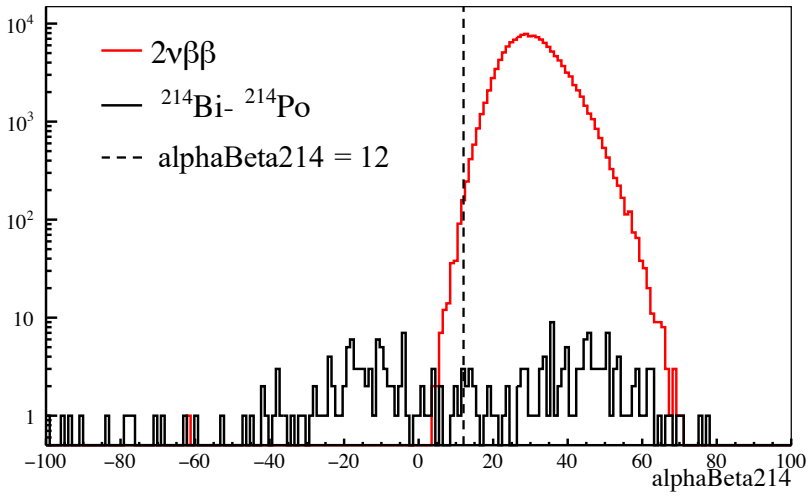

Figure 7.5: Distribution of the values of the alphaBeta214 classifier for ^{214}Bi-^{214}Po (black) and $2\nu\beta\beta$ (red) simulated events, after rejecting the majority of out-of-window coincidences using the tagging method described in the text. The low statistics in the ^{214}Bi-^{214}Po distribution is caused by the small fraction of in-window coincidences of this decay sequence, given the ^{214}Po half-life of 164 μs.

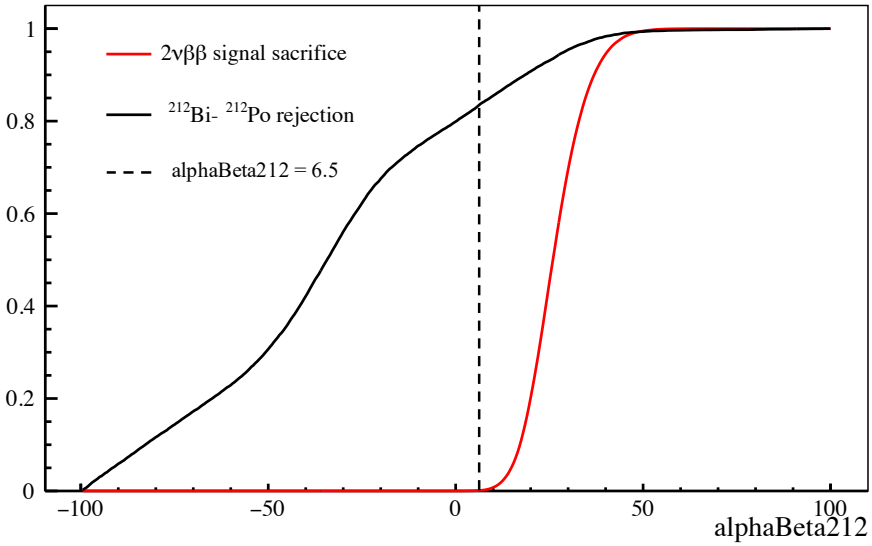

Figure 7.6: $2\nu\beta\beta$ signal sacrifice (red) and in-window ^{212}Bi-^{212}Po rejection (black) curves as a function of the value of the alphaBeta212 classifier cut.

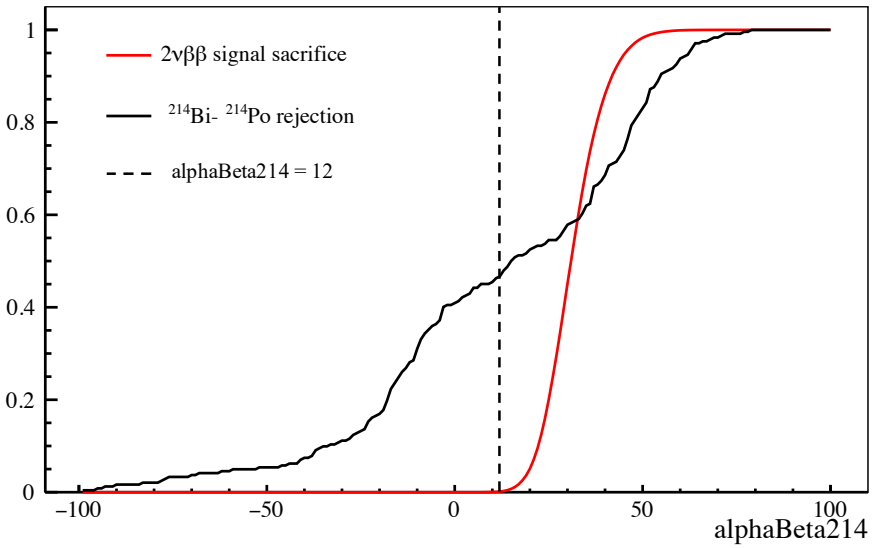

Figure 7.7: $2\nu\beta\beta$ signal sacrifice (red) and in-window ^{214}Bi-^{214}Po rejection (black) curves as a function of the value of the alphaBeta214 classifier cut.

7.2.3 PDFs and fake datasets

PDFs for the binned maximum likelihood fit are extracted from the signal and backgrounds' simulations. They consist of histograms of the reconstructed energy distributions of the Monte Carlo events after applying the analysis cuts described in the previous Section. Since the energy distributions contain the principal information for distinguishing the signal from the background, fine binning for the PDF histograms is needed. The histograms range from 1 MeV to 3 MeV, with 2000 bins in steps of 1 keV. The large number of bins was chosen not only to ensure an accurate description of strongly curved distributions, such as the tails of the β and $\beta\beta$ decays, but also to minimize biases in the generation of the fake data, described bellow. The area of the PDFs is normalized to 1, so that each bin represents the probability of detecting an event, after the analysis cuts, in that bin. The number of events in each PDF varies with the detection efficiency for the corresponding background and the efficiency of the event selection cuts. For that reason, there are statistical fluctuations on a bin per bin basis, particularly in the tails of the spectra.

Given the expected performance of the tellurium purification processes and the strict FV cuts, PDFs for the cosmogenic and external backgrounds are not included. Likewise, the backgrounds whose energy spectra ends below 1 MeV are not considered in the analysis. Figure 7.8 shows the PDFs used in the fit, scaled by the expected decay rates, in a FV with R = 3.3 m.

Since SNO+ does not have tellurium data yet, the studies in this Chapter used fake data. The fake data events were randomly sampled according to the normalized PDFs using the *inverse transform method* [202]. This method relies on inverting the cumulative distribution function (CDF) F(x), defined as the total probability that a random variable X, which follows the PDF $f(x)$, takes on a value $X \leq x$:

$$F(x) = \int_{-\infty}^{x} f(x')dx' \tag{7.3}$$

The inverted CDF $F^{-1}(u)$ is an increasing function between 0 and 1. By generating random numbers between 0 and 1, and evaluating $F^{-1}(u)$, it is possible to generate data samples following the original PDF $f(x)$.

The fake data generation starts by calculating the CDF and inverted CDF based on an input PDF. The binning of the PDFs introduces a level of granularity for the CDF, hence the importance of creating PDFs with a large number of bins, needed to avoid binning artefacts such as sampling multiple times the same value. The total number of fake events to be generated for PDF *i* is calculated by Poisson fluctuating the corresponding target rate, and taking into account the efficiency of the analysis cuts and an hypothetical livetime for the dataset. For each of the total number of fake events, a random number is sampled from a uniform distribution between 0 and 1. Subsequently, the inverse CDF is used to convert the sampled number into an appropriate energy value of the corresponding PDF. The energies of the fake events, after repeating this routine for all considered PDFs, are stored in an histogram with the same number of bins and energy range as the PDFs. Figure 7.9 shows the CDF for the $2\nu\beta\beta$ decay PDF. Figure 7.10 shows the energy spectrum of a fake data set produced using this method.

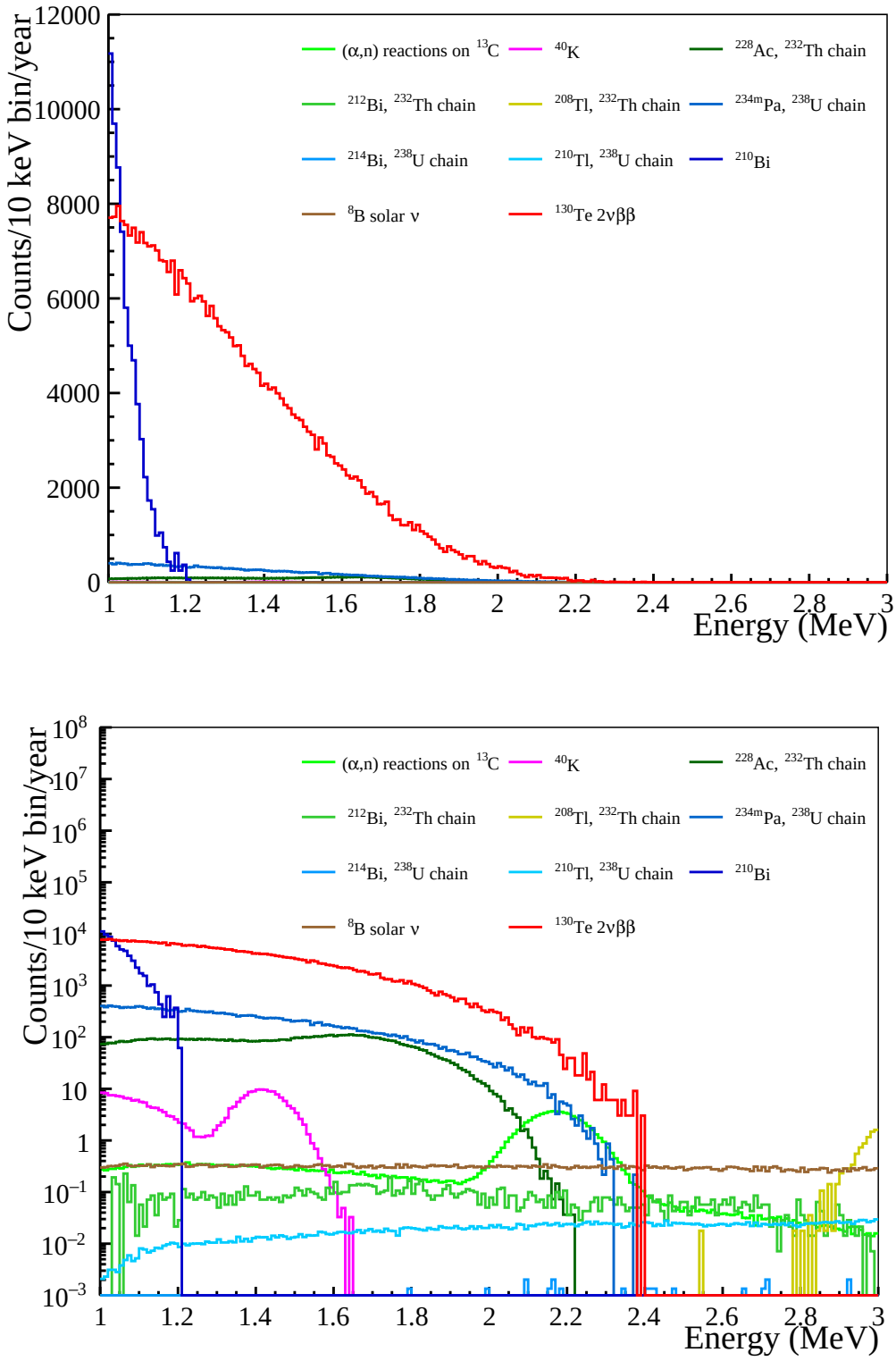

Figure 7.8: Energy distribution of the PDFs used in this analysis, for a FV with R = 3.3 m, scaled by the corresponding expect rates in one year. Distributions in linear scale on top, and in logarithmic scale on the bottom.

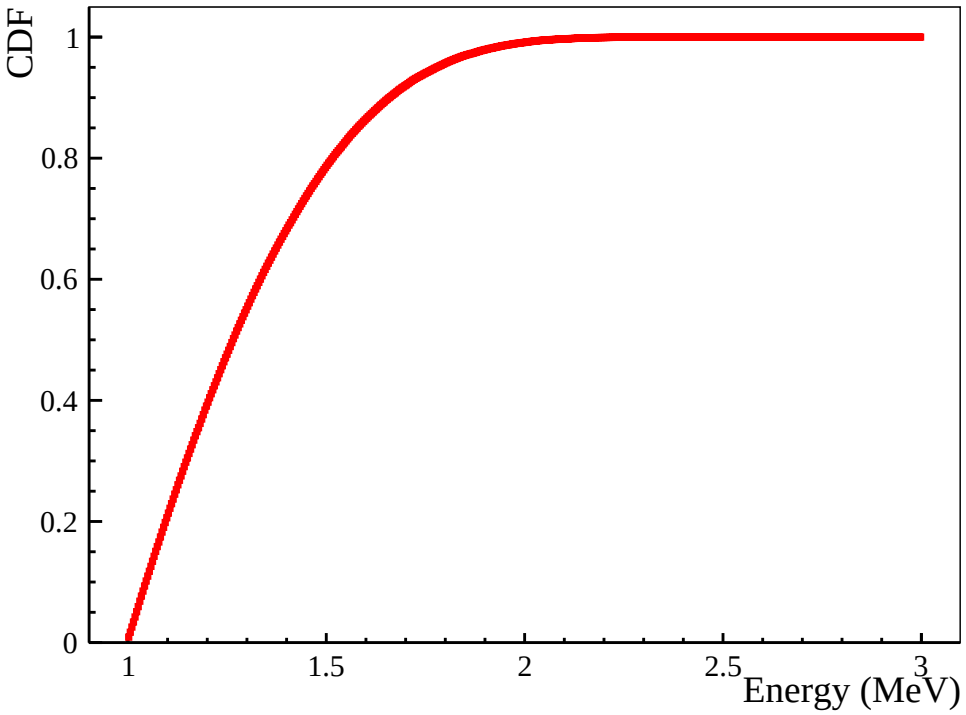

Figure 7.9: Example of a cumulative distribution function for the $2\nu\beta\beta$ signal.

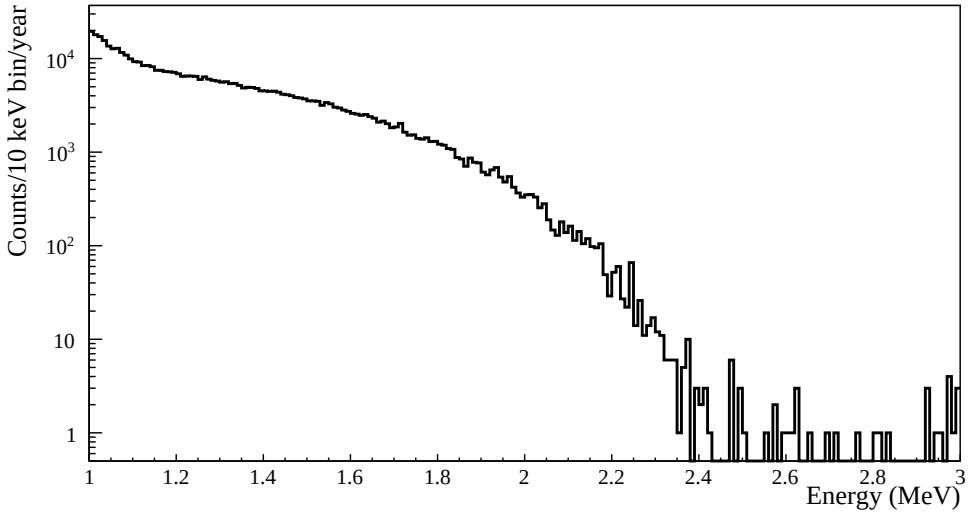

Figure 7.10: Energy distribution of one of the fake datasets produced, assuming one year of livetime.

7.2.4 Binned maximum likelihood fit

The number of $2\nu\beta\beta$ decay events, and consequently the half-life, is extracted from the dataset by performing a binned maximum likelihood fit. Given that this analysis expects to deal with a large number of signal and background events, spread over a wide energy range, performing a binned likelihood fit takes significantly less computation time than an unbinned maximum likelihood fit, like the one that was developed for the ^{8}B solar neutrino analysis presented in Chapter 6.

Considering a total number $N_{model} = N_S + N_B$ of signal and background processes in the model, each will have a corresponding PDF histogram with N_{bins} bins, with the centre of the bins denoted as $\{x_1, x_2, ..., x_j, ..., x_{bins}\}$. The total expected number of events μ_j in bin *j* can be expressed as the sum of the total normalizations for each process, N_i, multiplied by the probability that an event of process i ends up in bin *j*:

$$\begin{aligned} \mu_j &= \sum_{i=1}^{N_{model}} N_i \int_{\Delta x_j} P_i(x)dx \\ &\approx \sum_{i=1}^{N_{model}} N_i P_i^j. \end{aligned} \tag{7.4}$$

The value of P_i^j is the content of bin *j* of the PDF corresponding to the process *i*.

The goal of the maximum likelihood fit is to determine the set of normalizations $\vec{N}_{model} = \{N_0, ..., N_i, ...\}$ that yield the best agreement between the model and the data $\vec{n}_{data} = \{n_0, ..., n_j, ...\}$. The data counts in each bin, n_j, are expected to be random numbers drawn from a Poisson distribution with an expectation value μ_j. The extended likelihood function $\mathcal{L}(\vec{n}_{data}|\vec{N}_{model})$, expressing the likelihood for the observation of the data given the model, can be written as:

$$\mathcal{L}(\vec{n}_{data}|\vec{N}_{model}) = \prod_{j=1}^{N_{bins}} \frac{(\mu_j)^{n_j}}{n_j!} e^{-\mu_j}. \tag{7.5}$$

The normalizations N_i are then obtained by minimizing $-\ln\left[\mathcal{L}(\vec{n}_{data}|\vec{N}_{model})\right]$:

$$-\ln\left[\mathcal{L}(\vec{n}_{data}|\vec{N}_{model})\right] = \sum_{i=0}^{N_{model}} N_i - \sum_{N_{bins}}^{j=0} n_j \ln\left(\sum_{i=0}^{N} N_i P_i^j\right). \tag{7.6}$$

The negative sign for the logarithm is introduced to decrease the requirements involved in the optimization of the fit parameters – therefore, searching the maximum of the $\mathcal{L}$ function corresponds to searching the minimum of the $-\ln\mathcal{L}$. The likelihood function is minimized using ROOT's Minuit package [190]. The fit runs first the `SIMPLEX` method for minimization in order to find good starting values for the normalizations, followed by the `MIGRAD` method for the main minimization. The uncertainties of the fitted normalizations are first evaluated with the `HESSE` method, which calculates the Hessian matrix (second derivatives) of the likelihood function, and with the `MINOS` method, which calculates asymmetric errors.

The $2\nu\beta\beta$ decay normalization is always a free parameter in the fit. The background normalizations can either be free parameters or constrained to float within the uncertainties of prior measurements. In the studies presented here, the constraints come from the background measurements performed during the water and scintillator phases. These constraints are incorporated by multiplying Equation 7.5 by a Gaussian term based on the expected backgrounds and the uncertainty on those expectations:

$$\text{Gauss}(N_i, \hat{N}_i, \sigma_i) = \frac{1}{\sqrt{2\pi\sigma_i^2}} \exp\left\{-\frac{(N_i - \hat{N}_i)^2}{2\sigma_i^2}\right\}, \tag{7.7}$$

where $\hat{N}_i$ is the expected normalization for events of type *i*, and σ_i is the uncertainty on $\hat{N}_i$. This term modifies Equation 7.6 into:

$$-\ln\left[\mathcal{L}(\vec{n}_{data}|\vec{N}_{model})\right] = \sum_{i=0}^{N_{model}} N_i - \sum_{N_{bins}}^{j=0} n_j \ln\left(\sum_{i=0}^{N} N_i P_i^j\right) + \sum_{i=0}^{N_{model}} \frac{(N_i - \hat{N}_i)^2}{2\sigma_i^2}. \tag{7.8}$$

7.2.4.1 Constraints for the PDF normalizations

Table 7.2 lists the PDFs which have been considered for the studies presented in the following sections, along with the assumed uncertainties for the normalization constraints, σ_i. The PDFs that do not have a value for the constraint uncertainty are free to float in the fit. The values of the constraints $\hat{N}_i$ are calculated based on the rates in Table A.1. When available, the measured rates were considered as default. Likewise, the values of the uncertainties σ_i are based on the uncertainties of the measured rates.

In the case of the isotopes coming from the U (^{234m}Pa, ^{214}Bi-^{214}Po, ^{210}Tl) and Th (^{228}Ac, ^{212}Bi-^{212}Po, ^{208}Tl) chains, the current measurements only concern the contribution of the pure liquid scintillator, and are not fully representative of the U/Th concentrations in the final cocktail. However, this analysis assumes that, during the Te-phase, their rates are going to be determined with similar precision using the Bi-Po coincidence tagging methods.

Since currently there is no way of demonstrating secular equilibrium at the top of the Th and U chains, the rates derived from the Bi-Po tagging may not accurately represent the amount of the ^{228}Ac and ^{234m}Pa isotopes in the liquid scintillator. For this reason, it is not possible to assume constraints for the normalizations of ^{228}Ac and ^{234m}Pa, and they are left free to float in the fit.

7.2.4.2 Fit validation

The robustness of the fit was evaluated based on the bias and pull distributions. The bias tests the accuracy in recovering the expected normalizations and the pull checks both the fitted normalization and uncertainty:

$$\text{Bias} = \frac{N^{\text{fit}} - N^{\text{expected}}}{N^{\text{expected}}}, \qquad \text{Pull} = \begin{cases} \frac{N^{\text{expected}} - N^{\text{fit}}}{\sigma_+^{\text{fit}}}, & \text{if } N^{\text{fit}} \leq N^{\text{expected}} \\ \frac{N^{\text{fit}} - N^{\text{expected}}}{\sigma_-^{\text{fit}}}, & \text{otherwise.} \end{cases} \tag{7.9}$$

Table 7.2: List of PDFs used in the fit. The second column shows the uncertainty σ_i of each normalization constraint $\hat{N}_i$. The PDFs that do not have a value for the constraint uncertainty are free to float in the fit.

i	PDF	$\sigma_i/\hat{N}_i$ (%)
0	^{130}Te $2\nu\beta\beta$	–
1	(α,n) ^{13}C interactions in LS	–
2	^{8}B solar ν	2.5
3	^{40}K	–
4	^{228}Ac	–
5	^{212}Bi-^{212}Po	28.3
6	^{208}Tl	28.3
7	^{234m}Pa	–
8	^{214}Bi-^{214}Po	25.5
9	^{210}Tl	25.5
10	^{210}Bi	11

Figures 7.11 and 7.12 show the bias and pull distributions for the $2\nu\beta\beta$ signal, after running the fit over 10000 fake datasets, produced considering the FV with R = 3.3 m. The bias distribution has a mean of (-4 $\pm$ 1)$\times 10^{-4}$, and a width of (1.103 $\pm$ 0.008)$\times 10^{-2}$. The pull distribution has a mean of 0.03 $\pm$ 0.01 and a width of 1.41 $\pm$ 0.01. These results show that the fit has a very small average bias, but the larger than unity pull width indicates a underestimation of the fit uncertainties, whose values can be affected by parameter correlations.

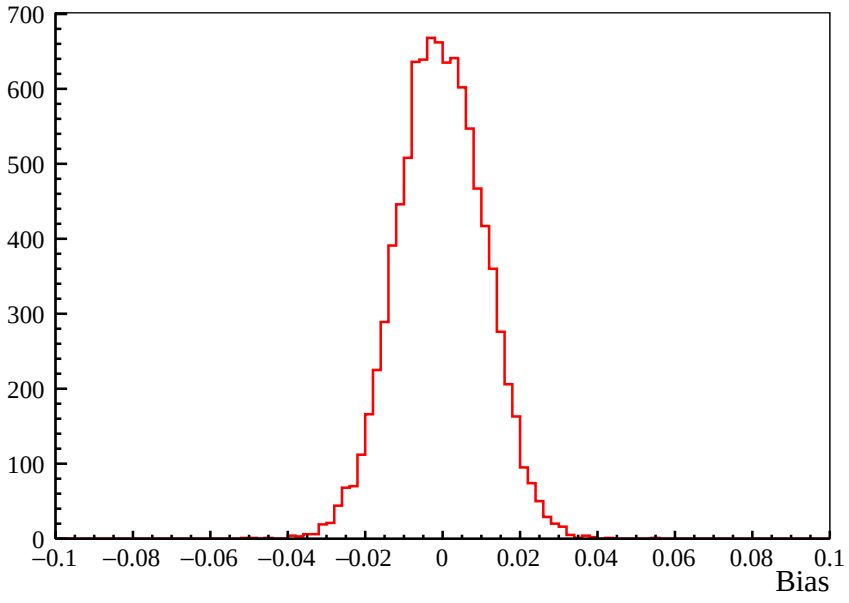

Figure 7.11: Bias of the binned maximum likelihood fit for $2\nu\beta\beta$ decay normalization.

7.2.4.3 Parameter correlations

Figure 7.13 displays the correlation space for the fit parameters, numbered according to Table 7.2. A strong anti-correlation between the ^{130}Te $2\nu\beta\beta$ normalization (i = 0) and the

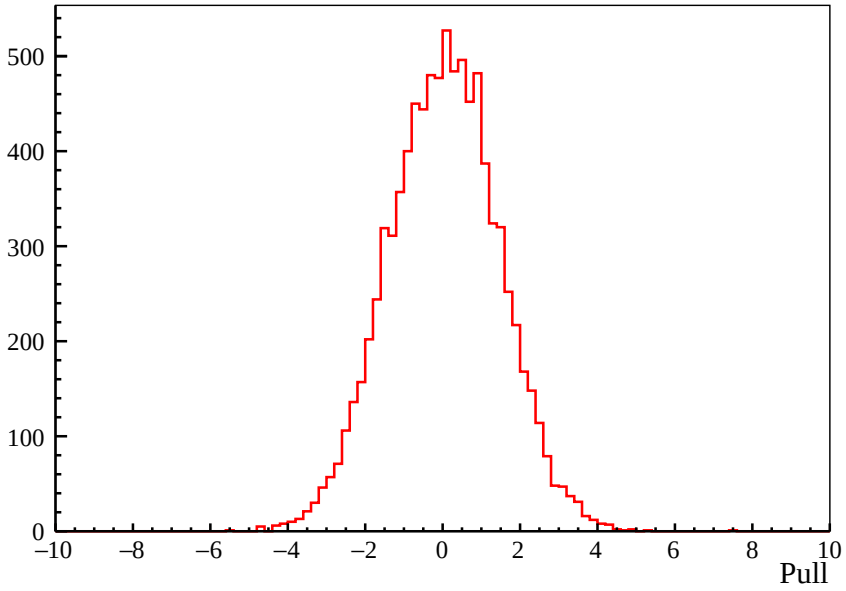

Figure 7.12: Pull of the binned maximum likelihood fit for $2\nu\beta\beta$ decay normalization.

^{234m}Pa normalization (i = 7) is observed. This is due to the similarities between their energy spectra, shown in Figure 7.14. For some of the fake datasets, depending on the bins' statistical fluctuations, the correlations between the unconstrained PDFs lead to overfitting or underfitting the $2\nu\beta\beta$ normalization. Hence, there is some variability in the fitted half-lives relative to the input half-life used to produce the fake data. For this reason, the results of the next Sections are averages produced after running the fit for 1000 fake datasets.

7.2.5 $2\nu\beta\beta$ decay half-life calculation

The expression for the ^{130}Te $2\nu\beta\beta$ decay half-life is derived from the standard exponential radioactive decay formula:

$$N(t) = N_0 e^{-\lambda t}\,, \tag{7.10}$$

where $N(t)$ is the number of atoms left that have not decayed after time t and N_0 is the initial number of atoms at $t = 0$. λ denotes the decay constant which is defined as $\lambda = \ln(2)/T_{1/2}$, with $T_{1/2}$ being the half-life. The number of decays N_{dec} during a measurement time t is:

$$\begin{aligned} N_{dec} &= N_0 - N(t) \\ &= N_0(1 - e^{-\lambda t}). \end{aligned} \tag{7.11}$$

In the limit where λ tends to zero, valid for the very long half-lives of the $2\nu\beta\beta$ decay, this expression can be expanded to:

$$N_{dec} = N_0 t \frac{\ln(2)}{T_{1/2}}. \tag{7.12}$$

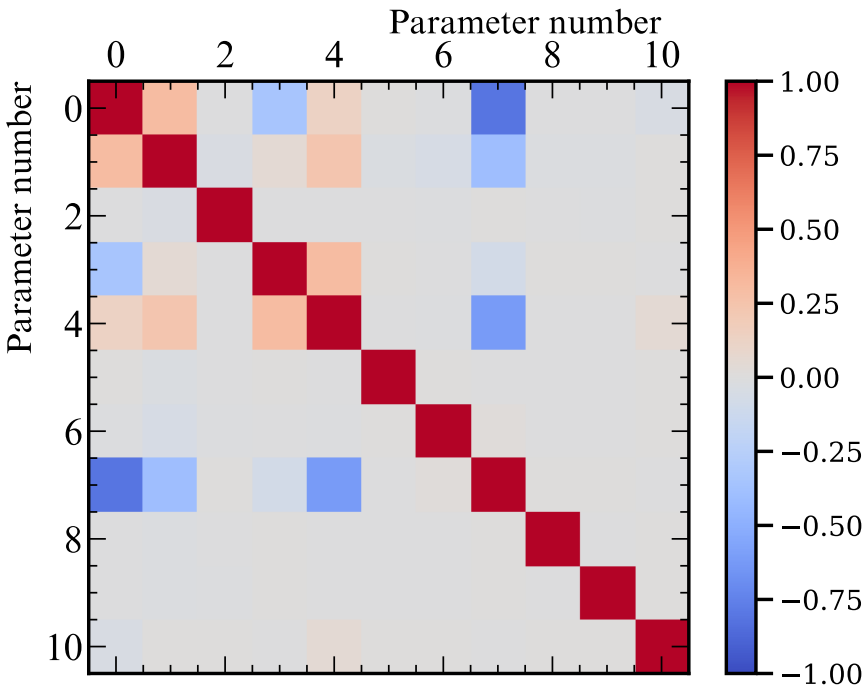

Figure 7.13: Correlation space for the parameters in the fit, numbered as Table 7.2.

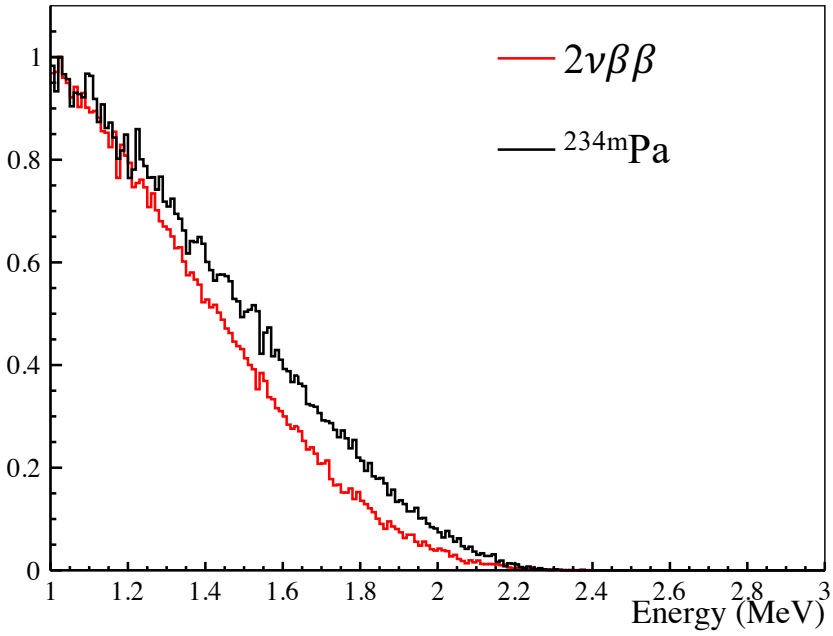

Figure 7.14: Comparison of the energy spectra of the ^{130}Te $2\nu\beta\beta$ decay (red) and ^{234m}Pa.

The number of parent nuclei N_0 can be expressed in terms of the mass of isotope in the detector m_{130} as:

$$N_0 = m_{130} N_A \frac{1}{M}, \tag{7.13}$$

where N_A is Avogadro's number, and M is the atomic mass of ^{130}Te. Combining Equations 7.12 and 7.13, the half-life is expressed as:

$$T_{1/2} = m_{130} \frac{N_A}{M} \frac{\ln(2)}{N_{dec}} t. \tag{7.14}$$

The fitted $2\nu\beta\beta$ decay normalization, $N_{2\nu,fit}$, is converted into a half-life by considering the signal efficiency ϵ, changing Equation 7.14 to:

$$T_{1/2} = \epsilon m_{130} \frac{N_A}{M} \frac{\ln(2)}{N_{2\nu,fit}} t. \tag{7.15}$$

The signal efficiency ϵ includes the detection efficienty, the efficiency of the analysis cuts, described in Section 7.2.2, and the fraction of $2\nu\beta\beta$ events in the fit region. Some of the parameters in this equation conceal possible sources of systematic uncertainties for the half-life. The systematic uncertainties coming from the accuracy of the detector response model are propagated through ϵ; $M_{^{130}Te}$ introduces a systematic uncertainty for the number of ^{130}Te atoms inside the detector; $N_{2\nu\beta\beta,fit}$ not only includes a statistical uncertainty for the half-life, but also a systematic uncertainty concerning the background model, since the varying constraints for the background rates can alter the fitted number of $2\nu\beta\beta$ events.

7.3 ^{130}Te $2\nu\beta\beta$ decay half-life precision

7.3.1 Statistical precision

7.3.1.1 Loading of the first tellurium batch

In order to transition from the pure liquid scintillator phase to the Te-loaded phase, SNO+ will start by loading a single batch (1/52) of the total 0.5% tellurium loading, followed by a 3-month duration data taking campaign. The single batch corresponds to about 25.5 kg of the ^{130}Te isotope. The goals of this intermediate stage are performing a robust characterization of the backgrounds introduced with the tellurium (U/Th and cosmogenics), and verifying the changes caused in the detector response. Furthermore, this stage will provide the first opportunity to observe the $2\nu\beta\beta$ decay spectrum and measure its half-life.

The expected precision for a $2\nu\beta\beta$ decay half-life measurement was evaluated by running the binned maximum likelihood fit on a fake dataset with 1/52 of the expected ^{130}Te mass. As described in Appendix A, the addition of the TeBD introduces further U and Th contamination in the scintillator cocktail. Therefore, in this scenario, the U/Th concentrations coming from the telluric acid and butanediol were also scaled by the factor of 1/52. Half of the amount of DDA is expected to be mixed in the cocktail before the first batch is added, with the remaining

being added along with the tellurium. Hence, the U/Th contributions from DDA were scaled by 53/104, coming from 1/2 of the already loaded DDA and from the 1/104 introduced with the first tellurium batch.

The PDFs and fake data were produced following the steps described in Section 7.2.3, after applying the cuts presented in Section 7.2.2 to the Monte Carlo simulations. The fit was run as described in Section 7.2.4. Three main FVs with R = 3.3 m, 3.5 m and 4.0 m were assumed in order to study the evolution of the statistical precision of the fit with FV. For all of them, the external backgrounds were considered negligible, hence their PDFs were not included in the fit. Table 7.3 reports the average fitted half-life and statistical precision, from running the fit over 1000 fake datasets. Figures 7.15 and 7.16 show the energy distribution for one example fake data, with the PDFs scaled by the fit results, for the FVs with R = 3.3 m and 4.0 m, respectively.

Table 7.3: Average fitted $2\nu\beta\beta$ decay half-lives and statistical uncertainties for different exposures (varying FV) for a three month data taking run using 1/52 of the total ^{130}Te isotope loading. The results were obtained from running the fit over 1000 fake datasets.

R (m)	Exposure (kg year)	$T_{1/2}^{2\nu\beta\beta}$ ($\times 10^{20}$ years)	Stat. uncertainty (%)	Bias (%)
3.3	1.06	$7.49^{+1.20}_{-1.20}$ (stat.)	16	-2.85
3.5	1.27	$7.45^{+1.12}_{-1.12}$ (stat.)	15	-3.37
4.0	1.88	$7.50^{+1.05}_{-1.05}$ (stat.)	14	-2.72

The results are compatible with the input half-life used to generate the fake $2\nu\beta\beta$ events (Equation 7.1), albeit with large statistical uncertainties and O(3%) bias. Given the small isotope mass and, consequently, low expected number of events, the correlations between the $2\nu\beta\beta$ normalization and the other free normalizations in the fit have a larger impact on the results. Figure 7.17 shows the mean bias of the fitted $2\nu\beta\beta$ normalizations for 1000 randomly generated fake datasets, as a function of the radius of the FV. The error bars represent the width of the bias distribution. The observed bias is explained by the low number of expected signal events in the fit range, O(10^3), and the correlations between the signal normalization and the remaining free parameters.

With the initial 3-month tellurium assay, SNO+ is then expected to be able to clearly observe the ^{130}Te $2\nu\beta\beta$ decay signal, and measure its half-life with a statistical precision of $\sim$15%, dependent on the size of the fiducial volume. Although this is not going to be a competitive physics measurement, it is going to be an important proof-of-concept of the SNO+ double beta decay analysis.

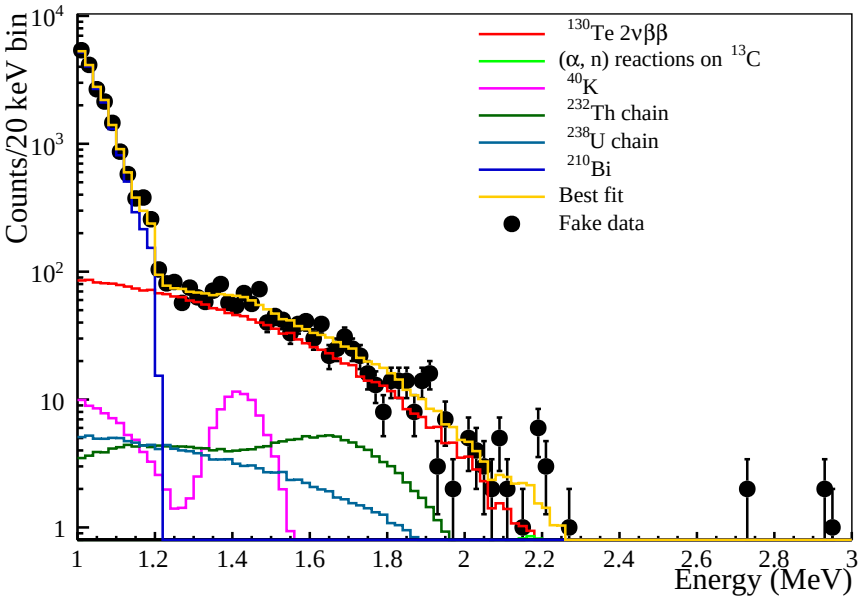

Figure 7.15: Energy distribution of the fake data (black dots) against the best fit model (yellow line), for 3 months of data taking time in a FV with R = 3.3 m during the first Te assay run, with a total of 25.5 kg of isotope (1/52 of the full loading). The remaining coloured lines represent the individual PDFs scaled by the fit normalizations.

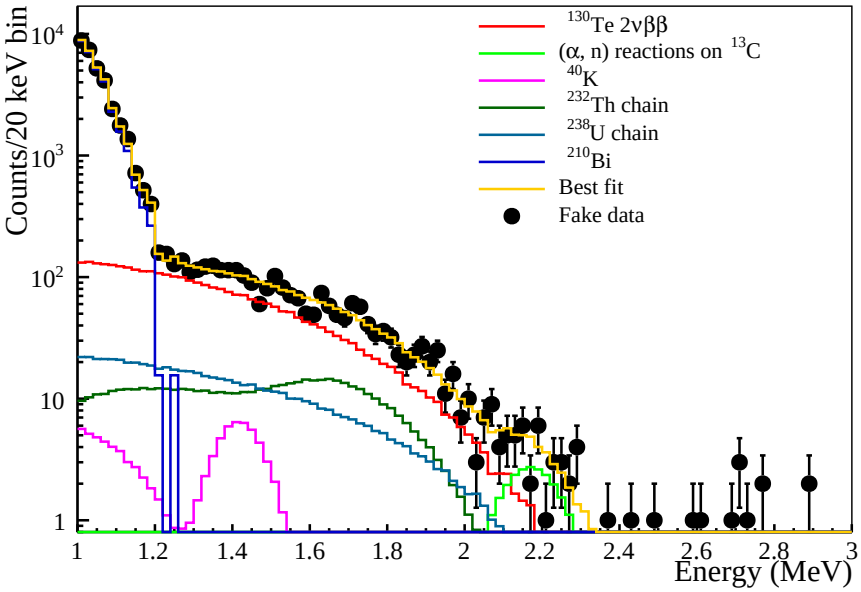

Figure 7.16: Energy distribution of the fake data (black dots) against the best fit model (yellow line), for 3 months of data taking time in a FV with R = 4.0 m during the first Te assay run, with a total of 25.5 kg of isotope (1/52 of the full loading). The remaining coloured lines represent the individual PDFs scaled by the fit normalizations.

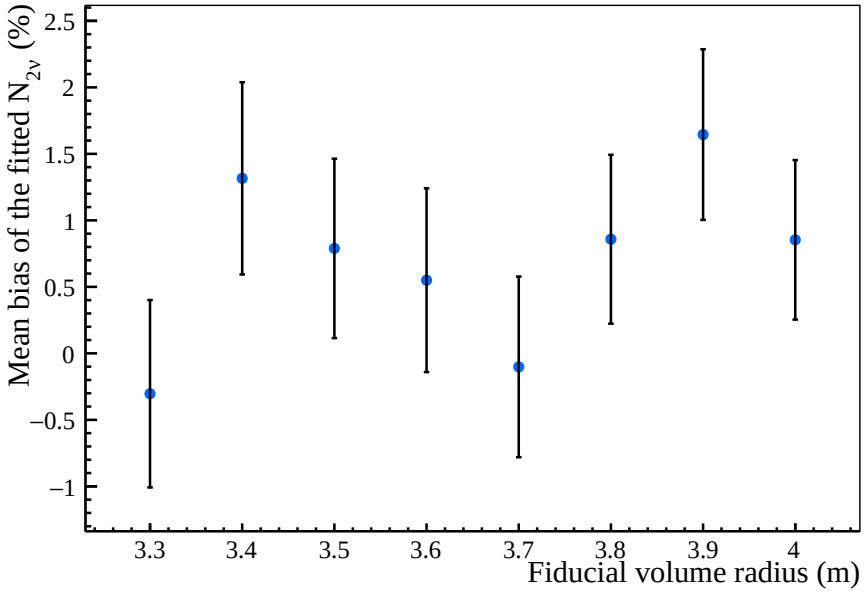

Figure 7.17: Mean bias of the fitted $N_{2\nu}$ for the first Te assay run, with a total of 25.5 kg of isotope (1/52 of the full loading), as a function of fiducial volume radius. A livetime of 3 months is assumed.

7.3.1.2 Precision during the Te-loaded phase

Once the tellurium loading is finished, SNO+ is expected to take stable data for 3 to 5 years to perform the $0\nu\beta\beta$ decay search. During that period, the ^{130}Te $2\nu\beta\beta$ signal is going to be continuously measured and monitored. The evolution of the expected precision for the $T^{2\nu}_{1/2}$ measurement with time was studied by running the binned maximum likelihood fit over 1000 fake datasets, each produced assuming different exposure times from 0.25 years (3 months) to 5 years.

Table 7.4 lists the fitted half-lives for the smaller (3.3 m) and larger (4.0 m) FVs assumed in these studies, assuming 6 months, 1 year and 3 years livetime. The results show that, with 6 months of data, a precision of $\sim$1% can be achieved for $T^{2\nu}_{1/2}$. With 1 year of data, the precision improves by $\sim$25%. Increasing the FV volume, keeping the same livetime, increases the exposure by a factor of 1.78 and slightly decreases the statistical uncertainty, which is dominated by the parameter correlations. The bias of the fitted half-lives is smaller than reported in the scenario discussed in the previous Section. This is further illustrated in Figure 7.18, which shows the mean bias of the fitted $2\nu\beta\beta$ normalization as a function of the fiducial volume radius for a livetime of 6 months (left) and 1 year (right). The fact that the biases have negative values means that the fitted normalizations are smaller than the expected normalization used to produce the fake datasets.

Figure 7.19 shows the best fit $2\nu\beta\beta$ half-life and corresponding statistical uncertainties as a function of exposure for 0.5% isotope loading, in the FV with radius of 3.3 m. The dashed line represents the input half-life used to generate the fake $2\nu\beta\beta$ events (Equation 7.1). As the exposure time increases, the fitted half-life is expected to converge to the real ^{130}Te $2\nu\beta\beta$ decay half-life, with increasingly smaller statistical uncertainties.

Table 7.4: Fitted $2\nu\beta\beta$ decay half-lives for different exposures for the total ^{130}Te isotope loading.

Livetime (year)	R (m)	Exposure (kg year)	$T_{1/2}^{2\nu\beta\beta}$ ($\times 10^{20}$ years)	Stat. uncertainty (%)	Bias (%)
0.5	3.3	110.6	$7.720^{+0.084}_{-0.086}$ (stat.)	1.10–1.11	0.12
1	3.3	221.1	$7.721^{+0.061}_{-0.063}$ (stat.)	0.79–0.81	0.06
3	3.3	663.4	$7.749^{+0.034}_{-0.036}$ (stat.)	0.44–0.46	0.53
0.5	4.0	196.9	$7.730^{+0.081}_{-0.084}$ (stat.)	1.09–1.10	0.19
1	4.0	393.8	$7.735^{+0.056}_{-0.057}$ (stat.)	0.72–0.74	0.14
3	4.0	1181.4	$7.759^{+0.030}_{-0.033}$ (stat.)	0.39–0.43	0.61

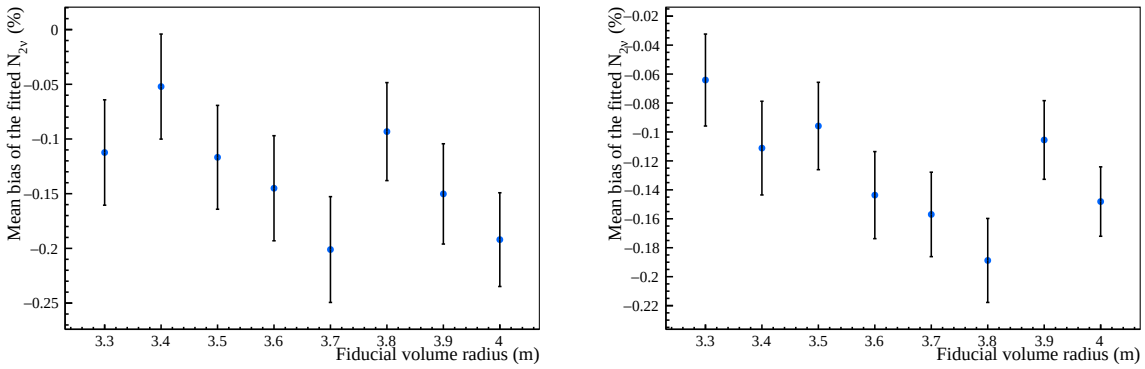

Figure 7.18: Mean bias of the fitted $N_{2\nu}$ as a function of fiducial volume radius, assuming a livetime of 6 months (left) and 1 year (right).

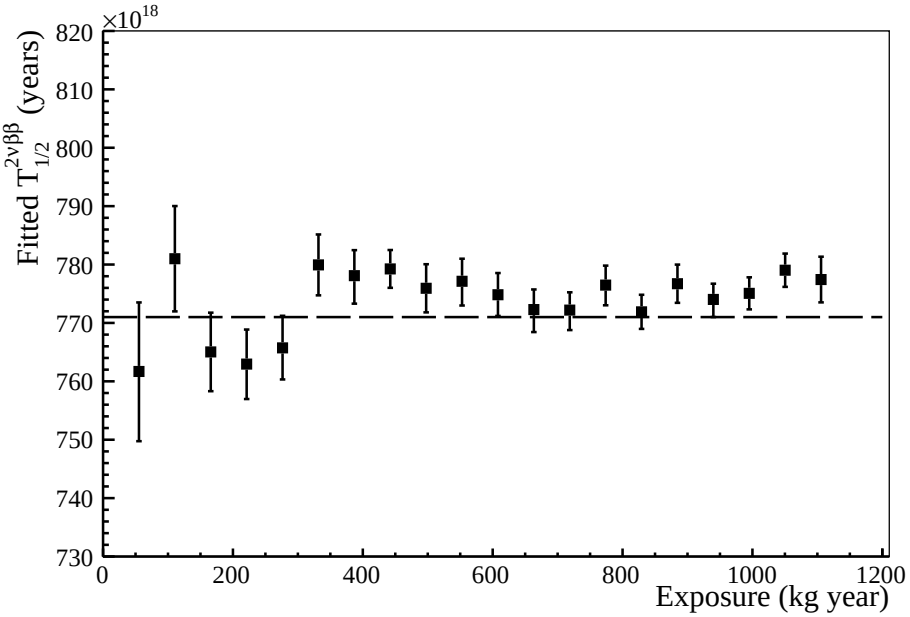

Figure 7.19: Best fit $2\nu\beta\beta$ half-life and corresponding statistical uncertainties as a function of exposure, for the FV with a 3.3 m radius. The dashed line represents the input half-life used to generate the fake $2\nu\beta\beta$ events.

Figure 7.20 shows the evolution of the statistical uncertainties provided by the fit as a function of exposure, for three different spherical fiducial volumes with R = 3.3, 3.5 and 4.0 m. The results show that, with an exposure larger than 200 kg year with 0.5% isotope loading, assuming the best current knowledge of the expected background rates, SNO+ expects a half-life measurement precision of 1% or better. Furthermore, with double the exposure, the half-life statistical precision is expected to improve by a factor of 2. Naturally, increasing the FV increases exposure and the expected number of observed decays and, by consequence, leads to lower statistical uncertainties. However, this improvement is not observed to scale linearly with the FV increase, since it is limited by the correlations between the unconstrained PDFs.

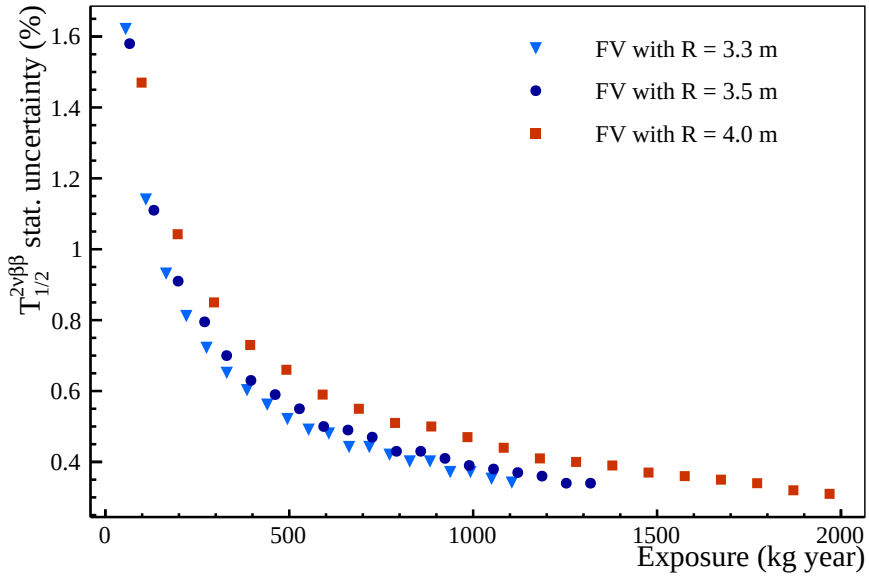

Figure 7.20: Evolution of the best fit half-life statistical uncertainties as a function of exposure time, for three different spherical fiducial volumes with R = 3.3 m (light blue inverted triangles), 3.5 m (dark blue circles) and 4.0 m (red squares).

7.3.2 Systematic uncertainties

Apart from the statistical uncertainties on the fitted signal normalization, the $T^{2\nu}_{1/2}$ measurement is subject to a number of systematic uncertainties. They mainly arise from the modelling of the detector response, the energy scale and resolution, and the background model. Furthermore, the conversion from signal normalization to a half-life relies on an estimate of the amount of isotope loaded into the detector – the accuracy of this estimate will be an additional source of systematic uncertainty.

This Section presents studies aimed at evaluating the impact of systematic effects to the $2\nu\beta\beta$ decay half-life precision, particularly related to the absolute energy scale and to the optical properties of the scintillator and PMTs. Some of the assumptions made about the systematics in this Chapter are conservative. However, the goal is not to determine a true systematic uncertainty, but to study how systematics could affect the fit when this analysis is performed using the first Te-loaded data.

The systematics are propagated using a shift+refit method. An uncertainty was attributed to the absolute energy scale of the detector, to the scintillator attenuation and to the angular response of the PMTs and concentrators. New Monte Carlo and PDFs were created with each of these values shifted by the corresponding uncertainty. The $2\nu\beta\beta$ fit was repeated for each case. Systematic uncertainties were determined by comparing the half-life of the nominal fit, $T^{2\nu}_{1/2,N}$, with the half-lives determined in each fit with the described systematics shifts, $T^{2\nu}_{1/2,S}$:

$$\sigma_{\text{syst}} = \frac{T^{2\nu}_{1/2,S} - T^{2\nu}_{1/2,N}}{T^{2\nu}_{1/2,N}}. \tag{7.16}$$

7.3.2.1 Absolute energy scale

The calibration of the absolute energy scale is a major priority for the SNO+ physics analyses, including the $T^{2\nu}_{1/2}$ measurement, since it ensures that the reconstructed energy for each event represents the energy deposited in the detector during an interaction. The energy scale can be determined with deployable calibration sources or backgrounds, and the uncertainty of the energy scale calibration results in a systematic uncertainty for the analyses. Due to the strict radiopurity requirements for the Te-loaded phase, the deployment of calibration sources is going to be limited to avoid the risk of radon entering the scintillator volume. Therefore, the periodic monitoring of the energy scale is going to be performed using naturally present backgrounds. Appendix B presents a method for calibrating and monitoring the energy scale using the decays of external ^{40}K. Monte Carlo based studies inferred a systematic uncertainty of 0.61% for the absolute energy scale calibration with this method.

To evaluate the effect that a 0.61% systematic in the absolute energy scale would have on the $T^{2\nu}_{1/2}$ measurement, the reconstructed energy of the simulated events was scaled up and down by that uncertainty. The changes in signal efficiency were re-calculated, and new PDFs were produced. Figure 7.21 compares the nominal PDFs with the scaled PDFs. By scaling the reconstructed energy of the events by a factor of 1.0061 (scaling up by the energy scale uncertainty), the signal efficiency increases by 1.32%, whereas scaling by a factor of 0.9939 (scaling down), the signal efficiency decreases by 1.34%. The new PDFs are fitted against the original fake datasets, and the resulting half-lives are compared with the ones from the nominal fit. Figure 7.22 shows the $T^{2\nu}_{1/2}$ relative error caused by the absolute energy scale uncertainty, for different fiducial volumes. The 0.61% uncertainty in the absolute energy scale propagates as a 3–6% error to the $T^{2\nu}_{1/2}$ measurement.

This systematic error is enhanced by the correlations between the ^{234m}Pa and the $2\nu\beta\beta$ decay. The small variations in the energy scale of the PDFs lead the fit to overestimate the ^{234m}Pa normalization, reducing by the same number of events the normalization of the $2\nu\beta\beta$ decay. Table 7.5 illustrates this, by comparing the fitted normalizations for these two PDFs, for one example dataset within the FV with radius of 3.3 m, and assuming a livetime of 1 year. Furthermore, it compares the fitted normalizations assuming 20% and 10% constraints for the ^{234m}Pa normalization, whose central value is 4.04×10^5 counts/year (from Table A.1). Constraining the ^{234m}Pa normalization significantly decreases the systematic error for the $2\nu\beta\beta$, from $\sim$6% to $\sim$1%.

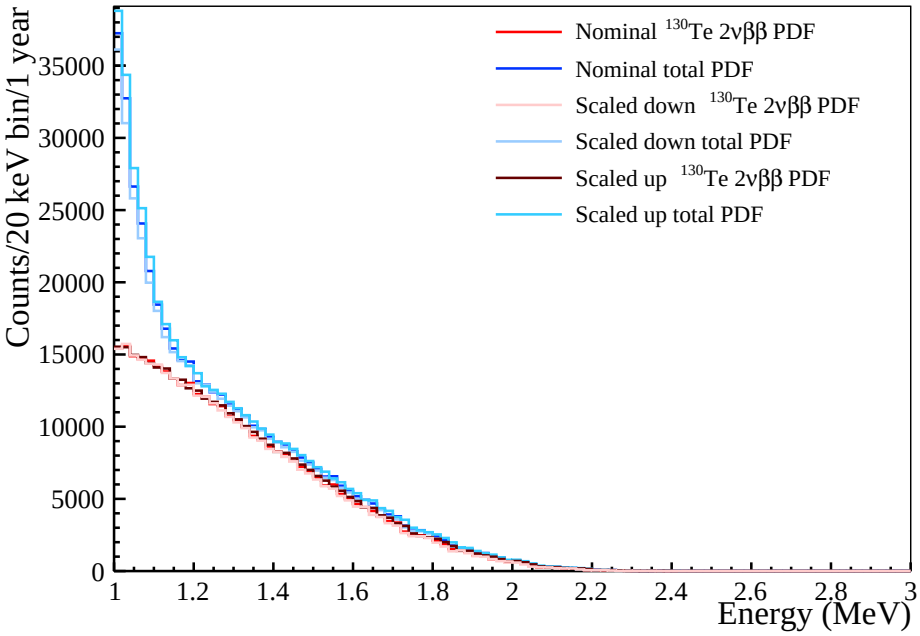

Figure 7.21: Comparison between the nominal PDFs and the scaled energy PDFs, using a FV with radius of 3.3 m. The curves in different shades of red are for the ^{130}Te $2\nu\beta\beta$, and in blue are the summed PDFs.

Table 7.5: Fitted normalizations for the $2\nu\beta\beta$ and ^{234m}Pa PDFs, which have been scaled up by the uncertainty of the absolute energy scale, after running the fit for one of the fake datasets assuming 1 year of livetime and a FV with radius of 3.3 m. The default fit with both normalizations unconstrained is compared with the cases where the ^{234m}Pa rate has constraints of 20% and 10%.

		Fitted Normalization	Difference from nominal (%)
Unconstrained PDFs	$2\nu\beta\beta$	5.19×10^{6}	6%
	^{234m}Pa	7.97×10^{5}	97%
^{234m}Pa constraint = 20%	$2\nu\beta\beta$	5.37×10^{6}	3%
	^{234m}Pa	5.53×10^{5}	36%
^{234m}Pa constraint = 10%	$2\nu\beta\beta$	5.479×10^{6}	1.1%
	^{234m}Pa	4.12×10^{5}	2%

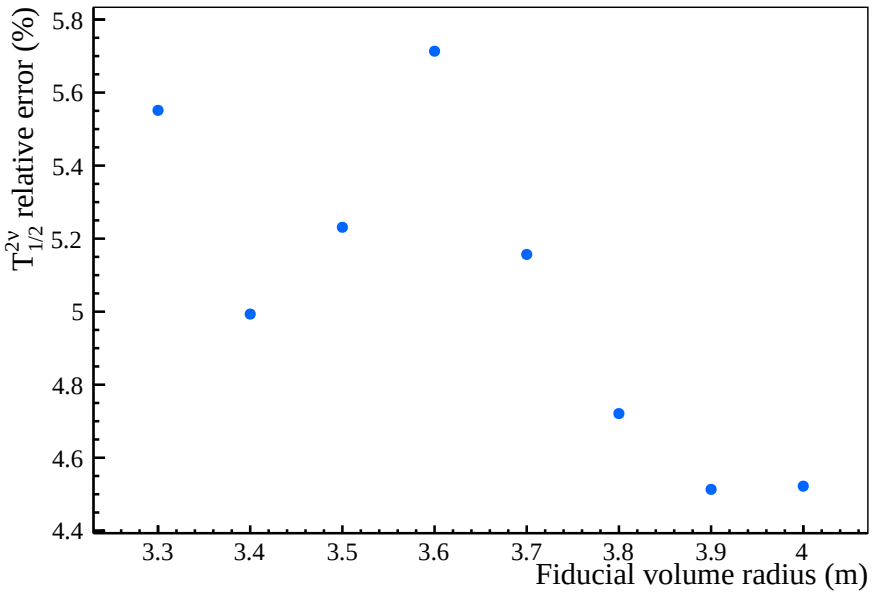

(a)

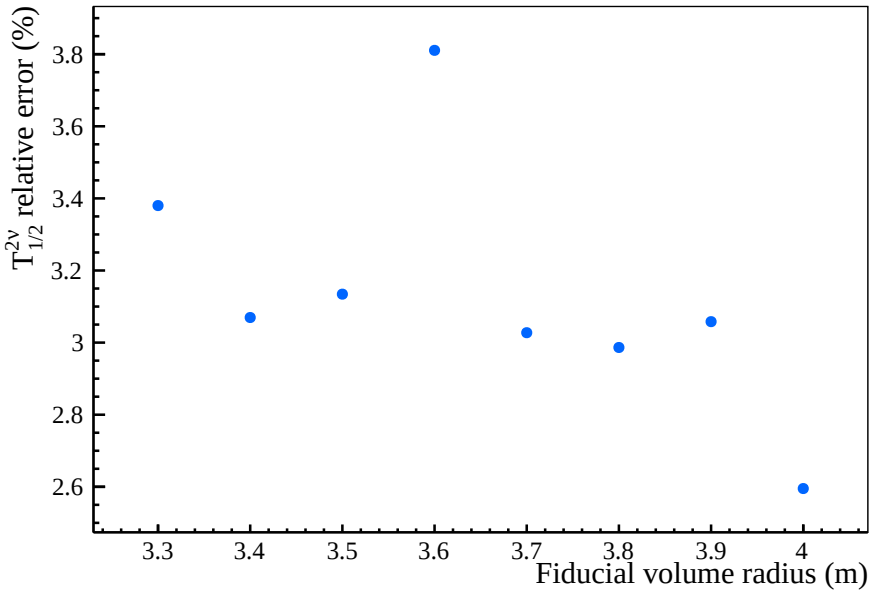

(b)

Figure 7.22: Relative $T^{2\nu}_{1/2}$ error as a function of fiducial volume radius in the cases of energy PDFs (a) scaled up by 1.0061 and (b) scaled down by 0.9939.

7.3.2.2 Detector optics

As reported in Chapter 4, the optical properties of the SNO+ detector play an important role when modelling the detector response and reconstructing the events. In particular, the optical effects are responsible for creating a position dependence in absolute energy scale. Consequently, variations in the optical properties of the detector are expected to impact the absolute energy scale and the resolution of the recorded spectra. If not accounted for by the PDFs, this will result in a systematic uncertainty for the $T_{1/2}^{2\nu}$ measurement.

The studies presented below evaluated how the scintillator attenuation uncertainty, and PMT angular response ageing, would impact the $2\nu\beta\beta$ decay half-life measurement precision. It is important to note, however, that realistically the impact of optical variations are going to be absorbed by the energy scale systematic uncertainty. Therefore, the uncertainties presented in the following studies are not independent from the total energy scale uncertainty, as that would lead to "double-counting" the systematic errors.

Ageing of the PMT+Concentrator angular response The submersion in ultra-pure water have led to degradation of the concentrators surrounding the PMTs and, by consequence, to a worse angular response at high incidence angles. This was observed from the regular optical calibrations performed during the SNO experiment [171], and is also observed when comparing the optical calibration measurements of the SNO+ water phase (July 2018) with the last calibration in SNO (August 2006). Figure 7.23 shows the ratio between the PMT+concentrator angular response measured in July 2018 and August 2006, in the incident angle range between 0 and 42 degrees[2]. Over this 12 year period, the angular response has worsened by up to 8% in the incident angle range from 35 to 42 degrees. Between the two calibrations, the detector spent 4 years exposed to air, with the remaining years allocated to the water fill operations and cavity leak checking.

The concentrators are expected to keep degrading with time. In fact, the Te-loaded phase is expected to start at the end of 2024, at which point the PMTs and concentrators would have spent an additional 6 to 7 years in water, relative to the water phase calibration date. Conservatively, it can be assumed that the PMT angular response will, at most, worsen at the same scale as it did during the transition from SNO to SNO+. If not calibrated, the ageing of the PMT angular response can lead to a mismatch between the detector modelling and the data. The following studies aim to quantify the impact of the PMT ageing on the $2\nu\beta\beta$ half-life analysis.

These studies rely on scaling the absorption probabilities of the PMT grey disc (GD) model (described in Section 3.7.1) in order to replicate the response ageing. The scaling, as a function of wavelength, is based on Figure 7.23, which was fitted with a polynomial of degree 4, yielding:

$$\begin{aligned} f_{scale,R}(\theta_{inc}) =& 1 - 8 \times 10^4 \theta_{inc} + 1.7 \times 10^4 \theta_{inc}^2 - 1.1 \times 10^5 \theta_{inc}^3 \\ &+ 3.8 \times 10^7 \theta_{inc}^4 - 5.4 \times 10^9 \theta_{inc}^5. \end{aligned} \tag{7.17}$$

New Monte Carlo simulations of the $2\nu\beta\beta$ signal and backgrounds were produced, with GD

[2]The PMT angular response measurement from SNO were limited to the incident angle range between 0 and 42 degrees because the optical calibration analysis only used internal laserball data.

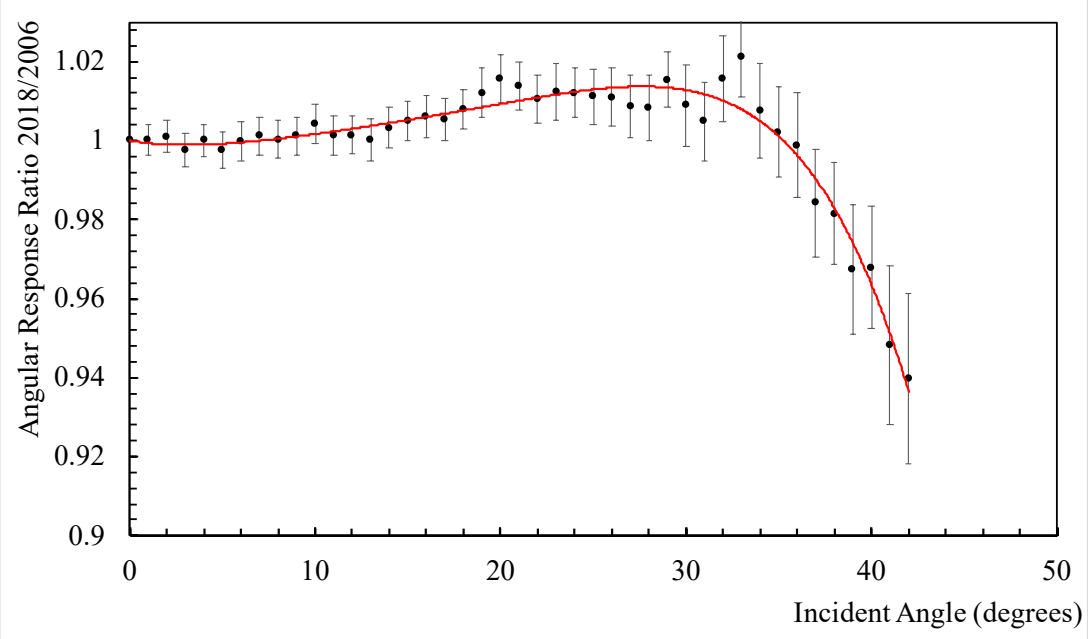

Figure 7.23: Ratio between th PMT-concentrator assembly angular measured in the SNO+ water phase (July 2018) and in the last SNO optical calibration (August 2006), as a function of incident angle. The red line represents a polynomial fit to the ratio.

absorption probabilities scaled down using Equation 7.17. The reconstruction fitters were not coordinated for these simulations, in order to verify the impact of the aged response on the reconstructed physics quantities. The impact was directly investigated by comparing simulations of electrons as several energies, 1 MeV, 2.5 MeV, and 5 MeV, in a FV with radius of 3.3 m, between the nominal MC and the MC with scaled GD parameters. The comparisons are shown in Figure 7.24. Table 7.6 compares the mean and width of the energy peaks between the two simulation types. Based on these results, the aged PMT angular response has an impact of less than 0.1% on the absolute energy scale and of less than 1% on the energy resolution.

Table 7.6: Mean and width of the energy distribution of electron simulations, in a FV with radius of 3.3 m, for the nominal MC settings and for the MC with scaled GD absorption probabilities. The values were obtained by fitting the peaks in Figure 7.24 with a Gaussian function.

	Nominal MC		MC with scaled GD absorption probabilities	
Energy (MeV)	Mean (MeV)	Width (MeV)	Mean (MeV)	Width (MeV)
1	0.997±0.050	0.049±0.040	0.996±0.049	0.049±0.034
2.5	2.493±0.077	0.074±0.057	2.495±0.079	0.075±0.057
5	4.999±0.123	0.118±0.087	4.996±0.118	0.117±0.081

In order to verify the impact on the fit, new PDFs were produced for the $2\nu\beta\beta$ analysis. The fit was repeated using the original fake datasets and the new PDFs. The exact same analysis cuts and procedures described in Sections 7.2.2 were followed. Figure 7.25 shows the relative error obtained for the fitted $T^{2\nu}_{1/2}$, which is smaller than 0.3% and consistent with the bias of the binned maximum likelihood fit due to statistical fluctuations. This result is not entirely surprising given that the analysis uses internal fiducial volumes from which, on average, light will reach the PMTs at small incidence angles. In the scenario assumed, the PMT angular response ageing

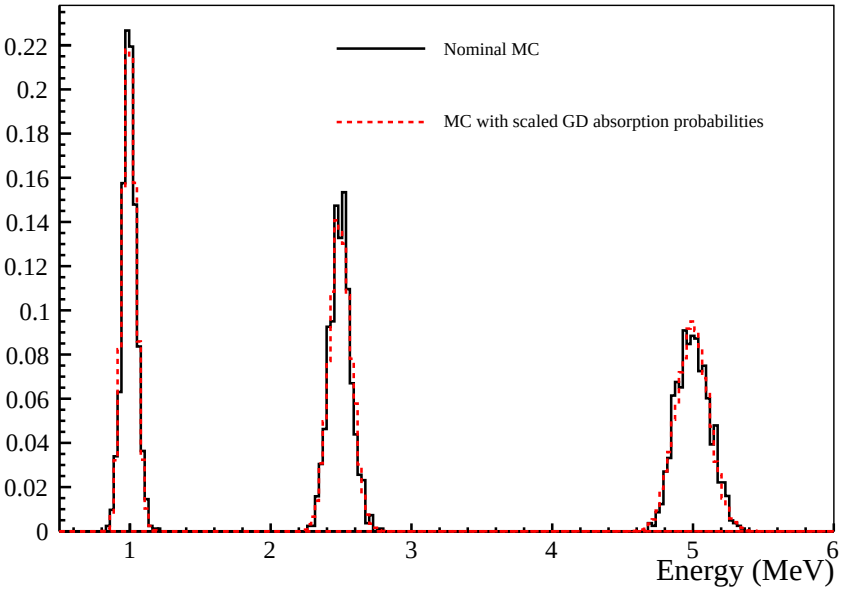

Figure 7.24: Energy distribution of simulated electrons at 1 MeV, 2.5 MeV and 3 MeV, within a spherical FV with R = 3.3 m. The black peaks correspond to the nominal MC, and the red peaks correspond to the MC with scaled GD absorption probabilities.

happens for incidence angles larger than 30–35 degrees, which are only attainable for events at greater distances from the centre of the AV and closer to the PMTs. Therefore, the results indicate that the ageing of the PMT angular response is not expected to impact the double beta decay analyses and the $T^{2\nu}_{1/2}$ measurement, since they usually use more internal FVs to minimize the external backgrounds. For this reason, the PMT angular responses measured during the water phase can be propagated and used in the following phases of the experiment, if no other laserball calibration is performed, without significant impact on the physics results.

Scintillator cocktail attenuation The detector media attenuation coefficients are key optical parameters for modelling the propagation of light inside the detector. From the three media (water, acrylic and scintillator), the scintillator attenuation coefficients will be the most relevant for the double beta decay analysis because it is the medium where the events of interest will occur and where light will travel a greater distance. The scintillator cocktail attenuation is going to be measured and monitored over time using the laserball and the AMELLIE fibers, respectively.

In order to study the impact of the scintillator attenuation on the $T^{2\nu}_{1/2}$ measurement, the following studies assumed that the future scintillator attenuation measurement will have an uncertainty of the order of the water attenuation systematics, obtained from the water phase optical calibration (Chapter 4). This assumption is, in principle, quite conservative, since the scintillator attenuation measurements with the laserball are expected to have a better precision. The water attenuation systematics are dominated by the uncertainty of the laserball position, which greatly affects the solid angle calculations, the dominant optical effect in the water phase. The scintillator, however, has considerably smaller attenuation lengths than the water, hence the

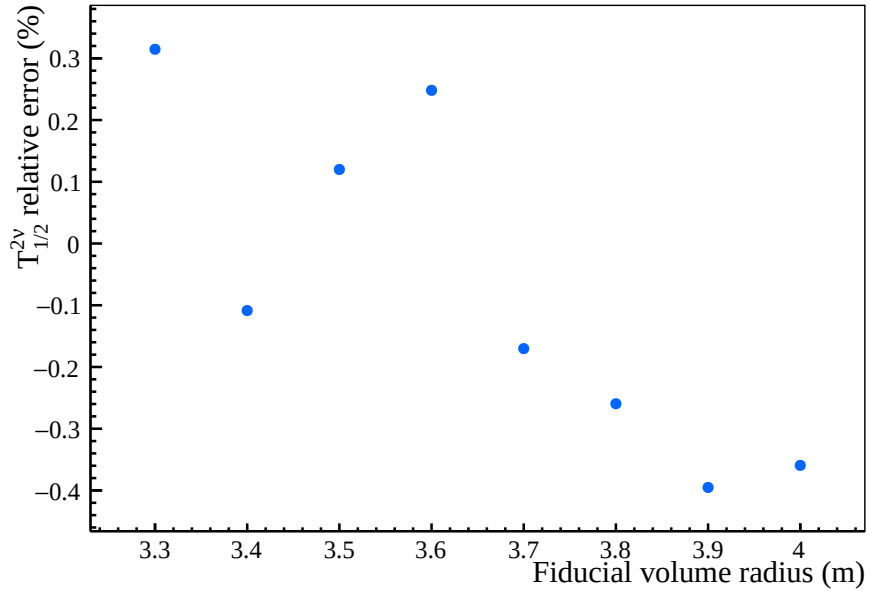

Figure 7.25: Relative $T^{2\nu}_{1/2}$ error as a function of fiducial volume radius, obtained by running the fit with PDFs based on the MC with scaled GD absorption probabilities.

solid angle effect is not expected to be as dominant as during the water phase. Therefore, the optical calibration during the scintillator and Te-loaded phases is expected to have a larger sensitivity to the scintillator attenuation lengths, with smaller systematic uncertainties due to the reduced impact of the solid angle and, as a consequence, of the laserball position systematics.

These studies rely on scaling the attenuation lengths that characterize the scintillator medium in the SNO+ Monte Carlo geometry. RAT includes arrays, as a function of wavelength, of absorption lengths for each component of the scintillator cocktail (LAB, PPO, Te-Diol, bisMSB) and of Rayleigh scattering lengths for the total cocktail (Figure 7.26). The absorption and scattering length values were converted into absorption and scattering coefficients, and the latter were summed to calculate the total attenuation coefficients. The attenuation coefficients were increased and reduced by the systematic uncertainty of the measured water attenuation coefficient at 420 nm, of 4.23×10^{-6} mm^{-1}. The systematic errors of the water attenuation coefficients shown in Table 4.3 are dominated by the source position uncertainty and its impact on the solid angle factor, and do not vary significantly with wavelength. Therefore, the choice of attenuation scaling for these studies was made assuming that an optical calibration during the scintillator phase would, at most, yield systematic errors of the same order across all wavelengths.

New absorption and scattering arrays were created from the scaled attenuations, by taking into account the fractional contributions of each scintillator absorption component and of the Rayleigh scattering to the total attenuation at each wavelength. The variation relative to the nominal attenuation caused by adding and subtracting the uncertainty is represented by the faded lines in Figure 7.26.

New Monte Carlo simulations of the $2\nu\beta\beta$ signal and backgrounds were produced using the shifted absorption and scattering lengths. For the simulations, the reconstruction fitters were not coordinated, in order to verify the impact of this variation on the reconstructed physics quanti-

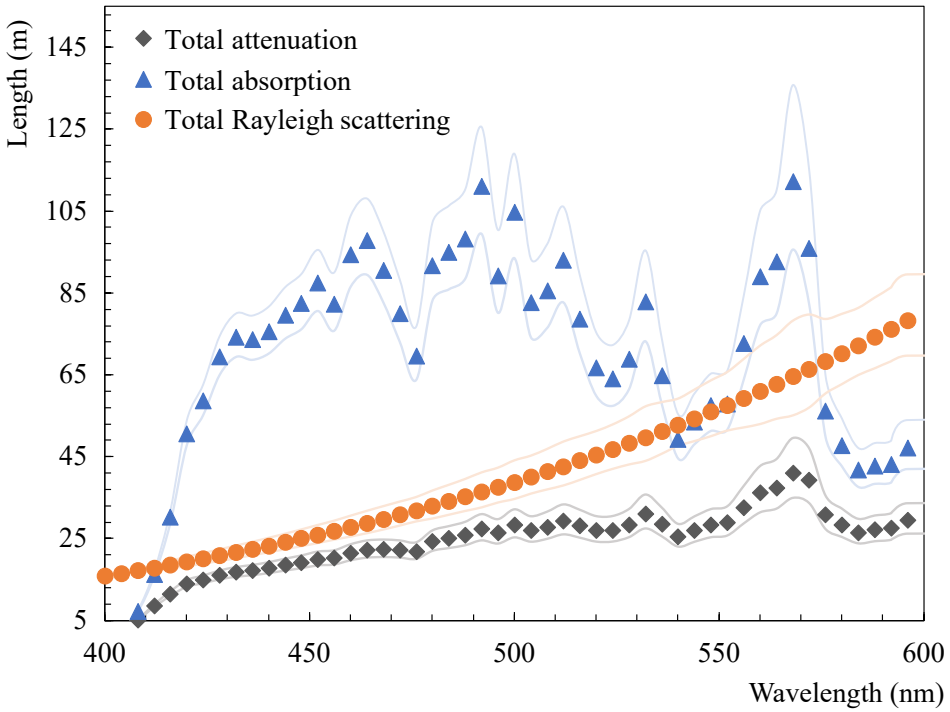

Figure 7.26: Total attenuation (black), absorption (blue) and Rayleigh scattering (orange) lengths for the tellurium cocktail as a function of wavelength. The faded lines around the points represent the variation induced by increasing and decreasing the total attenuation coefficients by a systematic uncertainty of 4.23×10^{-6} mm^{-1}.

ties. The impact was directly investigated by comparing simulations of electrons at energies of 1, 2.5, and 5 MeV in a FV with radius of 3.3 m, produced using the nominal MC settings and with scaled attenuations. The comparisons are shown in Figure 7.27. Table 7.7 compares the mean and width of the energy peaks between the two simulation types. The changes in attenuation result in up to 0.1% change in the absolute energy scale, but between 1% to 9% variation in the energy resolution.

Table 7.7: Mean and width of the energy distribution of electron simulations, in a FV with radius of 3.3 m, for the nominal MC settings and for the MC with scaled scintillator attenuation lengths. The values were obtained by fitting the peaks in Figure 7.27 with a Gaussian function.

	Nominal MC		Increased attenuation lengths		Decreased attenuation lengths	
Energy (MeV)	Mean (MeV)	Width (MeV)	Mean (MeV)	Width (MeV)	Mean (MeV)	Width (MeV
1	0.997±0.050	0.049±0.040	0.998±0.049	0.048±0.037	0.996±0.047	0.046±0.034
2.5	2.493±0.077	0.074±0.057	2.495±0.083	0.081±0.058	2.494±0.074	0.072±0.061
5	4.999±0.123	0.118±0.087	4.993±0.121	0.117±0.087	4.994±0.116	0.113±0.094

In order to verify the impact on the fit, new PDFs were produced for the $2\nu\beta\beta$ analysis. Figure 7.21 compares the nominal PDFs with the scaled PDFs. The $2\nu\beta\beta$ signal efficiency increases by 2.3% when the attenuation lengths are longer (less attenuation), and decreases by 2% when the attenuation lengths are shorter (more attenuation). The fit was repeated using the original fake datasets and the new PDFs. The exact same analysis cuts and procedures described in Sections 7.2.2 were followed. Figure 7.29 shows the relative error obtained for the fitted $T^{2\nu}_{1/2}$, which is between 3% and 4.2%.

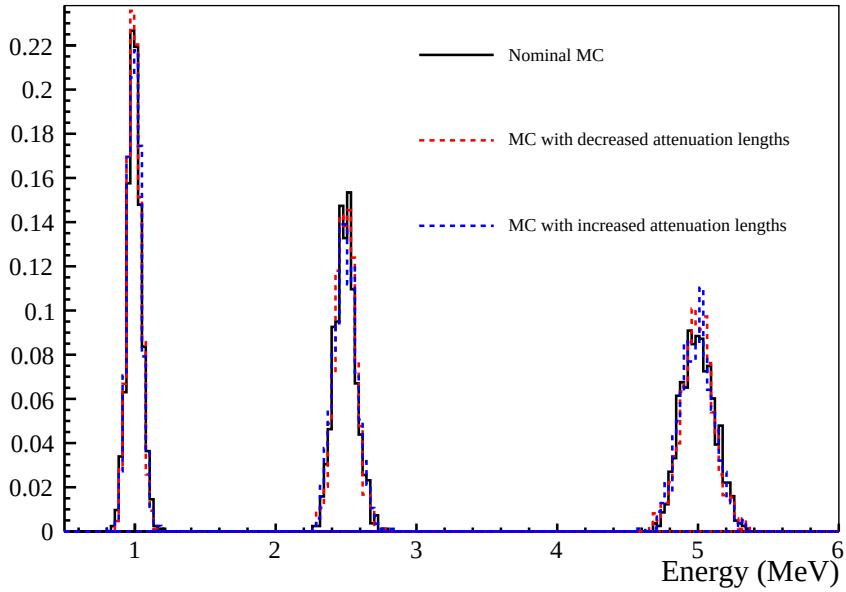

Figure 7.27: Energy distribution of simulated electrons at 1 MeV, 2.5 MeV and 3 MeV, within a spherical FV with R = 3.3 m. The black peaks correspond to the nominal MC, the red peaks to MC with decreased attenuation lengths, and the blue peaks correspond to MC with increased attenuation lengths.

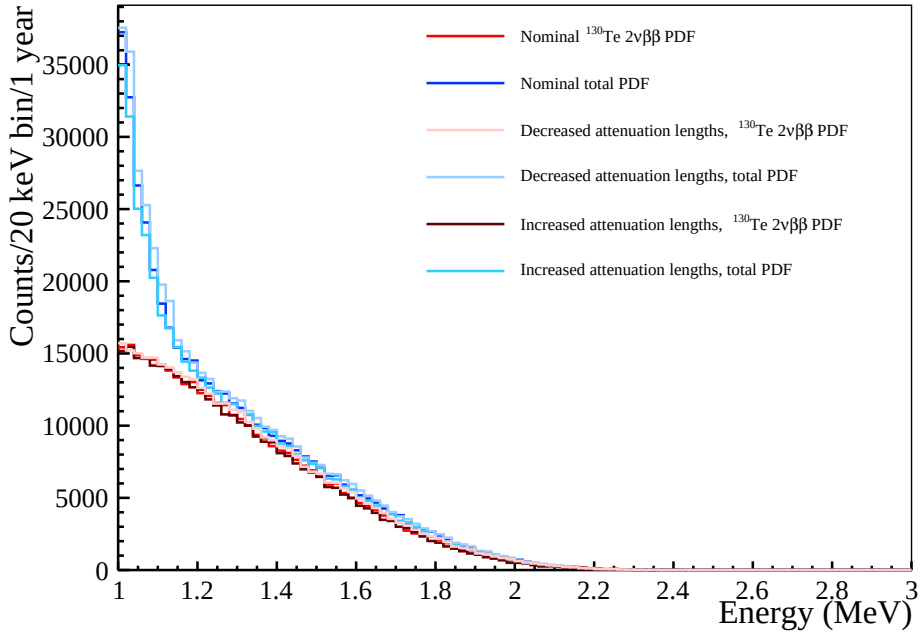

Figure 7.28: Comparison between the nominal PDFs and the PDFs based on the MC with scaled attenuation lengths, using a FV with radius of 3.3 m. The curves in different shades of red are for the ^{130}Te $2\nu\beta\beta$, and in blue are the summed PDFs.

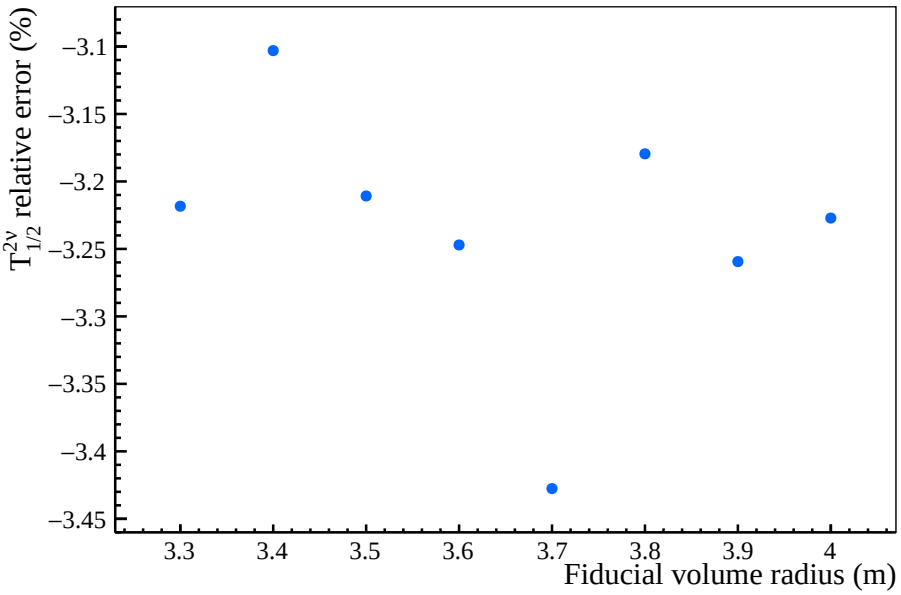

(a)

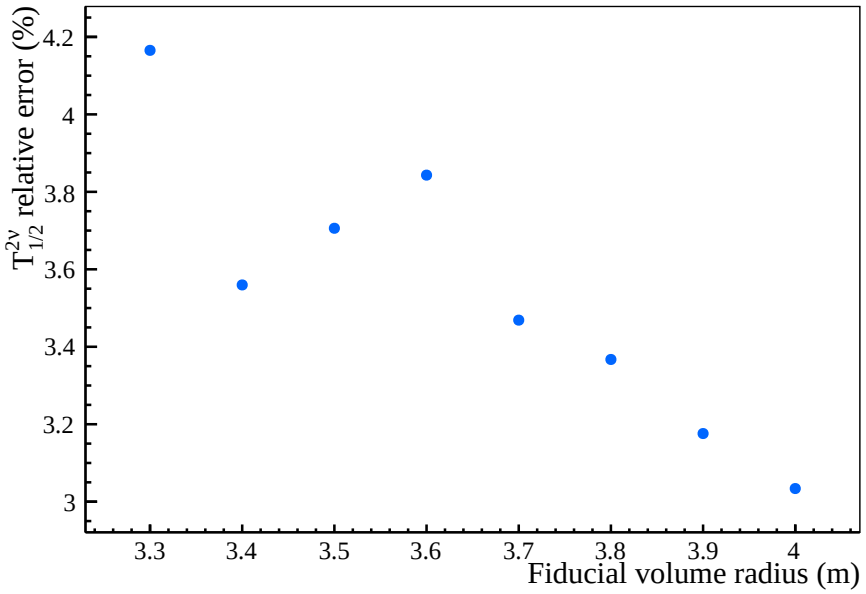

(b)

Figure 7.29: Relative $T^{2\nu}_{1/2}$ error as a function of fiducial volume radius, obtained by running the fit with PDFs based on the MC with decreased attenuation lengths (a) and the MC with increased attenuation lengths (b).

7.3.3 Impact of the $2\nu\beta\beta$ half-life precision on the $0\nu\beta\beta$ sensitivity

The tail of the $2\nu\beta\beta$ spectrum is an unavoidable background to the $0\nu\beta\beta$ decay search. Given its expected rate, and the expected precision for its measurement based on the studies on the previous sections, it is possible to estimate the size and uncertainty of the $2\nu\beta\beta$ background contribution to the $0\nu\beta\beta$ ROI.

For the purposes of this study, the $0\nu\beta\beta$ ROI is defined as the region within -0.5σ to +1.5σ around the centre of the $0\nu\beta\beta$ peak ($Q_{\beta\beta} = 2.5$ MeV). This ROI definition is the same as used in [132], and used to produce Figure 3.20. Figure 7.30 shows the energy distribution of the ^{130}Te $0\nu\beta\beta$ decay from Monte Carlo simulations, for the FV with radius of 3.3 m. The spectrum was normalized so that its integral is equal to unity. Fitting the spectrum with a Gaussian function yields a mean energy of 2.51 $\pm$ 0.08 MeV and a width of 0.078 $\pm$ 0.055 MeV. The $[-0.5\sigma, +1.5\sigma]$ ROI goes from 2.46 MeV to 2.62 MeV, and comprises 64.57% of the $0\nu\beta\beta$ peak.

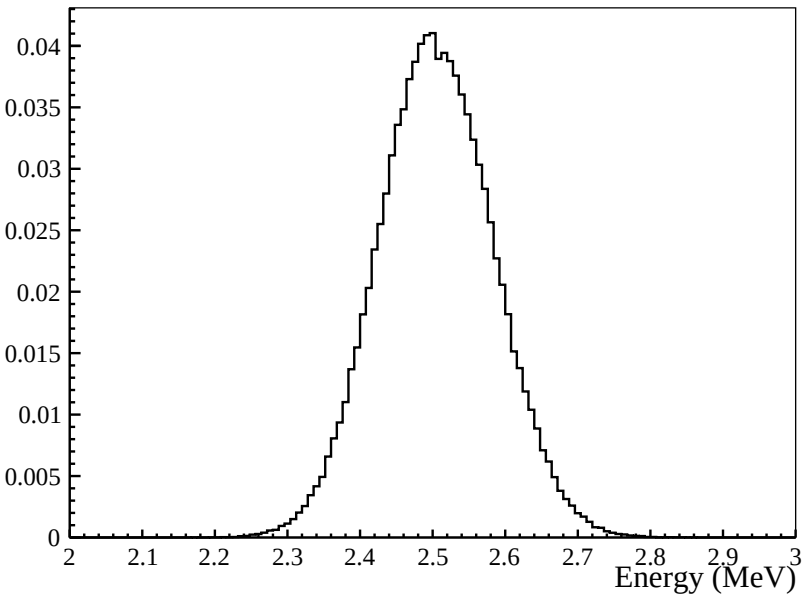

Figure 7.30: Energy distribution of the simulated $0\nu\beta\beta$ decay events, reconstructed within the FV with radius of 3.3 m.

The number of background counts in the $0\nu\beta\beta$ ROI, b, can be defined as:

$$b = B\ \Delta E\ m\ t_{exp}, \tag{7.18}$$

where B is background index in the ROI (kg^{-1} keV^{-1} year^{-1}), ΔE is the width of the ROI, m is the fiducial detector mass, and t_{exp} is the livetime. Recalling Equation 2.11, the $0\nu\beta\beta$ half-life

sensitivity is given by:

$$\begin{aligned} S^{0\nu} &= \frac{\ln 2}{n_\sigma} \frac{x \cdot a \cdot N_A \cdot \epsilon}{M} \sqrt{\frac{m t_{exp}}{B \Delta E}} \\ &= \frac{\ln 2}{n_\sigma} n_{130} \epsilon f_{\text{ROI}} \frac{t_{exp}}{\sqrt{b}} , \end{aligned} \tag{7.19}$$

where $n_\sigma = 1.64$ expresses the sensitivity at the 90% confidence level (C.L.), $\epsilon = 0.1639$ represents the detection efficiency of the $0\nu\beta\beta$ signal within the fiducial volume, $f_{\text{ROI}} = 0.6457$ the fraction of signal contained in the ROI, t_{exp} is the livetime, and n_{130} is the number of ^{130}Te atoms in the detector (Equation 7.13):

$$n_{130} = m_{130} N_A \frac{1}{M} \tag{7.20}$$

with $m_{130} = x \cdot a \cdot m_{det} = 1.33 \times 10^6$ g being the mass of isotope within the AV (x = 0.5% is the fraction of tellurium per LAB molecule, $a = 34.08\%$ is the isotopic abundance of ^{130}Te, $m_{det} = 780 \times 10^6$ g is the total scintillator cocktail mass), N_A the Avogadro constant, and $M = 129.9$ the atomic mass of ^{130}Te.

In order to accurately determine the $2\nu\beta\beta$ contribution to the ROI, more Monte Carlo of $2\nu\beta\beta$ decays had to be produced to increase the statistics in the tail of the spectrum. For this estimate, a total of 4.6×10^7 $2\nu\beta\beta$ events were simulated, one order of magnitude more than the initial simulations used for the studies in the previous sections. From all the simulated events, 13 are reconstructed within the 3.3-m radius FV and within the 2.46 MeV to 2.62 MeV ROI, yielding a detection efficiency of 2.79×10^{-5}%. Multiplying the efficiency by ^{130}Te $2\nu\beta\beta$ total expected rate, 5.54×10^6 counts/year, yields an estimate of 1.55 $2\nu\beta\beta$ counts/year in the $0\nu\beta\beta$ ROI.

Table 7.8 lists the backgrounds expected to contribute to the ROI, with the corresponding number of counts per year, which were calculated by considering the fractions of the spectra within the ROI and the rates from Tables A.1 to A.3. The ^{8}B solar neutrinos are the biggest background contributions to the ROI, making up almost half of the total budget, followed by the $2\nu\beta\beta$ and external backgrounds.

The background rate of 9.89 events/year obtained for these studies is comparable to that presented in Figure 3.20, 9.47 counts/year in a smaller ROI between 2.42 and 2.56 MeV. Even though both ROIs are defined as the range $[-0.5\sigma, +1.5\sigma]$, the results is this thesis are based on new and more realistic Monte Carlo which includes the calibrated optical model for the PMTs, acrylic and external water, as well as other general improvements to the detector model and reconstruction algorithms, when compared with the older Monte Carlo used to estimate the background rates and $0\nu\beta\beta$ sensitivity reported in Section 3.10. Furthermore, the count rates for each background are based on the updated background rates of Appendix A with constraints from the water phase and partial fill period.

Based on the values presented, Figure 7.31 shows the sensitivity to the ^{130}Te $0\nu\beta\beta$ half-life as a function of exposure time t_{exp}. This simple counting analysis predicts a $T^{0\nu}_{1/2}$ lower limit of 8.8×10^{25} years at 90% C.L. with 1 years of livetime, and 2×10^{26} years at 90% C.L. with 5 years

Table 7.8: Backgrounds contributing to the $0\nu\beta\beta$ decay ROI (2.46 MeV to 2.62 MeV), and expected counts per year.

Background source	Counts/year in ROI
(α,n) ^{13}C interactions in LS	0.53
^{8}B solar ν	4.62
^{130}I	0.13
^{130m}I	5.39×10^{-3}
^{212}Bi	0.94
^{208}Tl	0.018
^{214}Bi	5.37×10^{-3}
^{210}Tl	0.38
^{130}Te $2\nu\beta\beta$	1.55
^{208}Tl AV	0.14
^{208}Tl external water	1.19
^{208}Tl hold-down ropes	0.35
^{208}Tl hold-up ropes	0.032
Cosmogenics (total)	1.83×10^{-4}
Total	9.89

of livetime. These results are compatible with the limit of 2.1×10^{26} years at 90% C.L. reported in Section 3.10, obtained for an optimized FV and energy ROI of 3.55 m and $[-\sigma, +1.6\sigma]$, respectively. Moreover, the final SNO+ $0\nu\beta\beta$ half-life sensitivity will be further improved by using a spectral fit instead of a counting analysis, discussed in [200]. The sensitivity estimates presented here are also in agreement with the results in [200].

The impact of the $T^{2\nu}_{1/2}$ measurement precision on the $T^{0\nu}_{1/2}$ sensitivity was evaluated by recalculating the number of background counts in the ROI assuming precisions of 1% and 5%. Taking into account the ratio of $2\nu\beta\beta$ counts to the total ROI counts, a precision of 1%(5%) on $T^{2\nu}_{1/2}$ propagates into a 0.08%(0.4%) uncertainty for the $0\nu\beta\beta$ half-life sensitivity. Despite being small, when searching for such a rare process like the $0\nu\beta\beta$ decay, the uncertainties on the rate of the $2\nu\beta\beta$ and of the other backgrounds (which were not studied here) will play a key role if an observation is made. In order to claim a discovery, SNO+ needs to minimize all the sources of uncertainties, and increasing the precision of the $T^{2\nu}_{1/2}$ half-life is one important step towards that goal. Furthermore, it will be especially relevant to use calibration sources to place tight constraints on any possible non-Gaussian energy response tails that may affect the $2\nu\beta\beta$ contribution to the $0\nu\beta\beta$ ROI beyond the rate uncertainty effects outlined here.

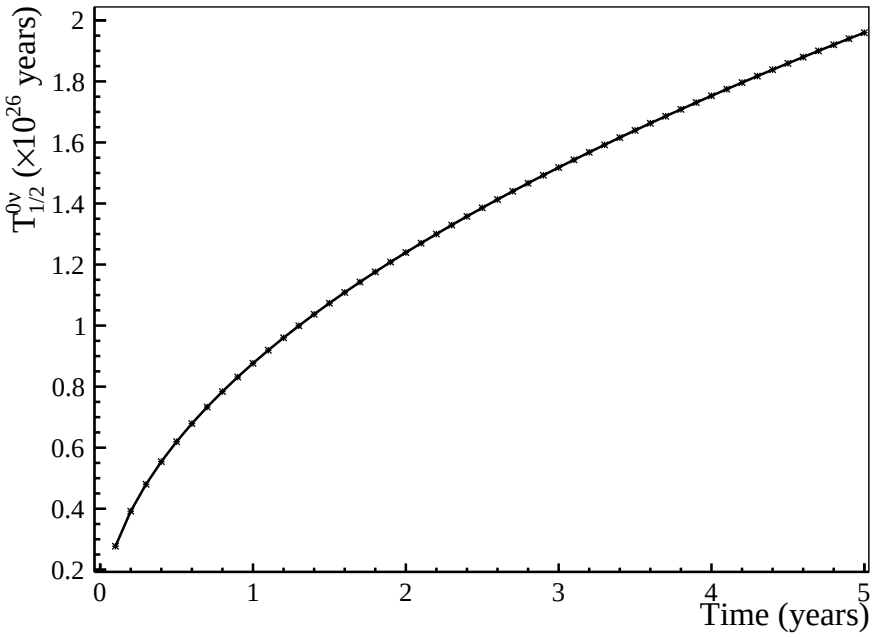

Figure 7.31: $T^{0\nu}_{1/2}$ sensitivity at 90% C.L. as a function of livetime, calculated based on Equation 7.19.

7.4 Prospects and challenges for the Te-loaded phase

The studies presented in this Chapter provided a valuable guide for the future double beta decay analysis once the first data with tellurium is available. As shown in Section 7.3.1, during the 3-month assay run with the first batch of tellurium (1/52 of the total isotope amount, 25.5 kg) SNO+ is expected to be sensitive to the $2\nu\beta\beta$ decay spectrum and perform a first measurement to constrain its half-life, albeit with large statistical uncertainties (>10%). Furthermore, with the total 0.5% loading, corresponding to 1.3 tonnes of ^{130}Te, SNO+ will be able to achieve exposures of more than 100 kg year after 6 months, depending on the FV used for the analysis, competitive with the exposure of 102.7 kg year of the CUORE experiment for its $2\nu\beta\beta$ half-life measurement in [85]. This will allow for $T^{2\nu}_{1/2}$ measurements with competitive statistical precisions of better than 1%.

In fact, it is expected that the future SNO+ measurement will be limited by systematic uncertainties. The studies in this Chapter showed that a 0.6% uncertainty in the absolute energy scale propagates into a ∼6% systematic error for $T^{2\nu}_{1/2}$, a factor of 3 to 4 times larger than the systematic error reported by the CUORE measurement (1.6%–1.9%). The systematic error is enhanced by the correlations between the spectral shapes of the backgrounds and the signal, particularly between the ^{234m}Pa and $2\nu\beta\beta$, which were left unconstrained in the fit. The systematic error can be reduced to 1% if the ^{234m}Pa rate is constrained with a precision of 10%. Based on these results, in order to achieve the goal of measuring $T^{2\nu}_{1/2}$ with a precision competitive with CUORE, there are three critical factors that need to be carefully evaluated when the SNO+ tellurium phases starts – determining with as much precision as possible the amount of isotope within the AV, calibrating the absolute energy scale and minimizing its uncertainties, and constraining the background rates.

The amount of isotope entering the AV can be estimated based on the amount of telluric acid processed in the underground plants. Moreover, after the production of the TeBD cocktails, *ex situ* measurements could be performed in order to determine the concentration of isotope in the batches entering the detector. Nevertheless, inefficiencies in the scintillator loading process and in the recirculation systems could hypothetically affect the amount of isotope entering the AV. This could be evaluated by carefully monitoring the detected $2\nu\beta\beta$ rate during the tellurium loading and verify that it scales accordingly with the amount of isotope loaded. Alongside, samples could be drawn from the AV, for example using sample lines, and the concentration could be measured *ex situ* using methods like X-ray fluorescence (XRF) or inductively coupled plasma mass spectrometry (ICP-MS). The uncertainty on the amount of isotope loaded propagates directly as a systematic to the $T^{2\nu}_{1/2}$. Therefore, it will be important to determine the isotope mass as accurately as possible, potentially with a better precision than the other systematics.

The sensitivity to the ^{130}Te $2\nu\beta\beta$ decay spectrum will depend on the background levels of the scintillator cocktail. The background analyses will play a key role for determining this, and informing if further scintillator purification is needed. Additionally, the accuracy of the fit presented in this Chapter, and of a future $T^{2\nu}_{1/2}$ measurement, relies strongly on prior constraints of the expected background sources in the scintillator, particularly of the isotopes in the U and Th chains. Even though a large fraction of these background can be measured using dedicated analyses, for example using the Bi-Po coincidence tagging methods, if secular equilibrium does not hold, isotopes like ^{228}Ac and ^{234m}Pa can affect the measurements due to their strong correlations with the $2\nu\beta\beta$. The top part of the U(Th) chain could be constrained by identifying and counting the α-decays of ^{238}U, ^{234}U, ^{230}Th (^{232}Th, ^{228}Th). However, given the overlap between the quenched energies for these isotopes and the ^{210}Po, which has a considerable higher rate, based on the partial fill period observations, even with α-β separation it will be difficult to identify them in the SNO+ data. An alternative would be to try to constrain the top of the U and Th chains *ex situ* with samples drawn from the AV, using, for example, a high resolution germanium detector.

The 1-dimensional binned maximum likelihood fit presented in this Chapter is highly affected by the correlations between the backgrounds and signal, particularly those which have similar spectrum shapes. Besides including constraints for the backgrounds, expanding the fit to further dimensions could improve its performance. For instance, fitting in energy and position would break the correlations with the external backgrounds, allowing to increase the exposure by extending the FV to larger radii.

Chapter 8

Conclusions

The SNO+ experiment has been collecting data since 2017, initially as a Cherenkov detector filled with 905 tonnes of ultra-pure water, and is currently using 780 tonnes of liquid scintillator. The analysis of the data collected during the water and pure scintillator phases has provided invaluable knowledge about the detector to carry out the experiment's ultimate goal – searching for the $0\nu\beta\beta$ decay of ^{130}Te using 1.3 tonnes of isotope. The work presented in this thesis contributed to this goal in three ways: by improving the characterization of the optical properties of the detector with the analysis of calibration data taken with a deployed source during the water phase; by developing and validating the preliminary model of the backgrounds in the liquid scintillator from the analysis of data taken during the partial fill period when the detector was half-filled with 365 tonnes of scintillator on top of water; and by creating an analysis framework for the measurement of the half-life of the ^{130}Te $2\nu\beta\beta$, one of the major intrinsic backgrounds for the $0\nu\beta\beta$ decay search.

The optical calibration during the water phase, described in Chapter 4, was fundamental to establish the knowledge of the optical properties of the detector media and evaluating how the concentrators around the PMTs have changed since the transition from SNO to SNO+. The internal and external AV regions, both filled with ultra-pure water, were treated as the same material, which broke the correlation between the external water and acrylic attenuation coefficients, allowing for the first time an in-situ measurement of the latter. Furthermore, the use of external laserball data allowed the analysis to be sensitive to the PMT angular response at incidence angles above 45 degrees. The measurements were propagated to the detector simulation model, which was subsequently validated by comparing simulations with data from the ^{16}N gamma source. These results, which were published in [150], decreased the absolute energy scale systematic in the water phase by a factor of $\sim$2, from 2% to 1.02%, which substantially improved the water phase physics analyses, such as the search for invisible nucleon decay [160]. The calibrated detector optical model has been propagated to the following phases, with the exchange of the internal water with liquid scintillator.

As the transition from the water phase to the scintillator phase unfolded, evaluating the intrinsic background levels of the scintillator and starting the development of a background model for the physics analyses became the main priorities for SNO+. The background measurements were crucial to verify that the liquid scintillator meets the radiopurity requirements prior to the

^{130}Te isotope loading, and to monitor the decay of the radon daughters that entered the detector during the fill operations. This is the subject of Chapter 5, which started by introducing the radioactive background sources in the detector, divided into internal and external, depending on whether they originate from contaminants in the target volume (ultra-pure water or liquid scintillator, depending on the phase) or in the detector components surrounding it, respectively. The majority of the discussion then focused on the background analyses of the partial fill period, when the detector took data for 7 months half-filled with 365 tonnes of liquid scintillator on top and water on the bottom of the AV. Despite the challenging configuration, it provided the ideal stability conditions to start developing the scintillator background model.

A method for tagging bismuth-polonium coincidences, originating from the ^{238}U and ^{232}Th chains, was applied to the data. The tagged coincidences allowed the measurement of the U, Th and Rn levels in the scintillator, and also provided clean samples of known events for determining and monitoring the scintillator light yield, crucial for understanding the nHit scale of the data recorded during this period. The background model of the partial fill period included background sources which will not exist in the final scintillator and Te-loaded phase: γs from radioactive decays within the water below the scintillator, and impurities from a deployed auxiliary PFA tube. Dedicated sideband analyses measured the contributions of these two background sources to the partial fill model. The final model was validated with a $0\nu\beta\beta$ target-out analysis, which showed that the observed events in the $0\nu\beta\beta$ region-of-interest were consistent with the predictions of the background model, even without considering all the sources of systematic uncertainties in the dataset. Even though the background model of the partial fill period is not entirely representative of the final Te-loaded phase, the consistency between observation and expectation validated the preliminary SNO+ background model and analysis approaches for the full scintillator fill and for the Te-loaded phase. In fact, the analysis will be repeated during the quiet data taking period of the scintillator phase. That ultimate measurement will constitute an important determination of the count rate in the ROI, in the absence of tellurium, with all planned analysis cuts applied. The expected background levels for the Te-loaded phase, included the constraints from the partial fill period background measurements, were collected in Appendix A, including updated calculations of the expected cosmogenically induced backgrounds from the activation of tellurium while on surface.

With the complete background model and calibrated detector response, a measurement of ^{8}B solar neutrinos was performed using the partial fill data, presented in Chapter 6. This was the first physics measurement using liquid scintillator in SNO+, providing an important proof of concept for solar neutrino analyses during the full scintillator and Te-loaded phases. The measurement took advantage of the much higher light yield than during the water phase, allowing lower thresholds and improved resolution. With a lower energy threshold of 1000 nHits ($\sim$3 MeV, considering the scale of 320 nHit/MeV), a flux of $\Phi_{^8B} = 6.534^{+26.11\%}_{-22.39\%}$ (stat.) $^{+11.38\%}_{-9.64\%}$ (syst.) $\times$ 10^6 cm^{-2} s^{-1} was measured with an exposure of 11.2 kt day. This measurement is compatible with those from other experiments, including the solar neutrino measurement performed during the SNO+ water phase. However, it is limited by the statistical uncertainty, given the small exposure and small interaction rate of ^{8}B solar neutrinos (about $\sim$1.6 events per day). The systematic uncertainties presented were obtained from preliminary studies of the nHit scale

and position reconstruction differences between data and Monte Carlo, using the tagged Bi-Po coincidences.

The last Chapter of this thesis presented a Monte Carlo based sensitivity analysis for the measurement of the half-life of the ^{130}Te $2\nu\beta\beta$ decay in SNO+. The $2\nu\beta\beta$ is one of the irreducible backgrounds expected in the ROI for the $0\nu\beta\beta$ decay searches. Therefore, a precise measurement of its half-life is needed in order to accurately constrain the leakage of this background into the $0\nu\beta\beta$ region-of-interest. The studies presented in Chapter 7 showed that, during a 3-month assay run with the first batch of tellurium (1/52 of the total isotope amount, 25.5 kg), SNO+ is expected to be sensitive to the $2\nu\beta\beta$ decay spectrum and perform a first measurement to constrain its half-life, albeit with large uncertainties ($>10\%$). Furthermore, with the final 1.3 tonnes of ^{130}Te, SNO+ will be able to achieve exposures competitive with the CUORE experiment in less time, given its larger isotope mass. This will allow for $T^{2\nu}_{1/2}$ measurements with statistical precision better than 1% after a few months of data taking. The main challenges for this measurement are the correlations between the spectral shapes of the backgrounds and the signal, particularly between the ^{234m}Pa and $2\nu\beta\beta$. These correlations were enhanced when studying the impact of systematic effects on the $2\nu\beta\beta$ half-life measurement. The studies performed showed that a 0.6% uncertainty in the absolute energy scale propagates as a $\sim$6% systematic error if the rate of the ^{234m}Pa is unconstrained in the analysis. The systematic error can be reduced to 1% if the ^{234m}Pa rate is constrained with a precision of 10%. The half-life measurement is then expected to be limited by the systematic uncertainties, which will have to be accurately determined and minimized using calibrations. These studies and the analysis framework developed is expected to guide the future SNO+ analyses once the Te-loaded phase starts.

Bibliography

[1] S. L. Glashow. *Partial-symmetries of weak interactions*. Nucl. Phys. **22**, p.579–588 (1961)

[2] A. Salam. *Weak and Electromagnetic Interactions*. Conf. Proc. C, p.367–377 (1968)

[3] S. Weinberg. *A Model of Leptons*. Phys. Rev. Lett. **19**, p.1264–1266 (1967)

[4] H. Fritzsch et al. *Advantages of the color octet gluon picture*. Phys. Lett. B **47**, p.365–368 (1973)

[5] P. W. Higgs. *Broken Symmetries and the Masses of Gauge Bosons*. Phys. Rev. Lett. **13**, p.508–509 (1964)

[6] F. Englert et al. *Broken Symmetry and the Mass of Gauge Vector Mesons*. Phys. Rev. Lett. **13**, p.321–323 (1964)

[7] G. S. Guralnik et al. *Global Conservation Laws and Massless Particles*. Phys. Rev. Lett. **13**, p.585–587 (1964)

[8] G. Aad et al. (ATLAS Collaboration). *Observation of a new particle in the search for the Standard Model Higgs boson with the ATLAS detector at the LHC*. Phys. Lett. B **716** 1, p.1–29 (2012)

[9] S. Chatrchyan et al. (CMS Collaboration). *Observation of a new boson at a mass of 125 GeV with the CMS experiment at the LHC*. Phys. Lett. B **716** 1, p.30–61 (2012)

[10] T. D. Lee et al. *Question of Parity Conservation in Weak Interactions*. Phys. Rev. **104**, p.254–258 (1956)

[11] C. S. Wu et al. *Experimental Test of Parity Conservation in Beta Decay*. Phys. Rev. **105**, p.1413–1415 (1957)

[12] M. Goldhaber et al. *Helicity of Neutrinos*. Phys. Rev. **109**, p.1015–1017 (1958)

[13] L. D. Landau. *On the conservation laws for weak interactions*. Nucl. Phys. **3**, p.127–131 (1957)

[14] T. D. Lee et al. *Parity Nonconservation and a Two-Component Theory of the Neutrino*. Phys. Rev. **105**, p.1671–1675 (1957)

[15] A. Salam. *On parity conservation and neutrino mass*. Nuovo Cim. **5**, p.299–301 (1957)

[16] B. Pontecorvo. *Inverse beta processes*. Chalk River Report, Pd-205 (1946)

[17] R. Davis et al. *Search for Neutrinos from the Sun*. Phys. Rev. Lett. **20**, p.1205–1209 (1968)

[18] B. T. Cleveland et al. *Measurement of the Solar Electron Neutrino Flux with the Homestake Chlorine Detector*. ApJ **496**, p.505–526 (1998)

[19] R. Davis. *A review of the homestake solar neutrino experiment*. Prog. Part. Nucl. Phys. **32**, p.13–32 (1994)

[20] J. N. Abdurashitov et al. (SAGE Collaboration). *Solar neutrino flux measurements by the Soviet-American Gallium Experiment (SAGE) for half the 22 date solar cycle*. J. Exp. Theor. Phys. **95**, p.181–193 (2002)

[21] W. Hampel et al. (GALLEX Collaboration). *GALLEX solar neutrino observations: Results for GALLEX IV*. Phys. Lett. B **447**, p.127–133 (1999)

[22] K. S. Hiratae et al. (Kamiokande-II Collaboration). *Observation of* ^{8}B *solar neutrinos in the Kamiokande-II detector*. Phys. Rev. Lett. **63**, p.16–19 (1989)

[23] K. S. Hirata et al. (Kamiokande-II Collaboration). *Experimental Study of the Atmospheric Neutrino Flux*. Phys. Lett. B **205**, p.416 (1988)

[24] J. Bahcall. *Solar Neutrino Viewgraphs*. http://www.sns.ias.edu/~jnb. (2005)

[25] Y. Fukuda et al. (Super-Kamiokande Collaboration). *Evidence for Oscillation of Atmospheric Neutrinos*. Phys. Rev. Lett. **81**, p.1562–1567 (1998)

[26] Q. R. Ahmad et al. (SNO Collaboration). *Direct Evidence for Neutrino Flavor Transformation from Neutral-Current Interactions in the Sudbury Neutrino Observatory*. Phys. Rev. Lett. **89**, p.011301 (2002)

[27] B. Pontecorvo. *Inverse beta processes and nonconservation of lepton charge*. Zh. Eksp. Teor. Fiz. **34**, p.247 (1957)

[28] Z. Maki et al. *Remarks on the unified model of elementary particles*. Prog. Theor. Phys. **28**, p.870–880 (1962)

[29] L. Wolfenstein. *Neutrino oscillations in matter*. Phys. Rev. D **17**, p.2369–2374 (1978)

[30] S. P. Mikheyev et al. *Resonance Amplification of Oscillations in Matter and Spectroscopy of Solar Neutrinos*. Sov. J. Nucl. Phys. **42**, p.913–917 (1985)

[31] S. P. Mikheyev et al. *Resonant amplification of* ν *oscillations in matter and solar-neutrino spectroscopy*. Nuovo Cim. **9**, p.17–26 (1986)

[32] S. P. Mikheyev et al. *Neutrino oscillations in a medium with variable density*. Sov. Phys. Usp. **29**, p.1155–1157 (1986)

[33] C. Giunti et al. *Fundamentals of Neutrino Physics and Astrophysics*. Oxford University Press, ISBN: 978-0-19-850871-7, Oxford (2007)

[34] P. F. de Salas et al. *2020 global reassessment of the neutrino oscillation picture*. JHEP **2021** 2 (2021)

[35] I. Esteban et al. *The fate of hints: updated global analysis of three-flavor neutrino oscillations*. JHEP **2020** 9 (2020)

[36] *NuFIT 5.1: Three-neutrino fit based on data available in October 2021*. (2021). URL: www.nu-fit.org

[37] F. Kaether et al. *Reanalysis of the GALLEX solar neutrino flux and source experiments*. Phys. Lett. B **685**, p.47–54 (2010)

[38] J. N. Abdurashitov et al. (SAGE Collaboration). *Measurement of the solar neutrino capture rate with gallium metal. III. Results for the 2002–2007 data-taking period*. Phys. Rev. C **80**, p.015807 (2009)

[39] K. Abe et al. (Super-Kamiokande Collaboration). *Solar neutrino measurements in Super-Kamiokande-IV*. Phys. Rev. D **94**, p.052010 (2016)

[40] B. Aharmim et al. (SNO Collaboration). *Combined analysis of all three phases of solar neutrino data from the Sudbury Neutrino Observatory*. Phys. Rev. C **88**, p.025501 (2013)

[41] G. Bellini et al. (Borexino Collaboration). *Precision Measurement of the* $^{7}\mathrm{Be}$ *Solar Neutrino Interaction Rate in Borexino*. Phys. Rev. Lett. **107**, p.141302 (2011)

[42] S. Abe et al. (KamLAND Collaboration). *Precision Measurement of Neutrino Oscillation Parameters with KamLAND*. Phys. Rev. Lett. **100**, p.221803 (2008)

[43] P. Adamson et al. (MINOS+ Collaboration). *Precision Constraints for Three-Flavor Neutrino Oscillations from the Full MINOS+ and MINOS Dataset*. Phys. Rev. Lett. **125**, p.131802 (2020)

[44] K. Abe et al. (T2K Collaboration). *Improved constraints on neutrino mixing from the T2K experiment with* 3.13×10^{21} *protons on target*. Phys. Rev. D **103**, p.112008 (2021)

[45] M. A. Acero et al. (NOνA Collaboration). *An Improved Measurement of Neutrino Oscillation Parameters by the NOνA Experiment*. arXiv: 2108.08219 (2021)

[46] K. Abe et al. (Super-Kamiokande Collaboration). *Atmospheric neutrino oscillation analysis with external constraints in Super-Kamiokande I-IV*. Phys. Rev. D **97**, p.072001 (2018)

[47] M. G. Aartsen et al. (IceCube Collaboration). *Measurement of Atmospheric Neutrino Oscillations at 6–56 GeV with IceCube DeepCore*. Phys. Rev. Lett. **120**, p.071801 (2018)

[48] X. Qian et al. *Neutrino mass hierarchy*. Prog. Part. Nucl. Phys. **83**, p.1–30 (2015)

[49] D. Adey et al. (Daya Bay Collaboration). *Measurement of the Electron Antineutrino Oscillation with 1958 Days of Operation at Daya Bay*. Phys. Rev. Lett. **121**, p.241805 (2018)

[50] T. Abrahão et al. (Double Chooz Collaboration). *Reactor rate modulation oscillation analysis with two detectors in Double Chooz*. JHEP **2021** (2021)

[51] S. B. Kim. *New results from RENO and future RENO-50 project*. Nuovo Cim. C **39**, p.317 (2017)

[52] K. Abe et al. (T2K Collaboration). *Measurement of neutrino and antineutrino oscillations by the T2K experiment including a new additional sample of ν_e interactions at the far detector*. Phys. Rev. D **96**, p.092006 (2017)

[53] B. Abi et al. *Long-baseline neutrino oscillation physics potential of the DUNE experiment*. Eur. Phys. J. C **80** 10 (2020)

[54] K. Abe et al. (Hyper-Kamiokande Proto-Collaboration). *Hyper-Kamiokande Design Report*. arXiv:1805.04163 [physics.ins-det] (2018)

[55] E. Majorana. *Teoria simmetrica dell'elettrone e del positrone*. Nuovo Cim. **14**, p.171–184 (1937)

[56] A. B. Balantekin et al. *On the Properties of Neutrinos*. Annu. Rev. Nucl. Part. Sci. **68**, p.313–338 (2018)

[57] E. Akhmedov. *Majorana neutrinos and other Majorana particles: Theory and experiment*. arXiv: 1412.3320 (2014)

[58] V. Brdar et al. *Type I seesaw mechanism as the common origin of neutrino mass, baryon asymmetry, and the electroweak scale*. Phys. Rev. D **100**, p.075029 (2019)

[59] C. S. Fong et al. *Leptogenesis in the Universe*. Adv. High Energy Phys. **2012**, p.158303 (2012)

[60] T. Hambye. *CP violation and the matter–antimatter asymmetry of the Universe*. C. R. Phys. **13**. Flavour physics and CP violation / Physique de la saveur et violation de CP, p.193–203 (2012)

[61] N. Aghanim et al. (Planck Collaboration). *Planck 2018 results - VI. Cosmological parameters*. A&A **641**, p.A6 (2020)

[62] R. Emami et al. *Evidence of Neutrino Enhanced Clustering in a Complete Sample of Sloan Survey Clusters, Implying $\sum m_\nu = 0.119 \pm 0.034$ eV*. arXiv: 1711.05210 (2019)

[63] M. Aker et al. (KATRIN Collaboration). *Analysis methods for the first KATRIN neutrino-mass measurement*. Phys. Rev. D **104**, p.012005 (2021)

[64] A. B. Balantekin et al. *Addressing the Majorana vs. Dirac question with neutrino decays*. Phys. Lett. B **789**, p.488–495 (2019)

[65] A. J. Long et al. *Detecting non-relativistic cosmic neutrinos by capture on tritium: phenomenology and physics potential*. J. Cosmol. Astropart. **2014**, p.038–038 (2014)

[66] S. Weinberg. *Universal Neutrino Degeneracy*. Phys. Rev. **128**, p.1457–1473 (1962)

[67] E. Roulet et al. *On the capture rates of big bang neutrinos by nuclei within the Dirac and Majorana hypotheses*. J. Cosmol. Astropart. **2018**, p.049–049 (2018)

[68] S. Betts et al. *Development of a Relic Neutrino Detection Experiment at PTOLEMY: Princeton Tritium Observatory for Light, Early-Universe, Massive-Neutrino Yield*. arXiv: 1307.4738 (2013)

[69] A. de Gouvêa et al. *What can we learn from neutrino electron scattering?* Phys. Rev. D **74**, p.033004 (2006)

[70] M. Agostini et al. (Borexino Collaboration). *Limiting neutrino magnetic moments with Borexino Phase-II solar neutrino data*. Phys. Rev. D **96**, p.091103 (2017)

[71] J. Frère et al. *Triangle inequalities for Majorana-neutrino magnetic moments*. Phys. Rev. D **92**, p.053002 (2015)

[72] W. Pauli. *Pauli letter collection: letter to Lise Meitner*. Typed copy. (1930). URL: https://cds.cern.ch/record/83282

[73] E. Fermi. *An attempt of a theory of beta radiation. 1*. Z. Phys. **88**, p.161–177 (1934)

[74] E. Fermi. *Trends to a Theory of beta Radiation*. Nuovo Cim. **11**, p.1–19 (1934)

[75] M. Goeppert-Mayer. *Double Beta-Disintegration*. Phys. Rev. **48**, p.512–516 (1935)

[76] P. A. Zyla et al. (Particle Data Group). *Review of Particle Physics*. Prog. Theor. Exp. Phys. **2020**. 083C01 (2020)

[77] R. Arnold et al. (NEMO-3 Collaboration). *Measurement of the double-beta decay half-life and search for the neutrinoless double-beta decay of* $^{48}\mathrm{Ca}$ *with the NEMO-3 detector*. Phys. Rev. D **93**, p.112008 (2016)

[78] M. Agostini et al. (GERDA Collaboration). *Results on* $\beta\beta$ *decay with emission of two neutrinos or Majorons in* ^{76}*Ge from GERDA Phase I*. Eur. Phys. J. C **75**, p.416 (2015)

[79] S. S. Ratkevich et al. *Comparative study of the double-*K*-shell-vacancy production in single- and double-electron-capture decay*. Phys. Rev. C **96**, p.065502 (2017)

[80] L Pagnanini et al. *Results on* ^{82}*Se* $2\nu\beta\beta$ *with CUPID-0 Phase I*. J. Phys. Conf. Ser. **1643**, p.012025 (2020)

[81] J. Argyriades et al. (NEMO-3 Collaboration). *Measurement of the two neutrino double beta decay half-life of Zr-96 with the NEMO-3 detector*. Nucl. Phys. A **847**, p.168–179 (2010)

[82] E. Armengaud et al. (CUPID-Mo Collaboration). *Precise measurement of* $2\nu\beta\beta$ *decay of* ^{100}*Mo with the CUPID-Mo detection technology*. Eur. Phys. J. C **80** (2020)

[83] A. S. Barabash et al. *Final results of the Aurora experiment to study* 2β *decay of* $^{116}\mathrm{Cd}$ *with enriched* $^{116}\mathrm{CdWO_4}$ *crystal scintillators*. Phys. Rev. D **98**, p.092007 (2018)

[84] H. V. Thomas et al. *Geochemical constraints on the half-life of* $^{130}\mathrm{Te}$. Phys. Rev. C **78**, p.054606 (2008)

[85] D. Q. Adams et al. (CUORE Collaboration). *Measurement of the* $2\nu\beta\beta$ *Decay Half-Life of* $^{130}\mathrm{Te}$ *with CUORE*. Phys. Rev. Lett. **126**, p.171801 (2021)

[86] A. Gando et al. (KamLAND-Zen Collaboration). *Precision Analysis of the* $^{136}\mathrm{Xe}$ *Two-Neutrino* $\beta\beta$ *Spectrum in KamLAND-Zen and Its Impact on the Quenching of Nuclear Matrix Elements*. Phys. Rev. Lett. **122**, p.192501 (2019)

[87] R. Arnold et al. (NEMO-3 Collaboration). *Measurement of the $2\nu\beta\beta$ decay half-life of ^{150}Nd and a search for $0\nu\beta\beta$ decay processes with the full exposure from the NEMO-3 detector*. Phys. Rev. D **94**, p.072003 (2016)

[88] A. L. Turkevich et al. *Double-beta decay of ^{238}U*. Phys. Rev. Lett. **67**, p.3211–3214 (1991)

[89] R. Saakyan. *Two-Neutrino Double-Beta Decay*. Annu. Rev. Nucl. Part. Sci. **63**, p.503–529 (2013)

[90] J. Kotila et al. *Phase-space factors for double-β decay*. Phys. Rev. C **85**, p.034316 (2012)

[91] W. H. Furry. *On Transition Probabilities in Double Beta-Disintegration*. Phys. Rev. **56**, p.1184–1193 (1939)

[92] S. M. Bilenky et al. *Neutrinoless double-beta decay: A probe of physics beyond the Standard Model*. Int. J. Mod. Phys. A **30**, p.1530001 (2015)

[93] J. Schechter et al. *Neutrinoless double-β decay in SU(2)×U(1) theories*. Phys. Rev. D **25**, p.2951–2954 (1982)

[94] M. Agostini et al. *Discovery probability of next-generation neutrinoless double-β decay experiments*. Phys. Rev. D **96**, p.053001 (2017)

[95] A. Caldwell et al. *Global Bayesian analysis of neutrino mass data*. Phys. Rev. D **96**, p.073001 (2017)

[96] M. Agostini et al. *Discovery probabilities of Majorana neutrinos based on cosmological data*. Phys. Rev. D **103**, p.033008 (2021)

[97] P. Stöcker et al. (GAMBIT Cosmology Workgroup). *Strengthening the bound on the mass of the lightest neutrino with terrestrial and cosmological experiments*. Phys. Rev. D **103**, p.123508 (2021)

[98] F. Simkovic et al. *$0\nu\beta\beta$ and $2\nu\beta\beta$ nuclear matrix elements, quasiparticle random-phase approximation, and isospin symmetry restoration*. Phys. Rev. C **87**, p.045501 (2013)

[99] J. T. Suhonen. *Value of the Axial-Vector Coupling Strength in β and $\beta\beta$ Decays: A Review*. Front. Phys. **5** (2017)

[100] S. Dell'Oro et al. *Neutrinoless Double Beta Decay: 2015 Review*. Adv. High Energy Phys. **2016**, p.1–37 (2016)

[101] J. Engel et al. *Status and future of nuclear matrix elements for neutrinoless double-beta decay: a review*. Rep. Prog. Phys. **80**, p.046301 (2017)

[102] J. Menéndez et al. *Disassembling the nuclear matrix elements of the neutrinoless $\beta\beta$ decay*. Nucl. Phys. A **818**, p.139–151 (2009)

[103] T. R. Rodríguez et al. *Energy Density Functional Study of Nuclear Matrix Elements for Neutrinoless $\beta\beta$ Decay*. Phys. Rev. Lett. **105**, p.252503 (2010)

[104] J. Menéndez et al. *Testing the importance of collective correlations in neutrinoless $\beta\beta$ decay*. Phys. Rev. C **93**, p.014305 (2016)

[105] J. Barea et al. *$0\nu\beta\beta$ and $2\nu\beta\beta$ nuclear matrix elements in the interacting boson model with isospin restoration*. Phys. Rev. C **91**, p.034304 (2015)

[106] S. D. Biller. *Probing Majorana neutrinos in the regime of the normal mass hierarchy*. Phys. Rev. D **87**, p.071301 (2013)

[107] E. W. Beier. *NewNd $0\nu\beta\beta$ counting experiment*. SNO+ Internal Document 1830

[108] S. Umehara et al. *Neutrino-less double-β decay of ^{48}Ca studied by CaF_2(Eu) scintillators*. Phys. Rev. C **78**, p.058501 (2008)

[109] M. Agostini et al. (GERDA Collaboration). *Final Results of GERDA on the Search for Neutrinoless Double-β Decay*. Phys. Rev. Lett. **125**, p.252502 (2020)

[110] O. Azzolini et al. *Final Result of CUPID-0 Phase-I in the Search for the ^{82}Se Neutrinoless Double-β Decay*. Phys. Rev. Lett. **123**, p.032501 (2019)

[111] E. Armengaud et al. (CUPID-Mo Collaboration). *New Limit for Neutrinoless Double-Beta Decay of ^{100}Mo from the CUPID-Mo Experiment*. Phys. Rev. Lett. **126**, p.181802 (2021)

[112] D. Q. Adams et al. (CUORE Collaboration). *Search for Majorana neutrinos exploiting millikelvin cryogenics with CUORE*. Nature **604** 7904, p.53–58 (2022)

[113] S. Abe et al. (KamLAND-Zen Collaboration). *First Search for the Majorana Nature of Neutrinos in the Inverted Mass Ordering Region with KamLAND-Zen*. arXiv:2203.02139 [hep-ex] (2022)

[114] K.-H. Ackermann et al. (GERDA Collaboration). *The GERDA experiment for the search of $0\nu\beta\beta$ decay in 76Ge*. Eur. Phys. J. C **73** (2013)

[115] N. Abgrall et al. (Majorana Collaboration). *The Majorana Demonstrator Neutrinoless Double-Beta Decay Experiment*. Adv. High Energy Phys. **2014**, p.365432 (2014)

[116] S. I. Alvis et al. (Majorana Collaboration). *Search for neutrinoless double-β decay in ^{76}Ge with 26 kg yr of exposure from the Majorana Demonstrator*. Phys. Rev. C **100**, p.025501 (2019)

[117] I. Nutini et al. (CUORE Collaboration). *The CUORE Detector and Results*. J. Low Temp. Phys. **199**, p.519–528 (2020)

[118] J. B. Albert et al. (EXO-200 Collaboration). *Search for Neutrinoless Double-Beta Decay with the Upgraded EXO-200 Detector*. Phys. Rev. Lett. **120**, p.072701 (2018)

[119] Y. Gando et al. (KamLAND-Zen Collaboration). *The nylon balloon for xenon loaded liquid scintillator in KamLAND-Zen 800 neutrinoless double-beta decay search experiment*. JINST **16**, p.P08023 (2021)

[120] G. Anton et al. (EXO-200 Collaboration). *Search for Neutrinoless Double-β Decay with the Complete EXO-200 Dataset*. Phys. Rev. Lett. **123**, p.161802 (2019)

[121] R. Arnold et al. (NEMO-3 Collaboration). *Technical design and performance of the NEMO 3 detector*. Nucl. Instrum. Meth. A **536**, p.79–122 (2005)

[122] R. Arnold et al. (NEMO-3 Collaboration). *Final results on ^{82}Se double beta decay to the ground state of ^{82}Kr from the NEMO-3 experiment*. Eur. Phys. J. C **78** 10, p.821 (2018)

[123] R. Arnold et al. (NEMO-3 Collaboration). *Measurement of the $2\nu\beta\beta$ decay half-life and search for the $0\nu\beta\beta$ decay of ^{116}Cd with the NEMO-3 detector*. Phys. Rev. D **95**, p.012007 (2017)

[124] R. Arnold et al. (NEMO-3 Collaboration). *Measurement of the $\beta\beta$ Decay Half-Life of ^{130}Te with the NEMO-3 Detector*. Phys. Rev. Lett. **107**, p.062504 (2011)

[125] R. Arnold et al. (NEMO-3 Collaboration). *Results of the search for neutrinoless double-β decay in ^{100}Mo with the NEMO-3 experiment*. Phys. Rev. D **92**, p.072011 (2015)

[126] G. Adhikari et al. (nEXO Collaboration). *nEXO: neutrinoless double beta decay search beyond 1028 date half-life sensitivity*. J. Phys. G: Nucl. Part. Phys. **49**, p.015104 (2021)

[127] C. Adams et al. (NEXT Collaboration). *Sensitivity of a tonne-scale NEXT detector for neutrinoless double-beta decay searches*. JHEP **2021** (2021)

[128] K. Han (PandaX-III Collaboration). *PandaX-III: Searching for Neutrinoless Double Beta Decay with High Pressure Gaseous Time Projection Chambers*. J. Phys. Conf. Ser. **1342**, p.012095 (2020)

[129] F. Piquemal. *The SuperNEMO project*. Phys. Atom. Nucl. **69**, p.2096–2100 (2006)

[130] D. R. Artusa et al. *Enriched TeO_2 bolometers with active particle discrimination: Towards the CUPID experiment*. Phys. Lett. B **767**, p.321–329 (2017)

[131] N. Abgrall et al. (LEGEND Collaboration). *LEGEND-1000 Preconceptual Design Report*. arXiv: 2107.11462 (2021)

[132] S. Andringa et al. (SNO+ Collaboration). *Current Status and Future Prospects of the SNO+ Experiment*. Adv. High Energy Phys. **2016**, p.1–21 (2016)

[133] V. Albanese et al. (SNO+ Collaboration). *The SNO+ experiment*. JINST **16**, p.P08059 (2021)

[134] N. D. Scielzo et al. *Double-β-decay Q values of ^{130}Te, ^{128}Te, and ^{120}Te*. Phys. Rev. C **80**, p.025501 (2009)

[135] M. Agostini et al. (Borexino Collaboration). *Experimental evidence of neutrinos produced in the CNO fusion cycle in the Sun*. Nature **587**, p.577–582 (2020)

[136] W. C. Haxton et al. *CN Cycle Solar Neutrinos and the Sun's Primordial Core Metallicity*. ApJ **687** 1, p.678–691 (2008)

[137] A. M. Serenelli et al. *New solar composition: the problem with solar models revisited*. ApJ **705**, p.123—127 (2009)

[138] J. N. Bahcall. *Why do solar neutrino experiments below 1 MeV?* In: *Low Energy Solar Neutrino Detection*, p.172–176

[139] G. Fiorentini et al. *Geo-neutrinos and earth's interior*. Phys. Rep. **453** 5, p.117–172 (2007)

[140] P. Antonioli et al. *SNEWS: the SuperNova Early Warning System*. New J. Phys. **6**, p.114–114 (2004)

[141] M. Anderson et al. (SNO+ Collaboration). *Search for invisible modes of nucleon decay in water with the SNO+ detector*. Phys. Rev. D **99**, p.032008 (2019)

[142] J. Boger et al. (SNO Collaboration). *The Sudbury Neutrino Observatory*. Nucl. Instrum. Meth. A **449**, p.172–207 (2000)

[143] M. R. Anderson et al. (SNO+ Collaboration). *Development, characterisation, and deployment of the SNO+ liquid scintillator*. JINST **16**, p.P05009 (2021)

[144] J.B. Cumming et al. *Improving light yield measurements for low-yield scintillators*. Nucl. Instrum. Methods Phys. Res. A: Accel. Spectrom. Detect. Assoc. Equip. **925**, p.1–5 (2019)

[145] V. Lozza et al. *Cosmogenic activation of a natural tellurium target*. Astropart. Phys. **61**, p.62–71 (2015)

[146] S. Hans et al. *Purification of telluric acid for SNO+ neutrinoless double-beta decay search*. Nucl. Instrum. Methods Phys. Res. A: Accel. Spectrom. Detect. Assoc. Equip. **795**, p.132–139 (2015)

[147] M. R. Anderson et al. (SNO+ Collaboration). *A Method to Load Tellurium in Liquid Scintillator to Study Neutrinoless Double Beta Decay*. In preparation.

[148] S. Biller et al. *A New Technique to Load ^{130}Te in Liquid Scintillator for Neutrinoless Double Beta Decay Experiments*. J. Phys. Conf. Ser. **888**, p.012084 (2017)

[149] B. Moffat. *The Optical Calibration of the Sudbury Neutrino Observatory*. PhD Thesis. Queen's University, Canada (2001)

[150] M. R. Anderson et al. (SNO+ Collaboration). *Optical calibration of the SNO+ detector in the water phase with deployed sources*. JINST **16**, p.P10021 (2021)

[151] C. Jackson. *Photographs of aged concentrators*. SNO+ Document 3518-v1. (2016)

[152] S. Agostinelli et al. *Geant4 – a simulation toolkit*. Nucl. Instrum. Meth. A **506**, p.250–303 (2003)

[153] R. Brun et al. *ROOT: An object oriented data analysis framework*. Nucl. Instrum. Meth. A **389**, p.81–86 (1997)

[154] B. Aharmim et al. (SNO Collaboration). *Determination of the ν_e and total ^{8}B solar neutrino fluxes using the Sudbury Neutrino Observatory Phase I data set*. Phys. Rev. C **75**, p.045502 (2007)

[155] S. D. Biller et al. *Measurements of photomultiplier single photon counting efficiency for the Sudbury Neutrino Observatory*. Nucl. Instrum. Meth. A **432**, p.364–373 (1999)

[156] M. R. Dragowsky et al. *The ^{16}N calibration source for the Sudbury Neutrino Observatory*. Nucl. Instrum. Meth. A **481**, p.284–296 (2002)

[157] B. A. Moffat et al. *Optical calibration hardware for the Sudbury Neutrino Observatory*. Nucl. Instrum. Meth. A **554**, p.255–265 (2005)

[158] R. Alves et al. *The calibration system for the photomultiplier array of the SNO+ experiment*. JINST **10**, p.P03002–P03002 (2015)

[159] M. R. Anderson et al. (SNO+ Collaboration). *Measurement of neutron-proton capture in the SNO+ water phase*. Phys. Rev. C **102**, p.014002 (2020)

[160] A. Allega et al. (SNO+ Collaboration). *Improved search for invisible modes of nucleon decay in water with the SNO+ detector*. Phys. Rev. D **105**, p.112012 (2022)

[161] H. O. Back et al. (Borexino Collaboration). *New limits on nucleon decays into invisible channels with the Borexino counting test facility*. Phys. Lett. B **563**, p.23–34 (2003)

[162] V. I. Tretyak et al. *New limits on di-nucleons decay into invisible channels*. JETP Lett. **79**, p.106–108 (2004)

[163] M. Anderson et al. (SNO+ Collaboration). *Measurement of the* ^{8}B *solar neutrino flux in SNO+ with very low backgrounds*. Phys. Rev. D **99**, p.012012 (2019)

[164] Q. R. Ahmad et al. (SNO Collaboration). *Measurement of the Rate of* $\nu_e + d \rightarrow p + p + e^-$ *Interactions Produced by* ^8B *Solar Neutrinos at the Sudbury Neutrino Observatory*. Phys. Rev. Lett. **87**, p.071301 (2001)

[165] M. Agostini et al. (Borexino Collaboration). *Improved measurement of* ^{8}B *solar neutrinos with 1.5 kt·y of Borexino exposure*. Phys. Rev. D **101**, p.062001 (2020)

[166] B. Krar. *Solar LowBG Water Analysis*. SNO+ Internal Document 7401

[167] A. Allega et al. (SNO+ Collaboration). *Observation of Antineutrinos from Distant Reactors using Pure Water at SNO+*. arXiv:2210.14154 [nucl-ex] (2022)

[168] J. Paton. *Directionality in SNO+*. SNO+ Internal Document 7327

[169] C. Mills. *Reactor antinu oscillation sensitivity in scintillator phase*. SNO+ Internal Document 7373

[170] C. J. Jillings et al. *The photomultiplier tube testing facility for the Sudbury Neutrino Observatory*. Nucl. Instrum. Meth. A **373**, p.421–429 (1996)

[171] N. Barros. *Precision Measurements of Neutrino Oscillation Parameters: Combined Three-Phase Results of the Sudbury Neutrino Observatory*. PhD Thesis. Universidade de Lisboa, Portugal (2011)

[172] O. Simard. *Measurement of the Survival Probability and Determination of the Three-Flavour Neutrino Oscillation Parameters at the Sudbury Neutrino Observatory*. PhD Thesis. Ottawa-Carleton Institute for Physics, Carleton University, Canada (2009)

[173] K. Levenberg. *A method for the solution of certain non-linear problems in least squares*. Q. Appl. Math. **2**, p.164–168 (1944)

[174] D. Marquardt. *An Algorithm for Least-Squares Estimation of Nonlinear Parameters*. J. Soc. Indust. Appl. Math. **II**, p.431–441 (1963)

[175] R. M. Pope et al. *Absorption spectrum (380–700 nm) of pure water. II. Integrating cavity measurements*. Appl. Opt. **36**, p.8710–8723 (1997)

[176] J. D. Mason et al. *Ultraviolet (250–550 nm) absorption spectrum of pure water*. Appl. Opt. **55**, p.7163–7172 (2016)

[177] B. Aharmim et al. (SNO Collaboration). *Electron energy spectra, fluxes, and day-night asymmetries of ^{8}B solar neutrinos from measurements with NaCl dissolved in the heavy-water detector at the Sudbury Neutrino Observatory*. Phys. Rev. C **72**, p.055502 (2005)

[178] A. Zummo. *External Background Box Analysis Plot/Results*. SNO+ Internal Document 7329

[179] G. Alimonti et al. (Borexino Collaboration). *Measurement of the ^{14}C abundance in a low-background liquid scintillator*. Phys. Lett. B **422**, p.349–358 (1998)

[180] I. Morton-Blake. *First measurement of reactor antineutrinos in scintillator at SNO+ and study of alternative designs for large-scale liquid scintillator detectors*. PhD Thesis. University of Oxford, United Kingdom (2021)

[181] M. Smiley. *BerkeleyAlphaBeta Performance Check in Partial Fill*. SNO+ Internal Document 6705

[182] J. Paton. *Directionality Studies With Solar Neutrinos*. SNO+ Internal Document 7063

[183] M. Altmann et al. *Complete results for five years of GNO solar neutrino observations*. Phys. Lett. B **616** 3, p.174–190 (2005)

[184] M. Agostini et al. (Borexino Collaboration). *Simultaneous precision spectroscopy of pp, ^{7}Be, and pep solar neutrinos with Borexino Phase-II*. Phys. Rev. D **100**, p.082004 (2019)

[185] J. N. Bahcall et al. *Solar neutrinos: Radiative corrections in neutrino-electron scattering experiments*. Phys. Rev. D **51**, p.6146–6158 (1995)

[186] W. T. Winter et al. *The ^{8}B neutrino spectrum*. Phys. Rev. C **73**, p.025503 (2006)

[187] E. Vitagliano et al. *Grand unified neutrino spectrum at Earth: Sources and spectral components*. Rev. Mod. Phys. **92**, p.045006 (2020)

[188] N. Vinyoles et al. *A New Generation of Standard Solar Models*. ApJ **835**, p.202 (2017)

[189] Cepsa. *PETRELAB® 500-Q, C10-C13 Linear Alkylbenzene (LAB)*. Technical Data Sheet. (2019). URL: https://chemicals.cepsa.com/stfls/chemicals/Ficheros/PETRELAB_500_Q_Cepsa__Eng.pdf

[190] F. James et al. *Minuit: A System for Function Minimization and Analysis of the Parameter Errors and Correlations*. Comput. Phys. Commun. **10**, p.343–367 (1975)

[191] M. Bernard. *B8 Analysis in the Partial Fill*. SNO+ Internal Document 7023

[192] M. F. Kidd et al. *Two-neutrino double-β decay of ^{150}Nd to excited final states in ^{150}Sm*. Phys. Rev. C **90**, p.055501 (2014)

[193] R. Arnold et al. (NEMO-3 Collaboration). *Investigation of double beta decay of ^{100}Mo to excited states of ^{100}Ru*. Nucl. Phys. A **925**, p.25–36 (2014)

[194] A. Barabash. *Precise Half-Life Values for Two-Neutrino Double-β Decay: 2020 Review*. Universe **6** (2020)

[195] F. Simkovik et al. *Anatomy of the $0\nu\beta\beta$ nuclear matrix elements*. Phys. Rev. C **77**, p.045503 (2008)

[196] F. Simkovik et al. *Improved description of the $2\nu\beta\beta$-decay and a possibility to determine the effective axial-vector coupling constant*. Phys. Rev. C **97**, p.034315 (2018)

[197] O. A. Ponkratenko et al. *Event generator DECAY4 for simulating double-beta processes and decays of radioactive nuclei*. Phys. At. Nucl. **63** 7, p.1282–1287 (2000)

[198] V. I. Tretyak et al. *Tables of Double Beta Decay Data – An update*. At. Data Nucl. Data Tables **80** 1, p.83–116 (2002)

[199] J. Dunger. *Topological and Time Based Event Classification for Neutrinoless Double Beta Decay in Liquid Scintillator*. PhD Thesis. University of Oxford, United Kingdom (2018)

[200] T. Kroupová. *Improving the Sensitivity to Neutrinoless Double Beta Decay in SNO+*. PhD Thesis. University of Oxford, United Kingdom (2020)

[201] T. Kaptanoglu. *Reactor Antineutrinos in the SNO+ Water Phase and Detector R&D for Large-scale Neutrino Detectors*. PhD Thesis. University of Pennsylvania, United States of America (2020)

[202] G. Cowan. *Statistical data analysis*. Oxford University Press, ISBN: 978-0-19-850156-5, USA, (1998)

[203] V. Lozza et al. *Expected radioactive backgrounds in SNO+*. SNO+ Internal Document 507

[204] A. S. Inácio. *Using a Smaller Shell when Simulating Bi214 and Tl208 in the External Water and Ropes*. SNO+ Internal Document 5154

[205] W. Heintzelman. *The Radial Distribution of Interactions of gamma rays from PMT beta/gamma background events*. SNO+ Internal Document 1708

Appendix A

Background rates in SNO+

This Appendix collects preliminary background rates in the SNO+ detector, which were used for the sensitivity studies of Chapter 7.

A.1 Internal backgrounds

Table A.1 presents the expected background sources during the Te-loaded phase from intrinsic contamination within the Te-BD scintillator cocktail volume. The second column presents the target rates taken from [203]. The third column presents the expected rates constrained by the preliminary background measurements performed during the partial fill period. The expected ^{130}Te $2\nu\beta\beta$ decay rate was calculated based on the half-life measurement from [85].

The ^{232}Th and ^{238}U chains are assumed to be in secular equilibrium. The components of the Te-loaded cocktail introduce different concentrations of U and Th, weighted by their contribution to the total cocktail mass: telluric acid, LAB+PPO, BD and DDA contribute 0.9%, 97.8%, 1.026% and 0.32% to the total rate, respectively. The target ^{232}Th concentration is 5.57×10^{-16} gTh/gScint, which breaks down into:

$$\begin{aligned} C_{^{232}Th} = {} & 0.009 \cdot 5.0 \times 10^{-14}\ \text{gTh/gTeA} \\ & + 0.978 \cdot 6.80 \times 10^{-18}\ \text{gTh/gLAB} \\ & + 0.01026 \cdot 3.5 \times 10^{-15}\ \text{gTh/gBD} \\ & + 0.0032 \cdot 2.0 \times 10^{-14}\ \text{gTh/gDDA}. \end{aligned} \tag{A.1}$$

Similarly, the target concentration for ^{238}U is 1.29×10^{-15} gU/gScint:

$$\begin{aligned} C_{^{238}U} = {} & 0.009 \cdot 1.0 \times 10^{-13}\ \text{gU/gTeA} \\ & + 0.978 \cdot 1.60 \times 10^{-17}\ \text{gU/gLAB} \\ & + 0.01026 \cdot 3.5 \times 10^{-14}\ \text{gU/gBD} \\ & + 0.0032 \cdot 5.0 \times 10^{-15}\ \text{gU/gDDA}. \end{aligned} \tag{A.2}$$

The constraints for the isotopes of the U/Th chains were calculated using the target concentrations for the telluric acid, BD and DDA, and the measured concentrations in the LAB during

the partial fill period. No leaching is assumed for the ^{210}Bi, ^{210}Po and ^{210}Pb. The constraints for these isotopes are based on the variation of the measured rates during the partial fill period – 90 to 100 events/second for ^{210}Po and 4 to 5 events/s for ^{210}Bi. The central values of these ranges are taken as the average rate, and the width of the ranges are taken as uncertainties. The ^{210}Pb and its daughters are out of equilibrium with the remaining of the U chain; their rates appeared roughly constant during the partial fill period and showed no evidence for increasing due to leaching.

A.2 External backgrounds

Table A.2 presents the expected external background sources during the Te-loaded phase. The second column presents the target rates taken from [203]. The third column presents the rates measured during the water phase and partial fill period. The source of the external background is stated following the isotope name: external water, AV, dust on the inner/outer surfaces of the AV, hold-down rope system, hold-up rope system, internal (calibration) ropes and PMTs. The external (α,n) backgrounds are produced in interactions on one of the surfaces of the AV (AVin or AVout). The direction of the α dictates whether it interacts with a ^{13}C or ^{18}O inside the liquid scintillator (LS) or the acrylic (AV).

The simulation of the decays of ^{214}Bi and ^{208}Tl in the external water and ropes systems is one of the most time consuming amongst all the backgrounds. ^{214}Bi and ^{208}Tl exist throughout the full external water and rope volumes and, by default, were accordingly simulated by randomly generating their positions within the corresponding Monte Carlo geometries. However, only the events generated in the proximity of the AV end up creating a signal in the scintillator volume, yielding a small simulation efficiency (number of detected signals $\ll$ number of simulated events). Furthermore, given that the external ^{214}Bi and ^{208}Tl energy spectra covers or is in close proximity to the double beta decay ROI, a large number of events needs to be simulated in order to have accurate PDFs for the analyses. For these reasons, the simulation of these events was optimized [204] to only generate decays in these detector geometry elements within a spherical shell around the AV. For the backgrounds in the ropes, the shell effectively avoids generating decays in the rope lengths outside the shell.

The PMT β-γ include the background signals produced by ^{208}Tl and ^{214}Bi decays in the PMT glass, with the energy and radial distributions of γs and βs generated based on the model developed by W. Heintzelman [205].

A.3 Tellurium cosmogenics

Table A.3 presents the expected number of counts in one year of the isotopes produced from the cosmogenic activation of tellurium while on surface, without and with purification of the cocktail. The expected number of counts was calculated with the following assumptions:

- Telluric acid arriving to SNOLAB in three batches.

Table A.1: Expected internal background sources during the Te-loaded phase within the AV volume. No analysis cuts or detection efficiencies are considered. The second column presents the target rates taken from [203]. The third column presents the expected rates constrained by the preliminary background measurements performed during the partial fill period. No leaching is assumed for the ^{210}Pb and its daughters, as well as for the (α,n) reactions.

Background source	Target rate (Events/year)	Constrained rate (Events/year)
(α,n) ^{13}C interactions in LS	2.23×10^{2}	4.08×10^{2}
^{39}Ar	8.34×10^{4}	–
^{8}B solar ν_e	9.54×10^{2}	–
^{8}B solar ν_μ	3.15×10^{2}	–
^{14}C	2.50×10^{10}	5.90×10^{10}
^{130}I	5.47	–
^{130m}I	6.50	–
^{40}K	8.29×10^{3}	–
^{85}Kr	8.37×10^{4}	–
^{232}Th	5.57×10^{4}	$(6.01\pm1.70)\times10^{4}$
^{228}Ra	5.57×10^{4}	$(6.01\pm1.70)\times10^{4}$
^{228}Ac	5.57×10^{4}	$(6.01\pm1.70)\times10^{4}$
^{228}Th	5.57×10^{4}	$(6.01\pm1.70)\times10^{4}$
^{224}Ra	5.57×10^{4}	$(6.01\pm1.70)\times10^{4}$
^{220}Rn	5.57×10^{4}	$(6.01\pm1.70)\times10^{4}$
^{216}Po	5.57×10^{4}	$(6.01\pm1.70)\times10^{4}$
^{212}Pb	5.57×10^{4}	$(6.01\pm1.70)\times10^{4}$
^{212}Bi	5.57×10^{4}	$(6.01\pm1.70)\times10^{4}$
^{212}Po	3.57×10^{4}	$(3.85\pm1.09)\times10^{4}$
^{208}Tl	2.01×10^{4}	$(2.16\pm0.61)\times10^{4}$
^{238}U	3.95×10^{5}	$(4.04\pm1.03)\times10^{5}$
^{234}Th	3.95×10^{5}	$(4.04\pm1.03)\times10^{5}$
^{234m}Pa	3.95×10^{5}	$(4.04\pm1.03)\times10^{5}$
^{234}U	3.95×10^{5}	$(4.04\pm1.03)\times10^{5}$
^{230}Th	3.95×10^{5}	$(4.04\pm1.03)\times10^{5}$
^{226}Ra	3.95×10^{5}	$(4.04\pm1.03)\times10^{5}$
^{222}Rn	3.95×10^{5}	$(4.04\pm1.03)\times10^{5}$
^{218}Po	3.95×10^{5}	$(4.04\pm1.03)\times10^{5}$
^{214}Pb	3.95×10^{5}	$(4.04\pm1.03)\times10^{5}$
^{214}Bi	3.95×10^{5}	$(4.04\pm1.03)\times10^{5}$
^{214}Po	3.95×10^{5}	$(4.04\pm1.03)\times10^{5}$
^{210}Tl	8.30×10^{1}	$(8.49\pm2.16)\times10^{1}$
^{210}Pb	4.32×10^{5}	$(1.42\pm0.16)\times10^{8}$
^{210}Bi	4.32×10^{5}	$(1.42\pm0.16)\times10^{8}$
^{210}Po	3.58×10^{9}	$(6.56\pm0.16)\times10^{9}$
^{130}Te $2\nu\beta\beta$	5.54×10^{6}	–

Table A.2: Expected external background sources during the Te-loaded phase. No analysis cuts or detection efficiencies are considered. The second column presents the target rates taken from [203]. The third column presents the rates measured during the water phase and partial fill period.

Background source	Target rate (Events/year)	Measured rate (Events/year)
(α,n) ^{13}C AVin AV	8.53×10^{2}	1.06×10^{3}
(α,n) ^{18}O AVin AV	2.63×10^{2}	3.26×10^{2}
(α,n) ^{13}C AVin LS	1.13×10^{3}	1.40×10^{3}
(α,n) ^{13}C AVout AV	8.53×10^{2}	3.26×10^{2}
(α,n) ^{18}O AVout AV	2.63×10^{2}	1.06×10^{3}
^{210}Bi AV inner dust	3.63×10^{10}	4.50×10^{10}
^{210}Bi AV outer dust	3.63×10^{10}	4.50×10^{10}
^{214}Bi AV	1.28×10^{7}	$(2.69^{+8.21}_{-2.69})\times10^{6}$
^{214}Bi external water (shell of 7.1 m)	4.62×10^{7}	$(2.03^{+1.48}_{-1.25})\times10^{7}$
^{214}Bi hold-down ropes (shell of 7.25 m)	2.72×10^{6}	$(9.79\pm4.61)\times10^{5}$
^{214}Bi hold-up ropes (shell of 7.25 m)	2.92×10^{5}	$(1.05\pm0.5)\times10^{5}$
^{214}Bi internal ropes	4.97×10^{3}	–
^{212}Bi^{212}Po AV	2.67×10^{6}	–
^{40}K AV	7.32×10^{7}	–
^{40}K internal ropes	2.81×10^{4}	–
^{40}K hold-down + hold-up ropes	2.28×10^{8}	–
^{210}Pb AV inner dust	3.63×10^{10}	4.50×10^{10}
^{210}Pb AV outer dust	3.63×10^{10}	4.50×10^{10}
PMT β-γ	7.18×10^{4}	$(6.25^{+6.95}_{-2.54})\times10^{4}$
^{210}Po AV inner dust	3.63×10^{10}	4.50×10^{10}
^{210}Po AV outer dust	3.63×10^{10}	4.50×10^{10}
^{208}Tl AV	1.50×10^{6}	$(3.15^{+9.65}_{-3.15})\times10^{5}$
^{208}Tl external water (shell of 7.5 m)	1.96×10^{6}	$(8.62^{+6.28}_{-5.29})\times10^{5}$
^{208}Tl hold-down ropes (shell of 7.25 m)	1.55×10^{6}	$(5.60\pm2.65)\times10^{5}$
^{208}Tl hold-up ropes (shell of 7.25 m)	1.67×10^{5}	$(6.02\pm2.85)\times10^{4}$
^{208}Tl internal ropes	4.18×10^{2}	–
^{210}Tl AV	2.68×10^{3}	$(5.63^{+17.2}_{-5.63})\times10^{2}$
^{210}Tl external water	2.77×10^{4}	$(1.22^{+0.89}_{-0.75})\times10^{4}$
^{210}Tl hold-down + hold-up ropes	1.03×10^{3}	$(3.70\pm1.75)\times10^{2}$

- Batch 1, containing 0.99 tonnes of natural tellurium (natTe), arrived in January 2015; Batch 2, containing 1.09 tonnes of natTe, arrived in August 2016; Batch 3, containing 2.2 tonnes of natTe, arrived in June 2018.
- Batches have spent 12, 13 and 14 months on surface, respectively.
- Neglected underground cosmogenic activation.
- Assumed underground cooldown times of 8, 6.6 and 4.5 years, respectively.
- Used cosmogenic activation rates and followed calculations from [145]:

$$
\begin{aligned}
&A_1^{EOB} = R_1(1 - e^{-\lambda_1 t_{exp}}),\\
&A_1(t) = A_1^{EOB} e^{-\lambda_1 t},\\
&A_2^{EOB} = R_2(1 - e^{-\lambda_2 t_{exp}}) + R_1 \cdot f \left(1 - \frac{\lambda_2}{\lambda_2 - \lambda_1} e^{-\lambda_1 t_{exp}} + \frac{\lambda_1}{\lambda_2 - \lambda_1} e^{-\lambda_2 t_{exp}}\right),\\
&A_2(t) = A_2^{EOB} e^{-\lambda_2 t} + A_1^{EOB} \cdot f \cdot \frac{\lambda_2}{\lambda_2 - \lambda_1}(e^{-\lambda_1 t} - e^{-\lambda_2 t}).
\end{aligned}
\tag{A.3}
$$

  where 1 and 2 are the indices for the parent and daughter nuclide with decay constant λ, respectively. A^{EOB} is the activity at the end of the exposure time (t_{exp}) on surface, and $A(t)$ is the activity after time t. f is the transition probability of a parent to a daughter nuclide, and R is the cosmogenic activation rate. From the activities, the numbers of a given nuclide was determined with:

$$N = A\frac{T_{1/2}}{\ln(2)}. \tag{A.4}$$

  The number of decays for a given counting time t, after a cooldown period t_{cool} following the cosmogenic activation, is given by:

$$N_{decays}(t) = N(t_{cool}) - N(t). \tag{A.5}$$

- Considered stage I purification reduction factor of up to 10^5 (nuclide dependent) [203], and stage II purification reduction factor of 100 (common to all nuclides), both at the underground level (no reactivation).

Table A.3: Expected cosmogenic backgrounds during the Te-loaded phase within the AV volume. No analysis cuts or detection efficiencies are considered.

Cosmogenic isotope	Counts in Year 1 (no purification)	Counts in Year 1 (Stage I purification)	Counts in Year 1 (Stage I and II purification)
^{22}Na	7.04×10^{3}	3.56×10^{-1}	3.56×10^{-3}
^{26}Al	9.67×10^{-2}	5.86×10^{-5}	5.86×10^{-7}
^{42}K	6.55×10^{2}	3.97×10^{-1}	3.97×10^{-3}
^{44}Sc	8.41×10^{1}	1.87×10^{-2}	1.87×10^{-4}
^{46}Sc	5.21×10^{-2}	1.16×10^{-5}	1.16×10^{-7}
^{56}Co	1.02×10^{-3}	2.79×10^{-9}	2.79×10^{-11}
^{58}Co	2.50×10^{-3}	6.79×10^{-9}	6.79×10^{-11}
^{60}Co	6.62×10^{3}	1.80×10^{-2}	1.80×10^{-4}
^{68}Ga	6.20×10^{2}	3.39×10^{-2}	3.39×10^{-4}
^{82}Rb	5.15×10^{-16}	4.02×10^{-20}	4.02×10^{-22}
^{84}Rb	8.88×10^{-12}	6.94×10^{-16}	6.94×10^{-18}
^{88}Y	2.23×10^{1}	1.74×10^{-3}	1.74×10^{-5}
^{90}Y	5.05×10^{2}	3.94×10^{-2}	3.94×10^{-4}
^{102}Rh	1.33×10^{3}	2.89×10^{-1}	2.89×10^{-3}
^{102m}Rh	9.54×10^{4}	2.07×10^{1}	2.07×10^{-1}
^{106}Rh	8.59×10^{1}	1.87×10^{-2}	1.87×10^{-4}
^{110m}Ag	7.96×10^{2}	6.22×10^{-2}	6.22×10^{-4}
^{110}Ag	1.07×10^{1}	8.35×10^{-4}	8.35×10^{-6}
^{124}Sb	1.77×10^{-2}	1.82×10^{-6}	1.82×10^{-8}
^{126m}Sb	3.06	3.14×10^{-4}	3.14×10^{-6}
^{126}Sb	2.92×10^{-35}	2.99×10^{-39}	2.99×10^{-41}

Appendix B

Energy scale calibration with external backgrounds

Determining the energy scale of the detector during the Te-loaded phase is going to be a priority for SNO+, given its importance for understanding the observed signals. The energy scale can be determined with deployable calibration sources or backgrounds, and the uncertainty of the energy scale calibration results into a systematic uncertainty for the analyses. Due to the strict radiopurity requirements for the Te-loaded phase, the deployment of calibration sources is going to be limited to avoid radon entering the scintillator volume. Therefore, the periodic monitoring of the energy scale is going to be performed using naturally present backgrounds, in particular those producing alpha[1] or gamma particles.

This Appendix describes a method for calibrating the absolute energy scale using external backgrounds, namely ^{40}K. Furthermore, Monte Carlo based studies will evaluate what would be the systematic uncertainty created by this calibration method. These results will be propagated as a systematic uncertainty to the ^{130}Te $2\nu\beta\beta$ decay half-life studies in Chapter 7. ^{40}K has an half-life of 1.28×10^{9} years, and β-decays 89.28% of the time, emitting an antineutrino and an electron with a maximum energy of 1.3 MeV. The other 10.72% of the time it decays by electron capture, with the emission of a neutrino and a 1.46 MeV gamma ray. Even though ^{40}K should also be present internally within the scintillator, the rate of external ^{40}K is expected to be 4–5 orders of magnitude higher, providing a constant, high rate source of 1.46 MeV gamma rays which can be used to calibrate the energy scale.

The biggest challenge for a calibration using external backgrounds, expected to mainly come from the AV and the ropes, is that the majority of the interactions are going to happen near the acrylic vessel, decreasing exponentially towards the centre of the detector. Furthermore, as reported in Section 4.5, due to optical effects the detector response for events happening near the acrylic is different than the response for events happening in the centre. As a consequence, an absolute energy scale determined using external ^{40}K events, which mostly reconstruct near the AV, will not automatically apply to the events reconstructed in more central volumes. The

[1]It is important to note that determining an absolute energy scale using alpha particles would require a good knowledge of the alpha quenching in the liquid scintillator cocktail, in order to decouple this effect from the calibration.

extrapolation of this "external" calibration to the analyses' FV can be done using the internal ^{214}Po αs. Due to the coincidence tagging described in Section 5.2.1, it is possible to obtain a clean sample of these events throughout the whole scintillator volume. They can be used to evaluate the variations with position of the quenched energy scale of the αs and, since the quenching factor is not supposed to vary with position, use that knowledge for the extrapolation of the external ^{40}K energy calibration.

B.1 Method

The energy scale calibration using external ^{40}K decays presented in this Appendix follow the steps:

1. Create a sideband to identify the external ^{40}K events. The goal of the calibration sideband is to maximize the selection of the external ^{40}K, while minimizing other backgrounds, in order to clearly find the peak corresponding to the 1.46 MeV gamma rays in the nHit spectrum;

2. Determine the mean nHit of the external ^{40}K gamma peak, $\overline{\text{nHit}}^{S}_{K}$, by fitting the sideband nHit spectrum with a function including a Gaussian (for the ^{40}K peak) and an exponential (to account for the other backgrounds);

3. Determine the absolute energy scale in the calibration sideband (S):

$$\xi^{S} = \overline{\text{nHit}}^{S}_{K}/1.46 \text{ MeV}. \tag{B.1}$$

4. Determine the mean nHit of the tagged ^{214}Po α peak in the same sideband, $\overline{\text{nHit}}^{S}_{Po}$, by also fitting its nHit spectrum;

5. Determine the mean nHit of the tagged ^{214}Po α peak in the FV of the $2\nu\beta\beta$ decay analysis, $\overline{\text{nHit}}_{Po}$;

6. Extrapolate the absolute energy scale to the $2\nu\beta\beta$ decay analysis FV, using the expression:

$$\xi = \xi^{S} \frac{\overline{\text{nHit}}_{Po}}{\overline{\text{nHit}}^{S}_{Po}}. \tag{B.2}$$

B.1.1 External sideband event selection

The external ^{40}K decays can originate in the support ropes and in the acrylic. The ^{40}K gammas produced in the hold-down rope net, surrounding the upper hemisphere of the AV, have to cross the entirety of the acrylic's thickness before creating a signal in the scintillator, on average travelling a larger distance than the ^{40}K gammas produced within the AV bulk, which only need to cross a part of it. Moreover, in the case of the hold-up ropes, which only connect to the AV around the equator, and the continuation of the hold-down ropes in the lower hemisphere, the gammas will also travel within the external water before reaching the AV. The

attenuation in the acrylic (and external water) will impact the recorded nHit of the 1.46 MeV gamma peak coming from the ropes, in comparison to the gammas coming from the AV bulk[2]. This is illustrated by Figure B.1, which shows the nHit spectra for the Monte Carlo simulations of external ^{40}K coming from the AV (red) and the ropes (blue). Fitting the total (AV+ropes) external ^{40}K gamma peak would then yield different energy scales depending on the ratio of the rate of ^{40}K from the AV over the rate of ^{40}K from the ropes, which would introduce an additional systematic uncertainty on the calibration. For that reason, this method rejects the events coming from the ropes by taking advantage of the symmetry of the ropes' placement around the AV – each of the 20 hold-down ropes is separated from its adjacent by 18° in azimuthal angle ϕ. The hold-up ropes are found in between every second pair of hold-down ropes. Hence, events reconstructed with azimuthal angles [6 + 18n, 12 + 18n] degrees, with n = 0, 1, 2, ..., are rejected from this analysis. This cut reduces the contribution of ^{40}K from the ropes to the expected nHit spectrum by 47%.

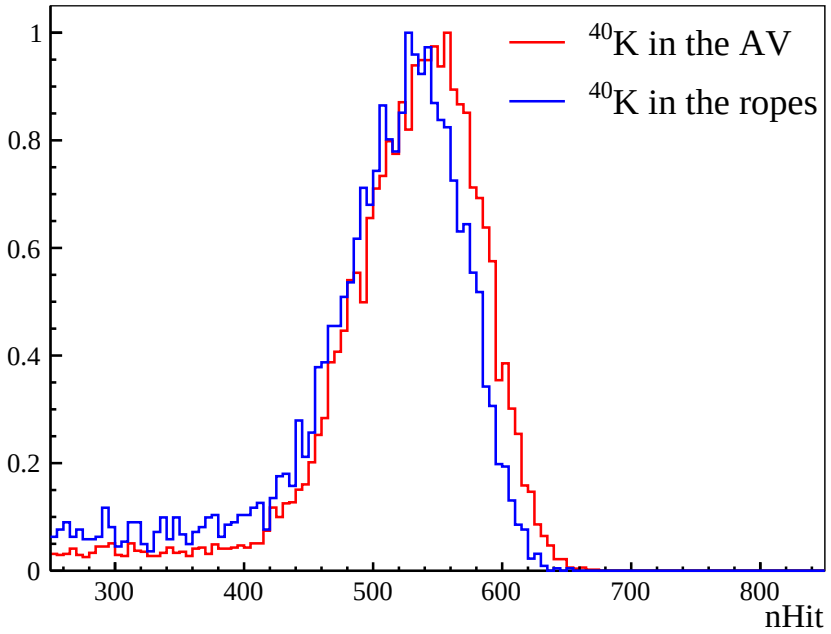

Figure B.1: nHit distribution of the simulated external ^{40}K in the AV bulk (red) and in the ropes (blue). The events were selected within a spherical shell from R = 5.0 m to R = 5.5 m, capped at Z = 3 m.

The selection of external events is maximized by defining a fiducial volume as close as possible to the AV boundaries. This analysis selects events within a spherical shell located between 1 and 0.5 m away from the acrylic. In order to both reject the hold-down rope intersections at the top of the AV, and to avoid the detector response asymmetries created by the neck, a cut is applied to reject all data reconstructed with Z $>$ 3 m (already taking into account the AV–PSUP vertical offset). Table B.1 summarizes the cuts applied to define the calibration sideband.

[2]In order to have a more accurate energy scale calibration using the ^{40}K from the AV, it would be necessary to consider the attenuation effect in the acrylic, even if small. That correction could be determined by a Monte Carlo based study comparing the observed spectrum of ^{40}K in the AV with that of ^{40}K within the scintillator.

Table B.1: Cut variables and values for the external ^{40}K absolute energy scale calibration analysis.

Cut	Value
Fit valid	True
nHit	$250 \leq$ nHit ≤ 850
Azimuthal angle	$\phi <$ 6 + 18n degrees
	$\phi >$ 12 + 18n degrees
	$\phi \in [18n, 18(n+1)]$, with n = 0,1,...
Radial position	5.0 m $<$ R $<$ 5.5 m
Z position	Z $<$ 3.0 m

B.2 Determining the absolute energy scale with Monte Carlo

For these studies, PDFs and fake datasets were prepared from the Monte Carlo simulations described in Section 7.2.1, and following the same steps of Section 7.2.3. Fake datasets were produced assuming one week of livetime. Based on the expected AV radiopurity, one week of data would allow to clearly observe the peak of the external ^{40}K decays and, most importantly, provide enough statistics for the tagged ^{214}Po in the calibration sideband, given the expected internal U concentrations. Figure B.2 shows the energy spectrum of the fake data alongside the PDFs scaled by the expected rates, in the calibration sideband. The external ^{40}K peak was fitted with a Gaussian+exponential function, and the tagged ^{214}Po peaks, in both the calibration sideband and in the $2\nu\beta\beta$ analysis FV, were fitted with a Gaussian function. Table B.2 lists the results of the respective fits. Replacing the values into Equation B.2, the absolute energy scale in the $2\nu\beta\beta$ analysis FV with radius of 3.3 m was determined to be ξ = 390.8 nHit/MeV.

Table B.2: Summary table of the fit results for each calibration variable. The last line shows the resulting absolute energy scale from this calibration method.

Variable	Fitted value
$\overline{\text{nHit}}^{S}_{\text{K}}$	537.7 $\pm$ 0.7 nHits
$\overline{\text{nHit}}^{S}_{\text{Po}}$	317.1 $\pm$ 0.6 nHits
$\overline{\text{nHit}}_{\text{Po}}$	336.5 $\pm$ 0.4 nHits
ξ	390.8 nHit/MeV

B.3 Systematic uncertainty of the energy calibration with the external backgrounds

Multiple components of the method described above contribute towards a systematic uncertainty for the absolute energy scale, namely:

1. The definition of the calibration shell volume, which is affected by the uncertainty of the position reconstruction algorithms;

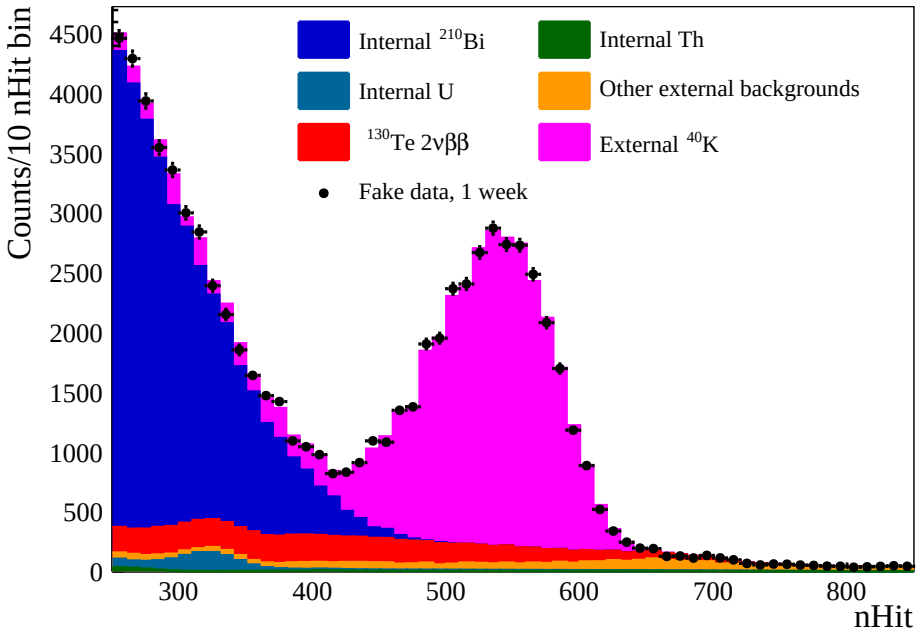

Figure B.2: nHit distribution of fake data (black points) in a spherical shell from R = 5.0 m to R = 5.5 m, capped at Z = 3 m, with azimuthal angle cuts listed in Table B.1. A livetime of 1 week is assumed. The PDFs used to produce the fake data are represented by the coloured histograms. The external ^{40}K PDF is the sum of the individual PDFs of the contribution from the AV and from the ropes.

2. The choice of Z cut to deal with the detector response asymmetry along the vertical axis, caused by the AV neck;

The following Sections will evaluate the impact of each of these components on the absolute energy scale determined in Section B.2. The results will inform a systematic uncertainty for the energy scale.

B.3.1 Calibration volume uncertainty

Monte Carlo studies in [200] show that the position reconstruction fitters have a bias of the order of mm in the x and y coordinates, and a bias of up to 2 cm in the z coordinate, due to the asymmetry caused by the AV neck. Furthermore, the reconstructed values are always higher in z than the true position of the simulations. In order to evaluate the effects of this bias, the reconstructed z coordinates of each simulated event are going to be shifted by $z' = z_{\text{recon}} + 2$ cm, which is equivalent to shifting down by 2 cm the centre of the spherical shell volume.

The shift is applied to the reconstructed position of each simulated event prior to the event selection procedure to create the PDFs. The same cut values of Table B.1 are employed. New fake data is produced based on the new PDFs. Repeating the analysis steps described before, the peak of the external ^{40}K, illustrated by Figure B.3, is fitted with a Gaussian+exponential function. Table B.3 summarizes the results, which yield an absolute energy scale of 389.4 nHit/MeV, a 0.35% systematic change relative to the nominal energy scale ξ.

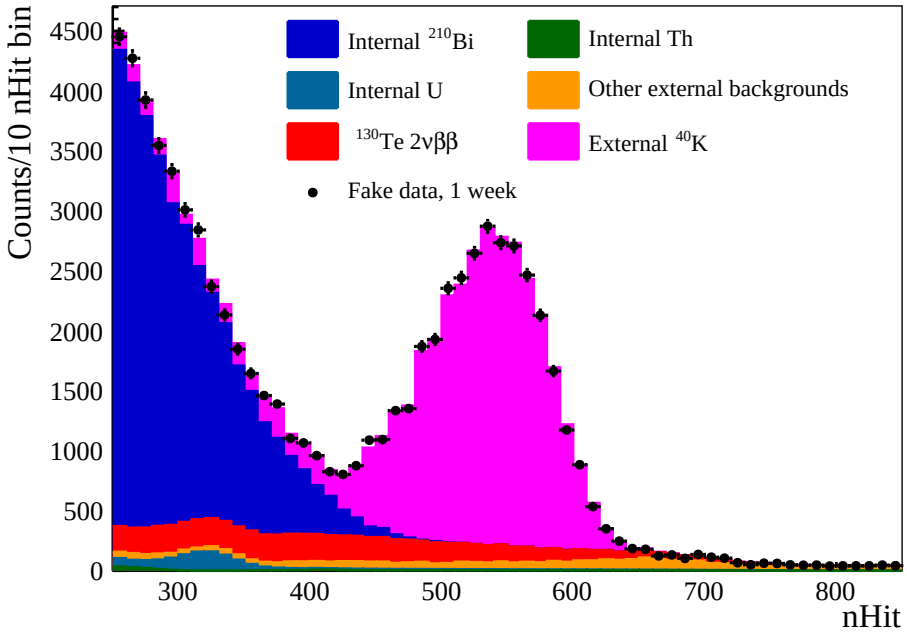

Figure B.3: nHit distribution of fake data (black points) in a spherical shell from R' = 5.0 m to R' = 5.5 m, capped at Z' = 3 m, whose centre is shifted down 2 cm along the vertical axis relative to the AV centre. The azimuthal angle cuts listed in Table B.1 are applied, and a livetime of 1 week is assumed. The PDFs used to produce the fake data are represented by the coloured histograms. The external ^{40}K PDF is the sum of the individual PDFs of the contribution from the AV and from the ropes.

Table B.3: Summary table of the fit results for each calibration variable, in the spherical shell from R' = 5.0 m to R' = 5.5 m, capped at Z' = 3 m, whose centre is shifted down 2 cm along the vertical axis relative to the AV centre. The last line shows the resulting absolute energy scale from this calibration method.

Variable	Fitted value
$\overline{\text{nHit}}^{S}_{\text{K}}$	537.5 ± 0.6 nHits
$\overline{\text{nHit}}^{S}_{\text{Po}}$	318.1 ± 0.7 nHits
ξ	389.4 nHit/MeV

B.3.2 Detector response asymmetry with Z

In order to fully reject the detector response asymmetries caused by the AV neck, all the events with a reconstructed Z coordinate above 1.5 m are rejected. This conservative cut was informed by the detector response asymmetry shown in Figure 4.17. The same procedures were repeated in order to determine the energy scale. Table B.4 summarizes the results, yielding an absolute energy scale of 388.7 nHit/MeV, a 0.5% systematic change relative to the nominal energy scale ξ. Figure B.4 shows the nHit distribution of the fake data generated for this example.

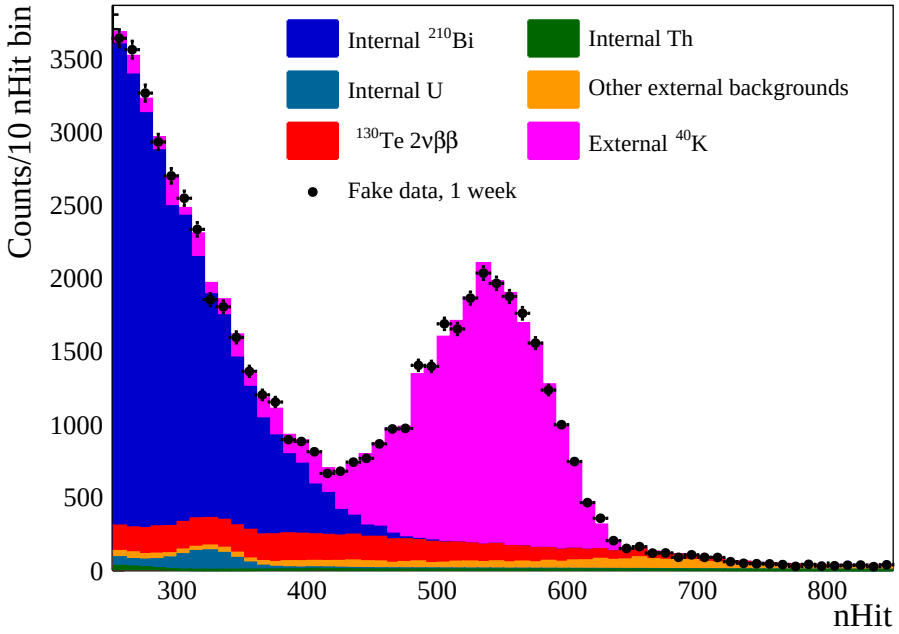

Figure B.4: nHit distribution of fake data (black points) in a spherical shell from R = 5.0 m to R = 5.5 m, capped at Z = 1.5 m, with azimuthal angle cuts listed in Table B.1. A livetime of 1 week is assumed. The PDFs used to produce the fake data are represented by the coloured histograms. The external ^{40}K PDF is the sum of the individual PDFs of the contribution from the AV and from the ropes.

Table B.4: Summary table of the fit results for each calibration variable, in the spherical shell from R = 5.0 m to R = 5.5 m, capped at Z = 1.5 m. The last line shows the resulting absolute energy scale from this calibration method.

Variable	Fitted value
$\overline{\text{nHit}}^{S}_{\text{K}}$	538.5 ± 0.9 nHits
$\overline{\text{nHit}}^{S}_{\text{Po}}$	319.3 ± 0.8 nHits
ξ	388.7 nHit/MeV

B.4 Discussion and conclusions

This appendix proposes a framework to determine and monitor the absolute energy scale of the SNO+ detector using the 1.46 MeV gamma peak of external ^{40}K, which could be used both during the scintillator and Te-loaded phases. This method would allow to determine the energy scale with a preliminary systematic uncertainty of 0.61%, dominated by the Z cut used in the calibration sideband to avoid the detector response asymmetries caused by the AV neck. The goal of these results was to inform a systematic uncertainty for the absolute energy scale, to be propagated into the ^{130}Te $2\nu\beta\beta$ decay half-life studies in Chapter 7.